TU Delft

Delft University of Technology

Carbon nanotube based solutions for on-chip thermal management

Silvestri, Cinzia

DOI
10.4233/uuid:b0407549-ef78-4c29-a07f-fb3f02ec9f30

Publication date
2017

Document Version
Final published version

Citation (APA)
Silvestri, C. (2017). *Carbon nanotube based solutions for on-chip thermal management*. [Dissertation (TU Delft), Delft University of Technology]. https://doi.org/10.4233/uuid:b0407549-ef78-4c29-a07f-fb3f02ec9f30

Important note
To cite this publication, please use the final published version (if applicable).
Please check the document version above.

Copyright
Other than for strictly personal use, it is not permitted to download, forward or distribute the text or part of it, without the consent of the author(s) and/or copyright holder(s), unless the work is under an open content license such as Creative Commons.

Takedown policy
Please contact us and provide details if you believe this document breaches copyrights.
We will remove access to the work immediately and investigate your claim.

This work is downloaded from Delft University of Technology.
For technical reasons the number of authors shown on this cover page is limited to a maximum of 10.

CARBON NANOTUBE BASED SOLUTIONS FOR ON-CHIP THERMAL MANAGEMENT

CARBON NANOTUBE BASED SOLUTIONS FOR ON-CHIP THERMAL MANAGEMENT

Proefschrift

ter verkrijging van de graad van doctor
aan de Technische Universiteit Delft,
op gezag van de Rector Magnificus prof. ir. K. C. A. M. Luyben,
voorzitter van het College voor Promoties,
in het openbaar te verdedigen op vrijdag 7 juli 2017 om 12:30 uur

door

Cinzia SILVESTRI

Master of Science in Electronic Engineering, Università Roma Tor Vergata
geboren te San Giovanni Rotondo, Italy.

Dit proefschrift is goedgekeurd door de

promotor: Prof. dr. ir. P. M. Sarro
promotor: Prof. dr. G. Q. Zhang

Samenstelling promotiecommissie:

Rector Magnificus,	voorzitter
Prof. dr. ir. P. M. Sarro,	Technische Universiteit Delft, promotor
Prof. dr. G. Q. Zhang,	Technische Universiteit Delft, promotor
Onafhankelijke leden:	
Prof. dr. ir. M. Rinaldi	Northeastern University
Prof. dr. ir. W. G. van der Wiel	Technische Universiteit Twente
Prof. dr. U. Staufer	Technische Universiteit Delft
Prof. dr. ir. R. Dekker,	Technische Universiteit Delft
Dr. ir. R. H. Poelma,	Technische Universiteit Delft
Prof. dr. P. J. French,	Technische Universiteit Delft, reservelid

Keywords: carbon nanotubes, thermal management, nanoscale, microhotplate, conduction, convection, radiation, thermographic analysis

Printed by: Ipskamp drukkers

Cover design by: Francesco Dibattista (www.francescodibattista.com)

Cover concept by: Cinzia Silvestri and Nikolas Gaio

Copyright © 2017 by C. Silvestri
All rights reserved. No part of this publication may be reproduced, stored in a retrieval system, or transmitted in any form or by any means without the prior written permission of the copyright owner.

ISBN: 978-94-028-0694-6

An electronic version of this dissertation is available at
http://repository.tudelft.nl/.

To my roots... those of a lemon tree

CONTENTS

1 Introduction **1**

1.1 The Downscaling Era . . . 1

1.2 Miniaturized Thermal Management Solutions . . . 3

1.3 Carbon Nanotube Based On-chip Cooling Solutions . . . 5

1.3.1 CNT based heat sink . . . 5

1.3.2 CNT based TIM . . . 6

1.3.3 CNT based heat spreader . . . 6

1.4 VA- and HA- CNTs for On-chip Thermal Management . . . 7

1.5 Motivation and Outline of this Thesis . . . 8

References . . . 9

2 CNT Synthesis and Morphological Characterization **15**

2.1 Introduction . . . 15

2.2 CNT Synthesis . . . 16

2.2.1 Growth conditions . . . 18

2.3 Morphological Investigation of CNTs . . . 19

2.3.1 Interaction catalyst/barrier layer . . . 19

2.3.2 Packing density and alignment of CNT arrays . . . 24

2.3.3 Tube diameter and crystalline structure . . . 25

2.3.4 Sample quality assessment . . . 26

2.3.5 Surface energy of materials involved . . . 31

2.3.6 Layer thickness . . . 32

2.4 Conclusion . . . 33

References . . . 34

3 Thermal Characterization of VA-CNTs using Microhotplate and Thermographic Analysis **39**

3.1 Introduction . . . 40

3.2 MEMS Microhotplate and Thermographic Analysis . . . 42

3.2.1 Device design . . . 42

3.2.2 Device fabrication . . . 43
3.2.3 Electrical characterization . . . 46
3.2.4 Infrared micro-thermography . . . 47
3.3 Theoretical Analysis . . . 49
3.4 Electro-thermal Measurement Performed in Air and Vacuum . . . 51
3.4.1 Natural Convective Heat Transfer Coefficient . . . 55
3.4.2 Radiative heat transfer coefficient . . . 56
3.4.3 Effective and individual thermal conductivity . . . 58
3.5 Modelling Approach . . . 62
3.5.1 Thermal anisotropy estimation . . . 64
3.5.2 Thermal conductivity variation . . . 64
3.6 Conclusion . . . 67
References . . . 68

4 Effects of Nanoscale Coatings on Thermal Performance of VA-CNTs 71
4.1 Introduction . . . 71
4.2 Coating Procedure and Morphological Characterization . . . 74
4.3 Coating Infiltration in VA-CNT arrays . . . 77
4.4 Heat Transfer Rate of Coated and Uncoated VA-CNTs . . . 79
4.4.1 a-SiC/CNTs . . . 79
4.4.2 Al_2O_3/CNTs . . . 81
4.5 Thermal Performance after Nanoscale Coatings . . . 82
4.5.1 Effective thermal conductivity . . . 82
4.5.2 Porosity . . . 86
4.6 Through Package Thermal Vias based on VA-CNTs . . . 88
4.6.1 Thermal characterization of VA-CNT encapsulated by FAM . . . 90
4.7 Conclusion . . . 91
References . . . 92

5 Self-directed Folding Technique 97
5.1 Introduction . . . 97
5.2 Self-directed Folding Technique . . . 98
5.2.1 Self-directed folding dynamic . . . 101
5.2.2 Densification phase . . . 102
5.2.3 Tilting phase . . . 103
5.2.4 Buckling phase . . . 105

5.3 Flattening Process Engineering . . . 106
5.3.1 Catalyst island optimization . . . 106
5.3.2 HA-CNT thickness . . . 110
5.3.3 Peculiar Effects . . . 112
5.3.4 Al_2O_3 and ZrN HA-CNT sheets . . . 113
5.4 Conclusion . . . 114
References . . . 115

6 Integration and Characterization of HA-CNT Sheets 117
6.1 Introduction . . . 118
6.2 Fabrication Process . . . 119
6.2.1 Phase 1: Pre-patterned wafer . . . 119
6.2.2 Phase 2: CNT synthesis . . . 121
6.2.3 Phase 3: Spatially Programmable Folding . . . 122
6.3 Integration Bottlenecks for ZrN Barrier Layer . . . 124
6.4 Coating Procedure . . . 129
6.5 Morphological Characterization . . . 130
6.6 Electrical Characterization of HA-CNT Sheets . . . 132
6.6.1 Resistance measurement of uncoated HA-CNTs . . . 134
6.6.2 Contact resistance HA-CNT/HA-CNTs . . . 136
6.6.3 Electrical anisotropy . . . 137
6.6.4 Electrical conductivity enhancement through coatings . . . 138
6.7 Electro-thermal Characterization . . . 141
6.7.1 Thermal coefficient of resistance (TCR) . . . 141
6.7.2 Remote Joule heating on HA-CNTs . . . 143
6.8 Conclusion . . . 146
References . . . 146

7 Conclusions and Recommendations 151
7.1 From Spaceland to Flatland . . . 151
7.1.1 Vertically Aligned CNTs - Spaceland . . . 151
7.1.2 Horizontally aligned CNTs - Flatland . . . 152
7.2 Suggestions and Future Works . . . 153

A Appendix A 155
A.1 Supporting Information Chapter 2 . . . 155
A.1.1 Water droplets on CNTs . . . 155
A.1.2 AFM applied on HA-CNT sheets . . . 156

B Appendix B **157**
B.1 Flowchart of VA-CNTs on microhotplate 157
B.1.1 MHP fabrication 157
B.1.2 CNT synthesis 158

C Appendix C **161**
C.1 Flowchart of HA-CNTs on pre-patterned wafers. 161
C.1.1 Wafer pattening 161
C.1.2 VA-CNT synthesis 162

Nomenclature **165**

Summary **169**

List of Publications **175**

1

INTRODUCTION

1.1. THE DOWNSCALING ERA

The continuous strive for miniaturization of electronics and the increased computing capability, all at an affordable price, are among the driving forces of our societal evolution. As result, the performances of modern high-density and highly functional devices are often severely limited by overheating and insufficient heat management [1, 2]. Therefore, when considering device fabrication and packaging, it is important to select materials based on their thermal performance. The increasing demand for more integrated functionality and miniaturization of microelectronic systems, is pushing the limits of traditional cooling and packaging approaches [3]. Efficient thermal management solutions are required at chip level as well as system level. For example, effective heat dissipation is fundamental in microprocessors and integrated circuits (IC) as in mobile electronics as well as server farms. Therefore, the thermal management may well be the major bottleneck of the next electronics revolution [4].

During the last decade, a novel trend driven, not by scaling but by functional diversification, to satisfy societal needs is emerging: the More than Moore (MtM) approach. The major requirement in MtM paradigm is the interaction between an electronic system and the outside world, interaction that is highly dependent on the application envisioned. This implies the heterogeneous co-integration of IC technology with MEMS/NEMS sensors and actuators to supply non-digital functionalities [5]. Hybrid, sustainability, (power) consumption reduction have become the mainstream concepts nowadays. In order to provide multi functionalities and to contain the chip-shrinking competition, emerging packaging strategies are moving towards the third dimension, in

order to increase the integration density and to shorten interconnecting structures [6]. By stacking multi-chip modules, lower power consumption, reduced signal path length with footprints comparable to the largest chip involved, can be achieved.

However, the MtM approach has to face an old challenge: efficient heat dissipation at chip level as well as at system level. No matter if you are approaching the MtM paradigm with hybrid multi-chip (Figure 1.1 (a)) or system-on-chip solutions (Figure 1.1 (b)), the major bottleneck in both cases will be the overheating of the chips. In fact, by integrating components diverse in both working principles and performances, unbalanced power densities and consequently non-uniform temperature distribution (in time and space domains) arises on the chip. Moreover, during the system operation the heat is not dissipated effectively through the various chips, producing localized high temperature regions, known as hot spots. The size of a localized hot spot on a chip may vary from $\sim 500\,\mu m^2$ up to $\sim 5\ mm^2$ [7]. The chip overheating is a serious source of failures causing reliability issues and performance degradation.

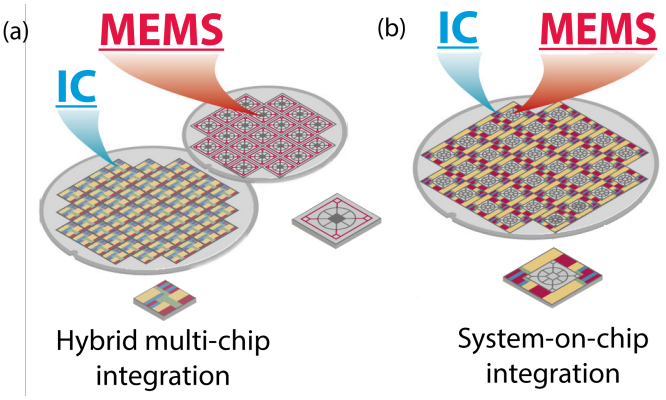


Figure 1.1: Integration methods adopted to combine MEMS and IC technologies. (a) Multi-chip-solutions are less complex and flexible compared to (b) the system-on-chip integration. However, the latter has smaller footprints and it is more robust. Figure adapted with the permission from [8].

Thermal management solutions predominantly promote the heat removal through one of the heat transfer mechanisms: conduction, convection and radiation. In heat spreader, thermal interface material (TIM) and thermal vias (TSV), it is fundamental to employ a material with high thermal conductivity to promote the heat distribution (Figure 1.2 (a-c)). For heat sink instead, it is required to have adequate surface area of the fins to uniformly and efficiently distribute the heat to the surrounding air streams (natural or forced convection as well) (Figure 1.2 (d-e)). High emissivity coatings, surface treatments and paints are widely used in high temperature applications to dissi-

pate heat through the surrounding by radiation. In this thesis, we study novel nanoscale material for improved passive cooling approaches, where there is no need to introduce external energy to enhance the heat transfer as for the active ones.

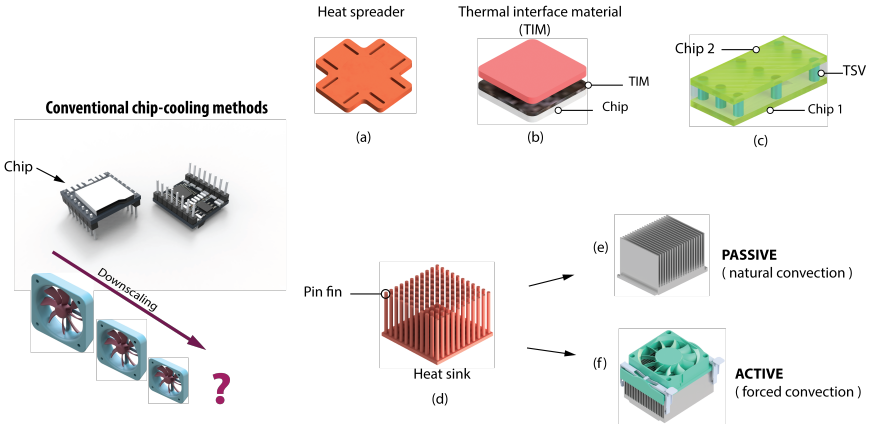


Figure 1.2: Schematic illustration of some of the conventional chip-cooling techniques. (a) A heat spreader is used to absorb the heat from the bottom layer and then distribute it uniformly toward the surrounding an heat sink. (b) A TIM is generally used to reduce the thermal resistance between the heat source and heat sink, by reducing the interstitial air gaps between the matching parts. (c) TSV interposer allows to conduct the heat from a die to die. (d) When a large amount of heat has to be dissipated an heat sink is required. It enhances the heat dissipation by increasing the surface area in contact with the surrounding coolant through fins. A heat sink can be both an active or passive cooling solution. It is passive (e), when the air flow is not externally induced. It is active (f), when the air flow is forced mechanically within the system.

1.2. MINIATURIZED THERMAL MANAGEMENT SOLUTIONS

Traditional cooling approaches both active and passive, are reaching their limits in electronic systems due to physical limitation of the heat transfer capabilities as well as for complexity and size constrain [9, 10]. However, it is very difficult to re-design a well-established cooling technique. A more suitable approach it is to overhaul the current cooling methods by using novel materials. Metals are the materials of choice in most of the cooling approaches due to their relatively high thermal conductivities and low cost. However, due to the thickness reduction of both the package and the chip, metal layers such as aluminum (Al) and copper (Cu), are subjected to an enhancement of electron scattering phenomenon at the layer surface. This implies a substantial thermal conductivity reduction compared to the bulk material (as example from 237 W m^{-1} K^{-1} to 94 W m^{-1} K^{-1} for bulk Al and 140 nm Al film, respectively) [11, 12].

Nowadays, a viable on-chip cooling solution, besides being effective, has to be simple to integrate with the whole system and it has to be reliable and mechanically stable.

1

The based cooling material needs to exhibit a superior thermal conductivity at small scale.

Recently, a better understanding of nanomaterial properties and their integration in microfabrication processes proved to improve heat transfer efficiency, while achieving non-bulky versions of well-known cooling solution (thermoelectric coolers, microchannel heat sinks, heat spreader, etc.). For example, a fully functional chip-scale thermoelectric cooler based on nanostructured thin-film has been demonstrated (Figure 1.3 (a)) [13, 14]. In addition, significant enhancement of the heat transfer has been obtained using silicon nanowire-coated two-phase microchannels (Figure 1.3 (b)) [15]. Lately, the exploitation of highly flexible ferroelectric ceramic nanowire arrays for wearable cooling devices has been reported (Figure 1.3 (c)) [16].

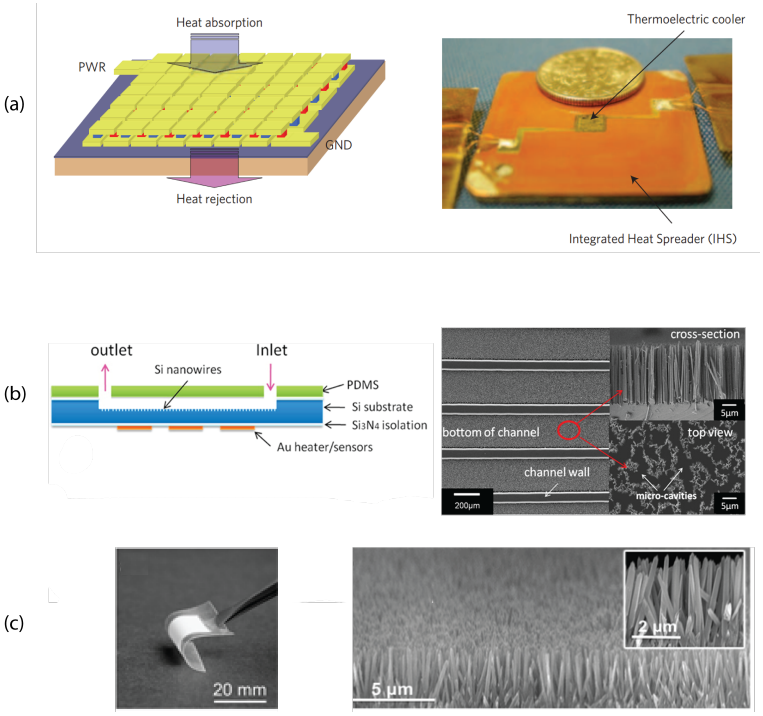


Figure 1.3: Lightweight and compact thermal management solution based on nanomaterials: (a) Schematic of a thin film thermoelectric array and the final device, reprinted with permission from [13]. (b) Two-phase microchannel liquid cooling technology decorated with Si nanowires to increase the flow boiling heat transfer (reprinted with permission from [15]). (c) Wearable cooling patch based on ferroelectric nanowire (reprinted with permission from [16]).

1.3. CARBON NANOTUBE BASED ON-CHIP COOLING SOLUTIONS

Since carbon allotropes and their derivatives possess superior thermal properties within a wide temperature range [17], are inert and have low density [18], carbon-based nanostructured materials appear to be a promising candidates for achieving lightweight and localized on-chip cooling solution [17]. Therefore, our aim is to scale from nano to a macrodomain. Applications spanning from heat spreading through graphene layers or nanocrystalline diamond [19–22], towards carbon nanotubes (CNTs) as thermal interface material (TIM) and heat sinks [23–25] have been reported. In particular, CNT with its exceptional high axial thermal conductivity (>3000 $W\,m^{-1}\,K^{-1}$ for multi-walled tubes) [26], resulting from the strong sp^2 bonds between the constituent carbon (C) atoms, has attracted the interest of many scientists.

1.3.1. CNT BASED HEAT SINK

Kordás et al. have reported the possibility to achieve a scalable micro-fin structure based on multi-walled CNTs (Figure 1.4) [25]. The obtained micro-scale heat sink has shown to have performance comparable to a copper fin design of equal dimensions, thus demonstrating the effectiveness of the cooling method. Therefore, employing CNT micropins as cooling elements is advantageous as it can avoid the use of bulky cooling elements, such as metal blocks and complex fluid-based structures. However, to employ these structures in commercial applications, several challenges need to be faced. First of all, higher effective thermal conductivity values of the fins, possibly while decreasing the CNT growth temperature, should be achieved. Also, it is necessary to increase their mechanical stability, to lower the thermal contact resistance between the CNTs and the substrate and to optimize the geometry and the aspect ratio of the micropins as well as the density of the CNTs within the fins. All these aspects require the development of a methodology to evaluate the heat transfer through CNT micropins as well as a deep understanding of convection and radiation phenomenon that are often neglected.

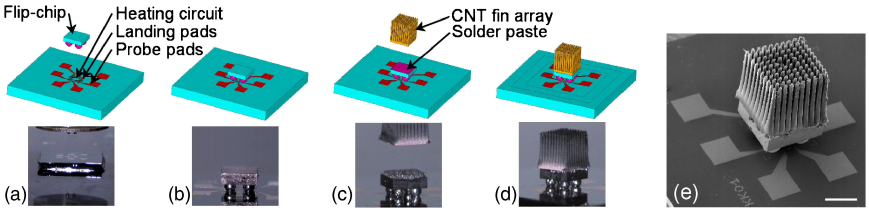


Figure 1.4: Mounting process of a CNT fin array, made of vertically aligned tubes of 10×10 fin, on top of 1 mm^2 surface. Image reprinted with permission from [25].

1

1.3.2. CNT BASED TIM

Over the last few years, TIM composed or containing a certain percentage of CNTs have been investigated by many research groups [12, 27–34]. Most of the TIM layers are made of short vertically oriented CNT forests (in the order of tens of microns) used as interposer between a die and a heat sink (Figure 1.5). To effectively conduct the heat from the source toward the heat sink, the CNTs have to reduce the asperities among the two elements [30–34]. Then, it is of primary importance to minimize the thermal contact resistance between the CNTs and the two interfaces. To achieve so, a gradual pressure is applied to the sample to increase the number of CNTs in close contact with the facing substrates and consequently decreasing the thermal contact resistance [32, 35].
Although in the above-mentioned works, the use of vertically aligned CNTs (VA-CNTs) for IC cooling is promoted, there are still aspects that discourage their practical application. Improved growth conditions or post growth treatments to increase the CNT thermal conductivity are required. Moreover, it is necessary to overcome the lack of a proper physical contact between the forest tip and the opposite interface. In fact, even when pressure was applied to the sample, the thermal contact resistance value obtained (in the order of 10^{-5} m^2 K W^{-1})[36] were comparable to the magnitude of solid-solid interface without TIM [37]. Therefore, also for TIM based solutions improvements are desirable.

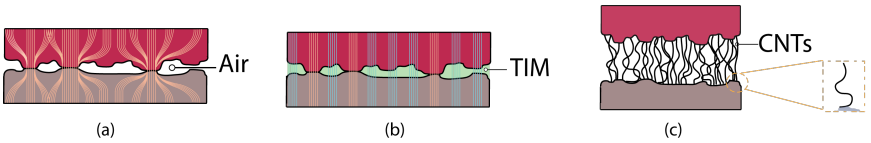


Figure 1.5: Schematic representation (not to scale) of : (a) Surface roughness at the interface between two chip; (b) Interface with addition of TIM, required to reduce air gaps and the thermal contact resistance; (c) TIM made of vertically aligned CNT forest with close up on the direct contact between the tubes and the substrate. The stripes illustrates the thermal paths through the two substrates.

1.3.3. CNT BASED HEAT SPREADER

Another approach to counteract the localized high heat fluxes is to add extra in plane thermal paths on the chip. It is fundamental that the material composing the heat spreader has a high in plane thermal conductivity. Therefore, graphene as 2D layered material with high thermal conductivity has been extensively studied as heat spreader [19, 38, 39]. For example, Gao et al. reported an hot spot temperature reduction of 13°C after the introduction of a single layer of graphene [38]. For practical applications graphene is less attractive since it needs an insulator support layer to be integrated at

chip level, which causes a thermal performance reduction [40]. An alternative solution can be provided by simply varying the CNTs orientation from vertically to horizontally aligned CNTs (HA-CNTs) [41]. By horizontally aligning the CNT it is still possible to take advantage of the high axial thermal conductivity of nanotubes in plane instead of out-of-plane as it was the case for the VA-CNTs. A complete thermal investigation on this novel arrangement is required.

1.4. VA- AND HA- CNTS FOR ON-CHIP THERMAL MANAGEMENT

Individual carbon nanotube has shown superior thermal, mechanical, electrical and optical properties. Unfortunately, these excellent properties are difficult to be preserved in macroscopic applications, and tend to vary with the synthesis method [42]. However, in order to make a step toward the implementation of CNTs as effective thermal management solution for practical applications, it is necessary to go against the "downscaling trend" and move from nano to macro scale configurations, while enhancing their as-grown properties.

As already mentioned, other researchers have worked toward the integration of VA-CNTs as TIM and heat sinks. We strongly believe that the VA-CNT core value is not the predicted desired high thermal conductivity, whereas it is their high aspect-ratio and consequently the surface driven heat transfer mechanisms. The most innovative aspects of this work are:

- The thermal investigation which takes into account both convection and radiation, while in previous works at least one of the two heat transfer mechanism was neglected. In particular, we report for the first time the temperature dependence of the convective heat transfer coefficient of VA-CNT micropins in air.

- A non-destructive *in situ* characterization method for hierarchical structured nanomaterials, which combines electrical characterization and high-resolution thermographic analysis, was developed. The employed experimental procedure allows to perform the investigations over a broad range of temperatures (294.15-575 K) while preserving the as grown VA-CNT properties.

- The foam-like morphology of VA-CNTs allows the infiltration of conformal coatings within the array, achieving a hybrid composite with enhanced thermal performances. The CNT scaffold concept opens the route toward the application of

VA-CNT as thermal and electrical interposer.

However, for applications as heat spreading, a VA-CNT structure can be unpractical. Therefore, HA-CNT sheets are needed. This planar arrangement shows higher robustness than the VA counterpart, thus increasing the possibility to introduce CNTs in standard microfabrication processes. Recently, research efforts has been spent in finding the proper technique to achieve HA-CNTs, from the direct synthesis [43–45] toward horizontal redirection of VA-CNTs by external stimulus [46–52]. The achieved structures were often investigated in terms of electrical performance. In this thesis we report for the first time:

- The thermal and electrical characterization of HA-CNT sheets integrated at wafer scale using standard microfabrication techniques.
- The usage of HA-CNT sheets as scaffold to create reinforced heterostructures, by varying their morphology through nanocoatings.
- An unprecedented enhancement in electrical conductivity and the possibility to turn the thermal response of HA-CNT sheets from semiconductor to metallic behaviour, through coating infiltration.
- HA-CNT sheets obtained on ZrN, a conductive barrier layer, which has the potential to reduce both the electrical and thermal contact resistance.

1.5. MOTIVATION AND OUTLINE OF THIS THESIS

The performance of microelectronic and optoelectronic devices is often severely limited by high temperatures and insufficient heat management. Therefore, when considering device fabrication and packaging, it is important to select materials based on their thermal performance. The goal of this research is to investigate and to demonstrate that CNT arrays can be used as building block for thermal management solutions. The focus will mostly be on assessing the thermal performance achieved in both VA- and HA-CNTs, by jointly using MEMS technology and high-resolution thermographic microscopy analysis.

The initial research problem to be addressed is: *Can VA-CNT micropins be used as localized on-chip cooling solution?* The answer to this question required several steps, addressed in separate chapters:

- What is the thermal behaviour of a CNT configuration? How can it be determined? (Chapter (3))

- How to improve the achieved thermal conductivity? Can VA-CNT micropins be integrated at wafer level? (Chapter (4))

The second research problem is: *How can CNTs be used as heat spreader?* The answer at this question is addressed in two parts:

- How can we achieve and optimize HA-CNT sheets on an insulator and conductor barrier layer? (Chapter (5))
- What are the electrical and thermal performances of the integrated HA-CNT? (Chapter (6))

The thesis is composed of seven chapters and its structure is described below. **Chapter (2)** contains a brief introduction on CNT properties, growth methods and characterization. In particular, it serves the purpose of introducing the reader to the CNT morphological aspects (such as diameter, crystallinity, packing density, etc.) and CNTs grown on two different support layers, aluminum oxide (Al_2O_3) and zirconium nitride (ZrN) are compared. **Chapter (3)** reports on the heat transfer performances of lithographically defined micropins made of VA-CNT nanofoam directly grown on microhotplates. The obtained results and the proposed non-destructive characterization method are discussed in detail. In **Chapter (4)**, we present the thermal conductivity improvement achieved by performing conformal nanocoatings. The successful attempt to integrate amorphous-silicon carbide coated micropins in an epoxy molding compound is presented. **Chapter (5)** introduces a spatially programmable folding used to promote the permutation from VA- to HA-CNT sheets. In **Chapter (6)**, we present the integration of HA-CNT sheets on multiple device configurations and the electrical and thermal properties achieved for samples with and without nanocoatings. **Chapter (7)** summarizes the main results of the thesis and gives recommendations for future work.

REFERENCES

[1] S. Kaur, N. Raravikar, B. a. Helms, R. Prasher, and D. F. Ogletree, *Enhanced thermal transport at covalently functionalized carbon nanotube array interfaces,* Nature Communications **5**, 141 (2014).

[2] D. Lu and C. P. Wong, *Materials for advanced packaging* (Springer US, 2009) p. 719.

[3] J. Cho and K. E. Goodson, *Thermal transport: Cool electronics,* Nature Materials **14**, 136 (2015).

[4] J.-A. Carballo, W.-T. J. Chan, P. A. Gargini, A. B. Kahng, and S. Nath, *ITRS 2.0: Toward a reframing of the Semiconductor Technology Roadmap,* in *2014 IEEE 32nd International Conference on Computer Design (ICCD)* (IEEE, 2014) pp. 139–146.

[5] G. Q. Zhang and A. Roosmalen, eds., *More than Moore* (Springer US, Boston, MA, 2009).

[6] R. Mahajan and B. Sankman, *3D Packaging Architectures and Assembly Process Design,* (Springer International Publishing, 2017) pp. 17–46.

[7] A. L. Moore and L. Shi, *Emerging challenges and materials for thermal management of electronics,* Materials Today **17**, 163 (2014).

[8] A. C. Fischer, F. Forsberg, M. Lapisa, S. J. Bleiker, G. Stemme, N. Roxhed, and F. Niklaus, *Integrating MEMS and ICs,* Microsystems & Nanoengineering **1**, 15005 (2015).

[9] S. V. Garimella, A. S. Fleischer, J. Y. Murthy, A. Keshavarzi, R. Prasher, C. Patel, S. H. Bhavnani, R. Venkatasubramanian, R. Mahajan, Y. Joshi, B. Sammakia, B. A. Myers, L. Chorosinski, M. Baelmans, P. Sathyamurthy, and P. E. Raad, *Thermal Challenges in Next-Generation Electronic Systems,* IEEE Transactions on Components and Packaging Technologies **31**, 801 (2008).

[10] G. J. Snyder, M. Soto, R. Alley, D. Koester, and B. Conner, *Hot spot cooling using embedded thermoelectric coolers,* in *Semiconductor Thermal Measurement and Management Symposium, 2006 IEEE Twenty-Second Annual IEEE* (IEEE, 2006) pp. 135–143.

[11] N. Stojanovic, Jongsin Yun, E. Washington, J. Berg, M. Holtz, and H. Temkin, *Thin-Film Thermal Conductivity Measurement Using Microelectrothermal Test Structures and Finite-Element-Model-Based Data Analysis,* Journal of Microelectromechanical Systems **16**, 1269 (2007).

[12] X. Hu, L. Jiang, and K. E. Goodson, *Thermal conductance enhancement of particle-filled thermal interface materials using carbon nanotube inclusions,* in *Thermal and Thermomechanical Phenomena in Electronic Systems, 2004. ITHERM'04. The Ninth Intersociety Conference on*, Vol. 1 (IEEE, 2004) pp. 63–69.

[13] I. Chowdhury, R. Prasher, K. Lofgreen, G. Chrysler, S. Narasimhan, R. Mahajan, D. Koester, R. Alley, and R. Venkatasubramanian, *On-chip cooling by superlattice-based thin-film thermoelectrics.* Nature nanotechnology **4**, 235 (2009).

[14] X. C. Tong, *Advanced materials for thermal management of electronic packaging*, Vol. 30 (Springer Science & Business Media, 2011).

[15] D. Li, G. S. Wu, W. Wang, Y. D. Wang, D. Liu, D. C. Zhang, Y. F. Chen, G. P. Peterson, and R. Yang, *Enhancing flow boiling heat transfer in microchannels for thermal management with monolithically-integrated silicon nanowires,* Nano Letters **12**, 3385 (2012).

[16] G. Zhang, X. Zhang, H. Huang, J. Wang, Q. Li, L.-Q. Chen, and Q. Wang, *Toward Wearable Cooling Devices: Highly Flexible Electrocaloric Ba _{0.67} Sr _{0.33} TiO ₃ Nanowire Arrays,* Advanced Materials **28**, 4811 (2016).

[17] A. a. Balandin, *Thermal properties of graphene and nanostructured carbon materials.* Nature materials **10**, 569 (2011), arXiv:1106.3789 .

[18] L. L. Zhang and X. S. Zhao, *Carbon-based materials as supercapacitor electrodes,* Chemical Society Reviews **38**, 2520 (2009).

[19] Z. Yan, G. Liu, J. M. Khan, and A. A. Balandin, *Graphene quilts for thermal management of high-power GaN transistors,* Nature Communications **3**, 827 (2012).

[20] J. Zhang, G. Shi, C. Jiang, S. Ju, and D. Jiang, *3D Bridged Carbon Nanoring/Graphene Hybrid Paper as a High-Performance Lateral Heat Spreader.* Small (Weinheim an der Bergstrasse, Germany) **11**, 6197 (2015).

[21] V. Goyal, A. V. Sumant, D. Teweldebrhan, and A. A. Balandin, *Direct Low-Temperature Integration of Nanocrystalline Diamond with GaN Substrates for Improved Thermal Management of High-Power Electronics,* Advanced Functional Materials **22**, 1525 (2012).

[22] G. Yuan, X. Li, Z. Dong, A. Westwood, Z. Cui, Y. Cong, H. Du, and F. Kang, *Graphite blocks with preferred orientation and high thermal conductivity,* Carbon **50**, 175 (2012).

[23] Q. Liang, X. Yao, W. Wang, Y. Liu, and C. P. Wong, *A three-dimensional vertically aligned functionalized multilayer graphene architecture: an approach for graphene-based thermal interfacial materials.* ACS nano **5**, 2392 (2011).

[24] C.-T. Hsieh, C.-E. Lee, Y.-F. Chen, J.-K. Chang, and H.-s. Teng, *Thermal conductivity from hierarchical heat sinks using carbon nanotubes and graphene nanosheets,* Nanoscale **7**, 18663 (2015).

[25] K. Kordás, G. Tóth, P. Moilanen, M. Kumpumäki, J. Vähäkangas, a. Uusimäki, R. Vajtai, and P. M. Ajayan, *Chip cooling with integrated carbon nanotube microfin architectures,* Applied Physics Letters **90** (2007), 10.1063/1.2714281.

[26] P. Kim, L. Shi, a. Majumdar, and P. L. McEuen, *Thermal transport measurements of individual multiwalled nanotubes.* Physical review letters **87**, 215502 (2001), arXiv:0106578 [cond-mat] .

[27] X. J. Hu, A. a. Padilla, J. Xu, T. S. Fisher, and K. E. Goodson, *3-Omega Measurements of Vertically Oriented Carbon Nanotubes on Silicon,* Journal of Heat Transfer **128**, 1109 (2006).

[28] C.-T. Hsieh, Y.-F. Chen, C.-E. Lee, S.-H. Juang, Z.-W. Lin, and M. M. Huq, *Enhancing thermal transport efficiency in carbon composites using nanospacers,* RSC Advances **6**, 61351 (2016).

[29] T. Tong, Y. Zhao, L. Delzeit, A. Kashani, M. Meyyappan, and A. Majumdar, *Dense Vertically Aligned Multiwalled Carbon Nanotube Arrays as Thermal Interface Materials,* IEEE Transactions on Components and Packaging Technologies **30**, 92 (2007).

[30] K. Zhang, Y. Chai, M. M. F. Yuen, D. G. W. Xiao, and P. C. H. Chan, *Carbon nanotube thermal interface material for high-brightness light-emitting-diode cooling.* Nanotechnology **19**, 215706 (2008).

[31] H. Huang, C. H. Liu, Y. Wu, and S. Fan, *Aligned Carbon Nanotube Composite Films for Thermal Management,* Advanced Materials **17**, 1652 (2005).

[32] Y. Xu, Y. Zhang, E. Suhir, and X. Wang, *Thermal properties of carbon nanotube array used for integrated circuit cooling,* Journal of Applied Physics **100**, 074302 (2006).

[33] M. a. Panzer, G. Zhang, D. Mann, X. Hu, E. Pop, H. Dai, and K. E. Goodson, *Thermal Proper-*

ties of Metal-Coated Vertically Aligned Single-Wall Nanotube Arrays, Journal of Heat Transfer **130**, 052401 (2008).

[34] R. Cross, B. A. Cola, T. Fisher, X. Xu, K. Gall, and S. Graham, *A metallization and bonding approach for high performance carbon nanotube thermal interface materials,* Nanotechnology **21**, 445705 (2010).

[35] B. A. Cola, J. Xu, and T. S. Fisher, *Contact mechanics and thermal conductance of carbon nanotube array interfaces,* International Journal of Heat and Mass Transfer **52**, 3490 (2009).

[36] Z. L. Wang, Q. Li, and D. W. Tang, *Experimental Reconstruction of Thermal Parameters in CNT Array Multilayer Structure,* International Journal of Thermophysics **32**, 1013 (2011).

[37] T. Fukuoka and M. Nomura, *Evaluation of Thermal Contact Resistance at the Interface of Dissimilar Materials,* Journal of Pressure Vessel Technology **135**, 021403 (2013).

[38] Z. Gao, Y. Zhang, Y. Fu, M. M. Yuen, and J. Liu, *Thermal chemical vapor deposition grown graphene heat spreader for thermal management of hot spots,* Carbon **61**, 342 (2013).

[39] H. Han, Y. Zhang, N. Wang, M. K. Samani, Y. Ni, Z. Y. Mijbil, M. Edwards, S. Xiong, K. Sääskilahti, M. Murugesan, Y. Fu, L. Ye, H. Sadeghi, S. Bailey, Y. A. Kosevich, C. J. Lambert, J. Liu, and S. Volz, *Functionalization mediates heat transport in graphene nanoflakes,* Nature Communications **7**, 11281 (2016).

[40] Z.-Y. Ong and E. Pop, *Effect of substrate modes on thermal transport in supported graphene,* Physical Review B **84**, 075471 (2011).

[41] L. Qiu, X. Wang, G. Su, D. Tang, X. Zheng, J. Zhu, Z. Wang, P. M. Norris, P. D. Bradford, and Y. Zhu, *Remarkably enhanced thermal transport based on a flexible horizontally-aligned carbon nanotube array film.* Scientific reports **6**, 21014 (2016).

[42] X. Sun, T. Chen, Z. Yang, and H. Peng, *The Alignment of Carbon Nanotubes: An Effective Route To Extend Their Excellent Properties to Macroscopic Scale,* Accounts of Chemical Research **46**, 539 (2013).

[43] H. Guerin, D. Tsamados, H. Le Poche, J. Dijon, and A. M. Ionescu, *In-situ grown horizontal carbon nanotube membrane,* Microelectronic Engineering **97**, 166 (2012).

[44] L. Ding, D. Yuan, and J. Liu, *Growth of High-Density Parallel Arrays of Long Single-Walled Carbon Nanotubes on Quartz Substrates,* Journal of the American Chemical Society **130**, 5428 (2008).

[45] J. Lu, J. Miao, T. Xu, B. Yan, T. Yu, and Z. Shen, *Growth of horizontally aligned dense carbon nanotubes from trench sidewalls,* Nanotechnology **22**, 265614 (2011).

[46] S. Tawfick, K. O'Brien, and a. J. Hart, *Flexible high-conductivity carbon-nanotube interconnects made by rolling and printing,* Small **5**, 2467 (2009).

[47] D. Wang, P. Song, C. Liu, W. Wu, and S. Fan, *Highly oriented carbon nanotube papers made of aligned carbon nanotubes,* Nanotechnology **19**, 075609 (2008).

[48] Y. Hayamizu, T. Yamada, K. Mizuno, R. C. Davis, D. N. Futaba, M. Yumura, and K. Hata, *Inte-*

grated three-dimensional microelectromechanical devices from processable carbon nanotube wafers. Nature nanotechnology **3**, 289 (2008).

[49] S. Tawfick, M. De Volder, and A. J. Hart, *Structurally Programmed Capillary Folding of Carbon Nanotube Assemblies,* Langmuir **27**, 6389 (2011).

[50] H. Li, W. Liu, A. M. Cassell, F. Kreupl, and K. Banerjee, *Low-Resistivity Long-Length Horizontal Carbon Nanotube Bundles for Interconnect Applications—Part II: Characterization,* IEEE Transactions on Electron Devices **60**, 2870 (2013).

[51] M. De Volder, S. H. Tawfick, S. J. Park, D. Copic, Z. Zhao, W. Lu, and A. J. Hart, *Diverse 3D Microarchitectures Made by Capillary Forming of Carbon Nanotubes,* Advanced Materials **22**, 4384 (2010).

[52] T. Yamada, N. Makiomoto, A. Sekiguchi, Y. Yamamoto, K. Kobashi, Y. Hayamizu, Y. Yomogida, H. Tanaka, H. Shima, H. Akinaga, D. N. Futaba, and K. Hata, *Hierarchical three-dimensional layer-by-layer assembly of carbon nanotube wafers for integrated nanoelectronic devices,* Nano Letters **12**, 4540 (2012).

2

CNT Synthesis and Morphological Characterization

2.1. Introduction

Carbon nanotubes (CNTs) can be pictured as a graphene sheet rolled-up to form a tube. Depending on the number of concentric tubes placed one into another a single (SWCNT), a double (DWCNT) or a multi -walled carbon nanotube (MWCNT) is obtained. It is well known that single and multi-walled carbon nanotubes possess superior properties at individual tube level (stated in Table 2.1), namely high electrical and thermal conductivity [1, 2], high strength and flexibility [3, 4], high aspect ratio and leightweight [5, 6]. These findings have generated a significant interest in the scientific community as the considerable increase in publications and patents indicates [7]. Recently, the trend is to create and to engineer a novel class of multiscale macroscopic composite materials, which include or are based on CNTs such as arrays, sheets, buckypapers and yarns (see Figure 2.1). Although, these assemblies aim at exploiting the exceptional properties at macroscopic scale of the as-grown CNT, they often show a remarkable drop (up to several orders of magnitude) of the abovementioned properties. This is related to the difficulty in achieving uniform distribution of catalysts, defect-free tubes, an effective interfacial bonding between CNTs and substrate, etc. In this chapter the synthesis method and the growth conditions of high-aspect ratio CNT arrays are briefly described. In particular, two materials have been selected to be used as barrier layer: Al_2O_3 and ZrN, in-

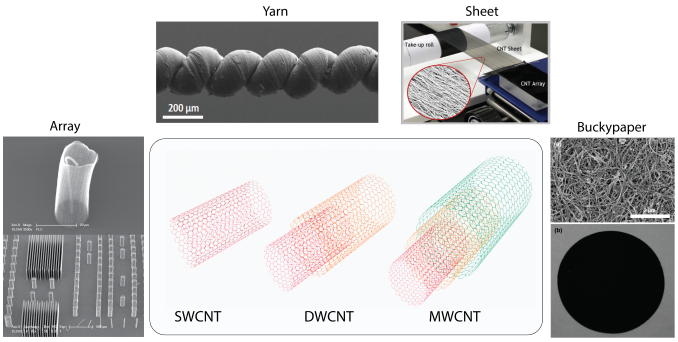


Figure 2.1: Macroscopic composite material based on CNTs: (a) nanotube yarn infused with paraffin from [8]; (b) CNT sheet from [9]; (c) high-aspect ratio CNT array (this work); (d) buckypaper from [10].

sulator and conductive layers, respectively. Both materials allow to achieve lithographically defined high-aspect ratio arrays, while providing CNTs different in both quality and morphology. Moreover, due to their conductive behaviour, the ZrN can potentially reduce the interface contact resistance between barrier layer and CNTs. The techniques employed to characterize the CNTs morphology and physical properties, are briefly introduced throughout the chapter.

Table 2.1: Experimental properties of an individual multi-walled carbon nanotube.

Properties	Description	Ref.
Thermal conductivity	3000 - 1400 W m^{-1} K^{-1}	[11, 12]
Electrical conductivity	0.083×10^{5}-2×10^{5} S cm^{-1}	[13, 14]
Tensile strength	20 -150 GPa	[15, 16]
Young's modulus	0.9 - 2.4 TPa	[15, 17]
Density	1.74 g cm^{-3}	[18, 19]
Thermal stability	diameter increase <500°C in air	[20]

2.2. CNT SYNTHESIS

To grow CNT, three main ingredients are needed: catalyst nanoparticles, a barrier layer and a carbon source. The way in which the carbon source is provided distinguishes the method of CNT production. The main synthesis methods are arch discharge, laser ablation, and chemical vapour deposition (CVD). The arc discharge was the first synthesis method used by Iijima in 1991 to discover CNTs [21]. From then, research started to expand in different directions. Both the reproducibility and the scaling up of the carbon

nanotubes growth were improved by optimizing the synthesis methods [22]. In this thesis the low-pressure CVD method is employed for the CNT nucleation, as it is considered the most viable process for large-scale fabrication and, consequently, economically attractive [23].

When growing CNTs by CVD, the sample loaded into the reactor contains a nano-sized transition metal layer (such as iron (Fe), nickel (Ni), cobalt (Co) and molybdenum (Mo)) deposited on top of a barrier layer. The most common barrier layer materials are Al_2O_3 and SiO_2, which have thermal and chemical stability under the synthesis conditions [22, 24, 25]. When heated up in the reactor, the nanocatalyst layer breaks apart into small particles to minimize the surface energy, increasing the specific surface area and providing nucleation template for CNTs growth. After the grinding of the catalyst layer into small nanoparticles (at temperatures from 500°C to 1100°C), the feedstock, containing a mixture composed by a carrier gas and hydrocarbon precursors (like methane (CH_4) or acetylene (C_2H_2)), is introduced in the reactor. Ones the gases come in contact with the catalyst nanoparticles (Figure 2.2 (i)) they dissociate. The carbon is absorbed by the surface catalyst nanoparticle, leading to the nucleation of a tubular sp^2 carbon structure (Figure 2.2 (ii)), while the hydrogen is released into the reactor [26]. During the CNT growth the metal particle can be lifted up (tip growth) or pulled down (base growth), Figure 2.2 (a) and (b), respectively. The collective growth direction and the lateral confinement of a CNT forest is dictated by the packing density of the catalyst particles and, consequently, to their van der Waals interactions (called crowding effect). By varying the process temperature, the working pressure, the hydrocarbon concentration, the pre-treatment of the catalyst layer and the reaction time the CNT characteristics can be tuned [27].

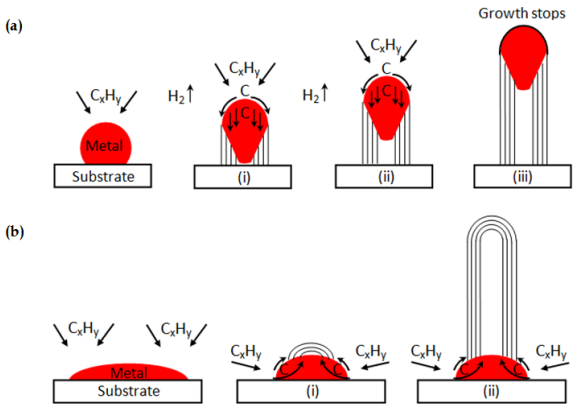


Figure 2.2: CNT growth mechanisms: (a) tip growth and (b) base growth. Reprinted with permission from[28].

Meanwhile, different combinations of substrates, barrier layers and catalyst nanoparticles have been investigated aiming at achieving CNTs with higher quality and density. It is widely recognised that iron (Fe), nickel (Ni) and cobalt (Co) are the three most promising catalysts for CNT growth [29], which are used in combination with oxide barrier layers. CNTs directly grown on metallic barrier layer present many advantages in applications that requires low electrical contact resistance such as interconnects [30], supercapacitors [31], high power switches [32]. However, to achieve CNT growth on metallic substrate is challenging due to the incompatibility between such substrates and the catalysts nanoparticles, fundamental requirement for the CNT nucleation [29]. In fact, the high temperature (> 500°C) involved in the CVD process promotes the diffusion of the catalyst into the thin metallic layer, resulting in low or even no CNT nucleation. Therefore, to overcome the diffusion problem it is common practice to deposit on top of the metallic substrate a thin layer, usually ceramic, prior the catalyst evaporation. An exception is represented by the CNT growth achieved on ZrN layers, an alternative only reported by our research group [33–35].

In this work two different growing recipes will be used for the CNT synthesis associated to the different barrier layer used, namely the Al_2O_3 and the ZrN. The growth conditions for both layer are almost the same. Therefore, in the following section the synthesis recipe for the Al_2O_3 is briefly introduced. Further details for the ZrN can be found in [35].

2.2.1. GROWTH CONDITIONS

The experiments reported in this thesis are based on CNTs grown using an AIXTRON Black Magic CVD reactor. The system allows synthesis at wafer scale (up to 4 inch) and it can operate in LPCVD, the carbon source decomposes when heated, or plasma-enhanced CVD (PECVD) mode, the carbon source decomposes via plasma irradiation. In this work the LPCVD mode is used.

The synthesis process starts by loading the sample in the reactor chamber. Later the chamber is pumped down to < 0.1 mbar and 700 sscm of H_2 is introduced. After reaching the target pressure of 80 mbar, the chamber is heated up to 600°C for 3 minutes to pre-anneal the sample. During this phase the Fe, used as catalyst layer, is grinded into small nanoparticles on the support layer (Al_2O_3 or ZrN). The temperature is then ramped up to the growth temperature of 650°C and a mixture of 50 sccm of C_2H_2 is introduced. By varying the growth time, the CNT array height can be tuned. Once the growth time is elapsed, the C_2H_2 and H_2 are cut off as well as the heating, and the system is pumped

down. The insertion into the reactor of N_2 defines the start of the purging cycle of the reactor that lasts until the reactor temperature is below 400°C. After reaching a temperature below 300°C, the system can be vented and the sample taken out.

By using these growing conditions VA-CNTs are obtained, up to 500µm in height. As mentioned in Chapter (1), we are also interested in achieving HA-CNTs. Although the direct synthesis of HA-CNTs by CVD process has been reported [36, 37], it is generally more difficult, less reproducible and the CNT alignment and density is poor. Therefore, even for achieving horizontally oriented CNT we started from VA-CNTs and then a permutation technique is adopted (see Chapter (6)).

2.3. MORPHOLOGICAL INVESTIGATION OF CNTS

After growing the CNT sample, detailed morphological investigations can be performed by using various characterization techniques. The scanning electron microscopy (SEM) allows to observe the shape, dimensions, degree of alignment and density of the CNTs. To analyse the interior structure of the nanotube, transmission electron microscopy (TEM) is used. Raman spectroscopy is necessary to gain insights about the nanotube crystallinity and the effects on it after performing various process steps. Atomic force microscopy (AFM) provides a better understanding of the interface barrier layer/Fe particles, and for HA-CNTs allows to determine the sheet thickness and nanotube diameter. The sessile drop test is used to evaluate the surface energy and the wettability of both the barrier layers and the CNTs. These techniques are briefly introduced and related to the study of CNT arrays nucleated on ZrN and Al_2O_3.

2.3.1. INTERACTION CATALYST/BARRIER LAYER

Atomic force microscopy (AFM) is a non-destructive characterization technique, with nanometer resolution, used to quantitative characterize the surface morphology of various materials. This technique consists in scanning the sample surface with the sharp tip at the end of a cantilever, named probe. Depending on the sample surface, different scanning modes are available. For our measurements the AFM was operated in semi-contact mode (also known as tapping mode), in which the probe touches periodically the surface. This mode is appropriate for fragile or soft samples on hard substrates. After performing the scan, the data are post-processed to extract quantitative information on the surface morphology. The main parameters monitored during our surface topography analysis are:

- R_{MAX}: maximum height of the profile;
- R_A: average profile roughness, no distinction between peaks and valleys;
- R_Q: root mean square (RMS) roughness, i.e. the square root of the surface roughness profile. It is considered more accurate than R_A because is more sensitive to peaks and valleys;

For more details on all the parameters that can be extracted from the AFM measurement we refer to [38, 39].

In this thesis, the AFM system (NTEGRA Aura AFM) was primarily employed to quantify the roughness of the barrier layer and the de-wetting of the nanocatalyst layer after performing the annealing in the reactor. Since the barrier layer plays a vital role both in promoting the Fe grinding, by confining the catalyst surface migration, and in obtaining VA-CNTs, by achieving a sufficient nanocatalyst particle density, it is fundamental to have a close look at its surface.

Barrier layer surface roughness

Figure 2.3 illustrates the surface morphology of 30 nm thin layer of Al_2O_3 and ZrN, with a scanned area of 500×500 nm^2. The R_Q equal to 0.3 nm and the R_{MAX} of 2.9 nm indicate that the Al_2O_3 barrier layer is very uniform and no spikes are present. On the contrary, the ZrN barrier layer presents a moderate number of hillocks, the biggest one of 58.4 nm in height and around 85 nm in diameter. The R_Q of the whole scanned area is 4.9 nm, while by selecting an area with smaller hillocks it drops down to 1.58 nm with a R_{MAX} of 22.6 nm. The data are summarized in Table 2.2.

Catalyst nanoparticles

The sizes of the metal nanoparticles are influenced by the thickness of the deposited catalyst layer, the activation temperature and the roughness of the two barrier layers [40]. To observe the catalyst nanoparticle size and distribution an activation step, consisting of annealing the sample in the CVD reactor under H_2 flow, is required. In our experiment the catalyst activation temperature on both the Al_2O_3 and the ZrN layers was 495°C. Prior the annealing. the thickness of the evaporated Fe catalyst layer was 1.2 nm and 0.8 nm for the Al_2O_3 and the ZrN, respectively. When heated, the evaporated Fe catalyst film de-wets driven by the total surface free energy minimization at the surface-metal interface, forming arrays of islands [41]. Since most of the oxide layers have a substantially lower surface free energy than the most common metal nanoparticles, the de-wetting of catalyst layer is almost naturally induced by the consistent difference in

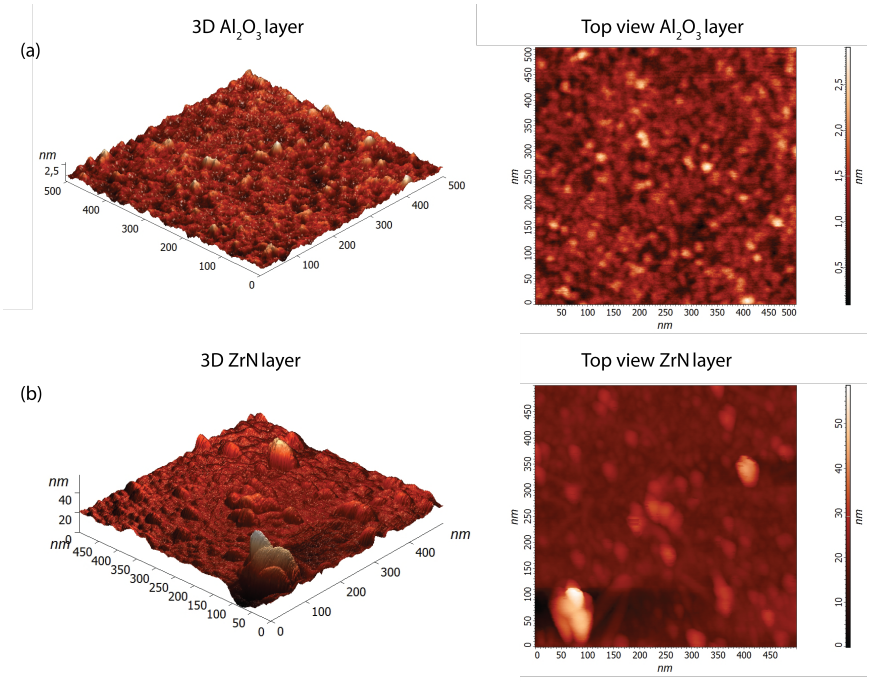


Figure 2.3: 3D and 2D images for an area of 500 × 500 nm^2 of (a) Al_2O_3 layer and (b) ZrN layer, both on LPCVD SiN_x. The surface of the 30 nm layer of Al_2O_3 is uniform with no hillocks. The 30 nm layer of ZrN shows a moderate number of hillocks with a maximum height of 58.4 nm. The analysis and post processing of the collected data were performed by using the Nova by NT-MDT and Gwyddion software.

surface energy among them [42]. Both the Al_2O_3 and the ZrN layers have surface energy and roughness suitable to achieve uniform distributed Fe nanoparticles. While the de-wetting of the ultra-thin Fe layers on Al_2O_3 has been extensively studied [42, 43], here for the first time the one of the Fe nanoparticles on ZrN are examined. The AFM maps with the Fe nanoparticles are illustrated in Figure 2.4.

The Fe nanoparticles are uniformly distributed, confirming their low mobility on the barrier layer [43]. However, difference in sizes, density and diffusion depth depending on the barrier layer underneath are presents. The finite radius of the cantilever tip results in a lateral broadening of the particle scan. Considering that, after the annealing the nanocatalyst film assumes the resemblance of spherical nanoparticles and their average diameter can be inferred by their heights. The number of detected Fe particles and clusters formed on scanned Al_2O_3 and ZrN area are reported in Table 2.2. The analysis of the AFM scans and the processed images shows a slight variation of Fe nanoparticle density with the barrier layer. In particular, the particles on the ZrN are smaller than the one on the Al_2O_3. It is worth noting that after the annealing, the topography of the ZrN with nanoparticles on top does not present hillocks anymore.
The different nanoparticle size achieved on the barrier layers indicates different agglomeration rates during the annealing phase [44]. In the most extreme case, if the nanoparticle clusters achieved are too big, this might inhibit the crowding effect and no vertically aligned CNTs will be obtained.

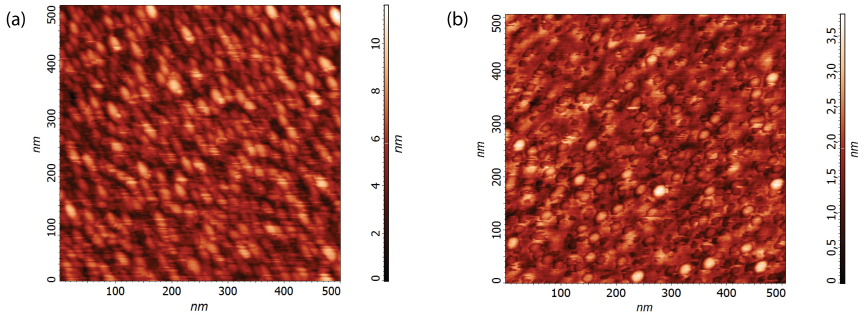


Figure 2.4: AFM surface images for a 500×500 nm^2 area of Fe particles on (a) Al_2O_3 and (b) ZrN barrier layer.

Table 2.2: Characteristics of barrier and catalyst layers used in this study.* The data reported refers to a ZrN area with smaller hillocks.

Properties	Description	Al_2O_3	ZrN
Thickness	Barrier layer thickness	30 nm ± 1.4 nm	30 nm ± 2.3 nm
R_Q	RMS roughness	0.3 nm	1.58 nm*
R_{MAX}	Maximum height of the profile	2.9 nm	22.6 nm*
S_e	Surface free energy barrier layer	38.3 – 44.9 mJ m^{-2}	49.8 – 60.7 mJ m^{-2}
Fe nanoparticles	Number of catalyst particles	479	396
Fe clusters	Number of catalyst clusters	25	13
Fe particle diameter	Average particle diameter	5.5 - 12 nm	2.8 – 4.9 nm

2.3.2. PACKING DENSITY AND ALIGNMENT OF CNT ARRAYS

After achieving the CNT growth with the mentioned conditions and barrier layers, the samples are inspected by SEM. In this thesis a SEM Philips XL50, with an accelerating voltage at 5 keV, is used to morphologically characterize the CNTs. In particular, the aspect ratio, the height, the average diameter, the packing density and the degree of alignment can be determined.

The two SEM images reported in Figure 2.5 are used in combination with a MATLAB® script to estimate the packing density of vertically aligned CNT on ZrN and Al_2O_3. The CNTs on Al_2O_3 show a packing density of ~112 tubes μm^{-2} with a 10% variation among the processed picture, while for the ZrN is ~68 tubes μm^{-2} and can vary up to 17%. This shows that Fe on ZrN gives a reasonable tube density but for the employed growth conditions, it does not reach the stability and density obtained by the combination Fe/Al_2O_3. The obtained value variations show the limitation in precisely determine the packing density by SEM.

The CNTs grown on Al_2O_3 have a higher degree of alignment in comparison to those grown on ZrN. Xu et al. have observed a strong correlation between the degree of alignment of CNT arrays and the catalyst nanoparticle spacing [45]. The link among the two aspects has been found in the crowding effect. At low catalyst density the interaction among neighboring CNTs was minimal (almost absent lateral confinement), producing tubes with arbitrary directions. On the contrary, at high catalyst density, the interaction among CNT increases (higher lateral confinement), thus orienting the tubes along a preferential direction, the vertical one, to minimize the interactions. However, our CNT forests, even if vertically oriented, show waviness and entanglement between neighboring tubes. They can be ascribed to a non-uniform growth rates, due to variation in

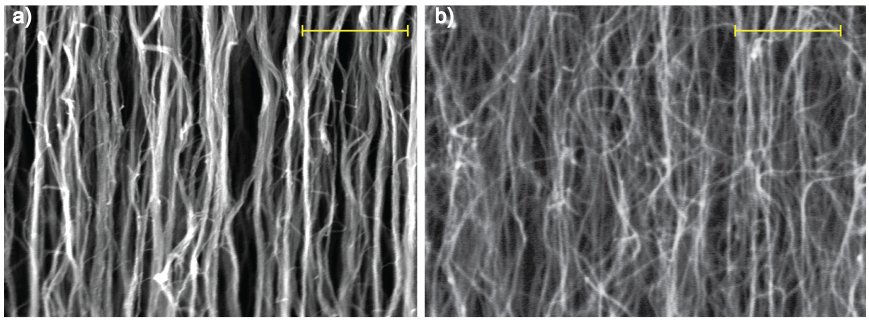


Figure 2.5: SEM picture of the vertically aligned CNT arrays growth (a) on Al_2O_3 and (b)on ZrN. The nanotubes achieved on the ZrN show a lower degree of alignment and more entangled compared to those on Al_2O_3. The scale bar is 500 nm in both pictures.

catalyst nanoparticle sizes, observed by AFM both ZrN and Al_2O_3, and van der Waals interactions being stronger than the crowding effect [46]. The alignment is important because straighter tubes induce potentially higher thermal, electrical and mechanical performances.

2.3.3. TUBE DIAMETER AND CRYSTALLINE STRUCTURE

Transmission electron microscopy (TEM) is used to precisely determine the diameter and the wall numbers that constitute the as-synthesized CNTs, due to its high resolution (down to few angstroms) compared to most other imaging. The core of a TEM system is a high-energy beam of electrons focused on a thin cross-section of a sample. The interaction between the electrons and the sample allows to observe the details related to the latter, like grain boundaries, crystal structure and defects. The samples for TEM are prepared by drop casting a solution containing carbon nanotubes, detached by their native substrate by sonication. The close inspection of the internal structure of nanotubes nucleated on ZrN and Al_2O_3 are reported in Figure 2.6, and the collected data are summarized in Table 2.3. The carbon nanotubes nucleated on Al_2O_3 are MWCNTs with wall numbers varying from 8 to 10. The ZrN sample reports few DWCNTs and a higher quantity of MWCNTs made of 4 walls. The data collected by TEM and AFM show that the outer diameters of the tubes are equivalent to the size of the activated Fe nanoparticles. This confirms the strong influence that the catalyst size has on the CNT structure. From other investigations, both samples have a base growth mode, that reveals a strong adhesion between the metal nanoparticles and the barrier layers [47].

Table 2.3: Summary of the values collected on CNT growth on both barrier layer by SEM and TEM.

CNT parameter	Al_2O_3	ZrN
Packing density	112 tubes μm^{-2}	68 tubes μm^{-2}
MWCNT d_{in}	3.8 ± 0.6 nm	3.5 ± 0.8 nm
MWCNT d_{out}	10 ± 1.2 nm	5.8 ± 0.6 nm
DWCNT d_{in}	/	3.8 ± 0.4 nm
DWCNT d_{out}	/	4.5 ± 0.3 nm

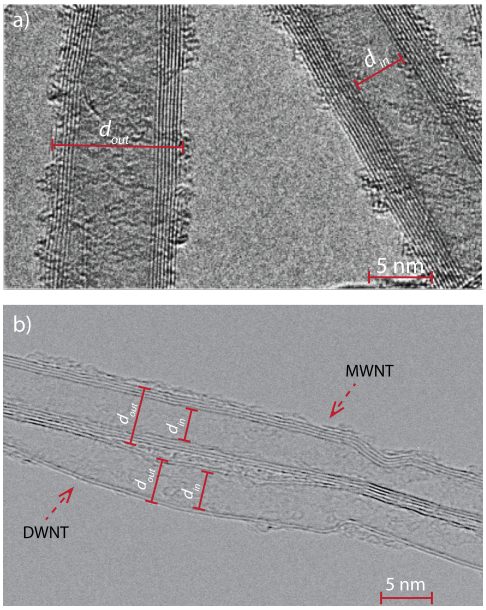


Figure 2.6: Low magnification TEM images of CNTs grown on (a) Al_2O_3 and (b) ZrN barrier layer. The walls, inner and outer diameters are indicated.

2.3.4. SAMPLE QUALITY ASSESSMENT

Although, the TEM it is the most appropriate technique to investigate the crystal structure of the CNTs, it is an expensive and time consuming technique that requires experienced operators in handling the system. A valuable alternative for the lab routine and a non-destructive characterization of the CNT arrays is Raman spectroscopy. The sample is placed under monochromatic light emitted by a laser, which interacts with molecular vibration in the material causing inelastic scatterings. The scattered light from the sample is collected by a spectrometer. Only a small portion of the light scattered varies in energy in comparison to the incident one, underlying the occurrence of interactions between photons and molecular vibrations in the sample. The Raman spectra are collected with a Renishaw inVia system with a laser wavelength, λ, of 514 nm (green laser) or a Horiba LabRAM HR Raman spectroscope, with a nitrogen cooled CCD, with λ of 488 nm (blue laser). The analysis outcome is a graph that reports on the x-axis the acquisition range (from 0 cm^{-1} to 3600 cm^{-1}) and on the y-axis the intensity of the scattered light. The various scattering processes relevant to CNT have been extensively studied [48–51]. The three main interesting regions in a CNT Raman spectra are the radial breathing mode (RBM) from 60 cm^{-1} to 300 cm^{-1}, the first-order region from 1100 cm^{-1} to 1700 cm^{-1} and the second-order region from 2400 cm^{-1} to 3100 cm^{-1}. A typical

spectrum of a MWCNT sample achieved on Al_2O_3 whit λ=488 nm is shown in Figure 2.7.

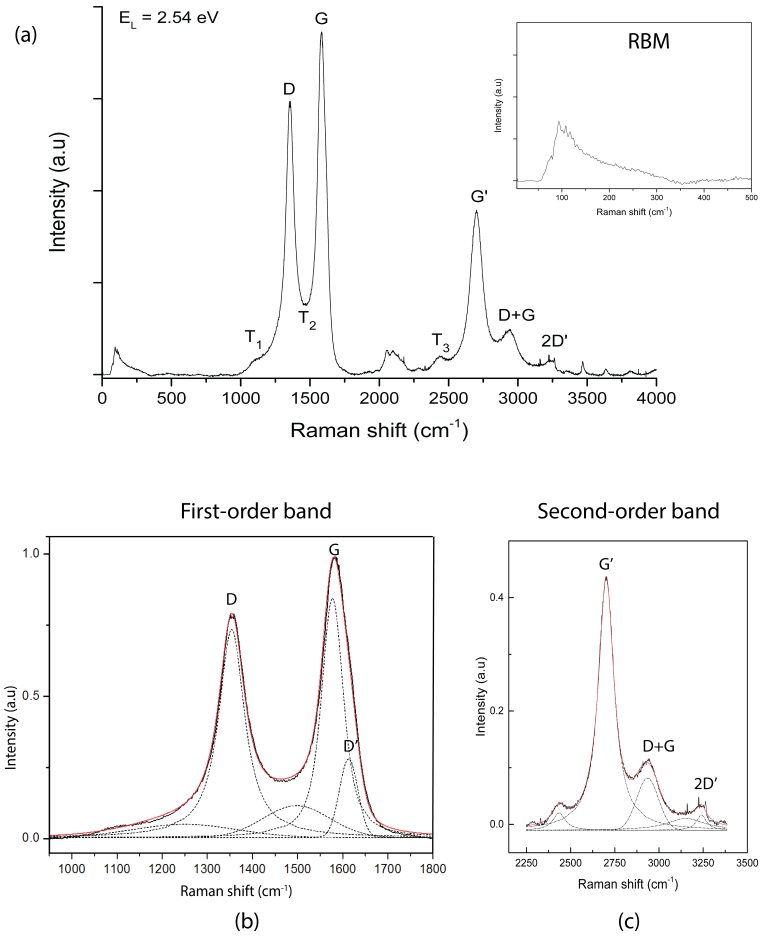


Figure 2.7: (a) Raman intensity versus wavenumber of the MWCNT grown on Al_2O_3, obtained using incident laser of λ=488 nm. Spectra normalized to the G peak. (b) First-order band and (c) second-order band. The dashed lines indicates the fitted spectra.

The first-order band (Figure 2.7 (b)) shows three characteristics peaks related to the D band (1350 cm^{-1}), the G band (1580 cm^{-1}) and the D' band (1610 cm^{-1}). The D band arises from one-phonon scattering process and indicates the sample defects such as broken sp^2 and carbonaceous impurities. The graphitic nature of the MWCNT is reflected in the G band. It corresponds to the stretching vibration of C-C bond. When the G band begin to broaden and consolidate in a single peak it means that contains an increasing number of concentric walls [52].

The second-order band is composed by the overtones and the combination of modes

of the first-order band (Figure 2.7 (c)) [53]. The G' band (2700 cm^{-1}), also named as 2D, arises from the two-phonon scattering process and it is an overtone mode of the D band [54]. Its intensity decreases while the sample crystallinity decreases due to the reduction of the chance to couple two phonons [55], thus leading to information on the lattice order of the synthetized material. The D+G band (2700 cm^{-1}), is defect activated, and is a combined overtone of the G and the D band. The 2D' (3250 cm^{-1}), is an overtone of the D' band.

The low frequency region containing the RBM, originated from a radial coherent contraction-expansion of the carbon atoms and it is usually not visible in the MWCNT spectra. In fact, it is detectable only in tubes having diameter as small as < 2 nm, that are usually SWCNTs. However, we observed low-energy modes in MWCNT as in a few cases reported in literature (see Figure 2.7 inset) [52, 56, 57]. The RBM frequencies of the synthesized MWCNTs are in the same range (120 cm^{-1} to 160 cm^{-1}) of the SWCNT ones detected with the same excitation laser wavelength [56, 58]. Possible explanations of the observed low-energy modes (LEM) are that the observed modes originates from individual SWNT contained in the bundle, or good resonance conditions have been achieved. Further investigations need to be carried out to understand the origin of the observed peaks.

The most valuable data extracted from Raman spectra are the relative intensity ratios of the peaks, which are less affected by errors ascribable to both environmental condition and measurement system. The intensity ratio of D over G band, I_D/I_G, gives an estimation of the number of defect in the tube. The intensity ratios G' over G band, $I_{G'}/I_G$, and G' over D band, $I_{G'}/I_D$, correlate the field emission properties and a more accurate indication of the CNT quality, respectively [55]. Here we report the comparison between the intensity ratios of MWCNT arrays synthesized on Al_2O_3 and ZrN, which is summarized in Table 2.4 and shown in Figure 2.8. A spectra fitting was performed through a MALTLAB® routine, explained in details in [35], before the band intensity ratio evaluation. In particular, the G-, D-, D'-band peaks were fitted to Laurentzians curves, the T_2 with Gaussian curve. The CNTs nucleated on ZrN shows a higher lattice order than for the Al_2O_3, has observed by the lower I_D/I_G ratio.

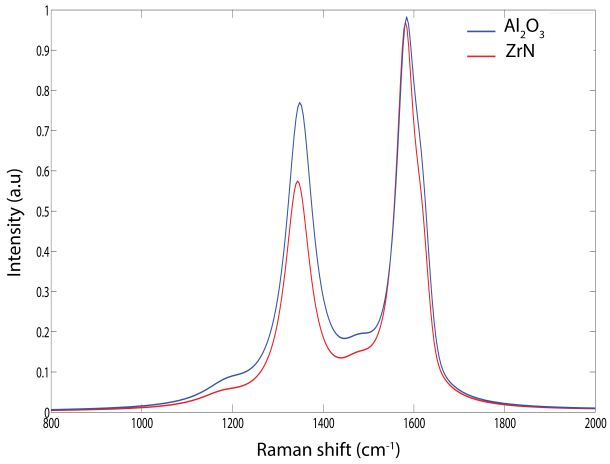


Figure 2.8: (Fitted Raman spectra for Al_2O_3 (in blue) and ZrN (in red).

Table 2.4: Band intensity ratio of the fitted Raman spectra, obtained from MWCNTs grown on Al_2O_3 and ZrN

Sample	I_D/I_G	$I_{G'}/I_G$	$I_{G'}/I_D$
Al_2O_3	0.78	0.34	0.42
ZrN	0.59	0.79	1.33

Crystallinity variation over the length of CNTs

Usually, before the acquisition of Raman spectra, the laser is focused on the tip of the CNT array. However, by acquiring the Raman spectra in different positions along the array length, in both VA- and HA -CNT samples, a crystallinity variation is observed. In previous work carried out by our group [59], the crystallinity variation has been highlighted through the Raman band ratios versus the position along the VA-CNTs (tip, centre and bottom). Here we report the intensity ratio-spatial variations of HA-CNTs (Figure 2.9). For both VA- and HA –CNTs it has been found that the centre has higher quality than the top and bottom.

The observed quality variation can be attributed to the growth dynamics reported in Section 2.2.1 and studied in details by Bedewy et al.[60]. In particular, they explained the evolution and the termination of CNT forest growth in four stages (see Figure 2.10). During the initial phase of CNTs nucleation, the tube within the array starts to self-align due to the Van der Waals interactions. In this phase the CNT results more bent and, as also indicated by our Raman inspection, more defective. The aligned CNTs keep on growing under steady growth conditions, corresponding to the central region of the for-

est. Since the gas and the heater are abruptly cut-off after the growing time elapses, the CNT bundle is subjected to a further morphological variation. In fact, at the bundle tip the tube self-alignment worsen due to the presence of carbon feedstock leftover, which induces defects.

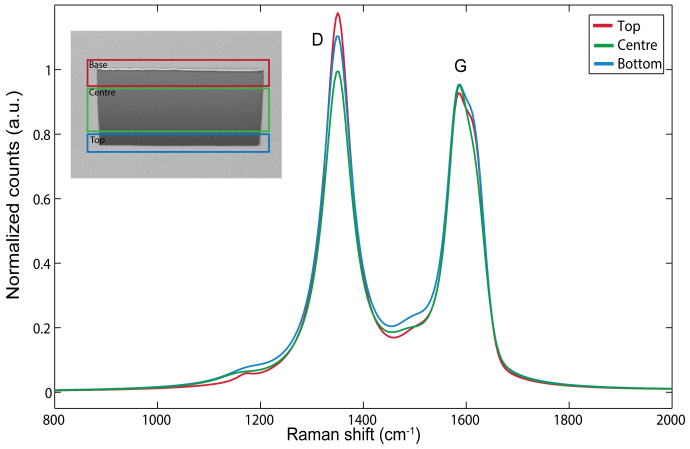


Figure 2.9: Raman Spectra showing the crystallinity variations over the length of a HA-CNT sheet (see inset).

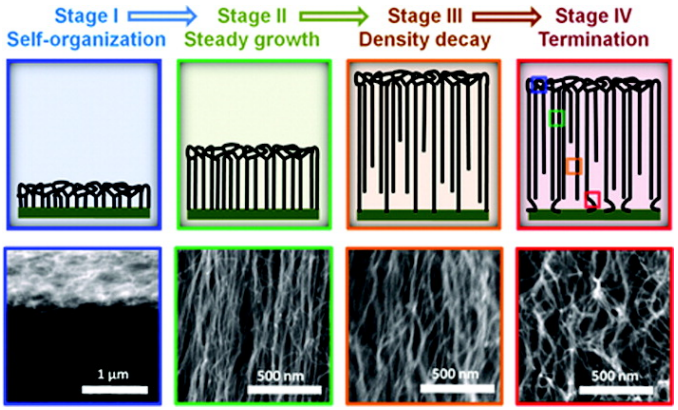


Figure 2.10: (A) Schematic illustration of the four stages of a CNT forest growth: self-organization, steady growth, density decrease, and abrupt self-termination and consequent loss of alignment. High resolution SEM images showing the tube alignment in different section over the length forest; (B) entangled tips of the forest; (C) aligned and dense array; (D) packing density decay; (E, F) randomly oriented morphology at the bottom. Reprinted with permission from [60].

2.3.5. SURFACE ENERGY OF MATERIALS INVOLVED

The surface energy of the barrier layers and the CNTs plays an important role in the work explained in this thesis. In fact, since the surface morphology of the barrier layers and the diffusion of the catalyst ultimately affect the characteristics of the MWCNT forests (such as packing density, tube diameter, etc.), it is important to investigate the surface energy of the barrier materials. In addition, to achieve a successful permutation from VA- to HA-CNTs induced by a liquid, and specifically isopropanol (IPA), it is rather fundamental to understand the surface energies involved to optimize the flattening process. The following section is therefore focused on the wettability study of these two elements: barrier layer and CNTs. To experimentally determine the surface energy a sessile drop test is used. The sessile drop test is an optical measurement that consists in dispensing a microliter droplet of a liquid on top of the sample through a needle. The drop is then captured through a CCD camera and the analysis of its shape allows to optically measure the contact angle. The system adopted in our lab is a OCA-20 goniometer. To infer the surface energy, three different models available in the SCA-21 software can be used to compare the results: the Wu method, the Equation of State (EOS), and the Owens, Wendt, Rabel and Kaelble method (OWRK), for details we cross-refer to [61]. As observed by the AFM maps, the catalyst nanoparticles de-wet on both barrier layers (Al_2O_3 and ZrN) during the annealing phase to minimize the interfacial surface energy. However, they are different in size and distribution, according to the catalyst thickness and roughness, and the surface energy of the support layer [62]. As mentioned in Section 2.3.1, to promote the catalyst layer grinding its surface energy has to be higher than the one of the barrier layer [43]. The surface energy of the two barrier layers used in this thesis was determined by dispensing 5 µL droplets of three solutions: DI water, ethylene glycol and a mixture of both in equal parts. The surface free energy obtained ranges from 38.3 mJ m^{-2} to 44.9 mJ m^{-2} for the Al_2O_3 and from 49.8 mJ m^{-2} to 60.7 mJ m^{-2} for the ZrN. The values are close to each other and they are considerably lower than the Fe surface energy [43], experimentally assessed around 1.72 - 2.12 J m^{-2}. Moreover, attempts were made to capture a sessile drop of IPA on both barrier layers. However, due to the high wettability of the liquid on both Al_2O_3 and ZrN on top of the fast evaporation rate of the IPA at room temperature, it made it impossible to measure. As soon as the IPA touches the surface, it spreads completely on the surface in the attempt to lower its surface energy. This reveals a higher surface tension of the substrate compared to the liquid one. Microliter droplets of DI water and IPA were then dispensed with the same volume on top of CNT forests grown on the Al_2O_3 and the ZrN layer (Figure 2.11). The CNT arrays exhibit high hydrophobicity, as observed by the contact angle formed be-

tween DI water drop and solid surface (CNT). In particular, contact angle of ~123°for CNT arrays grown on ZrN and ~150°for CNT array grown on Al_2O_3 have been obtained. Similar values are reported in literature [63, 64]. However, due to CNT foam-like morphology, the water drop will start to seep into the forest voids as soon as is deposited. The CNT clustering, due to the slow water spreading, is reported in Appendix (A). The difference in packing density among the two samples is reflected in the droplet permeation time into the forest, as well as in the contact angle. As observed in Section 2.3.2, the Al_2O_3 forest shows higher packing density than the ZrN one, implying smaller voids and a longer permeation time of the water droplet. The surface energy difference among the two CNT forests can be mainly attributed to different nano-roughness due to the voids among nanotubes. A study carried by Zhang and Resasco [65] has showed that the void space generates nanoscale roughness, thus causing the formation of a higher hydrophobic surface. In particular, higher exposed areas due to bigger voids imply higher hydrophobicity, as can be seen in ZrN forest. For the IPA droplet dispensed on CNTs, both samples have been found completely wetted by the liquid. This behaviour is explained in detail in Chapter (5) and it is adopted to permute VA-CNTs into HA-CNTs.

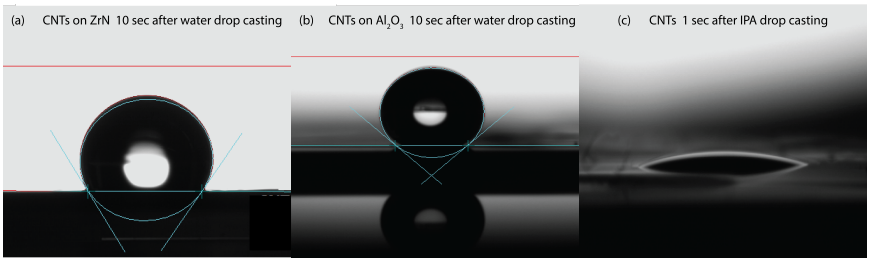


Figure 2.11: Optical image of 5 µL of DI water droplet taken 10 sec after the drop casting on (a) ZrN/CNT and (b) Al_2O_3/CNT. (c) 5 µL of IPA on a CNT forest. The highly wettability and the fast evaporation rate of the IPA make the assessing of the contact angle challenging. The blue line represents the fitted contour.

2.3.6. LAYER THICKNESS

During a microfabrication process it is quite important to determine and to monitor the thickness of the deposited layers. In this thesis, three techniques have been used to quantify the layer thicknesses: spectroscopic ellipsometry, contact profilometer and optical reflectometry, depending on the layer to investigate. We briefly introduce the first two listed techniques, mainly used during the processing and monitoring of the CNTs and their heterogeneous composite. Spectroscopic ellipsometry is an indirect measurement method that allows to accurately determine the thickness of single or multi-layer

thin film materials. A light beam with a specified polarization is focused on the sample. The interaction between the layer and the incident light produces a reflected beam different in polarization. The polarization variation, calculated by an ellipsometer, is due to the physical (thickness, crystallinity, composition, roughness, etc.) and optical properties of the material that constitutes the layer. In this work, a variable angle spectroscopic ellipsometry (VASE) was used to characterize the barrier layer thickness, its variation during etching tests and the achieved coating thicknesses (used in Chapter (4) and Chapter (6)). The contact profilometer is a direct measurement method of the layer thickness, consisting of a diamond-tipped stylus that scans the sample recording the height variation. The stylus is pressed onto the sample surface with a certain force that can be tuned depending on the substrate hardness. The sample is moved through a motorized stage, following a predefined trajectory. The measurement resolution can vary from a few nanometers up to hundreds of microns, depending on the step height to measure. This method is very precise, robust and can be used in routine monitoring to control the profile and the thickness of the structure on a pre-patterned wafer prior to the CNT growth (Chapter (5)), or to assess the thickness of the HA-CNT sheet (Chapter (6)).

2.4. CONCLUSION

In conclusion, the growth and characteristics of two sample set comprising CNTs grown on Al_2O_3 and ZrN have been studied. ZrN revealed to be a promising candidate as conductive support layer for the synthesis of high aspect ratio vertically-aligned CNTs. Compared to the Al_2O_3, the CNT grown on ZrN show lower packing density and alignment (SEM inspection, drop test) but higher degree of crystallinity (Raman spectroscopy), including not only MWCNTs but also few DWCNTs (TEM inspections). The attempt to integrate lithographically defined high-aspect ratio CNT structures achieved on this unconventional conductive support layer are reported in Chapter (6).

As future work, we suggest to compare the surface topography and roughness of the reported ZrN with one subjected to an annealing process. Moreover, to study the Fe nanoparticle diffusion into the ZrN layer, a composition depth profile by using the Auger electron spectroscopy (AES) needs to be carried out. In fact, depending on the diffusion depth, the catalytic activity and the CNT growth can be partially inhibited.

REFERENCES

[1] A. a. Balandin, *Thermal properties of graphene and nanostructured carbon materials.* Nature materials **10**, 569 (2011), arXiv:1106.3789 .

[2] M. J. Biercuk, M. C. Llaguno, M. Radosavljevic, J. K. Hyun, A. T. Johnson, and J. E. Fischer, *Carbon nanotube composites for thermal management,* Applied Physics Letters **80**, 2767 (2002).

[3] E. T. Thostenson, Z. Ren, and T.-W. Chou, *Advances in the science and technology of carbon nanotubes and their composites: a review,* Composites Science and Technology **61**, 1899 (2001).

[4] M.-F. Yu, O. Lourie, M. J. Dyer, K. Moloni, T. F. Kelly, and R. S. Ruoff, *Strength and Breaking Mechanism of Multiwalled Carbon Nanotubes Under Tensile Load,* Science **287** (2000).

[5] V. G. Hadjiev, M. N. Iliev, S. Arepalli, P. Nikolaev, and B. S. Files, *Raman scattering test of single-wall carbon nanotube composites,* Applied Physics Letters **78**, 3193 (2001).

[6] O. Valentino, M. Sarno, N. G. Rainone, M. R. Nobile, P. Ciambelli, H. C. Neitzert, and G. P. Simon, *Influence of the polymer structure and nanotube concentration on the conductivity and rheological properties of polyethylene/CNT composites,* Physica E: Low-dimensional Systems and Nanostructures **40**, 2440 (2008).

[7] H. Golnabi, *Carbon nanotube research developments in terms of published papers and patents, synthesis and production,* Scientia Iranica **19**, 2012 (2012).

[8] M. D. Lima, N. Li, M. Jung de Andrade, S. Fang, J. Oh, G. M. Spinks, M. E. Kozlov, C. S. Haines, D. Suh, J. Foroughi, S. J. Kim, Y. Chen, T. Ware, M. K. Shin, L. D. Machado, A. F. Fonseca, J. D. W. Madden, W. E. Voit, D. S. Galvão, and R. H. Baughman, *Electrically, Chemically, and Photonically Powered Torsional and Tensile Actuation of Hybrid Carbon Nanotube Yarn Muscles,* Science **338** (2012).

[9] P. D. Bradford, *Carbon nanotube fabrics: A new nonwoven material – Advanced Textiles Source,* (2013).

[10] M. B. Jakubinek, B. Ashrafi, J. Guan, M. B. Johnson, M. A. White, and B. Simard, *3D chemically cross-linked single-walled carbon nanotube buckypapers,* RSC Adv. **4**, 57564 (2014).

[11] P. Kim, L. Shi, a. Majumdar, and P. L. McEuen, *Thermal transport measurements of individual multiwalled nanotubes.* Physical review letters **87**, 215502 (2001), arXiv:0106578 [cond-mat] .

[12] Q. Li, C. Liu, X. Wang, and S. Fan, *Measuring the thermal conductivity of individual carbon nanotubes by the raman shift method,* Nanotechnology **20**, 145702 (2009).

[13] T. Ebbesen, H. Lezec, H. Hiura, J. Bennett, H. Ghaemi, and T. Thio, *Electrical conductivity of individual carbon nanotubes,* (1996).

[14] D. Mattia, M. P. Rossi, B. M. Kim, G. Korneva, H. H. Bau, and Y. Gogotsi, *Effect of Graphitization on the Wettability and Electrical Conductivity of CVD-Carbon Nanotubes and Films,* The

Journal of Physical Chemistry B **110**, 9850 (2006).

[15] B. Demczyk, Y. Wang, J. Cumings, M. Hetman, W. Han, A. Zettl, and R. Ritchie, *Direct mechanical measurement of the tensile strength and elastic modulus of multiwalled carbon nanotubes,* Materials Science and Engineering: A **334**, 173 (2002).

[16] N. Khandoker, S. Hawkins, R. Ibrahim, C. Huynh, and F. Deng, *Tensile strength of spinnable multiwall carbon nanotubes,* Procedia Engineering **10**, 2572 (2011), 11th International Conference on the Mechanical Behavior of Materials (ICM11).

[17] R. S. Ruoff, D. Qian, and W. K. Liu, *Mechanical properties of carbon nanotubes: theoretical predictions and experimental measurements,* Comptes Rendus Physique **4**, 993 (2003), dossier: Carbon nanotubes: state of the art and applications.

[18] S. Kim, G. Mulholland, and M. Zachariah, *Density measurement of size selected multiwalled carbon nanotubes by mobility-mass characterization,* Carbon **47**, 1297 (2009).

[19] J. H. Lehman, M. Terrones, E. Mansfield, K. E. Hurst, and V. Meunier, *Evaluating the characteristics of multiwall carbon nanotubes,* Carbon **49**, 2581 (2011).

[20] Z. Luo, A. Oki, L. Carson, L. Adams, G. Neelgund, N. Soboyejo, G. Regisford, M. Stewart, K. Hibbert, G. Beharie, *et al., Thermal stability of functionalized carbon nanotubes studied by in situ transmission electron microscopy,* Chemical physics letters **513**, 88 (2011).

[21] S. Iijima, *Helical microtubules of graphitic carbon,* Nature **354**, 56 (1991).

[22] A. Szabó, C. Perri, A. Csató, G. Giordano, D. Vuono, and J. B. Nagy, *Synthesis Methods of Carbon Nanotubes and Related Materials,* Materials **3**, 3092 (2010).

[23] A. Magrez, J. W. Seo, R. Smajda, M. Mionić, and L. Forró, *Catalytic CVD Synthesis of Carbon Nanotubes: Towards High Yield and Low Temperature Growth,* Materials **3**, 4871 (2010).

[24] V. N. Popov, *Carbon nanotubes: properties and application,* Materials Science and Engineering: R: Reports **43**, 61 (2004).

[25] E. Shawat, V. Mor, L. Oakes, Y. Fleger, C. L. Pint, and G. D. Nessim, *What is below the support layer affects carbon nanotube growth: an iron catalyst reservoir yields taller nanotube carpets,* Nanoscale **6**, 1545 (2014).

[26] S. Hofmann, G. Csányi, A. C. Ferrari, M. C. Payne, and J. Robertson, *Surface Diffusion: The Low Activation Energy Path for Nanotube Growth,* Physical Review Letters **95**, 036101 (2005).

[27] M. Paradise and T. Goswami, *Carbon nanotubes – Production and industrial applications,* Materials & Design **28**, 1477 (2007).

[28] M. Kumar, *Carbon Nanotube Synthesis and Growth Mechanism,* in *Carbon Nanotubes - Synthesis, Characterization, Applications* (InTech, 2011).

[29] J. García-Céspedes, J. Álvarez-García, X. Zhang, J. Hampshire, and E. Bertran, *Optimal deposition conditions of TiN barrier layers for the growth of vertically aligned carbon nanotubes onto metallic substrates,* Journal of Physics D: Applied Physics **42**, 104002 (2009).

[30] S. Vollebregt and R. Ishihara, *Carbon Nanotubes as Vertical Interconnects for 3D Integrated*

Circuits, in *Carbon Nanotubes for Interconnects* (Springer International Publishing, 2016) pp. 195–213.

[31] G. Fiorentino, S. Vollebregt, F. D. Tichelaar, R. Ishihara, and P. M. Sarro, *Impact of the atomic layer deposition precursors diffusion on solid-state carbon nanotube based supercapacitors performances.* Nanotechnology **26**, 064002 (2015).

[32] M. Park, B. A. Cola, T. Siegmund, J. Xu, M. R. Maschmann, T. S. Fisher, and H. Kim, *Effects of a carbon nanotube layer on electrical contact resistance between copper substrates,* Nanotechnology **17**, 2294 (2006).

[33] S. Vollebregt, S. Banerjee, F. D. Tichelaar, and R. Ishihara, *The growth of carbon nanotubes on electrically conductive ZrN support layers for through-silicon vias,* Microelectronic Engineering **156**, 126 (2016).

[34] S. Banerjee, *Super-growth of CNTs based on ZrN for TSV application*, Ph.D. thesis, Delft University of Technology (2014).

[35] S. Vollebregt, *Carbon Nanotubes as Vertical Interconnects in 3D Integrated Circuits*, Ph.D. thesis, Delft University of Technology (2014).

[36] Y. Hayashi, B. Jang, T. Iijima, T. Tokunaga, R. a. Afre, M. Tanemura, and G. a. J. Amaratunga, *Direct growth of horizontally aligned carbon nanotubes between electrodes and its application to field-effect transistors,* INEC 2010 - 2010 3rd International Nanoelectronics Conference, Proceedings , 215 (2010).

[37] A. Reina, M. Hofmann, D. Zhu, and J. Kong, *Growth mechanism of long and horizontally aligned carbon nanotubes by chemical vapor deposition,* The Journal of Physical Chemistry C **111**, 7292 (2007).

[38] M. Raposo, Q. Ferreira, and P. Ribeiro, *A guide for atomic force microscopy analysis of soft-condensed matter,* Modern research and educational topics in microscopy **1**, 758 (2007).

[39] R. De, D. Albuquerque, T. Cruz, F. Yamaji, and F. Leite, *Measurement of the Nanoscale Roughness by Atomic Force Microscopy: Basic Principles and Applications,* in *Atomic Force Microscopy - Imaging, Measuring and Manipulating Surfaces at the Atomic Scale* (InTech, 2012).

[40] Y. Wang, Z. Luo, B. Li, P. S. Ho, Z. Yao, L. Shi, E. N. Bryan, and R. J. Nemanich, *Comparison study of catalyst nanoparticle formation and carbon nanotube growth: Support effect,* Journal of Applied Physics **101**, 124310 (2007).

[41] C. V. Thompson, *Solid-State Dewetting of Thin Films,* Annual Review of Materials Research **42**, 399 (2012).

[42] S. K. Youn, N. Yazdani, J. Patscheider, and H. G. Park, *Facile diameter control of vertically aligned, narrow single-walled carbon nanotubes,* RSC Adv. **3**, 1434 (2013).

[43] C. Zhang, F. Yan, C. S. Allen, B. C. Bayer, S. Hofmann, B. J. Hickey, D. Cott, G. Zhong, and J. Robertson, *Growth of vertically-aligned carbon nanotube forests on conductive cobalt disilicide support,* Journal of Applied Physics **108**, 024311 (2010).

[44] C. Ducati, I. Alexandrou, M. Chhowalla, G. A. J. Amaratunga, and J. Robertson, *Temperature selective growth of carbon nanotubes by chemical vapor deposition,* Journal of Applied Physics **92**, 3299 (2002).

[45] M. Xu, D. N. Futaba, M. Yumura, and K. Hata, *Alignment Control of Carbon Nanotube Forest from Random to Nearly Perfectly Aligned by Utilizing the Crowding Effect,* ACS Nano **6**, 5837 (2012).

[46] H. Cui, G. Eres, J. Howe, A. Puretkzy, M. Varela, D. Geohegan, and D. Lowndes, *Growth behavior of carbon nanotubes on multilayered metal catalyst film in chemical vapor deposition,* (2003).

[47] Y. Wang, B. Li, P. S. Ho, Z. Yao, and L. Shi, *Effect of supporting layer on growth of carbon nanotubes by thermal chemical vapor deposition,* Applied Physics Letters **89**, 183113 (2006).

[48] T. Shimada, T. Sugai, C. Fantini, M. Souza, L. Cançado, A. Jorio, M. A. Pimenta, R. Saito, A. Grüneis, G. Dresselhaus, *et al.*, *Origin of the 2450cm- 1 raman bands in hopg, single-wall and double-wall carbon nanotubes,* Carbon **43**, 1049 (2005).

[49] M. Dresselhaus, G. Dresselhaus, R. Saito, and A. Jorio, *Raman spectroscopy of carbon nanotubes,* Physics Reports **409**, 47 (2005).

[50] C. Thomsen and S. Reich, *Raman Scattering in Carbon Nanotubes,* in *Light Scattering in Solid IX* (Springer Berlin Heidelberg, Berlin, Heidelberg, 2006) pp. 115–234.

[51] S. S. Reich, C. C. Thomsen, and J. J. Maultzsch, *Carbon nanotubes : basic concepts and physical properties* (Wiley-VCH, 2004) p. 215.

[52] X. Zhao, Y. Ando, L.-C. Qin, H. Kataura, Y. Maniwa, and R. Saito, *Radial breathing modes of multiwalled carbon nanotubes,* (2002).

[53] J. Li, Q. Ye, A. Cassell, H. T. Ng, R. Stevens, J. Han, and M. Meyyappan, *Bottom-up approach for carbon nanotube interconnects,* Applied Physics Letters **82**, 2491 (2003).

[54] R. Saito, A. Grüneis, G. G. Samsonidze, V. W. Brar, G. Dresselhaus, M. S. Dresselhaus, A. Jorio, L. G. Cançado, C. Fantini, M. A. Pimenta, and A. G. S. Filho, *Double resonance Raman spectroscopy of single-wall carbon nanotubes,* New Journal of Physics **5**, 157 (2003).

[55] R. A. DiLeo, B. J. Landi, and R. P. Raffaelle, *Purity assessment of multiwalled carbon nanotubes by Raman spectroscopy,* Journal of Applied Physics **101**, 064307 (2007).

[56] H. Jantoljak, J.-P. Salvetat, L. Forró, and C. Thomsen, *Low-energy Raman-active phonons of multiwalled carbon nanotubes,* Applied Physics A: Materials Science & Processing **67**, 113 (1998).

[57] J. Benoit, J. Buisson, O. Chauvet, C. Godon, and S. Lefrant, *Low-frequency raman studies of multiwalled carbon nanotubes: experiments and theory,* Physical Review B **66**, 073417 (2002).

[58] K. Cui, A. S. Anisimov, T. Chiba, S. Fujii, H. Kataura, A. G. Nasibulin, S. Chiashi, E. I. Kauppinen, and S. Maruyama, *Air-stable high-efficiency solar cells with dry-transferred single-walled carbon nanotube films,* J. Mater. Chem. A **2**, 11311 (2014).

[59] S. Vollebregt, P. Padmanabhan, C. Silvestri, and P. M. Sarro, *Crystallinity variations over the length of vertically aligned carbon nanotubes grown by chemical vapour deposition,* in *41st Micro and Nano Engineering conference* (2015).

[60] M. Bedewy, E. R. Meshot, H. Guo, E. A. Verploegen, W. Lu, and A. J. Hart, *Collective Mechanism for the Evolution and Self-Termination of Vertically Aligned Carbon Nanotube Growth,* The Journal of Physical Chemistry C **113**, 20576 (2009).

[61] Attension, *Surface free energy -theory and calculations*, Tech. Rep.

[62] S. J. Randolph, J. D. Fowlkes, A. V. Melechko, K. L. Klein, H. M. Meyer III, M. L. Simpson, and P. D. Rack, *Controlling thin film structure for the dewetting of catalyst nanoparticle arrays for subsequent carbon nanofiber growth,* Nanotechnology **18**, 465304 (2007).

[63] L. Zhu, J. Xu, Y. Xiu, Y. Sun, D. W. Hess, and C.-P. Wong, *Electrowetting of aligned carbon nanotube films,* The Journal of Physical Chemistry B **110**, 15945 (2006).

[64] H. Liu, J. Zhai, and L. Jiang, *Wetting and anti-wetting on aligned carbon nanotube films,* Soft Matter **2**, 811 (2006).

[65] L. Zhang and D. E. Resasco, *Single-Walled Carbon Nanotube Pillars: A Superhydrophobic Surface,* Langmuir **25**, 4792 (2009).

3

THERMAL CHARACTERIZATION OF VA-CNTS USING MICROHOTPLATE AND THERMOGRAPHIC ANALYSIS

This chapter is based on:

1. **Cinzia Silvestri**, Michele Riccio, René H. Poelma, Bruno Morana, Sten Vollebregt, Fabio Santagata, Andrea Irace, Kouchi Zhang, Pasqualina M. Sarro. "Thermal characterization of carbon nanotube foam using MEMS microhotplates and thermographic analysis".*Nanoscale*, Volume 8, pp. 8266-8275, 2016.
2. **Cinzia Silvestri**, Paolo Piacciafoco, Bruno Morana, Fabio Santagata, Kouchi Zhang, Pasqualina M. Sarro. "Electro-thermal simulation and characterization of vertically aligned CNTs directly grown on a suspended microhoplate for thermal management applications". In *IEEE Sensors Conference*, pp. 827-830, 2014.
3. **Cinzia Silvestri**, Bruno Morana, Giuseppe Fiorentino, Sten Vollebregt, Gregory Pandraud, Fabio Santagata, Kouchi Zhang, P.M. Sarro. "CNT bundles growth on microhotplates for direct measurement of their thermal properties". *In 27th IEEE International Conference on Micro Electro Mechanical Systems (MEMS 2014)*, San Francisco, USA, pp. 48-51, 2014.

3.1. INTRODUCTION

CNT-based nanofoam materials appear to be a promising candidate for achieving effective local heat dissipation [1]. However, the outstanding thermal properties only apply to individual CNTs. When grown in a nanoporous network of vertically aligned CNT arrays, a remarkable drop in thermal conductivity is observed, ranging from 0.1 to 220 W m^{-1} K^{-1} [2]. The main explanation for the significant thermal conductivity reduction, as compared to single CNTs, is the relative high porosity of the foam-like CNT arrays and the weak thermal coupling between neighbouring nanotubes in van der Waals contact [3].

Nevertheless, foam-like VA-CNT arrays exhibit significant advantages. Firstly, they are one of the few nanoscale materials that can be grown from a bottom-up template, which is lithographically defined and patterned using a CMOS compatible process. This makes the material extremely suitable for large-scale integration with microelectronics, replacing the need for heterogeneous integration and assembly of bulky macro-cooling solutions, such as heat sinks and fans. Secondly, the material can grow fast (growth rate of around 20µm min^{-1} and can span size scales ranging from nanometers to centimeters. Therefore, it is very suitable for creating high-aspect-ratio three-dimensional (3D) microarchitectures [4]. No other nanoscale material has shown similar capabilities. By combining both lithographically defined patterns and the fast vertical growth, almost infinite combinations of customized shapes and arrangements can be achieved, making the CNT nanofoam suitable for fabrication of localized, passive, customized on-chip cooling solutions, like microfins and pins, arrays and other 3D structures (see Figure 3.1). The achieved high-aspect ratio foam-like CNT micropins can be grown on top of free standing membranes [5]. This has highlighted the possibility to take advantage of the increased surface area, due to the high nanoporosity and high-aspect ratio of the CNT arrays, to enhance convective and radiative heat dissipation from device towards the surrounding environment. Thirdly, by combining the nanoporous morphology of VA-CNTs with different nanoscale conformal coatings, we have the unique opportunity to control the functionality and tune the material properties [6]. In fact, it has been demonstrated that by using thin coatings of only a few nanometers, a high elastic recovery to the CNT nanofoam can be obtained while maintaining a high compliancy [7]. This makes the nanofoam promising as TIM, replacing the contaminating and difficult to apply pastes. Moreover, they have great potential to be used as low weight framework for a broad range of applications, from three-dimensional carbon electrodes [8], to thermo-acoustic transducers [9], to thermo-chromic displays [10], to nanotexturing for solar cells [11].

For analysing and predicting microelectronic system performance, it is imperative

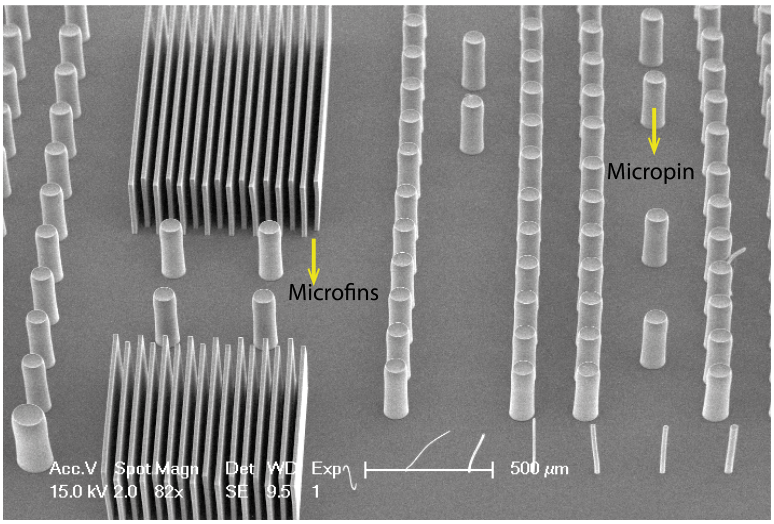


Figure 3.1: SEM images showing the customized shape of high-aspect ratio CNT nanofoams defined by photolithographic patterning of the catalyst particles by lift-off.

that material properties are characterized and optimized. Even though considerable research efforts have been devoted to characterizing the thermal conductivity of carbon based nanomaterials, significantly less attention has been paid to the more complex interaction between gas and nanoporous material which is expressed in terms of a convective heat transfer coefficient. This coefficient is important as it accounts for a significant amount of dissipated heat, and should be included for accurate characterization of thermal performance. The heat transfer coefficient across the solid-gas interface and its variation with pressure, has been measured for a single nanowire in a gas environment by Cheng et al. [12]. However, no experimental data can be found in literature discussing the natural convective heat transfer coefficient of foam-like vertically aligned CNT arrays and its temperature dependency at micron scale. Moreover, thermal investigations on CNT arrays are often carried out at relatively low temperature (up to 390 K), thus the thermal radiative heat transfer is often negligible [13]. Foam-like CNT arrays have a large surface area to volume ratio. When combined with the almost perfect black body radiative properties, significant radiative losses at low temperature can be achieved [14].

In this chapter, we report on the heat dissipative properties of lithographically defined foam-like CNT arrays in vacuum and in the natural convective regime. To perform these thermal measurements a novel experimental approach was developed combining

MEMS microhotplates (MHPs), on which the nanofoam materials are grown, with high-resolution thermographic analysis. Using direct growth of CNTs on the chip, we can limit contact resistance, facilitate the sample handling and examine more directly the intrinsic properties of the nanofoam material. Using a MHP device as both the heating source and as integrated thermal sensor, we characterize under a steady-state temperature condition several CNT arrays patterned in different configurations. The equivalent natural convective heat transfer coefficient between solid-air interface (H_c), the radiative heat transfer coefficient (H_{rad}) and the CNT nanofoam effective thermal conductivity (k_{eff}) over a wide temperature range are quantified. Furthermore, we develop a 3D finite-element model to be used as predictive tool of the thermal behaviour of different CNT bundle arrangements, and we estimate the anisotropic thermal conductivity of CNT nanofoam. This study demonstrates the effectiveness of lithographically defined CNT nanofoam structures as on-chip cooling solutions for consumer electronics applications.

3.2. MEMS MICROHOTPLATE AND THERMOGRAPHIC ANALYSIS

Performing thermal measurements on nano- and microscale CNT structures is challenging. Difficulties arise from handling of the material, controlling contributions from contact resistances as well as lack of an appropriate measurement apparatus with sufficient resolution. To overcome these issues, we developed a measurement approach that combines a micro-electro-mechanical systems (MEMS) based experimental platform with high-resolution IR thermographic imaging. This new method provides several advantages. First of all, the material to be analysed is directly grown on our measurement device; hence no complex sample handling or further processing is needed. Moreover, there is no additional contact resistance caused by the assembly of the material on the measurement apparatus as needed in conventional techniques. Lastly, the MEMS integrated temperature sensor and power controller have a high accuracy because they are placed within nanometer distance from the material to be analysed. Details about other experimental characterization techniques can be found in [15].

3.2.1. DEVICE DESIGN

To accurately discern the dissipative contribution of the high-aspect ratio CNT nanofoam and nanomaterial in general, firstly it is mandatory to conceive a structure that will confine and direct the heat through the material under test, and secondly that will

allow to know precisely the in situ temperature value. The mentioned objectives can be reached by employing a suspended membrane, constituted from a material with a low thermal conductivity in which a heating element is embedded. The answer to our requirement is called microhotplate (MHP). The MHP consists of a low-stress 400 nm thick SiN_x square membrane with an area of 1 mm^2, in which a platinum (Pt) microheater is integrated, as shown in Figure 3.2. The microheater has a spiral geometry, which covers a central area of 330µm × 330µm with a metal thickness of 180 nm. On top of the MHPs high-aspect ratio CNT micropins are then directly grown on lithographically defined locations.

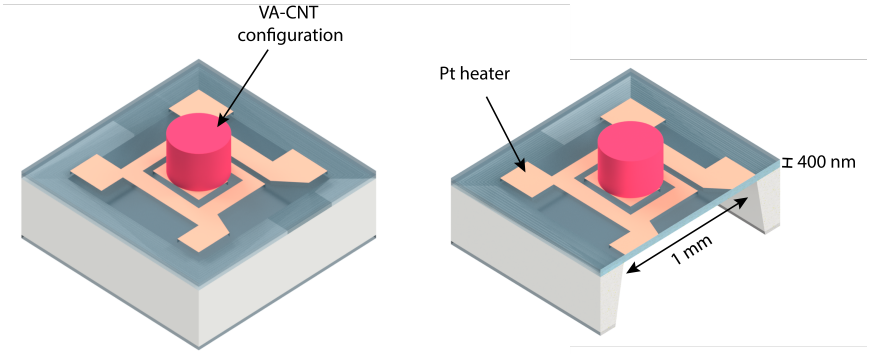


Figure 3.2: 3D sketch and cross-section of the microhotplate equipped with the VA-CNT micropins. Draw not on scale.

3.2.2. DEVICE FABRICATION

The device fabrication can be divided in two phases: the MHP fabrication and the CNT synthesis.

Phase 1: MHP fabrication

The starting material is a single side polished silicon (Si) wafer, with a thickness of 525µm and 100 mm in diameter. First, a 200 nm thick low stress LPCVD SiN_x layer is deposited to provide electrical insulation. This step is followed by the evaporation of 160 nm of Pt on an adhesion layer of 20 nm of Tantalum (Ta). A lift-off process is used to pattern the Ta/Pt layer into a 18µm wide resistive spiral. A second layer of 200 nm of low-stress LPCVD SiN_x is deposited to seal the heater and to create a symmetrical thermal configuration. The wafer is then annealed at 1000 °C for 1 hour to stabilize the resistivity of the metal. The final value of the spiral sheet resistance is 1.76 Ω/□. The Pt contact pads are opened by dry etching of the SiN_x to allow electrical characterization of the micro-

heaters. In order to release the 1×1 mm^2 membrane, the backside is patterned and the Si substrate is removed in a 33 wt% KOH solution at 85°C, using SiN_x as hard mask. The mentioned fabrication steps are summarized in Figure 3.3.

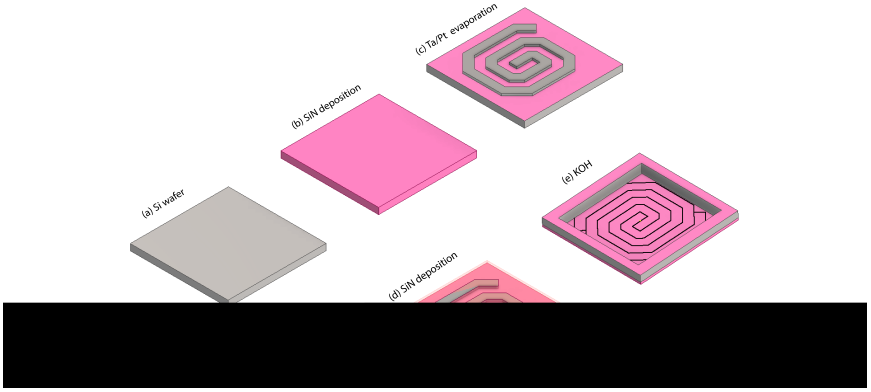


Figure 3.3: Microhotplate fabrication. (a) On a bare Si wafer (b) 200 nm of LPCVD SiN_x is deposited. The wafer is coated with 2µm of negative resist and patterned to define the microheater spiral, and then a layer stack of Ta/Pt is evaporated on the entire surface. (c) Once performed the lift-off, (d) other 200 nm of LPCVD SiN_x is deposited. After annealing the full wafer, (e) the KOH is performed to release the membrane.

Phase 2: CNT synthesis

After the MHP fabrication a sputtered Al_2O_3 layer of 10 nm thick and 1.2 nm of Fe are used as barrier and catalyst layer, respectively (Figure 3.4). The catalyst islands are defined by coating, exposing and developing 2µm negative photoresist spun on top of the MHP surface. The as defined wafer underwent the Fe catalyst deposition by e-beam evaporation, using a CHA Solution evaporator (Figure 3.4 (a-d)). After the metal evaporation, a lift-off process is applied by immersing the wafer in a stirred N-Methyl-2-pyrrolidone (NMP) solution at 85°C for 3 minutes. The lithographically defined catalyst (Fe) areas with diameters of 20µm or 200µm are now created (Figure 3.4 (e)). The CNT micropins are grown by CVD at 650°C for 5 minutes (Figure 3.4 (f)). Tests were performed on a wafer containing the same CNT arrangements on both suspended and not suspended MHPs. No significant difference in CNT growth rate was observed between the two types of samples, as confirmed by measuring the achieved height after 5 min synthesis under SEM inspection. This indicates a good uniformity of the heat distribution in the CVD reactor and the recipe robustness. Details on the fabrication process are reported in Appendix (B).

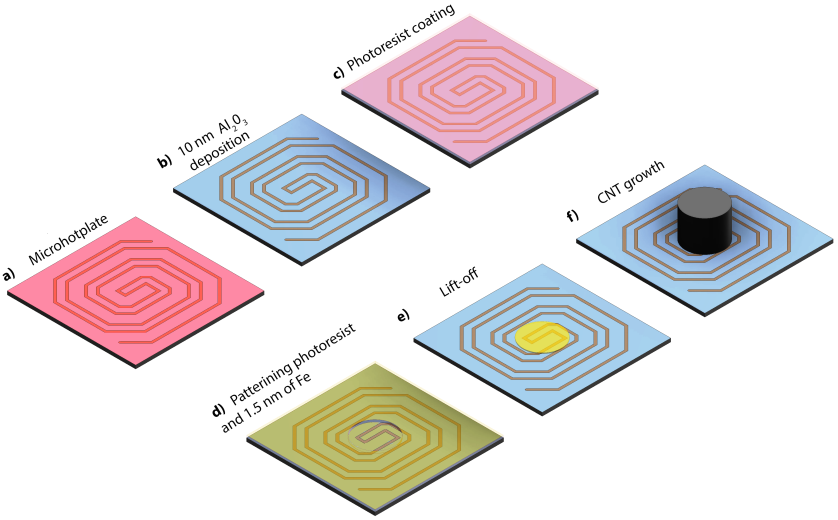


Figure 3.4: CNT growth process on MHP. (a) On a bare microhotplate device (b) 10 nm of Al_2O_3 barrier layer was sputtered. The wafer was (c) coated with 2µm of negative resist and patterned. (d) Then 1.2 nm of Fe catalyst was evaporated on the entire surface. (e) Once performed the lift-off, the stack of all required layer for the CNT growth was ready. Finally, the sample was loaded on a CVD reactor and (f) the CNTs were grown at 600°C for 5 minutes, to achieve the desired aspect-ratio.

The as-synthetized CNT micropin consists of interlaced MWCNTs held together by weak van der Waals interactions. As determined by SEM inspection, the MWCNTs have an average diameter of 9 nm, and are packed with a density of 112 tubes μm^{-2} resulting in a porosity of about 99.3%. These values are in agreement with those reported by others [7, 16]. The packing density of our foam-like CNT micropin is limited by the relatively large spacing between the iron (Fe) nanoparticles employed as catalyst for the CVD growth (see Chapter (2)). In Figure 3.5 (b) a close up view of the foam-like morphology of the tip of a CNT micropin is shown. We prepared two different sample configurations: the first configuration consists of a single CNT micropin of 200± 1µm in diameter and 158±2µm in height (Figure 3.5 (c)). The second configuration consists of multi-pins where each of the six micropins has a diameter of 20±1µm and a height of 180±4µm (Figure 3.5 (d)).

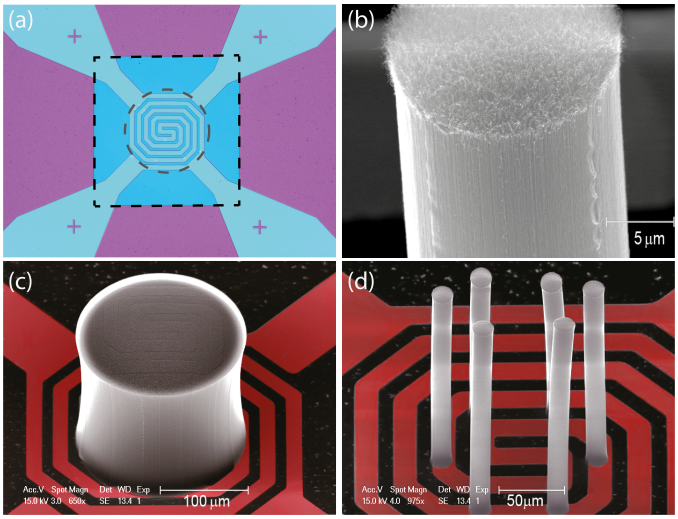


Figure 3.5: SEM images of two CNT sample configurations synthetized on top of the suspended MHP. (a) Optical microscopy image of the MPH. The square highlights the membrane and the circle shows where the hot spot is created by Joule heating the spiral heater; (b) Tilted SEM image close up of the micropin tip; (c) Single micropin of 200±1µm in diameter and 158±2µm in height; (d) multi-pin configuration in which each of the six micropins is 20±1µm in diameter with a height of 180±4µm. The MHP is indicated by a red false coloration.

3.2.3. ELECTRICAL CHARACTERIZATION

The employed MHP design generates a local hot spot in the centre of the suspended membrane. The heat produced by Joule heating is dissipated by conduction through the membrane towards the bulk substrate, and by radiation and convection towards the surrounding medium. The addition of the CNTs enhances the heat dissipation through convection and radiation. To quantify the heat dissipated by the as-grown CNT micropins, electrical measurements were performed in air and in vacuum. The difference in power dissipated towards the environment is measured by operating the MHP at equivalent temperatures for the different sample configurations and environmental conditions.

The dissipated power was acquired in steady-state heat transfer conditions at various temperatures, ranging from ambient temperature (T_∞ = 294.15 K) up to a maximum temperature T_{max} of 575 K. For reference, the measurements were repeated on a MHP without CNTs. The electrical characterization is performed in a customized stainless steel chamber equipped with four probe needles connected to an Agilent 4156C Parameter Analyzer (Figure 3.6). By connecting the chamber to a vacuum system, the device was characterized from atmospheric pressure to 1×10^{-5} mbar, which is the minimum pressure achievable in the system. All the configurations are measured by supplying a

step-wise current from 1 mA to 10 mA. The maximum input current is limited by the breakdown current of the heater, which occurs at around 14 mA. The MHP is used both as local heat source and as sensing element. For the latter functionality, it is necessary to first calibrate the Pt spiral heater. The temperature coefficient of resistance (TCR) obtained is equal to 2500±40 ppm K^{-1}. After recording the voltage drop across the microhotplate, the resulting resistance is related to the temperature using the measured TCR value.

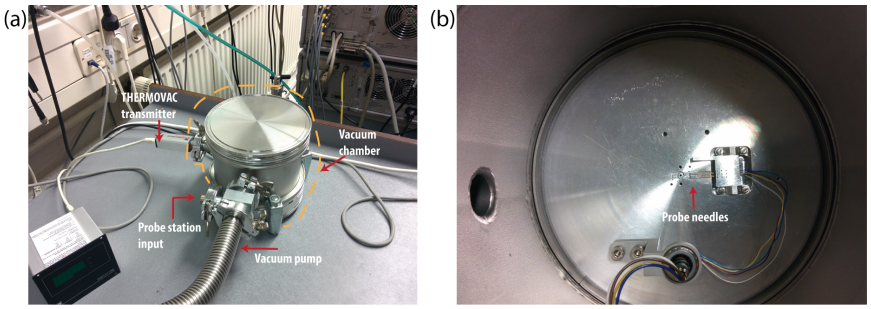


Figure 3.6: The electrical characterization is performed loading the MHP in a stainless still vacuum chamber connected to a vacuum pump and a probe station. (a) Chamber connected to the vacuum pump and a THERMOVAC transmitter. (b) Close-up of the interior of the vacuum chamber equipped with four probe needles.

3.2.4. INFRARED MICRO-THERMOGRAPHY

High-resolution thermographic microscopy analysis can be used as an effective method to extract thermal conductivity of vertically oriented CNT composites [17]. In our case the experimental IR thermal analysis was performed with a state-of-art system based on the use of an ultrafast thermo-camera (Figure 3.7) [18]. Before performing IR measurements on CNT configurations, a calibration procedure was performed to compensate for different material IR emissivity, temperature ranges and lens addition. The calibration procedure, based on the two point algorithm, is described elsewhere [19]. After the calibration step, the temperature distribution on the device top surface was recorded at four different power dissipation levels, when heating the device by Joule heating. The high-resolution micro-thermography system has a temperature sensitivity of about 1 K and a spatial resolution of 2.5µm. Figure 3.8 reports the high reliability between the average temperature measured by both IR thermal analysis and electrical stimulation for the micropin and multi-pin configurations.

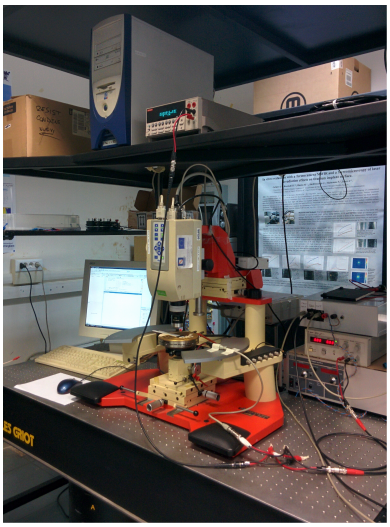


Figure 3.7: IR setup used to perform the thermal mapping. The sample under test is powered while the map is recorded.

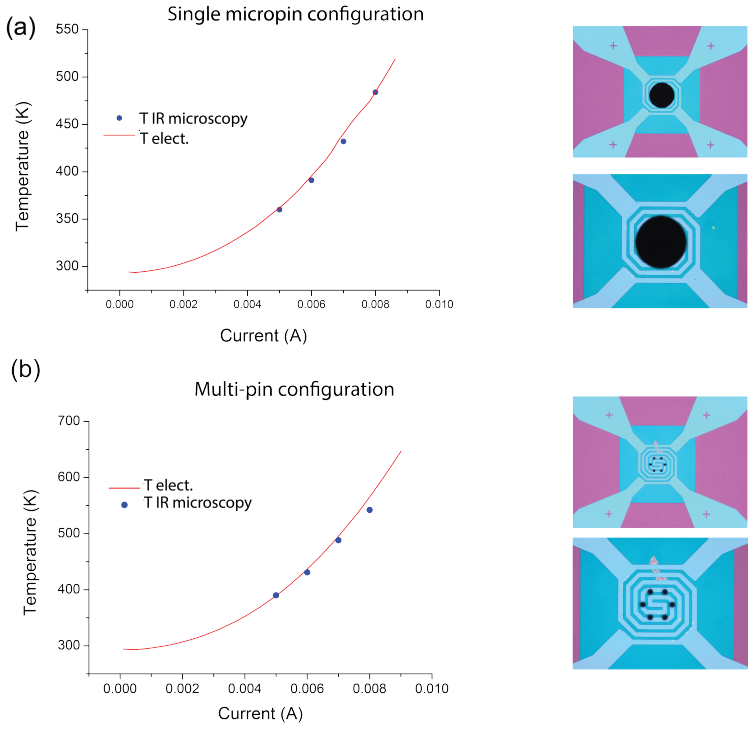


Figure 3.8: Comparison between temperatures recorded by electrical measurement and high-resolution micro-thermography for (a) single micropin and (b) multi-pin arrangements. The insets shows the optical microscopy image of the two configurations.

3.3. THEORETICAL ANALYSIS

To evaluate the heat transport in a VA-CNT micropin, the governing differential equation for a pin fin system subjected to appropriate boundary conditions is used [20]. Figure 3.9 shows a schematic illustration of a single CNT micropin with length $L = 180\,\mu m$ and diameter $D = 20\,\mu m$. As the micropin height L is much larger than the phonon mean free path (MFP), a diffusive heat transport regime can be applied. The estimated phonon mean free path in a MWCNT array can be as low as 20 nm due to defect scattering and intertube coupling [21].

Moreover, the conduction along the CNT micropin is assumed to be one-dimensional because of the high aspect ratio ($L \gg D$), hence the radial temperature variation can be considered negligible compared to the axial variation. The one-dimensional heat transfer model described above is used to extract the micropin effective conductivity k_{eff}, from the measurements. The heat transport analysis in micropin is primarily described by Fourier's equation [20]:

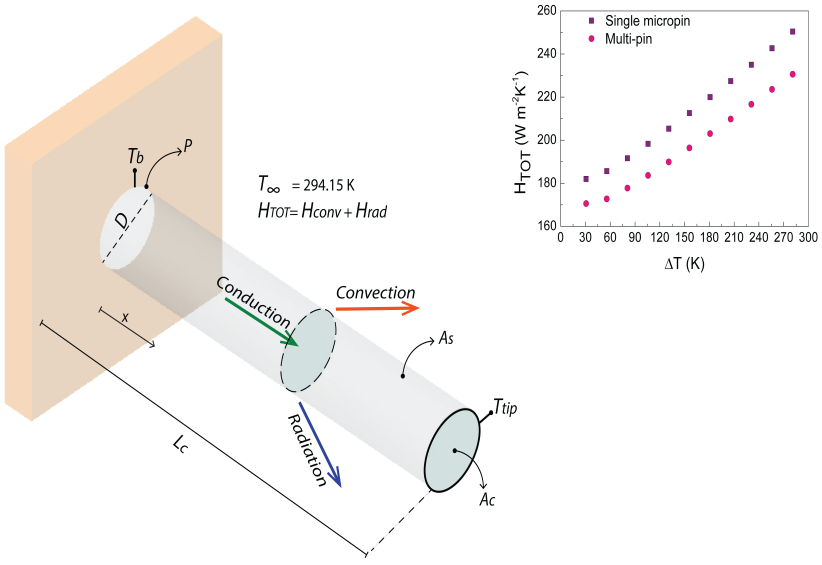


Figure 3.9: One dimensional heat transfer model along the axial direction of the CNT micropin. The heat dissipation mechanisms along the pin length (x direction) are shown. The heat conducted through the CNT array is dissipated by radiation and natural convection. The inset shows the total heat transfer coefficient H_{TOT}, which includes H_c and H_{rad}, as function temperature. The foam-like CNT micropin has a diameter $D = 20\,\mu m$, a length $L_c = L + D/4$, a cross sectional area $A_c = \pi D^2/4$, a fin tip perimeter $P = \pi D$ and a micropin surface area $A_s = \pi D L_c$

$$\frac{d^2 T_s}{dx^2} - \frac{H_c P}{k_{eff} A_c}(T_s - T_\infty) - \frac{\varepsilon \sigma P}{k_{eff} A_c}(T_s^4 - T_\infty^4) = 0 \tag{3.1}$$

and it describes the temperature variation along the micropin. With the radiative heat transfer coefficient expressed as $H_{rad} = \epsilon\sigma(T_s^2 + T_\infty^2)(T_s + T_\infty)$ and by defining $H_{TOT} = H_c + H_{rad}$, the equation reduces to:

$$\frac{d^2T_s}{dx^2} - \frac{H_{TOT}P}{k_{eff}A_c}(T_s - T_\infty) = 0 \tag{3.2}$$

where P is the micropin perimeter ($P = \pi D$), k_{eff} is the effective thermal conductivity of the CNT nanofoam, and A_c is the cross sectional area of the micropin ($A_c = \pi D^2/4$), T_∞ is the surrounding temperature. We then simply the notation of the second-order differential equation by defining $m = \sqrt{\frac{H_{TOT}P}{k_{eff}A_c}}$, obtaining:

$$\frac{d^2T_s}{dx^2} - m^2(T_s - T_\infty) = 0 \tag{3.3}$$

To solve the second-order differential equation we need to specify two boundary conditions.
The *first boundary condition* (**BC 1**) regards the micropin base temperature, T_b, at x=0:

$$T_s|_{x=0} = T_b \tag{3.4}$$

The *second boundary condition* (**BC 2**) regards the temperature at micropin tip, T_{tip}, for x=L. There are different assumptions depending on the physical situations, which all summarized in Table 3.1.

$$\frac{dT_s}{dx}|_{x=L_c} = 0 \tag{3.5}$$

Following, we assume an adiabatic tip condition, which means that the temperature gradient at the tip is zero. In order to take into account the convective and radiative effects at the micropin tip, a corrected micropin length, $L_c = L + D/4$, is added.
Considering the above mentioned boundary conditions, the resulting temperature distribution along the x-direction of the micropin (solution of Equation (3.3)) is written as:

$$T_s = T_\infty + \frac{\cosh m(L_c - x)}{\cosh m(L_c))}(T_b - T_\infty) \tag{3.6}$$

We are interested in extracting from Equation (3.6) the m and then the k_{eff}. From the high-resolution IR thermal maps collected at different power regime it is possible to

determine simultaneously T_{tip} and T_b . Therefore, m k_{eff} are determined as follow:

$$m = \frac{1}{L_c}(\text{arcosh}\,\frac{T_b - T_\infty}{T_{tip} - T_\infty}) \tag{3.7}$$

$$k_{eff} = \frac{4H_{TOT}}{m^2 D} \tag{3.8}$$

H_{TOT} is evaluated at an average temperature $T_{avg} = (T_{s_{avg}} + T_\infty)/2$, where $T_{s_{avg}} = (T_b + T_{tip})/2$.

Table 3.1: Boundary conditions (**BC 2**) at the fin tip [20]. **Case A** considers the convection and radiation at the micropin tip to be equal to the conduction along the micropin length; **Case B** is for adiabatic tip condition; **Case C**, corresponds to case B except for a corrected length factor $L_c = L + D/4$ which takes into account the heat loss from the tip.

Case	Tip condition	Temperature at the micropin tip
Case A	$H_c(T_s - T_\infty) = -k_{eff}\frac{dT_s}{dx}\|_{x=L}$	$T_{tip} = T_\infty + \frac{T_b - T_\infty}{\cosh mL + (\frac{H_{TOT}}{mk_{eff}})\sinh mL}$
Case B	$\frac{dT_s}{dx}\|_{x=L} = 0$	$T_{tip} = T_\infty + \frac{T_b - T_\infty}{\cosh mL}$
Case C	$\frac{dT_s}{dx}\|_{x=L_c} = 0$	$T_{tip} = T_\infty + \frac{T_b - T_\infty}{\cosh mL_c}$

3.4. ELECTRO-THERMAL MEASUREMENT PERFORMED IN AIR AND VACUUM

The measured MHP electric driving power and the temperature of the two configurations in both air and vacuum are shown in Figure 3.10.

In vacuum, all sample configurations show a similar relationship between power and temperature up to 450 K. At higher temperatures, the microhotplates equipped with CNT micropins start diverging, dissipating more power for an equivalent temperature, as compared to the reference sample without CNT structures (Figure 3.10 (a)). This is due to the additional heat loss through radiation. The radiation heat loss is directly proportional to the surface area As and to the material emissivity ϵ, consequently the increase of both results in more power being dissipated. The single- and multi-micropin CNT configuration increase the MHP surface area by respectively 0.163 mm^2 and 0.073 mm^2. Combined with the high emissivity coefficient of carbon, it explains why in vacuum the single micropin configuration dissipates more power compared to the multipin one. In air, the power versus temperature measurements start diverging at a lower

temperature, namely 350 K, see Figure 3.10 (b). Convective in addition to radiative heat transfer is now contributing to a better thermal performance for all three sample configurations. However, the addition of the CNT micropins enhances the radiative and convective heat transfer even further, as shown by the offset in Figure 3.10 (b) with respect to the reference (no CNT) sample, thus reducing the temperature at the center of the MHP. For a given input power of 30 mW, the single micropin and multi-pin arrangements show a remarkable reduction in the local hot spot temperature of respectively 66±8 K and 28±8 K (Figure 3.10 (c)).

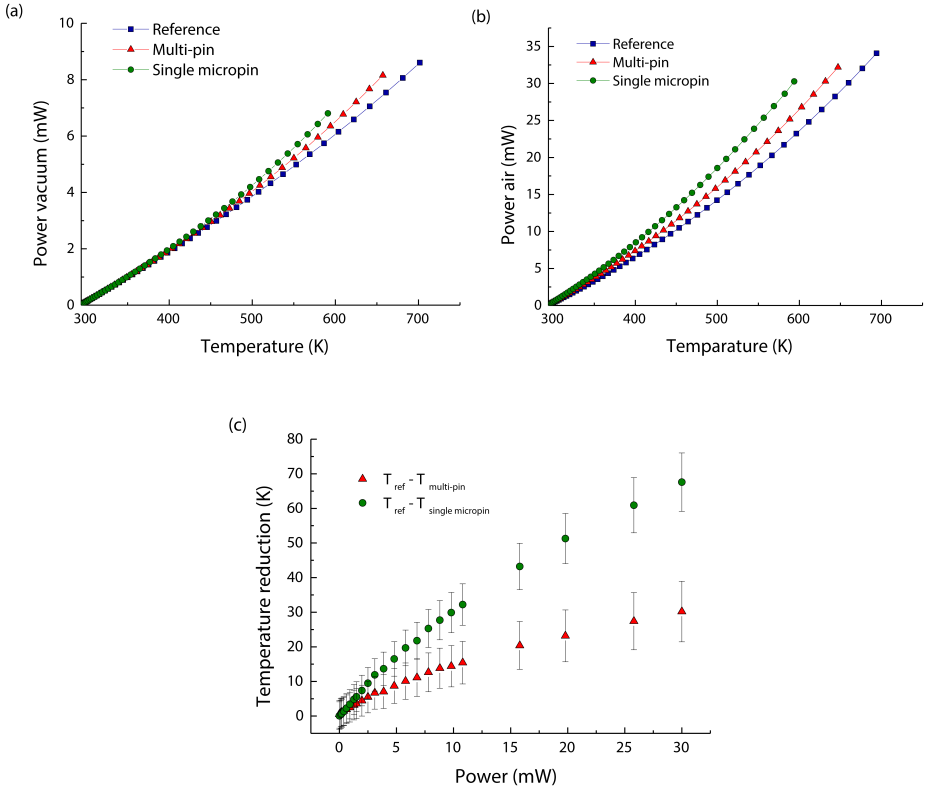


Figure 3.10: (a) Power-temperature characteristics in vacuum and (b) in air of the reference MHP (■), the MHPs equipped with the multiple micropins (▲) and the single micropin (•) configuration. In vacuum, the multi-pins and the single micropin arrangement require 6.7% and 14.5% additional power to achieve the same temperature as the reference sample. In air, the power can be increased even further up towards 12% and 31%, respectively. (c) Relative temperature reduction of the local hot spot for different power regimes.

In order to estimate the contribution of each heat transfer mechanism involved, we first calculate the radiative dissipation, P_{rad}, using the Stefan-Boltzmann law:

$$P_{rad}(T_{avg}) = \epsilon\sigma A_{s_{TOT}}(T_{avg}^4 - T_{\infty}^4) \tag{3.9}$$

where σ is the Stefan-Boltzmann constant (5.67×10^{-8} W m^{-2} K^{-4}), ϵ is the effective emissivity of the surfaces involved, $A_{s_{TOT}}$ is the device surface area, T_{avg} is the average temperature measured from the MHP.

The heat transferred by conduction on the entire device, P_{cond}, is obtained from the MHP driving power in vacuum P_{vac}, minus the power dissipated by radiation:

$$P_{cond}(T_{avg}) = P_{vac}(T_{avg}) - P_{rad}(T_{avg}) \tag{3.10}$$

The convective heat transfer P_{conv}, is obtained by subtracting the MHP driving power in air P_{air}, and the input power in vacuum:

$$P_{conv}(T_{avg}) = P_{air}(T_{avg}) - P_{vac}(T_{avg}) \tag{3.11}$$

In Figure 3.11 the power versus temperature of conduction, convection and radiation is reported for the investigated sample configurations. It is interesting to observe that for a given temperature, the power dissipated by conduction through the membrane is lower for the reference MHP than for the MHP with integrated CNT micropins (Figure 3.11(a)). This is because more power is dissipated by radiation and convection through the CNT micropins, as shown in Figure 3.11 (b-c). We also notice that the power dissipated by radiation increases upon the integration of the micropins. At T_{max} = 575 K, the increase in radiative dissipated power for the multi- and single micropin corresponds to about 106% and 161%, respectively. The power dissipated by convection increases less significantly with respect to the reference hotplate, 20% and 44%, respectively. In all cases the power is mainly dissipated by natural convection. This is shown in Table 3.2, where the relative power dissipated through conduction, radiation and convection at T_{max} is reported.

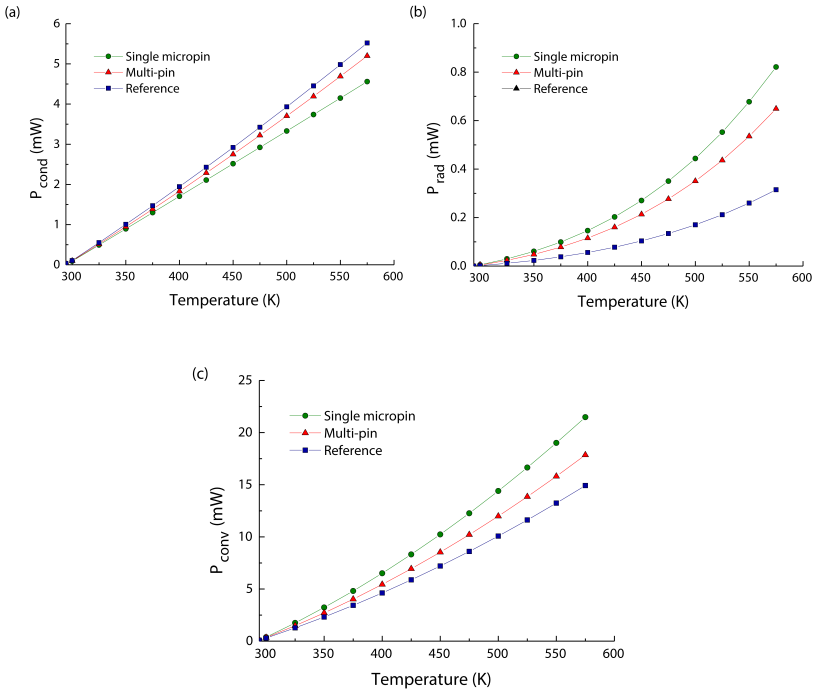


Figure 3.11: Measured power-temperature characteristics of the microhotplate showing the distribution of power dissipated in air by (a) conduction, (b) radiation and (c) convection for all sample configurations.

Table 3.2: Relative power dissipated by the reference and both CNT nanofoam configurations at T_{max} = 575 K in air. For all the configurations the convective contribution is the most significant. The decrease in the conductive contribute due to the CNT insertions is also visible.

Sample	Power (mW)	Conduction (%)	Radiation (%)	Convection (%)
Reference MHP	21.25	28.1	1.7	70.2
Multi-pin	23.71	21.9	2.8	75.3
Single micropin	27.63	16.4	5.8	77.8

In the following subsections we further explore the VA-CNT thermal properties in terms of the natural convective heat transfer coefficient H_c, radiative heat transfer coefficient H_{rad} and effective thermal conductivity k_{eff}.

3.4.1. NATURAL CONVECTIVE HEAT TRANSFER COEFFICIENT

Convective heat dissipation is an important factor that influences the overall thermal behaviour of the MHP and nanofoam material. The temperature dependence of the natural convective heat transfer coefficient H_c is defined by [22]:

$$H_c(\Delta T) = \frac{P_{conv}(T_{avg})}{(T_{avg} - T_\infty)} A_{s_{TOT}} \tag{3.12}$$

where $\Delta T = (T_{avg} - T_\infty)$. Figure 3.11 (a) shows the dependency of H_c on temperature. For the single micropin configuration H_c increases from 179 W m^{-2} K^{-1} to 241 W m^{-2} K^{-1}, when ΔT is increased from 30 K to 280 K. In the same temperature range, the H_c for the multi-pin configuration increases from 167 W m^{-2} K^{-1} to 222 W m^{-2} K^{-1}. The achieved values for the heat transfer coefficients are much higher than those recorded at the macroscale, which typically range between 2 and 25 W m^{-2} K^{-1} in gases. Therefore, at micrometer scale, the natural convection is subjected to a considerable enhancement. The increased value of H_c is an indication of the influence of surface effects, such as increased surface area (due to nanoporosity), surface friction, surface roughness, surface geometry on the flow and heat transfer at micro- and nanometer scale [23]. A similar enhancement has been recorded for cylinders and plates with characteristic length around 100 µm [24]. The main requirements to dissipate heat trough natural convection are the presence of a fluid that change density when heated up and there must be a gravitational field, producing a fluid motion. To better understand the nature of the H_c enhancement we performed a simple tests: we recorded the power-temperature characteristics of a MHP positioned horizontally or vertically. No significant influence has been identified by varying the sample orientation in the gravitational field. In particular, the change in operational power to maintain the MHP at a constant temperature, with regards to vertical or horizontal orientation, was less than 1%. This suggests that the heat-to-air transfer mechanism is dominated by the conduction between the heated solid interface and the air molecules, whereas the natural convective motion is negligible. To vision what happen at the interface VA-CNT/air due to the density gradient, a sketch of an horizontal cylinder in free air is reported in Figure 3.12. Two regions are created: a non-continuum and a continuum region. In the non-continuum region the heat transfer is dominated by absorbtion and desorption and/or scattering of air molecules with the CNT surface. It can be identified as the conduction region, and it extends for several free paths [25]. The second region is the continuum one, dominated by the traditional free convection and radiation heat transfers.

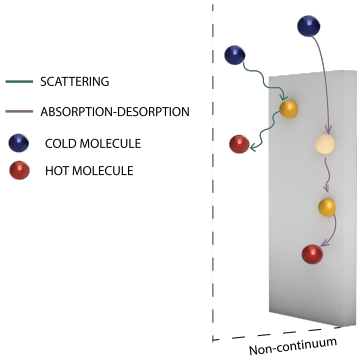


Figure 3.12: Heat transfer phenomena in the non-continuum region. Gas molecules such as O_2, N_2 and H_2O can be scattered (green arrow) or either absorbed and desorbed (violet arrow) at the CNT surface.

The above mentioned scenario, it has been experimentally demonstrated by studying the heat loss by natural convection from electrically heated microfilaments, where the heat was mainly transferred through air conduction rather than through air convection [26, 27]. In particular, it has been reported that the conductive contribution to H_c was almost ten times higher than the convective contribution. Therefore, H_c at micro and nanoscale can be considered as an *equivalent* convective heat transfer coefficient. It includes both the natural convection and conduction to surrounding air, with the latter as dominant heat dissipation mechanism. Our results as well as the literature demonstrate that a more complex interaction between heat exchange of microstructures, nanofoam materials and the surrounding fluid is present.

3.4.2. RADIATIVE HEAT TRANSFER COEFFICIENT

The radiative heat transfer coefficient H_{rad} and its temperature dependency are determined by:

$$H_{rad}(\Delta T) = \epsilon\sigma(T_s^2 + T_\infty^2)(T_s + T_\infty) \tag{3.13}$$

To precisely quantify the radiative contribution, the ϵ of the MHP and the CNTs is measured by high-resolution IR thermal microscopy. The ϵ of the CNT nanofoam is 0.95, which is very close to that of a black body; while the ϵ of the MHP is only about 0.22. Figure 3.11 (b) shows the obtained H_{rad} trends for both CNT micropin arrangements. For the single micropin configuration H_{rad} increases from 2.7 W m^{-2} K^{-1} to 9.2 W m^{-2} K^{-1} when ΔT is increased from 30 K to 280 K. For the multi-pin, H_{rad} goes from 2.4 W m^{-2} K^{-1} to 8.0 W m^{-2} K^{-1} for the same temperature range. As expected, the radiative emission increases with both temperature and emitting area.

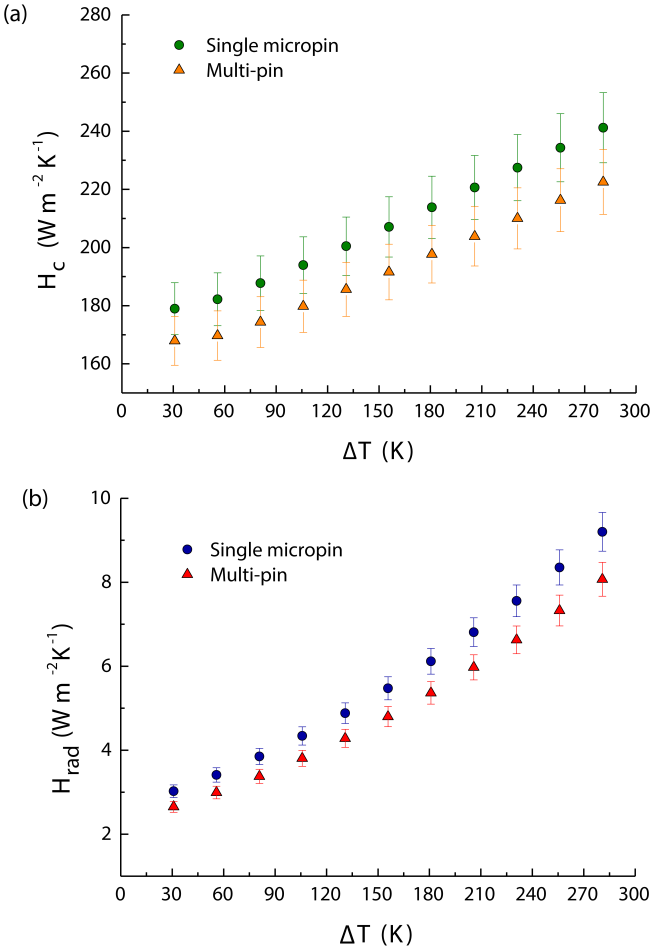


Figure 3.13: (a) Convective heat transfer coefficient (H_c) and (b) radiative heat transfer coefficient (H_{rad}) extracted from the electrical measurement performed on the device equipped with the single micropin and the multi-pin. The uncertainty in the experimental data was calculated applying the method developed by Kline and McClintock [28]

For calculating both P_{rad} and H_c the VA-CNT surface area is considered without nanoporosity based on the following assumptions. As reported in [29, 30] for the calculation of the radiative heat, it is reasonable to assume that the inner CNTs do not radiate as they are surrounded by many other neighboring tubes at the same temperature.
To calculate the H_c we consider the surface area without nanoporosity, as it is very difficult to accurately quantify the effective surface area in contact with the air flow. Specific porosity studies, like nitrogen absorption-desorption needs to be carried out in order

to know the value of the surface area involved into the natural convective heat transfer. However, a study on the penetration depth of the air flow in a CNT bundle was carried by Hu et al. [31]. By using molecular dynamics simulations, they found that to have air flow passing through CNT arrays, made of perfectly aligned tubes, at atmospheric pressure and a flow velocity of 5 m/s (typical velocity of an electrical fun) the maximum number of nanotubes in a row is limited to 400 tubes in series. This implies that the air molecules can effectively penetrate inside perfectly aligned CNT, with no overlap among them, for ~ 10µm at 5 m/s flow velocity. In our case, we have densely overlapped CNT matrix, so the air flow penetration most likely is even less.

However, it is important to remember that H_c is not only dependent on the exposed surface area but also on the temperature variation (ΔT), the material morphology and the shape factor of the entire configuration.

3.4.3. EFFECTIVE AND INDIVIDUAL THERMAL CONDUCTIVITY

The effective thermal conductivity k_{eff} of a micropin extracted from the multi-pin arrangement can be determined by using the one-dimensional heat transfer model coupled with high-resolution IR thermal maps (Figure 3.14). Equation 3.6, can be solved for k_{eff} by extracting the base temperature, T_b, and tip temperature, T_{tip}, of each micropin from the obtained thermal mapping. The measured thermal conductivity k_{eff} is averaged over the six VA-CNTs constituting the multi-pin configuration. By powering the MHP while recording the emitted infrared radiation, it is possible to determine the spatial temperature distribution and consequently the corresponding temperature dependency of k_{eff} over a broad temperature range, from room temperature up to 510 K.

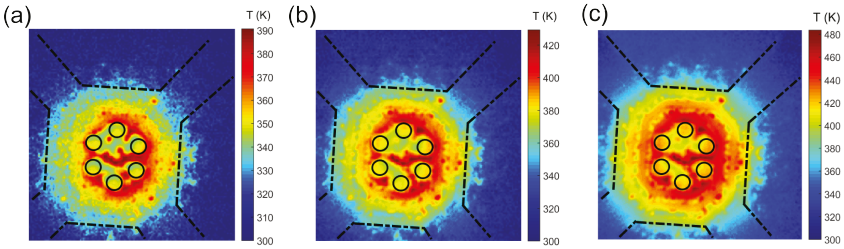


Figure 3.14: High-resolution thermographic microscopy analysis of the microhotplate with multi-pin configuration. Three IR thermal maps for three different input currents are shown: (a) 5 mA, (b) 6 mA, (c) 7 mA, to determine k_{eff} as function of the average system temperature.

Figure 3.15 (a) shows the obtained k_{eff} as a function of temperature. The CNT nanofoam k_{eff} increases gradually when the temperature increases, reaching about 2.18 ±

0.04 W m^{-1} K^{-1} at 510 K. The effective thermal conductivity k_{eff} increases 39.1% over a temperature range of 369 K to 406 K. Above 406 K the nanofoam showed a reduced conductivity increase rates equal to 25.6% and down 19.5% at 406-450K and at 450-510 K, respectively. The k_{eff} increasing rate change is caused by the competition between the various phonon-scattering processes triggered by temperature variation. In CNT nanofoam, we observed a continuous increase of the thermal conductivity, also above the typical peak temperature of individual CNTs [32]. It likely reveals a dominance of point defect and grain boundary scatterings over Umklapp scattering even at high temperature. The temperature dependence of the MWCNT array thermal conductivity has been reported at different temperature ranges 5-390 K [29], at 10-300 K [33] and at 300-830 K [30]. In order to investigate k_{eff} as a function of temperature, the cited work employed complex post-growth process and experimental techniques, which can affect the CNT quality and adds a potential source of error and uncertainty during the measurement phase. For example, suspending a CNT rope between two copper electrodes is a manually intensive procedure [30, 33], and when successful, infiltration of the contact material into the CNT arrays can influence the achieved result [29]. Our non-destructive thermal transport measurement, allows the direct characterization of nano- and micro-scale materials for a large temperature range. Furthermore, no sample handling is required when the materials can be grown bottom-up in predefined locations on the microhotplate.

The thermal conductivity of an individual MWCNT in vertically aligned arrays, k_{CNT}, can be estimated by correlating k_{eff} with the number of CNTs per unit area (N_{CNT} / A_{array}) and the average cross sectional area of a single nanotube (A_{CNT}) [34]:

$$k_{eff} = k_{CNT} A_{CNT} \frac{N_{CNT}}{A_{array}} \tag{3.14}$$

Figure 3.15 (b) reports the obtained k_{CNT} considering a nanotube average diameter of 9 nm. At the lowest investigated temperature k_{CNT} is about 136 W m^{-1} K^{-1}. The estimated value is affected by uncertainties in defining the CNT packing density within the CNT nanofoam.

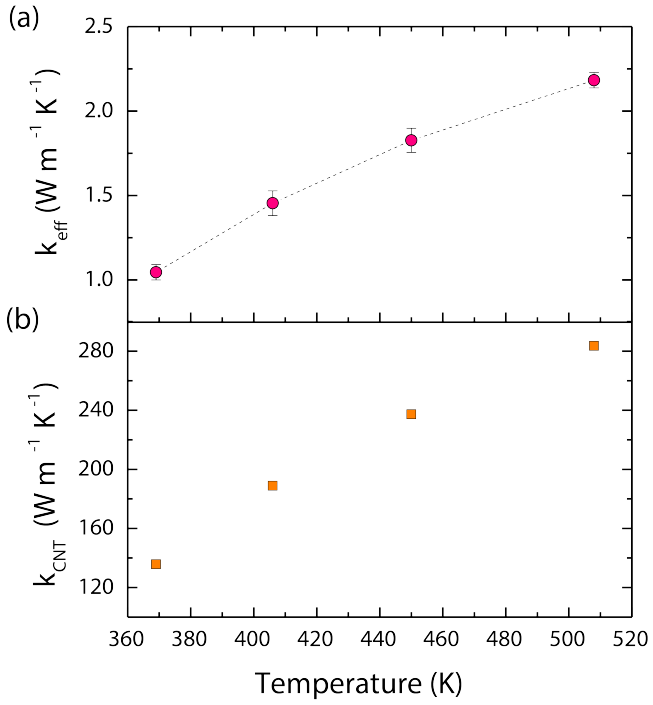


Figure 3.15: (a) Temperature dependence of the effective thermal conductivity of a foam-like CNT micropin.(b) Temperature dependence of the estimated individual CNT thermal conductivity. k_{eff} ~0.007 k_{CNT}.

Both k_{CNT} and k_{eff} are orders of magnitude lower than the experimental value of individual MWCNT (3000 - 1400 W m^{-1} K^{-1}). The quality of the CNTs, which typically depends on the growth method, is the main factor influencing the intrinsic thermal conductivity. The Raman spectra of the CNTs samples show an I_D/I_G ratio equal to 0.93, revealing a low crystallinity degree within the CNTs nanofoam. It is well known that, in comparison to laser ablation or arch-discharge methods, CNTs grown by chemical vapor deposition (CVD) have considerably lower quality. However, the thermal conductivity drop observed goes beyond factors related to the CNT quality like packing density, number of shells and dislocations.

Based on what reported in literature, the two major degrading factors of the overall CNT nanofoam thermal performance are the interface thermal resistance between adjacent tubes and the thermal boundary at the interface CNT- native substrate. The interaction between adjacent nanotubes, primarily caused by van der Waals forces, creates

new sites for phonon scattering, decreasing the intrinsic thermal conductivity, and enhancing the interface thermal resistance between neighboring CNTs. Aliev et al, by computer simulation, found that the inter-tube interactions and alignment imperfections reduce the thermal conductivity of a MWCNT arrays by a factor of three [14]. In particular, they estimated that to decrease the inter-tube scattering, the crosslinking between nanotubes should occur only over short distances (2-3% of their total length)(Figure 3.16 (a-c)). Considering a micropin length of about 180µm, the maximum overlapping length between neighboring tubes should be between 3.6µm and 5.4µm. This would prevent the degradation of the heat conduction. Careful inspection of the nanofoam morphology using SEM, indicates that crosslinking of nanotubes is higher than the expected desirable value (Figure 3.16(d)). This suggests that the inter-tubes interactions might significantly contribute to the observed thermal conductivity reduction.

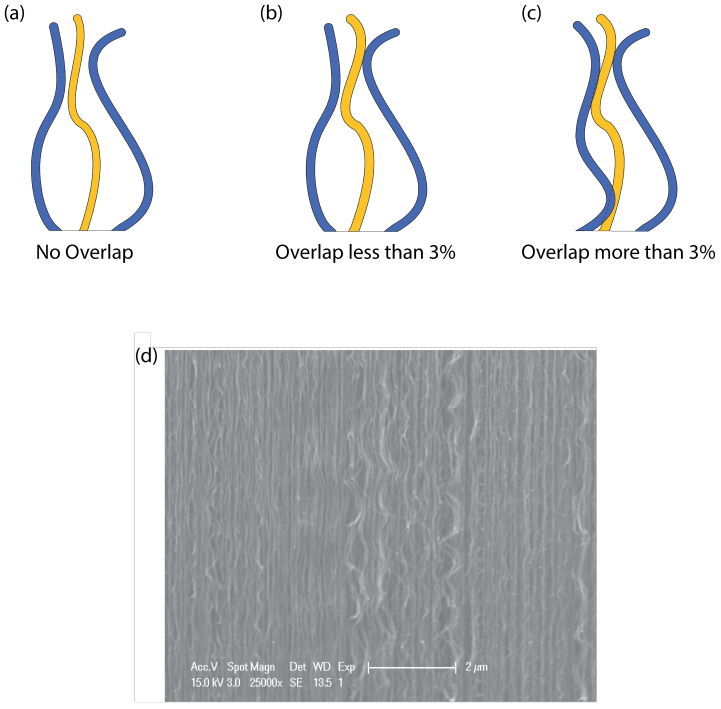


Figure 3.16: Schematic illustration regarding the concept of maximum overlapping length of CNTs, discussed in deeply in [14]. (a) No overlap among neighboring CNTs; (b) Overlap less than 3% (CNTs in the center); (c) Overlap more than 3% of the total CNT length, which causes thermal conductivity degradation. (d) SEM image showing the periodic waviness of the vertically aligned CNT nanofoam grown on top of the MHP. The rough estimated overlapping, made through visual inspection, is from 4% to 22% depending from the location.

The thermal boundary resistance at the interface CNT-substrate is considered an important limiting factor for both potential thermal and electrical applications. It depends strongly on the substrate material and CNTs packing density [34]. It has been demonstrated that in presence of a weak bond between substrate and the nanofoam, not all the CNTs participate effectively to the heat transport [35]. The total effective thermal resistance, R_{eff} , of a single bundle of 20µm in diameter and 180µm in height, including volumetric effects and interface contributions, can be estimated by [36, 37]: $R_{eff} = L/k_{eff} = 1.73\ \mathrm{cm^2\ K\ W^{-1}}$.

3.5. MODELLING APPROACH

In this section, we introduce the 3D electro-thermal model created with the intent to calculate the heat transfer through the investigated device and to predict the best ratio between CNT area coverage and the dissipated power. The 3D model of the reference and CNT arrangements are computed using a finite-element analysis (FEA) simulation tool (COMSOL Multiphysics 4.4). The 3D simulation was performed by coupling the electrical heat generation, by the Joule heating module (Equation (3.15)), with the heat transfer module (Equation (3.16)). The governing equations of the steady-state heat conduction for Joule heating process can be written as:

$$\nabla(\sigma_e \nabla V) = 0 \tag{3.15}$$

$$\nabla(k(T)\nabla T) + J^2/\sigma_e = 0 \tag{3.16}$$

where k indicates a generic thermal conductivity which varies depending on the materials involved, T is the temperature, σ_e is the linearized electrical conductivity of the Pt spiral and J is the current density provided to the MHP. During the implementation of the 3D model, the following assumptions were made:

- At the edges the temperature is equal to the ambient temperature (294.15 K), as for an ideal heat reservoir.
- The heat transfer is assumed to be by conduction from the heater to the entire membrane. From all the surfaces in contact with the surrounding environment (top and bottom membrane surface) the heat is dissipated by natural convection and by radiation. The H_c is experimentally extracted for each configuration(Section 3.4.1). The emissivity of both the CNT and the SiN_x were extracted from the calibration phase of the IR maps.

- Initially, to simplify the model the CNT k_{eff} is assumed constant with the temperature.
- A 99% porosity is considered while modelling the CNT material.
- The electrical conductivity of the Pt heater, σ_e, is modelled using the following temperature dependent equation:

$$\sigma_e(T) = [\rho_o(1 + \alpha(T - T_o))]^{-1} \tag{3.17}$$

where α is the thermal coefficient of resistance (TCR), ρ_o is the resistivity at reference temperature T_o =21°C.

The resulting mesh and temperature distribution within the devices is shown in Figure 3.17, for input currents of 6.7 mA and 10 mA, both in air. The match between the experimental results and the FEM model is extremely good (Figure 3.18), assessing the 3D electro-thermal model as predictive tool for the design and optimization of VA-CNT bundle based cooling solutions. More details can be found in [38].

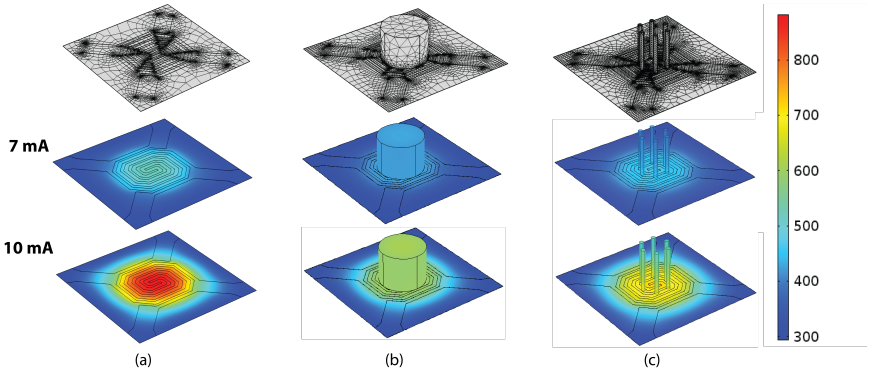


Figure 3.17: The resulting 3-D model and mesh for (a) reference MHP (b) MHP with single micropin and (c) multi-pin. The ambient temperature was set at 294.15 K. Two thermal maps are reported, for an input current equal to 7 mA and 10 mA.

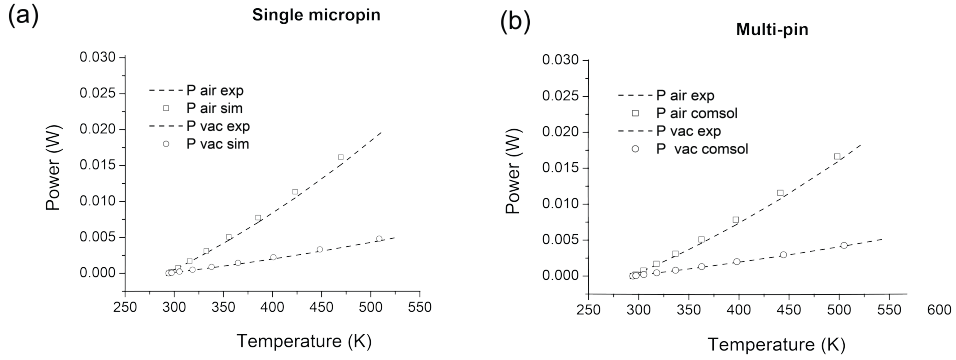


Figure 3.18: Comparison between the experimental power-temperature characteristics and the ones obtained by the developed 3D electro-thermal model for (a) single micropin and (b) multi-pin configuration. The maximum mismatch between experimental results and simulated ones for the single micropin configuration at T=575 K is 3.4% in air and 3.8% in vacuum. For the multi-pin configuration, a mismatch of 2% and 0.8% has been obtained in air and in vacuum, respectively.

3.5.1. THERMAL ANISOTROPY ESTIMATION

Similarly to other carbon related materials, MWCNTs are affected by intrinsic thermal and electrical anisotropy. By combining the temperature distribution obtained by high-resolution IR thermal microscopy with the developed 3D electro-thermal model of the single micropin, it has been possible to estimate the effective axial (k_a) and transversal (k_t) thermal conductivity (Figure 3.19). Figure 3.19 (c) shows the temperature distribution along a horizontal cutline obtained by the IR thermal map and the FEM simulations. By simulating the single micropin as an isotropic material, the temperature distribution obtained from the FEM is constant over the micropin tip (green line). The best fit between the temperature distribution obtained by IR thermal analysis and the simulated one was obtained for k_t equal to 0.2 W m^{-1} K^{-1} and k_a equal to the k_{eff} obtained for an input current of 7 mA ($k_{eff} \sim 1.82$ W m^{-1} K^{-1}). These results show the highly anisotropic thermal transport through the single micropin, with an anisotropic ratio of $k_a/k_t \approx 9$.

3.5.2. THERMAL CONDUCTIVITY VARIATION

A simplified 3D FEM model is employed to determine the temperature distribution along a micropin as function of the thermal conductivity variation. In particular, the model consists of a single micropin of 200 µm in diameter and height equal to $L = 158$ µm, with the bottom extremity maintained at T_b =383 K. The pin is exposed to ambient temperature (T_∞ = 294.15 K) with an average H_c of 188 W m^{-2} K^{-1}, and it is subjected to a ther-

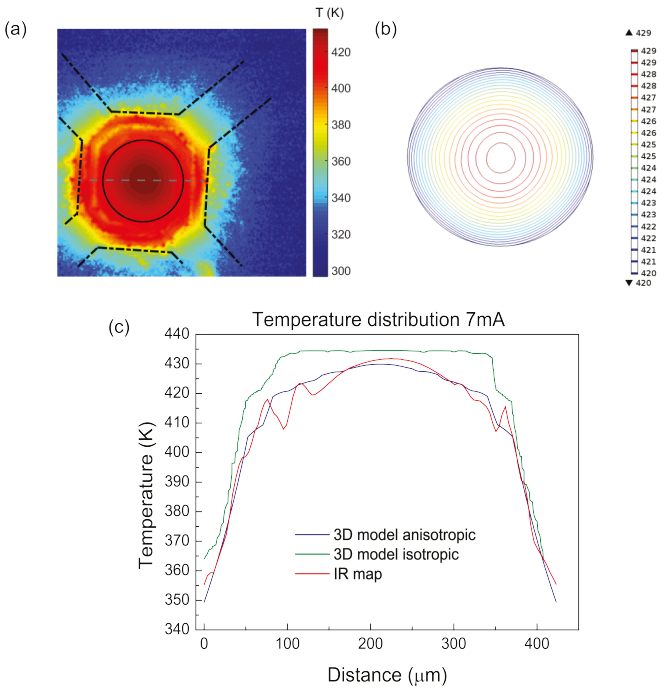


Figure 3.19: Single micropin :(a) IR thermal map of the device for an input current of 7 mA. The dashed line in grey represents the cutline. (b) Temperature distribution of the single micropin tip evaluated by FEM simulation for the same input current. (c) Temperature distribution along the cutline for both IR map (red line) and simulation (green and blue lines). The anisotropic thermal conductivity ratio is obtained by coupling the electro-thermal model temperature distribution with the one obtained from the IR map, resulting in the blue line trend. The green line represents the temperature distribution obtained by the FEM model for a single micropin with isotropic thermal conductivity.

mal conductivity variation from 0.1 to 100 W m^{-1} K^{-1}. Assuming steady state condition, isotropic and constant material properties, and negligible radiation, the temperature distribution along the micropin axial direction (x) is plotted in Figure 3.20 (a). As mentioned in Section 3.3 the temperature distribution along a micropin can be as:

$$T_x = T_\infty + (T_b - T_\infty)\frac{\cosh m(L-x) + (\frac{H_{TOT}}{mk_{eff}})\sinh m(L-z)}{\cosh mL + (\frac{H_{TOT}}{mk_{eff}})\sinh mL} \tag{3.18}$$

Both plots in Figure 3.20 reveal the impact of the thermal conductivity on the temperature distribution. For k values below 1 W m^{-1} K^{-1} a strong effect on the micropin cooling is observed, while it progressively decreases for $k \geq 5$ W m^{-1} K^{-1}. This behaviour is reflected in Equation (3.18) by the presence of m as argument of the hyperbolic sine and cosine functions.

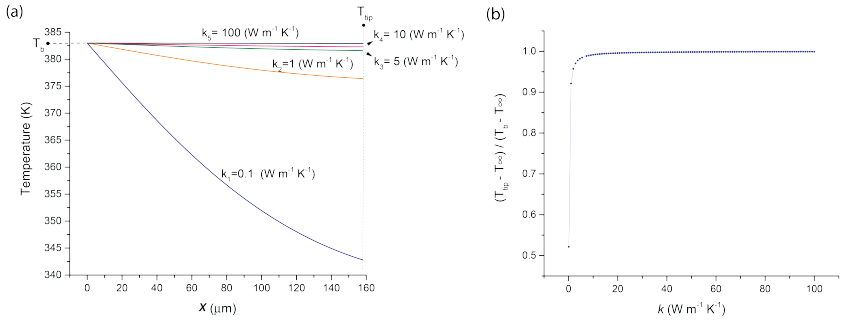


Figure 3.20: (a) Temperature distributions along the micropin axial direction for different thermal conductivity values. T_b and T_{tip} are the temperature at $x = 0$ (micropin bottom) and $x = 158$µm (micropin tip). (b) Temperature variation $((T_{tip}\text{-}T_\infty)/(T_b - T_\infty))$ versus thermal conductivity. After k> 0.9 W m^{-1} K^{-1} the temperature along the micropin saturates.

As consequence of the assumptions made (i.e fixed H_c), the main limiting factor of the micropin cooling is its height, L. The temperature distribution for a micropin with a length up to 30 mm is reported in Figure 3.21. Under this condition, the micropin can be considered as infinitely long. The graph suggests an optimal micropin length, L^*, for each thermal conductivity value investigated, beyond which only a slight increase of heat transfer can be obtained. The L^* corresponding to each k are reported in the table in the inset.

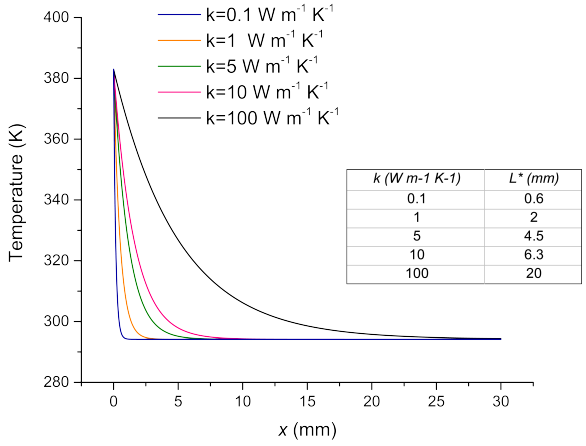


Figure 3.21: Temperature distribution along an infinitely long micropin. The inset reports the estimated L^*.

3.6. CONCLUSION

Lithographically defined CNT nanofoam structures can enhance the surface driven heat transfer mechanisms of microelectronic systems in the natural convective regime. Different configurations of VA-CNT structures were directly grown on MEMS microhotplates (MHPs) with controllable hotspot and an integrated temperature sensor. Combined with high-resolution infrared thermographic microscopy analysis, the thermal material properties of the patterned CNT structures were measured. Our approach eliminated measurement uncertainties arising from manual assembly and handling of samples. Augmentation of the MHP hotspot with CNT micropins (with a height of 158±2µm and a diameter of 200±2µm) resulted in a temperature reduction of up to 66±8 K in free air, compared to MHPs without micropins operating at similar power. In particular, the equivalent convective heat transfer coefficient H_c for a multi-pin configuration accounted for 167 W m^{-2} K^{-1}, and thus is much higher than the macroscale value (between 2 to 25 W m^{-2} K^{-1}). We conclude that the conduction between the air molecules and the heated solid interface dominates the heat-to-air transfer mechanism, whereas the natural convective motion is marginal. The CNT nanofoam also demonstrated a gradually increase of the effective thermal conductivity with temperature from: 1.04 W m^{-1} K^{-1} at 369 K to 2.24 W m^{-1} K^{-1} at 510 K. Finally, the lithographically defined VA-CNT structures are suitable for large-scale integration with microelectronics and represent a valuable alternative to bulky macro-cooling solutions. Therefore, these CNT nanofoam structures are suitable for localized, passive, customized on-chip cooling solutions, like micro-fins, pin arrays and other 3D microarchitectures. Furthermore, by using all the collected experimental data, it was possible to develop simulations with high accuracy. Relying on the validity of the proposed 3D electro-thermal model the anisotropy of the single micropin was studied. Moreover, due to the complex conjugate system, after simplifying the FEM model of a single micropin through different assumptions, the influence of the thermal conductivity and the micropin length over the temperature distribution have been estimated.

This work represents a first step toward the development of a valuable tool to predict the best design and geometry for chip level heat dissipation through CNTs bundles in micro-devices. The most critical parameter is the convective heat transfer coefficient, that heavily depend on the aspect ratio of the CNT structure and the foam-like morphology, and it is hard to theoretically predict.

REFERENCES

[1] A. a. Balandin, *Thermal properties of graphene and nanostructured carbon materials.* Nature materials **10**, 569 (2011), arXiv:1106.3789 .

[2] A. Volkov and L. Zhigilei, *Heat conduction in carbon nanotube materials: Strong effect of intrinsic thermal conductivity of carbon nanotubes,* Applied Physics Letters **101**, 043113 (2012).

[3] R. S. Prasher, X. J. Hu, Y. Chalopin, N. Mingo, K. Lofgreen, S. Volz, F. Cleri, and P. Keblinski, *Turning carbon nanotubes from exceptional heat conductors into insulators,* Physical Review Letters **102**, 1 (2009).

[4] M. De Volder, S. Park, S. Tawfick, and A. Hart, *Strain-engineered manufacturing of freeform carbon nanotube microstructures,* Nature communications **5** (2014).

[5] C. Silvestri, B. Morana, G. Fiorentino, S. Vollebregt, G. Pandraud, F. Santagata, G. Q. Zhang, and P. M. Sarro, *CNT bundles growth on microhotplates for direct measurement of their thermal properties,* in *2014 IEEE 27th International Conference on Micro Electro Mechanical Systems (MEMS)* (IEEE, 2014) pp. 48–51.

[6] R. H. Poelma, B. Morana, S. Vollebregt, E. Schlangen, H. W. van Zeijl, X. Fan, and G. Q. Zhang, *Tailoring the Mechanical Properties of High-Aspect-Ratio Carbon Nanotube Arrays using Amorphous Silicon Carbide Coatings,* Advanced Functional Materials **24**, 5737 (2014).

[7] R. H. Poelma, X. Fan, Z. Y. Hu, G. Van Tendeloo, H. W. Van Zeijl, and G. Q. Zhang, *Effects of Nanostructure and Coating on the Mechanics of Carbon Nanotube Arrays,* Advanced Functional Materials **26**, 1233 (2016).

[8] P. E. T. Al, S. Park, P. Dong-Won, C.-S. Yang, K.-R. Kim, J.-H. Kwak, H.-M. So, C. W. Ahn, B. S. Kim, H. Chang, and J.-O. Lee, *Vertically Aligned Carbon Nanotube Electrodes Directly Grown on a Glassy Carbon Electrode.* ACS nano **5**, 7061 (2011).

[9] Y. Wei, X. Lin, K. Jiang, P. Liu, Q. Li, and S. Fan, *Thermoacoustic chips with carbon nanotube thin yarn arrays.* Nano letters **13**, 4795 (2013).

[10] P. Liu, L. Liu, K. Jiang, and S. Fan, *Carbon-nanotube-film microheater on a polyethylene terephthalate substrate and its application in thermochromic displays.* Small (Weinheim an der Bergstrasse, Germany) **7**, 732 (2011).

[11] C. L. Pint, K. Takei, R. Kapadia, M. Zheng, A. C. Ford, J. Zhang, A. Jamshidi, R. Bardhan, J. J. Urban, M. Wu, J. W. Ager, M. M. Oye, and A. Javey, *Rationally Designed, Three-Dimensional Carbon Nanotube Back-Contacts for Efficient Solar Devices,* Advanced Energy Materials **1**, 1040 (2011).

[12] C. Cheng, W. Fan, J. Cao, S. G. Ryu, J. Ji, C. P. Grigoropoulos, and J. Wu, *Heat transfer across the interface between nanoscale solids and gas,* ACS Nano **5**, 10102 (2011).

[13] J. Hone, M. C. Llaguno, N. M. Nemes, A. T. Johnson, J. E. Fischer, D. A. Walters, M. J. Casavant, J. Schmidt, and R. E. Smalley, *Electrical and thermal transport properties of magnetically aligned single wall carbon nanotube films,* Applied Physics Letters **77**, 666 (2000).

[14] A. E. Aliev, M. H. Lima, E. M. Silverman, and R. H. Baughman, *Thermal conductivity of multi-walled carbon nanotube sheets: radiation losses and quenching of phonon modes.* Nanotechnology **21**, 035709 (2010).

[15] A. J. McNamara, Y. Joshi, and Z. M. Zhang, *Characterization of nanostructured thermal interface materials – A review,* International Journal of Thermal Sciences **62**, 2 (2012).

[16] S. Vollebregt, R. Ishihara, F. Tichelaar, Y. Hou, and C. Beenakker, *Influence of the growth temperature on the first and second-order Raman band ratios and widths of carbon nanotubes and fibers,* Carbon **50**, 3542 (2012).

[17] A. M. Marconnet, N. Yamamoto, M. a. Panzer, B. L. Wardle, and K. E. Goodson, *Thermal conduction in aligned carbon nanotube-polymer nanocomposites with high packing density.* ACS nano **5**, 4818 (2011).

[18] G. Romano, M. Riccio, G. De Falco, L. Maresca, A. Irace, and G. Breglio, *An ultrafast IR thermography system for transient temperature detection on electronic devices,* in *2014 Semiconductor Thermal Measurement and Management Symposium (SEMI-THERM)* (IEEE, 2014) pp. 80–84.

[19] M. Riccio, a. Pantellini, a. Irace, G. Breglio, a. Nanni, and C. Lanzieri, *Electro-thermal characterization of AlGaN/GaN HEMT on Silicon Microstrip Technology,* Microelectronics Reliability **51**, 1725 (2011).

[20] F. P. Incropera, D. P. DeWitt, T. L. Bergman, and A. Lavine, *Fundamentals of heat and mass transfer,* (2007).

[21] D. Yang, Q. Zhang, G. Chen, S. Yoon, J. Ahn, S. Wang, Q. Zhou, Q. Wang, and J. Li, *Thermal conductivity of multiwalled carbon nanotubes,* Physical Review B **66**, 2 (2002).

[22] A. Pike and J. W. Gardner, *Thermal modelling and characterisation of micropower chemoresistive silicon sensors,* Sensors and Actuators B: Chemical **45**, 19 (1997).

[23] Z. Y. Guo and Z. X. Li, *Size effect on microscale single-phase flow and heat transfer,* International Journal of Heat and Mass Transfer **46**, 149 (2003).

[24] J. Peirs, D. Reynaerts, and H. V. Brussel, *Scale effects and thermal considerations for micro-actuators,* Proceedings. 1998 IEEE International Conference on Robotics and Automation (Cat. No.98CH36146) **2**, 1516 (1998).

[25] G. Zhang, S. Jiang, W. Yao, and C. Liu, *Enhancement of natural convection by carbon nanotube films covered microchannel-surface for passive electronic cooling devices,* ACS Applied Materials & Interfaces **8**, 31202 (2016).

[26] I. Brody and F. Korösy, *Convection and conduction of heat in gases,* Journal of Applied Physics **10**, 584 (1939).

[27] I. Langmuir, *Convection and Conduction of Heat in Gases,* Physical Review (Series I) **34**, 401 (1912).

[28] S. Kline and F. McClintock, *Estimating the unertainty in single-sample experiments mech,*

Engng **75**, 3 (1953).

[29] M. B. Jakubinek, M. A. White, G. Li, C. Jayasinghe, W. Cho, M. J. Schulz, and V. Shanov, *Thermal and electrical conductivity of tall, vertically aligned carbon nanotube arrays,* Carbon **48**, 3947 (2010).

[30] X. Huang, J. Wang, G. Eres, and X. Wang, *Thermophysical properties of multi-wall carbon nanotube bundles at elevated temperatures up to 830 K,* Carbon **49**, 1680 (2011).

[31] M. Hu, S. Shenogin, and P. Keblinski, *Molecular dynamics simulation of interfacial thermal conductance between silicon and amorphous polyethylene,* Applied Physics Letters **91**, 241910 (2007).

[32] P. Kim, L. Shi, a. Majumdar, and P. L. McEuen, *Thermal transport measurements of individual multiwalled nanotubes.* Physical review letters **87**, 215502 (2001), arXiv:0106578 [cond-mat] .

[33] W. Yi, L. Lu, Z. Dian-lin, Z. W. Pan, and S. S. Xie, *Linear specific heat of carbon nanotubes,* Physical Review B **59**, R9015 (1999).

[34] A. M. Marconnet, M. a. Panzer, and K. E. Goodson, *Thermal conduction phenomena in carbon nanotubes and related nanostructured materials,* Reviews of Modern Physics **85**, 1295 (2013).

[35] M. a. Panzer, G. Zhang, D. Mann, X. Hu, E. Pop, H. Dai, and K. E. Goodson, *Thermal Properties of Metal-Coated Vertically Aligned Single-Wall Nanotube Arrays,* Journal of Heat Transfer **130**, 052401 (2008).

[36] Y. Xu, Y. Zhang, E. Suhir, and X. Wang, *Thermal properties of carbon nanotube array used for integrated circuit cooling,* Journal of Applied Physics **100**, 074302 (2006).

[37] B. A. Cola, J. Xu, and T. S. Fisher, *Contact mechanics and thermal conductance of carbon nanotube array interfaces,* International Journal of Heat and Mass Transfer **52**, 3490 (2009).

[38] C. Silvestri, P. Picciafoco, B. Morana, F. Santagata, G. Zhang, and P. Sarro, *Electro-thermal simulation and characterization of vertically aligned CNTs directly grown on a suspended microhoplate for thermal management applications,* in *Proceedings of IEEE Sensors*, Vol. 2014-Decem (2014) pp. 827–830.

4

EFFECTS OF NANOSCALE COATINGS ON THERMAL PERFORMANCE OF VA-CNTS

This chapter is based on:

1. **Cinzia Silvestri**, Michele Riccio, René H. Poelma, Aleksandar Jovic, Bruno Morana, Sten Vollebregt, Andrea Irace, Guo Qi Zhang, Pasqualina M. Sarro. "Enhancing Thermal Transport Efficiency in High Aspect Ratio Carbon Nanotube Arrays by Conformal Coatings". Submitted to *Nanoscale*, 2017.

4.1. INTRODUCTION

Due to the high potential of VA-CNTs, many research groups have investigated their thermal performance, expressed in terms of thermal resistance, R_{eff}, and effective thermal conductivity, k_{eff}. The collected data are reported in Figure 4.1 which refers to vertically aligned multi-walled CNTs grown by CVD method at temperatures between 500 °C to 800 °C. In general, a lower growth temperature produces CNTs with lower crystallinity degree[1], which may partially explain the broad range of k_{eff} reported. However, the sample fabrication (growth temperature, barrier and catalyst layers) is not the only dissimilarity between these works. There are difference in the adopted thermal measurement techniques and assumptions. Moreover, the graph reflects a lack of information for VA-CNT with heights spanning from 100 µm to 700 µm. The results pub-

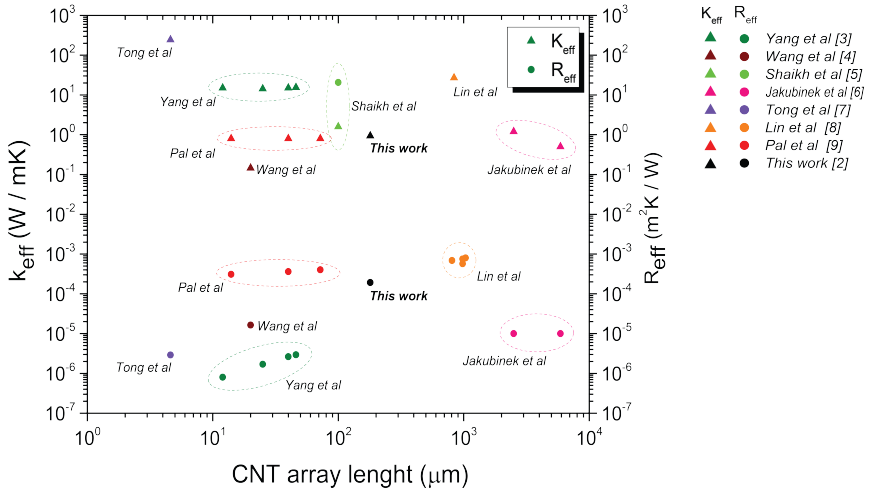


Figure 4.1: Literature overview of both effective thermal conductivity (▲ marker) and thermal resistance (• marker) for different CNT array lengths. This chart reports a subset of available data where both thermal resistance and effective thermal conductivity have been estimated [2–9]. The thermal resistance data refers to sample in absence of mechanical compression. CNTs mechanically compressed show higher thermal conductivity and lower thermal contact resistance [10]. There is a lack of data for CNT length from 100μm to 700μm. This work provides a detailed study on CNT array of 180μm in length.

lished in [2] contribute to enlarge the available data on VA-CNTs with height around 160-210μm. As shown in Chapter (3), the thermal conductivity of an individual MWCNT is several orders of magnitude higher than the effective one of a VA-CNT foam-like nanostructure, 136 W m^{-1} K^{-1} and 1.04 W m^{-1} K^{-1}, respectively. This decrease is mainly the result of the inter-tube scattering and the high thermal contact resistance between CNT-substrate.

Interesting properties in nanoscale assemblies have been found by combining the high-aspect ratio and the foam-like morphology with thin conformal coatings. As example, photoanodes obtained by coating zinc oxide (ZnO) nanoforest with a thin layer of titanium dioxide (TiO_2) for dye sensitized solar cells [11], or gold-coated vertical Si nanowire for biomolecule detection have been reported [12].
In this perspective, VA-CNT arrays with their foam-like structure represent an attractive 3D scaffold to create a novel class of heterogeneous materials with tailored behaviour:

- First, VA-CNTs are relatively easy to be grown bottom-up in lithographically defined shape and locations at wafer scale.

- Second, the achieved arrangements are lightweight high aspect ratio three-dimensio nal (3D) microstructures.

- Last but not the least, the porous-like morphology is favourable for the deep infiltration of nanoscale conformal coatings, resulting in a reinforced structure suitable for successful integration in devices.

The tailoring of the CNT-based nanostructure performance strongly depends on the achieved porosity and on the coating material selected. Recently, Poelma et al. have shown how the mechanical response of high aspect ratio foam-like CNTs can be tuned from foam-like toward brittle ceramic by simply varying the thickness of amorphous silicon carbide (a-SiC) coating [13, 14]. The achieved heterogeneous material can be interesting for a wide range of applications spanning from solid-state supercapacitors [15], to through-silicon-via (TSV) interconnects [16], to fuel cells [17], to on-chip cooling solution [2].

In this chapter, we explore the effect on the heat dissipation of conformally coated high aspect ratio VA-CNTs in vacuum and in air. The materials chosen to fill the CNT-based scaffold are Al_2O_3 and non-stoichiometric a-SiC. They are both ceramic materials with superior hardness, thermal conductivity of ~360 W m^{-1} K^{-1} and ~25 W m^{-1} K^{-1} for bulk SiC [18] and bulk Al_2O_3 [19], respectively, and adequate electrical insulating performance [20]. Using atomic layer deposition (ALD) for the Al_2O_3 deposition and LPCVD for the a-SiC deposition, we can obtain nanoscale accuracy over the deposition thickness of the thin films and a good conformality. The infiltration depth within the foam-like VA-CNTs and the consequent morphological variation due to the performed coating are assessed by high-resolution SEM inspection. The defect density of the obtained heterogeneous arrays is characterized by Raman spectroscopy. The thermal performances achieved with the coatings are explored through the electro-thermal characterization procedure used in Chapter (3). Improved thermal transport efficiency has been achieved for the a-SiC coated CNT scaffolds, resulting in a strong enhancement in terms of k_{eff}. The thermal conduction enhancement of high aspect ratio CNT arrays provided by the thin coatings mentioned is extensively studied, mainly in view of their integration as localized on-chip cooling solutions. In fact, a-SiC coated VA-CNT arrays have been successfully encapsulated by film assisted transfer molding, withstanding the insertion pressure of the epoxy molding compound. This preliminary test has shown the improved mechanical properties of the obtained composite material and the possibility to be used as through package thermal vias.

4.2. COATING PROCEDURE AND MORPHOLOGICAL CHARACTERIZATION

Nanoporous networks of VA-CNT arrays are among the most promising arrangements for practical thermal management applications, such as thermal interface material (TIM) and micro-scale heat sinks [21–24]. However, their main limitation is the thermal transport efficiency, which is strongly influenced by the defect density within the array as well as the high thermal interface resistance between the CNTs and the substrate [25–27]. To improve both the k_{eff} as well as the mechanical stability of the high aspect ratio structure it is essential to apply a nanometer-thick conformal coating. The VA-CNT micropin configurations are directly synthesized on top of suspended MEMS microhotplates (MHPs) (Chapter (3)). After the growth step, the CNT micropins are subjected to a coating step. Two coating materials are investigated: a-SiC and Al_2O_3, both with a targeted thickness of 15 nm.

To perform the a-SiC conformal coating, the samples are loaded in a Tempress hot-wall LPCVD furnace. The precursor gasses are acetylene (C_2H_2) and dichlorosilane (SiH_2Cl_2) diluted in 5% hydrogen (H_2) and the deposition temperature and pressure are fixed at 760°C and 0.8 mbar, respectively. Most probably, the coating nucleation starts from CNT surface defects. The average a-SiC deposition rate is 5 Å min^{-1}, with an incubation time of ~7 min before the film starts growing. A detailed description of the physical and chemical properties of the deposited a-SiC thin layer can be found in Morana et al. [28].

The Al_2O_3 conformal coating is applied using an ALD system (ASM F-120 reactor). The deposition temperature is set at 300°C and the pressure at 1.33 mbar. The ALD cycle sequence consists on exposing the sample to a trimethylaluminium (TMA) for 2 s, then a nitrogen (N_2) purge for 6 s, followed by 2 s of high purity water (H_2O) exposure, ending with 8 s of N_2 purge. The N_2 purge is performed after each precursor exposure to remove any unreacted precursors or reaction by-products in the chamber. The average deposition rate is self-limited to around 0.9 nm $cycle^{-1}$.

The formation of the heterogeneous composites, the Al_2O_3 coated (Al_2O_3/CNTs) and the a-SiC coated (a-SiC/CNTs) CNT nanofoam scaffolds, is sketched in Figure 4.2 (a-c). It is well known that CVD grown CNTs have a high density of surface defects. Moreover, it has been demonstrated that the surface defects provide bonding sites for the coating nucleation [29–32]. Therefore, no functionalization treatments are performed on the CNT scaffold prior to the coating procedures. Upon exposure to the precursor gases, the corresponding precursor molecules diffuse into the VA-CNT porous structure.

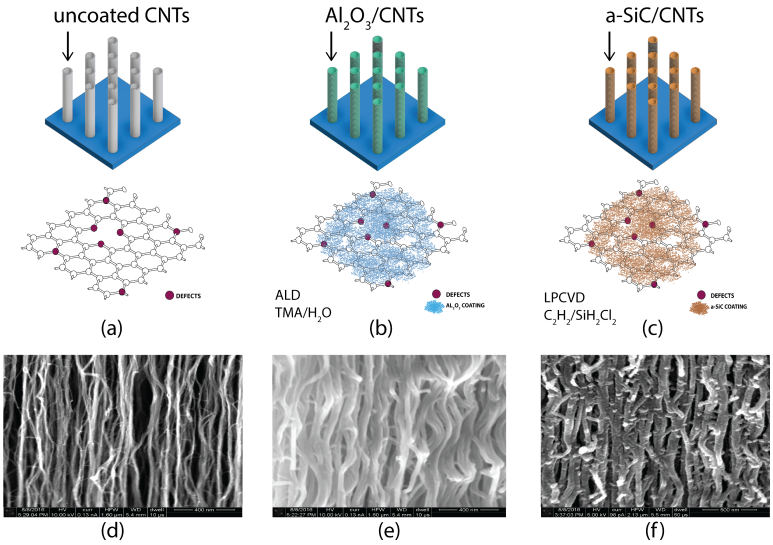


Figure 4.2: Coated Al_2O_3CNTs and a-SiC/CNTs hybrid structures. As in Chapter (3), the VA-CNTs are lithographically patterned to achieve micropin feature. (a-c) Schematic illustration of three-dimensional CNTs highlighting the gas precursors used during the coating procedure. (d) SEM close up of the of the as-grown VA-CNT array. The average nanotube diameter is 10 nm. (e) SEM image of the obtained hybrid Al_2O_3/CNTs at the micropin sidewall. The resulting diameter of an individual nanotube is equal to 35 nm. (f) SEM close up of the of the a-SiC/CNT composite sidewall. The average diameter of an individual a-SiC coated CNT is 30 nm.

The coating nucleation starts from the interaction between precursor gases and localized CNT surface defect sites, and/or precursors and CNT-CNT junctions. The product of the reaction is a nanometer size granule formation at the surface. A thin layer is then formed by the overlap of adjacent grains while the number of ALD cycles increase or the deposition time in the LPCVD furnace increases. Although the number of the ALD cycles depends on the CNT defect density, usually 100 cycles are enough to obtain conformally coated CNTs [33]. SEM images of VA-CNT sidewalls reported in Figure 4.2 (d-f), highlight the morphological variation of the cluster before and after the coating depositions. The as-grown VA-CNT array consists of wavy interlaced multiwalled carbon nanotubes (MWCNTs), oriented perpendicular to the substrate. The bridging between nearby nanotubes creates a regular foam-like structure with an average spacing of 60 nm. The nanotube average diameter, d_{CNT}, is 10 nm and the tube density within the micropin is around 112 tubes μm^{-2}, resulting in a porosity of 99.1% (Figure 4.2 (d)). For ideally aligned CNTs a 30 nm coating can not only fill, but also coalesce, the entire array. The SEM images of both micropin hybrid composites show remarkably uniform deposition around the nanotubes. The initial vertical orientation and the high surface area

of the CNT array are retained, while in correspondence to the CNT-CNT junctions some localized aggregations are formed. The average CNT coated diameter is 31 nm and 35 nm for the for the Al_2O_3/CNTs and for the a-SiC/CNTs, respectively (Figure 4.2 (e-f)). Therefore, the average coating thicknesses deposited on the MWCNT surface are ~17 nm for the a-SiC and ~13 nm for the Al_2O_3, in good agreement with the ones measured by ellipsometry on a bare silicon wafer.

Raman spectroscopy analysis is used to assess the quality of the CNT nanofoams before and after the composite formation. Figure 4.3 reports the collected spectra, from 750 to 3600 cm^{-1}, and their corresponding deconvolutions of the first order region, from 1000 to 2000 cm^{-1}, obtained applying a least square fitting procedure. Two main Raman band can be observed in all spectra, the D- and the G-band with peaks located around ~1346 and ~1580 cm^{-1}, respectively. The intensity ratio between the D- and G-band, I_D/I_G, and its variation provides us a look on the nanotube quality after coating. The obtained I_D/I_G ratios are 0.95, 1.11, and 1.17 for the uncoated VA-CNT, Al_2O_3/CNTs and a-SiC/CNTs, respectively. The observed high defect density of the as-grown MWCNT is beneficial, since the defects provide nucleation sites for the precursor absorption. Once coated with Al_2O_3, the signal from the CNTs tends to be suppressed due to the coated material. The spectra of the a-SiC/CNT hybrid array show instead a wide asymmetric band, combination of three contributions: the G-band peak and the D-band peak of the CNT scaffold, and a band peak at ~1483 cm^{-1}.

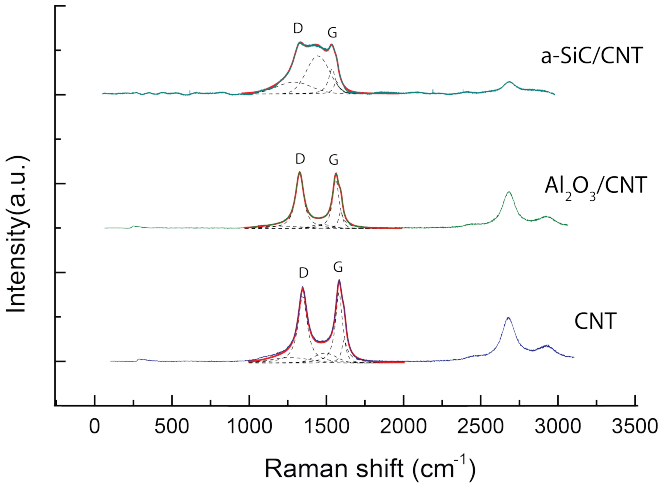


Figure 4.3: Raman spectra of the as-grown, Al_2O_3 coated and a-SiC coated VA-CNTs, with relative deconvolved peaks of the first order region. The Raman spectroscopy analysis was performed at room temperature using an excitation wavelength of 514 nm from an Ar^+ laser. The presence of carbon nanotubes is detectable in all the spectra. The dashed lines represent the fitted peaks. For further details, please refer to Section 2.3.4.

4.3. COATING INFILTRATION IN VA-CNT ARRAYS

The mechanical response of conformally coated CNTs micropin structures can be accurately tuned by varying the coating layer thickness as demonstrated by Poelma et al.[13, 14]. By analyzing the high-resolution SEM pictures at different microstructure locations, from top to bottom of the micropin ($z-axis$) as well as along the radius (r-$axis$), the coating uniformity and the penetration depth of both the a-SiC/CNTs and the Al_2O_3/CNTs are observed and reported in Figure 4.4 and Figure 4.5.

The a-SiC coated micropin (Figure 4.4) shows an excellent coating penetration along the radial direction. In particular, every 1 µm the coating reduces of roughly 0.1 nm when going from the sidewall to the core. The thickness variation along the z-$axis$ is just 6 nm on the full micropin height.

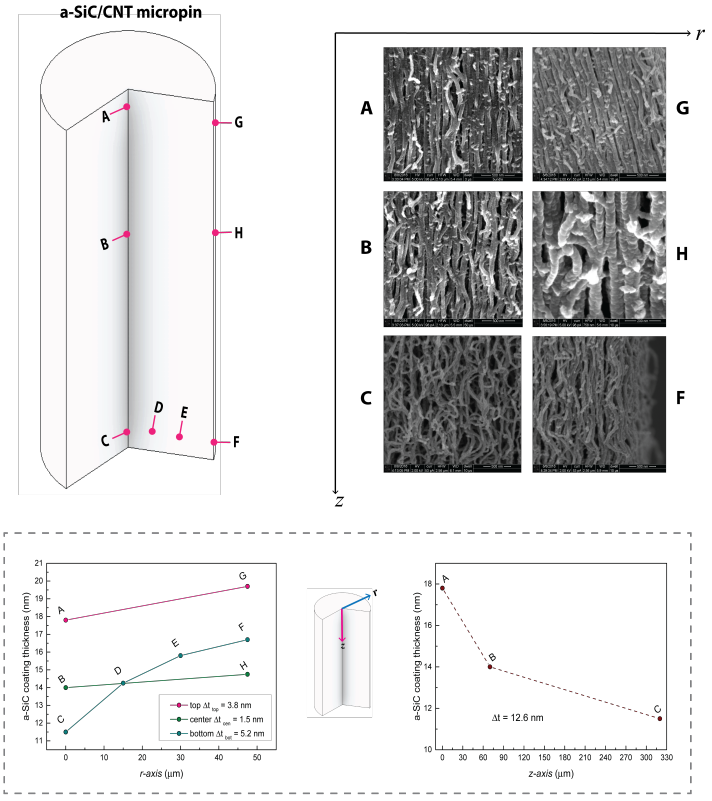


Figure 4.4: Penetration depth of the LPCVD a-SiC coating in the CNT micropin. On the 3D micropin illustration the location of the points analyzed by SEM are reported. The graphs report the thickness variation along the z and r directions.

This was also confirmed in other works focused on LPCVD coated CNTs [34–37].

From the analysis of the Al_2O_3 coated micropin, the coating at the sidewall looks uniform. However, after cleavage, the SEM analysis of the micropin cross-section reveals a poor and uneven infiltration of the precursors through the CNT array (Figure 4.5), demonstrating a diffusion-limited mechanism for the coating. The achieved heterogeneous material is made of a soft core of uncoated CNTs reinforced by a ceramic shell, which is approximately 1.4 µm thick, as shown Figure 4.6.

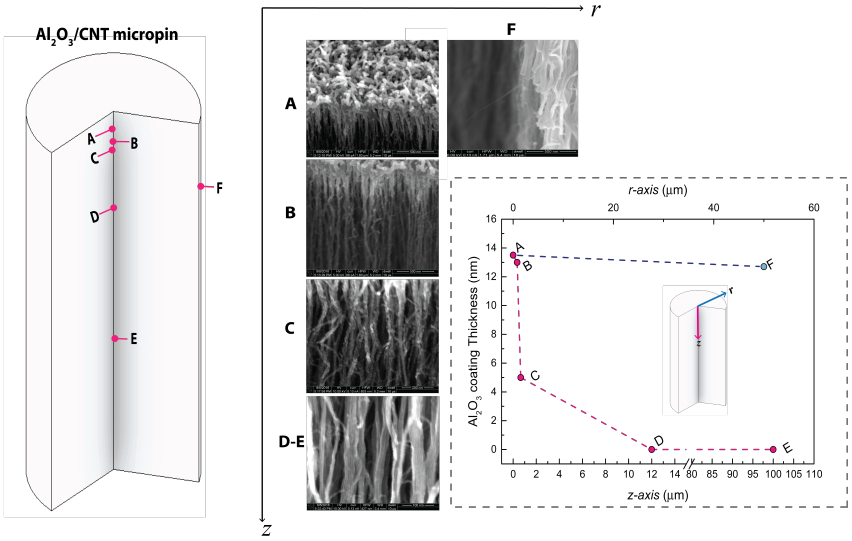


Figure 4.5: Penetration depth of the ALD Al_2O_3 coating in the CNT micropin. On the 3D micropin illustration the location of the points analyzed by SEM are reported. The graph reports the thickness variation along z and $r$directions.

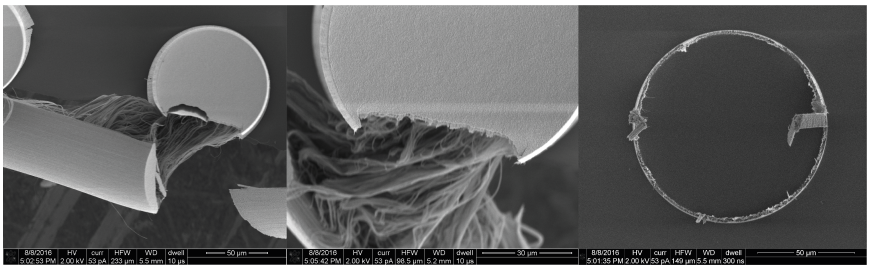


Figure 4.6: Thin shell of ALD Al_2O_3on VA-CNT microstructure.

From the cleaved micropin, a steep gradient is observed all over the outer layer. In particular, the coating thickness along the *z-axis* is ~13.5 nm at the micropin tip (z=0), it reduces down to 5 nm at z=650 nm. For $z > 650$ nm some isolated grains can be noted, while the coating traces disappear completely for $z > 12\,\mu m$. The same abrupt reduction in the coating thickness occurs along the *r-axis*. The coating thickness reduces of approximately of 12.8 nm every 1 µm. The resulting coating penetration depths are approximately 700 nm for the ALD coated Al_2O_3/CNTs and around 66 µm for the LPCVD a-SiC/CNTs, proving the superior ability of the LPCVD process to evenly coat complex high surface area nanostructures. The low penetration depth and the uneven uniformity of the ALD coating within the intricate CNT foam-like morphology has been object of several studies [32, 33, 38]. The main limiting factor is represented by the ALD coating process itself, due to the temperature conditions. The initial diffusion of precursor molecules inside the foam is slow and it decreases with the increasing of the CNT diameters. Moreover, after each cycle the CNT-CNT spacing reduces while the CNT surface area increases, limiting the diffusion coefficient even further. To achieve a uniform monolayer on a large surface area as the one of the VACNT array, a cycle to cycle scaling in both precursor dose and purging time are required [15, 33, 39].

4.4. HEAT TRANSFER RATE OF COATED AND UNCOATED VA-CNTS

In this section we discussed the results achieved by using the measurement approach and VA-CNT arrangements, the multi-pin configuration composed by six micropins (each with a radius of 10 µm) and the single micropin (100 µm in radius), employed in Chapter (3). Each sample was thermally stimulated by Joule heating the MHP before and after the coating steps, and the power consumption in steady-state heat transfer condition both in air and vacuum was recorded.

4.4.1. A-SIC/CNTS

Multi-pin performance

The a-SiC/ VA-CNT multi-pin arrangement shows remarkable enhancement of the heat dissipation performance after the a-SiC coating (Figure 4.7 (a)). To understand which of the heat transfer mechanism can be the cause of such improvement we consider the two different environmental conditions studied. In vacuum, the heat conducted through the VA-CNTs is dissipated by radiation. The evaluation of the emissivity by high-resolution infrared microscopy reveals an unvaried ϵ between the coated and uncoated CNTs (ϵ =

0.95). Moreover, the overall shape of the multi-pin configuration is substantially unaltered due to the nanometer thick coating. Therefore, the substantial improvement obtained in vacuum is due to an enhanced effective thermal conductivity, $k_{effa-SiC/CNT}$. Secondary effects such as annealing and influence of the a-SiC coating on the MHP can be excluded. First, the Pt spiral of the MHP was pre-annealed at 1000°C for one hour during the fabrication process. Secondly, a bare reference MHP without CNT underwent the coating with the VA-CNT samples and any variation in thermal performance prior and after the coating procedure was detected.
In air, the difference between the heat dissipative behaviour pre and post coating is even more remarkable. As example, for a given input power of 25 mW a reduction of the local hot-spot temperature of 103 K is achieved in air. The heat dissipation improvement recorded in air is related to both conduction and convection and therefore, can be related to the $k_{effa-SiC/CNT}$ and the porosity variation. The specific impact of each of the above-mentioned contribution needs to be determined.

Single micropin performance

Unexpectedly, the a-SiC/CNT single micropin does not show a detectable heat transfer improvement before and after the coatings (Figure 4.7 (b)). The extraordinary performance improvement of the multi-pin configuration and the unvaried one of the single micropin poses many questions. The unvaried single micropin behaviour may be partially related to its geometry, and in particular to the diameter. As mentioned in the Section 4.3, the maximum micropin radius to achieve evenly coated a-SiC/CNTs is 66µm. Consequently, the entire volume of each multi-pin element (10µm in radius) is fully coated, while the single micropin volume that is effectively coated is about 88% of the total one.

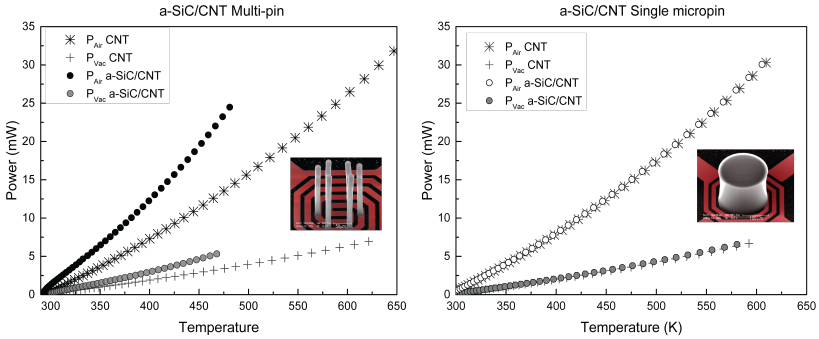


Figure 4.7: Power versus temperature trend before and after the a-SiC coating (CNT or a-SiC/CNT in the legend) for two sample configuration: (a) the multi-pin and (b) the single micropin. The measurements were performed in both air and vacuum (P_{AIR} and P_{VAC}) In particular, the increase in dissipated power, up to 75% in air at 480 K and up to 64% in vacuum at 468 K, is obtained by depositing a nanoscale thin coating of a-SiC on the multi-pin scaffolds. "$*$" and "+" symbols refer to P_{AIR} and P_{VAC} of the uncoated configurations, while • refers to the Al_2O_3/CNTs configurations.

4.4.2. AL_2O_3/CNTS

No evidence of heat dissipation enhancement is found for any investigated CNT configuration after the ALD Al_2O_3 coating treatment (Figure 4.8). This is explained by the observed low infiltration depth of the coating within the VA-CNTs.

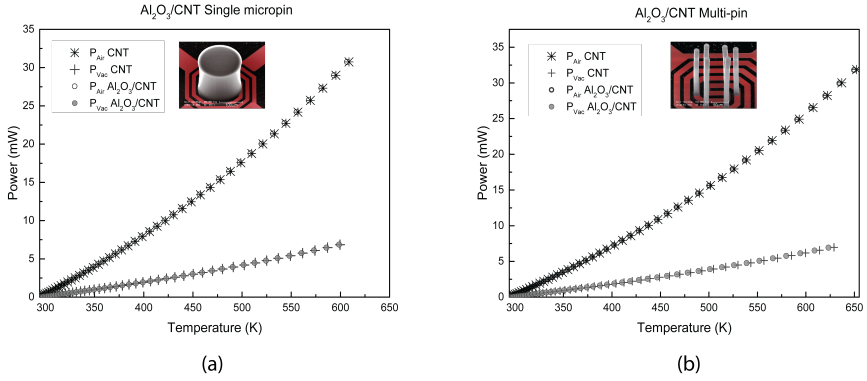


Figure 4.8: The thermal performance characterization is carried out on the (a) the single micropin configuration and (b) the multi-pin configuration. "$*$" and "+" symbols refer to P_{AIR} and P_{VAC} of the uncoated configurations, while • refers to the Al_2O_3/CNTs configurations.

4.5. THERMAL PERFORMANCE AFTER NANOSCALE COATINGS

In order to highlight how the two ceramic coatings affect the heat dissipation, we report in Figure 4.9 the average temperature reached by the various arrangements at fixed power. In both air and vacuum the multi-pin configuration a-SiC coated, $T_{6ma-SiC}$, outperform in comparison with the others.

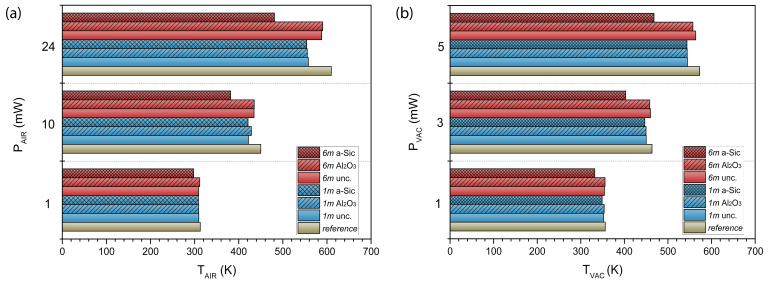


Figure 4.9: For a given input power in (a) air, P_{AIR}, and in (b) vacuum, P_{VAC}, the corresponding average temperature (T_{AIR} or T_{VAC}) reached by the analyzed sample sets are reported. $6m$, $1m$ and reference refer to the multi-pin, single micropin and bare MHP, respectively. The unpatterned bars indicate the samples taken as reference (uncoated VA-CNTs or bare MHP).

The not altered heat transfer performances of the Al_2O_3/CNTs and the impressive enhancement of the a-SiC multi-pin scaffolds might be related to the effective thermal conductivity and the porosity variation. In the following sections these two main causes and the various subfactors are discussed.

4.5.1. EFFECTIVE THERMAL CONDUCTIVITY

The effective thermal conductivities data are obtained by combining the temperature at the micropin tip and at the junction region CNTs-MHP through high-resolution IR microscopy, with the one-dimensional pin fin heat transfer model explained in Chapter (3). The temperature dependency of the k_{eff} of both Al_2O_3 and a-SiC VA-CNT multi-pins is obtained by acquiring the IR maps while powering the MHP (Figure 4.10).

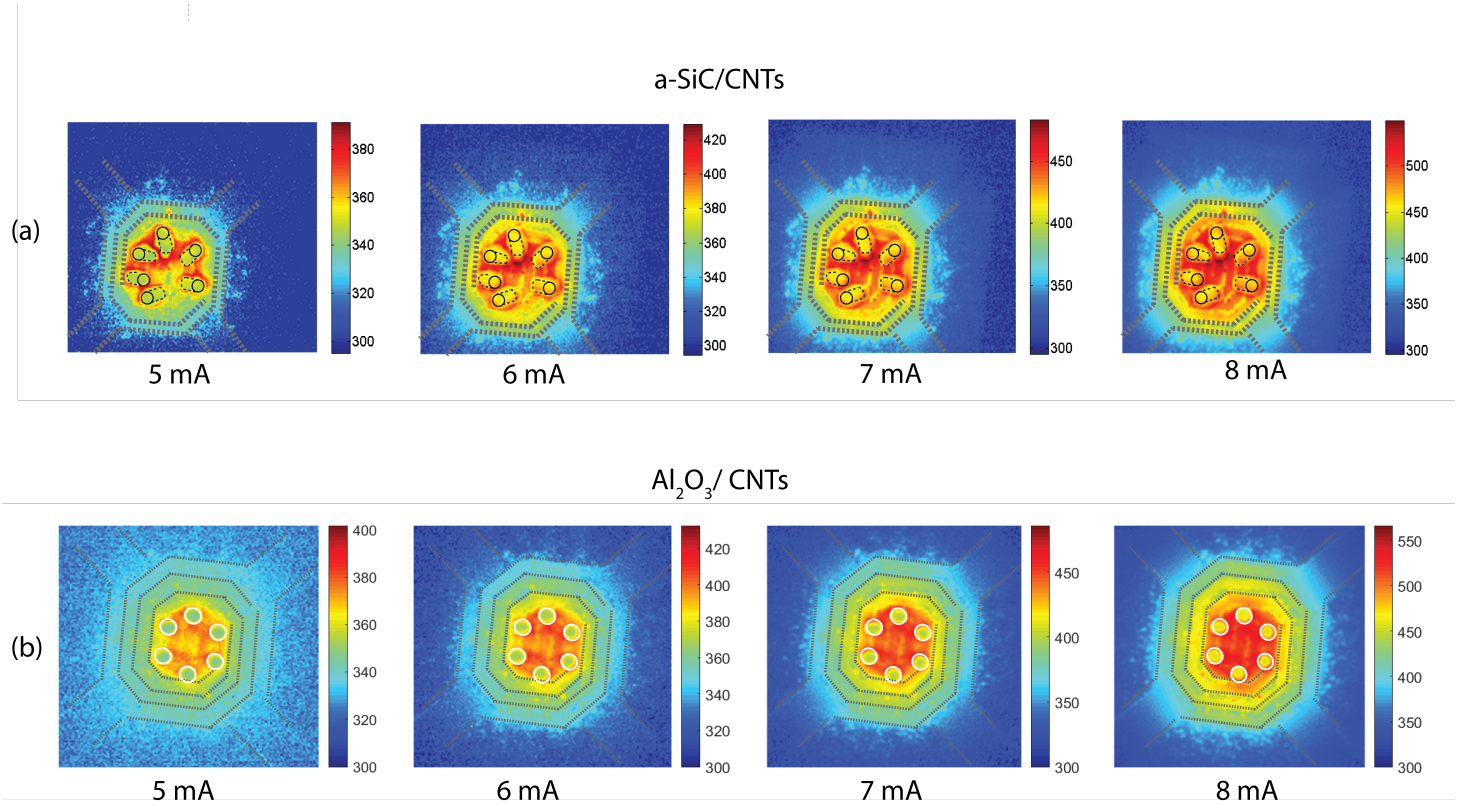


Figure 4.10: High-resolution IR maps of the multi pin configuration of (a) a-SiC/CNTs and (b) Al_2O_3/CNTs at four current inputs: 5 mA, 6 mA, 7 mA and 8 mA. The MHP structure is indicated by the grey dotted line.

Figure 4.11 (a) shows the obtained k_{eff} of the pre- (k_{effCNT}) and post-coated multi-pin arrangements ($k_{effa-SiC/CNT}$ and $k_{effAl2O3/CNT}$) at different temperature. The $k_{effAl2O3/CNT}$ shows no substantial variation compared to the uncoated VA-CNTs, in line with the power dissipation recorded. For the a-SiC/VA-CNTs instead, the graph clearly reveals a strong k_{eff} enhancement due to the conformal coating penetration into the CNT nanofoam architecture. At the lowest investigated temperature, the k_{eff} improved from 1.04 W m^{-1} K^{-1}, when uncoated, to 2.6 W m^{-1} K^{-1} when a-SiC coated. The (k_{effCNT}) reaches 4.2 W m^{-1} K^{-1} at the highest investigated temperature. In particular, the trend shows a steep increase around 392 K, while above it the increasing rate reduces. The enhancement factor, defined by the ratio ($k_{effa-SiC/CNT}$ - k_{effCNT}) / k_{effCNT}, highlights the thermal conductive transport enhancement at different operating temperatures and it goes from 104% up to 181% (Figure 4.11 (b)). The obtained results highlight the impressive effect that the amorphous carbide coating has on the improvement of thermal performance efficiency in VA-CNT scaffold. To the best of our knowledge, this is the highest-ever thermal conductivity enhancement of VA-CNTs obtained by coating.

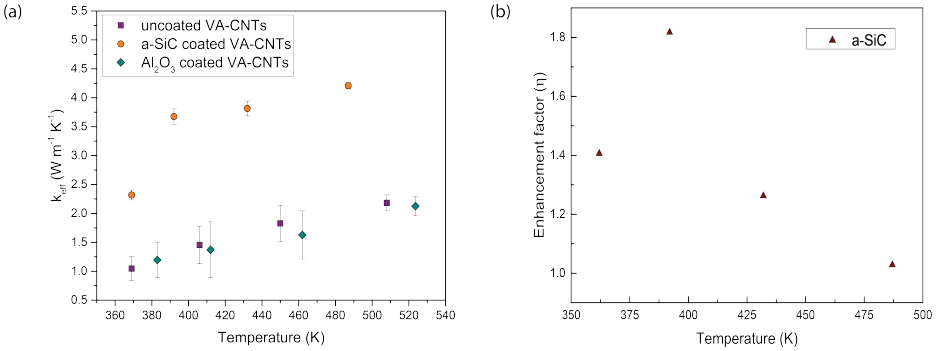


Figure 4.11: (a) Experimentally determined dependence of the effective thermal conductivity on temperature for uncoated (purple), a-SiC coated (orange) and Al_2O_3 coated (dark cyan) VA-CNTs. (b) The thermal conductivity enhancement, defined as $k_{effa-SiC/CNT}$ - k_{effCNT}) / k_{effCNT} is reported as function of temperature. The a-SiC coated sample reaches an enhancement up to 181%.

It is generally recognized that thermal conduction in a CNT arrays strongly depends on their morphology, vacancies, defects and CNT-CNT interactions as well as the thermal boundary resistance at the interface CNT-substrate and CNT-air. In particular, as shown by the Raman spectra as well as SEM picture, the as-grown foam-like morphology consists of many defects, CNT-CNT junctions and twists that highly affect the thermal transport and increase the phonon-boundary scattering. It has been demonstrated that the thermal resistance at the interface between two nanotubes, which interact through

van der Waals forces, it is notably large (tube-tube thermal resistance $\sim 11 \times 10^{-8}$ W m^2 K W^{-1} [40, 41]. All these aspects are reflected in the achieved k_{effCNT}. There are two main factors that might explain the thermal conductivity enhancement of the a-SiC/CNT composite: the nano coating conformality, the intrinsic thermal conductivity of the deposited material, which can be higher than the one of the as-grown MWCNTs, and a reduction in contact resistance CNT-substrate.

By conformally coating a VA-CNT scaffold a new percolating network is built on top of the original one, allowing to overcome defected regions, tube twists, and to promote additional heat conduction paths, thus enhancing the phonon transfer between the CNTs [42]. In fact, the CNT-CNT contact area increases while the interface thermal resistance between neighboring CNTs is reduced [41]. Moreover, new contact points are created which may lead to an increase in phonon scattering phenomena as well as to additional paths for the heat to transfer among adjacent tubes that were not in contact before [**?**].The Al_2O_3 coating with its inability in creating a conductive network spread over the whole scaffold surface (scarce penetration depth), prevents any significant heat transfer improvement (Figure 4.11 (a)).

Another possible enhancement factor is the thermal conductivity of the a-SiC itself. Since the coating thickness is close to phonon mean free path of both the MWCNTs (as low as 4 nm) [43] and the a-SiC (as low as 0.488 nm) [44] , the thermal conductivity ceases to be a material property and becomes dependent from size and shape of the boundary interface [45]. It has been reported that for thin films the thermal conductivity of amorphous SiC is likely to be rather smaller than for the bulk crystalline structure, 0.12-3.6 W m^{-1} K^{-1} instead of 320-490 W m^{-1} K^{-1} [44]. However, it is higher than the k_{effCNT}.

Last but not the least, the k_{effCNT} can increase due to a reduction of the thermal contact resistance at the interface CNT-substrate. It has been demonstrated that in presence of a weak bond between substrate and the nanofoam, not all the CNTs participate effectively to the heat transport [46]. A better thermal coupling between the support layer and the CNTs can be achieved through embedding the nanotube in metal contact [47] or by increasing the contact area by pressing the CNTs toward the substrate [48]. In our case, by perfroming the coating it might likely be that more CNTs are participating to the heat transfer due to the cross sectional area enhancement given by the a-SiC coating.

4.5.2. POROSITY

As observed in the previous sections, an impressive enhancement of the thermal performance of the a-SiC coated multi-pin configuration is recorded. However, the achieved results can't only be due to a thermal conductivity enhancement. Based on the micropin model described in Section 3.3, we calculate the heat loss through a unit element of the multi-pin configuration using the following equation [49]:

$$Q_{pin} = k_{eff} A_c m (T_b - T_\infty) \tanh(mL) = 0 \tag{4.1}$$

which depends upon two factors: conduction and convection.By applying the same methodology adopted in Chapter (3), we infer the improved k_{eff} and H_c. Table 4.1 reports the heat transfer rates, calculated through Equation (4.1), of a unit element of the micropin configuration (Q_{pin}) and of the whole cluster (Q_{Tpin} = 6 Q_{pin}). The theorical heat transfer rates are then compared to the experimental ones collected in air, for both the multi-pin configuration ($Q_{Tot_{device}}$) and of the bare MHP (Q_{MHP}). The heat transfer rate of the uncoated multipin configuration ($6m$) is well predicted by the Equation (4.1), while the improved k_{eff} and H_c alone cannot explain the significant heat transfer increase of the a-SiC coated configuration ($6m_{a-SiC}$).

Table 4.1: Calculation of the heat transfer rates of: a single micropin element (10µm in radius), Q_{pin} and of the multi-pin configurations, Q_{Tpin}, by using Equation (4.1). $Q_{Tot_{device}}$ and Q_{MHP} are the measured heat transfer rate in air of the multipin configuration plus the MHP contribution, and the bare MHP, respectively. $Q_{Tpin}{}^{*} = Q_{Tot_{device}} - Q_{MHP}$ shows the measured contribution of the pins. Therefore, the comparison between the measured $Q_{Tpin}{}^{*}$ and the analytical Q_{Tpin} gives an idea about the magnitude of the discrepancy that might be caused by the porosity.

Config.	k_{eff} (W m^{-1} K^{-1})	H_c (W m^{-2} K^{-1})	T_b (K)	Q_{pin} (mW)	Q_{Tpin} (mW)	$Q_{Tot_{device}}$ (mW)	$Q_{Tpin}{}^{*}$ (mW)
$6m$	1.04	173	387	0.135	0.815	4.9	0.8
$6m_{aSiC}$	2.4	316	374	0.226	1.4	7.7	3.7

The discrepancy between the analytical and measured heat transfer rate (Q_{Tpin} *vs* $Q_{Tpin}{}^{*}$) and the coated and uncoated micropin configurations, it is most likely caused by the porosity variation. The foam-like VA-CNT porosity of a multi-pin element reduces from 99.1% to 85.5% as consequence of the a-SiC coating infiltration. The porosity reduction affects the natural convective flow as well as the heat transfer. The convective heat flow is influenced by two opposite factors. It should decrease due to less air passing through the pores, because the volume filling fraction of CNTs increases, while the air volume and the flow within the micropin decreases. At the same time, the heat convec-

tion should increase due to the increase in effective surface area of the micropin after coating, which implies that more heat is convected to the surrounding. To quantify how these factors can mutually compensate each other it is hard. However, the enhanced heat transfer rate after a-SiC coating suggests that the surface to volume ratio increasing has a stronger influence than the air volume reduction.

To understand the influence of the porosity on the VA-CNT thermal performance, an uncoated single micropin underwent a densification treatment. In particular, by drop casting isopropyl alcohol (IPA) on VA-CNTs, a densification effect is induced on the tube array. As shown in Figure 4.12 (a-c) the VA-CNT array is now made by closely packed tubes, resembling a solid material. Since the overall shape of the CNT is not maintained after the IPA densification, this treatment represents a more invasive technique compared to the CNT coating. Moreover, it might affect the anchoring of the CNT micropin to the substrate. Figure 4.12 (d) reports the power versus temperature characteristic of the single micropin before and after the densification.

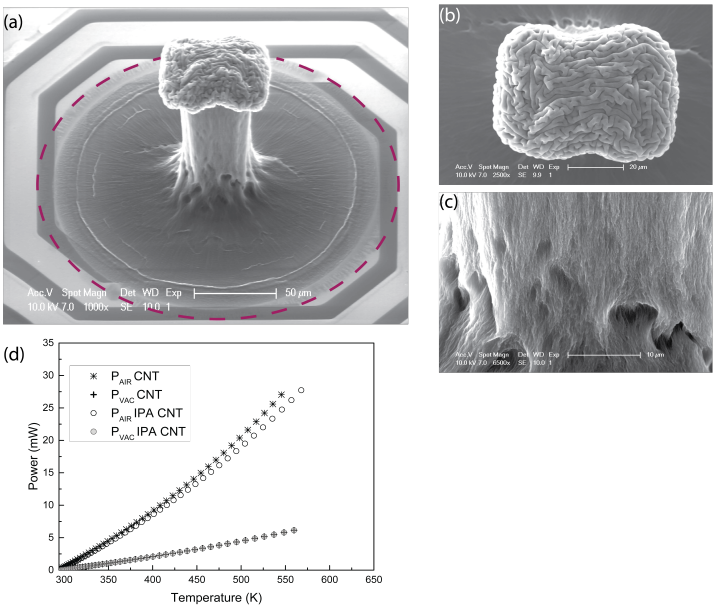


Figure 4.12: ((a) Single micropin after the IPA treatment. The dashed red line shows the initial diameter. The diameter reduces from 200µm to ~ 40µm and the height from 130µm to ~ 100µm. The micropin results shorter due to the CNTs flattened on top of the MHP. (b) Close up of the densified micropin tip; (c) close-up pf the micropin base, showing the high packing density. The foam-like morphology completely disappeared. (d) Thermal performance achieved in air and vacuum before and after the densification.

The IPA treatment slightly deteriorates the thermal performance of the sample in air, while no variation can be detected in vacuum. This thermal response decrease in air it is likely due to overall surface area to volume ratio reduction as well as the air removal from the micropin. Both factors strongly affect the natural convective heat transfer. In vacuum, the unvaried trend is consistent with the results achieved by the a-SiC coated single micropin.

Natural convective heat-transfer in porous media is an active research area field [50–52]. However, to fully understand the natural convective heat-transfer in foam-like VA-CNTs, including porosity variations, in depth numerical modelling and experimental studies are needed.

4.6. THROUGH PACKAGE THERMAL VIAS BASED ON VA-CNTS

In 3D stacked chips the most common thermal management solution is to include an interposer layer equipped with thermal vias. A thermal via allows to vertically transfer the heat from the on substrate chip to the outermost layer of the stack. However, during the interposer fabrication process it is not trivial to achieve a good filling of the vias, which strongly depend on their aspect ratio [53, 54].

Here for the first time, we create through package thermal vias based on VA-CNT micropins. They can represent an attractive alternative as thermal as well as electrical vias. The bottom-up growth, the possibility to fully customize both feature shape and aspect ratio, and the chance to tailor their mechanical, thermal and electrical behaviour through conformal coatings, make VA-CNT array a promising candidate as CNT-based via. A preliminary study is carried out to prove the possibility to embed a-SiC coated VA-CNT micropins into a wafer-level packaging process. Patterned VA-CNT arrays are grown on a Si wafer reaching a height around 300 µm. After conformally coating the nanotubes with 21 nm of LPCVD a-SiC, a film assisted molding (FAM) conducted at wafer-level to encapsulate the system is performed. The FAM is a proprietary technology of Boschman Technologies and APC, for details about the procedure we cross refer to [55, 56]. The crucial part of the encapsulation process is that VA-CNT micropins have to withstand the pressure (from 3 to 80 bar) used to insert the epoxy-molding compound, therefore a proper anchoring with the substrate and good mechanical strength are necessary. After the encapsulation the wafer is diced into individual chips of 6×6 mm. Figure 4.13 (a-f) shows micropins with different diameters before and after the coating and the resulting VA-CNT vias through the epoxy-molding compound (Figure 4.13 (g-i)). The molding results to be quite uniform over the entire wafer and most of the VA-CNT mi-

cropins have the tip sticking-out from the molding, allowing to perform subsequent optional metallization for routings (useful in electrical vias). Figure 4.14 shows compressive failure of some micropins, probably caused during the closure and clamping of the top mold. The compressive failure mechanism observed in our 20 nm coated a-SiC micropins has been extensively studied by others [13, 14]. The whole concept of high-aspect ratio via encapsulation has been patented by our research group [57].

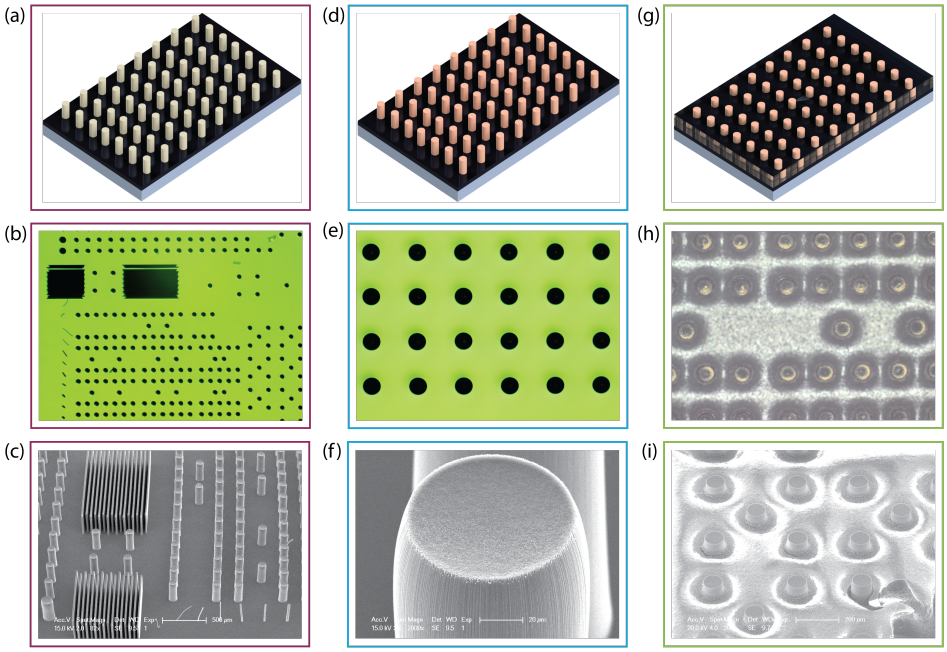


Figure 4.13: (a) On a $Si/SiO_2/Al_2O_3$ stack, photo-lithographically patterned VA-CNT micropins are grown. (b-c) Optical and SEM images of the as-grown VA-CNT micropins, with diameters ranging from 10µm to 100µm and height fixed at 300µm.(d-f) A 20 nm coating of a-SiC infiltrates the VA-CNTs. (g) A layer of epoxy molding compound is inserted. (h-i) Optical and SEM images showing for the first time the micropins enclosed into the molding by FAM.

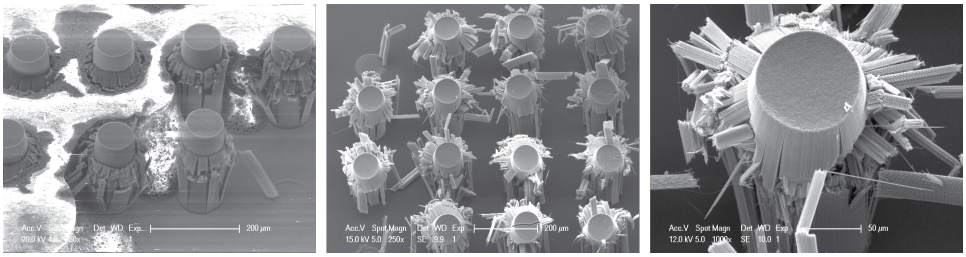


Figure 4.14: Partially molded wafer with coated CNT micropins. Some micropins were crushed due to their lenght exceeding the mold gap.

4.6.1. THERMAL CHARACTERIZATION OF VA-CNT ENCAPSULATED BY FAM

The obtained chip-interposer has been thermally characterized by high-resolution IR microscopy. The interposer is heated up via a thermal chuck to temperatures ranging from 180 °C to 210 °C. By focusing on the chip area the surface temperature reached by the interposer is monitored. The collected data are then compiled into thermal maps Figure 4.15. The current sample configuration does not allow enough distance between the heated chuck and the optic used to record the IR emission (distance 4-5 cm). This implies that also at low temperature the optic is heated up, which affects the recorded images. Therefore, with the current device configuration it is not possible to estimate the heat loss through the VA-CNT vias and the epoxy molding compound. Further tests needs to be carried out. However, each map clearly show the VA-CNT micropins and the temperature profile along them is symmetric, confirming the conformality of the a-SiC scaffold.

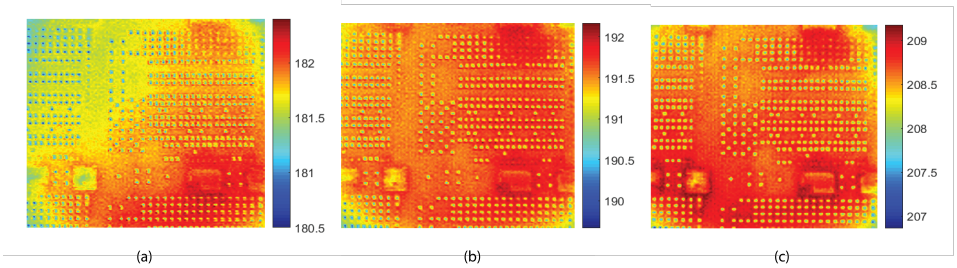


Figure 4.15: Surface temperature profile measured by IR spectroscopy while heating up the chuck at various temperatures: (a) T=180°C, (b) T=190°C and (c) 210°C. VA-CNT micropins different in diameter are clearly visible. The reported temperature in some areas are above the chick temperature due to the heating up of the optic.

4.7. CONCLUSION

To increase the heat transfer rate and the effective thermal conductivity of high aspect ratio VA-CNT micropins, the effect of ceramic coatings was studied. VA-CNT configurations directly grown on top of MHPs are subjected to a coating process with ALD Al_2O_3 and LPCVD a-SiC as coating materials. The thermal response of micropin configurations is characterized prior and after depositing the coatings, using a combination of Joule heating and IR micro-thermography, explained in details in Chapter (3). The obtained Al_2O_3/CNT hybrid material shows no significant variation in terms of heat dissipation compared to the uncoated one. We conclude that the unvaried behaviour is caused by the limited penetration depth of the ALD precursors within the CNT nanofoam. The a-SiC/CNT instead, shows a tremendous increase of the effective thermal conductivity by 181% compared to the as-grown CNT nanofoam. According to the obtained results and the carried morphological analysis, the key factor for CNT thermal transport enhancement is the precursor penetration within the nanofoam morphology. In fact, the solely presence of a thin shell around the micropin does not improve the overall performance. It is the formation of a 3D network along the entire micropin that contributes to the great enhancement of the thermal conductivity, by reducing the interface thermal resistance between tubes and between CNT-substrate and by proving additional thermal paths for the heat carriers. Preliminary experiments to investigate in detail the influence of the porosity variation are carried out, by inducing a densification of the VA-CNT array.

To prove that high aspect ratio conformal coated VA-CNTs can be used as 3D microstructure for localized and customized micro-cooling solutions, a chip-interposer is fabricated by wafer-level FAM. In particular, the encapsulation was successful due to the increased mechanical stability provided by the a-SiC conformal coating. A future step will be to understand the heat transfer of the interposer-chip, by obtaining more reliable IR maps and by using it as interposer among chip stacks.

This chapter highlights the opportunities provided by applying conformal coatings on VA-CNTs. Being able to tailor and synthesize high quantities of uniform high-aspect ratio arrays and further process them at wafer-level shows the potential for CNTs toward commercialization in several applications.

REFERENCES

[1] S. Vollebregt, R. Ishihara, F. Tichelaar, Y. Hou, and C. Beenakker, *Influence of the growth temperature on the first and second-order Raman band ratios and widths of carbon nanotubes and fibers,* Carbon **50**, 3542 (2012).

[2] C. Silvestri, M. Riccio, R. H. Poelma, B. Morana, S. Vollebregt, F. Santagata, A. Irace, G. Q. Zhang, and P. M. Sarro, *Thermal characterization of carbon nanotube foam using mems microhotplates and thermographic analysis,* Nanoscale **8**, 8266 (2016).

[3] D. Yang, Q. Zhang, G. Chen, S. Yoon, J. Ahn, S. Wang, Q. Zhou, Q. Wang, and J. Li, *Thermal conductivity of multiwalled carbon nanotubes,* Physical Review B **66**, 2 (2002).

[4] X. Wang, Z. Zhong, and J. Xu, *Noncontact thermal characterization of multiwall carbon nanotubes,* Journal of Applied Physics **97**, 1 (2005).

[5] S. Shaikh, L. Li, K. Lafdi, and J. Huie, *Thermal conductivity of an aligned carbon nanotube array,* Carbon **45**, 2608 (2007).

[6] M. B. Jakubinek, M. A. White, G. Li, C. Jayasinghe, W. Cho, M. J. Schulz, and V. Shanov, *Thermal and electrical conductivity of tall, vertically aligned carbon nanotube arrays,* Carbon **48**, 3947 (2010).

[7] T. Tong, Y. Zhao, L. Delzeit, A. Kashani, M. Meyyappan, and A. Majumdar, *Dense Vertically Aligned Multiwalled Carbon Nanotube Arrays as Thermal Interface Materials,* IEEE Transactions on Components and Packaging Technologies **30**, 92 (2007).

[8] W. Lin, J. Shang, W. Gu, and C. P. Wong, *Parametric study of intrinsic thermal transport in vertically aligned multi-walled carbon nanotubes using a laser flash technique,* Carbon **50**, 1591 (2012).

[9] S. K. Pal, Y. Son, T. Borca-Tasciuc, D.-A. Borca-Tasciuc, S. Kar, R. Vajtai, and P. M. Ajayan, *Thermal and electrical transport along MWCNT arrays grown on Inconel substrates,* Journal of Materials Research **23**, 2099 (2008).

[10] X. J. Hu, A. a. Padilla, J. Xu, T. S. Fisher, and K. E. Goodson, *3-Omega Measurements of Vertically Oriented Carbon Nanotubes on Silicon,* Journal of Heat Transfer **128**, 1109 (2006).

[11] C.-M. Lin, Y.-C. Chang, J. Yao, C. Wang, C. Luo, and S. S. Yin, *Multi-step hydrothermally synthesized TiO2 nanoforests and its application to dye-sensitized solar cells,* Materials Chemistry and Physics **135**, 723 (2012).

[12] I. Kim, S.-E. Kim, S. Han, H. Kim, J. Lee, D.-W. Jeong, J.-J. Kim, Y.-B. Lim, and H.-J. Choi, *Large current difference in Au-coated vertical silicon nanowire electrode array with functionalization of peptides.* Nanoscale research letters **8**, 502 (2013).

[13] R. H. Poelma, B. Morana, S. Vollebregt, E. Schlangen, H. W. van Zeijl, X. Fan, and G. Q. Zhang, *Tailoring the Mechanical Properties of High-Aspect-Ratio Carbon Nanotube Arrays using Amorphous Silicon Carbide Coatings,* Advanced Functional Materials **24**, 5737 (2014).

[14] R. H. Poelma, X. Fan, Z. Y. Hu, G. Van Tendeloo, H. W. Van Zeijl, and G. Q. Zhang, *Effects of*

Nanostructure and Coating on the Mechanics of Carbon Nanotube Arrays, Advanced Functional Materials **26**, 1233 (2016).

[15] G. Fiorentino, S. Vollebregt, F. D. Tichelaar, R. Ishihara, and P. M. Sarro, *Impact of the atomic layer deposition precursors diffusion on solid-state carbon nanotube based supercapacitors performances.* Nanotechnology **26**, 064002 (2015).

[16] S. Sun, W. Mu, M. Edwards, D. Mencarelli, L. Pierantoni, Y. Fu, K. Jeppson, and J. Liu, *Vertically aligned CNT-Cu nano-composite material for stacked through-silicon-via interconnects.* Nanotechnology **27**, 335705 (2016).

[17] K. M. Marr, B. Chen, E. J. Mootz, J. Geder, M. Pruessner, B. J. Melde, R. R. Vanfleet, I. L. Medintz, B. D. Iverson, and J. C. Claussen, *High Aspect Ratio Carbon Nanotube Membranes Decorated with Pt Nanoparticle Urchins for Micro Underwater Vehicle Propulsion via H ₂ O ₂ Decomposition,* ACS Nano **9**, 7791 (2015).

[18] M. E. Levinshtein, S. L. Rumyantsev, and M. S. Shur, *Properties of Advanced Semiconductor Materials: GaN, AIN, InN, BN, SiC, SiGe* (John Wiley & Sons, 2001).

[19] W. Chi, *Thermal Transport Properties of Thermally Sprayed Coatings: An Integrated Study of Materials, Processing and Microstructural Effects*, Ph.D. thesis (2007).

[20] T. Tanaka, W. Kada, and T. Hinoki, *Electrical insulating performances of SiC materials under gamma-ray irradiation,* Journal of Plasma and Fusion Research SERIES **9**, 282 (2010).

[21] A. M. Marconnet, M. a. Panzer, and K. E. Goodson, *Thermal conduction phenomena in carbon nanotubes and related nanostructured materials,* Reviews of Modern Physics **85**, 1295 (2013).

[22] K. Kordás, G. Tóth, P. Moilanen, M. Kumpumäki, J. Vähäkangas, a. Uusimäki, R. Vajtai, and P. M. Ajayan, *Chip cooling with integrated carbon nanotube microfin architectures,* Applied Physics Letters **90** (2007), 10.1063/1.2714281.

[23] J. Liu, B. Michel, M. Rencz, C. Tantolin, C. Sarno, R. Miessner, K. V. Schuett, X. Tang, S. Demoustier, and A. Ziaei, *Recent progress of thermal interface material research - an overview,* in *14th International Workshop on THERMal INvestigation of ICs and Systems, THERMINIC 2008* (2008) pp. 156–162.

[24] K. Zhang, Y. Chai, M. M. F. Yuen, D. G. W. Xiao, and P. C. H. Chan, *Carbon nanotube thermal interface material for high-brightness light-emitting-diode cooling.* Nanotechnology **19**, 215706 (2008).

[25] C.-T. Hsieh, Y.-F. Chen, C.-E. Lee, S.-H. Juang, Z.-W. Lin, and M. M. Huq, *Enhancing thermal transport efficiency in carbon composites using nanospacers,* RSC Adv. **6**, 61351 (2016).

[26] S. Kaur, N. Raravikar, B. a. Helms, R. Prasher, and D. F. Ogletree, *Enhanced thermal transport at covalently functionalized carbon nanotube array interfaces,* Nature Communications **5**, 141 (2014).

[27] R. S. Prasher, X. J. Hu, Y. Chalopin, N. Mingo, K. Lofgreen, S. Volz, F. Cleri, and P. Keblinski, *Turning carbon nanotubes from exceptional heat conductors into insulators,* Physical Review

Letters **102**, 1 (2009).

[28] B. Morana, G. Pandraud, J. F. Creemer, and P. M. Sarro, *Characterization of LPCVD amorphous silicon carbide (a-SiC) as material for electron transparent windows,* Materials Chemistry and Physics **139**, 654 (2013).

[29] D. S. Jensen, S. S. Kanyal, V. Gupta, M. A. Vail, A. E. Dadson, M. Engelhard, R. Vanfleet, R. C. Davis, and M. R. Linford, *Stable, microfabricated thin layer chromatography plates without volume distortion on patterned, carbon and Al2O3-primed carbon nanotube forests,* Journal of Chromatography A **1257**, 195 (2012).

[30] I. Lahiri, S. M. Oh, J. Y. Hwang, C. Kang, M. Choi, H. Jeon, R. Banerjee, Y. K. Sun, and W. Choi, *Ultrathin alumina-coated carbon nanotubes as an anode for high capacity Li-ion batteries,* Journal of Materials Chemistry **21**, 13621 (2011).

[31] S. M. George, *Atomic layer deposition: An overview,* Chemical Reviews **110**, 111 (2010).

[32] K. L. Stano, M. Carroll, R. Padbury, M. McCord, J. S. Jur, and P. D. Bradford, *Conformal atomic layer deposition of alumina on millimeter tall, vertically-aligned carbon nanotube arrays,* ACS Applied Materials and Interfaces **6**, 19135 (2014).

[33] N. Yazdani, V. Chawla, E. Edwards, V. Wood, H. G. Park, and I. Utke, *Modeling and optimization of atomic layer deposition processes on vertically aligned carbon nanotubes,* Beilstein Journal of Nanotechnology **5**, 234 (2014).

[34] J. Song, D. S. Jensen, D. N. Hutchison, B. Turner, T. Wood, A. Dadson, M. A. Vail, M. R. Linford, R. R. Vanfleet, and R. C. Davis, *Carbon-nanotube-templated microfabrication of porous silicon-carbon materials with application to chemical separations,* Advanced Functional Materials **21**, 1132 (2011).

[35] A. Mahajerin, *Thin Film Encapsulation Methods for Large Area MEMS Packaging,* Ph.D. thesis, University of California, Berkeley (2012).

[36] D. N. Hutchison, N. B. Morrill, Q. Aten, B. W. Turner, B. D. Jensen, L. L. Howell, R. R. Vanfleet, and R. C. Davis, *Carbon Nanotubes as a Framework for High-Aspect-Ratio MEMS Fabrication,* Journal of Microelectromechanical Systems **19**, 75 (2010).

[37] A. Chandrashekar, S. Ramachandran, G. Pollack, J.-S. Lee, G. Lee, and L. Overzet, *Forming carbon nanotube composites by directly coating forests with inorganic materials using low pressure chemical vapor deposition,* Thin Solid Films **517**, 525 (2008).

[38] L. Acauan, A. C. Dias, M. B. Pereira, F. Horowitz, and C. P. Bergmann, *Influence of different defects in vertically aligned carbon nanotubes on tio2 nanoparticle formation through atomic layer deposition,* ACS applied materials & interfaces **8**, 16444 (2016).

[39] A. Brieland-Shoultz, S. Tawfick, S. J. Park, M. Bedewy, M. R. Maschmann, J. W. Baur, and a. J. Hart, *Scaling the Stiffness, Strength, and Toughness of Ceramic-Coated Nanotube Foams into the Structural Regime,* Advanced Functional Materials , n/a (2014).

[40] H. Zhong and J. R. Lukes, *Interfacial thermal resistance between carbon nanotubes: Molecular dynamics simulations and analytical thermal modeling,* Physical Review B **74**, 125403 (2006).

[41] Z. Xu and M. J. Buehler, *Nanoengineering Heat Transfer Performance at Carbon Nanotube Interfaces,* ACS Nano **3**, 2767 (2009).

[42] S. Sarkar and P. Das, *Processing and properties of carbon nanotube/alumina nanocomposites: a review,* Rev. Adv. Mater. Sci (2014).

[43] M. T. Pettes and L. Shi, *Thermal and Structural Characterizations of Individual Single-, Double-, and Multi-Walled Carbon Nanotubes,* Advanced Functional Materials **19**, 3918 (2009).

[44] T. Jeong, J.-G. Zhu, S. Mao, T. Pan, and Y. J. Tang, *Thermal Characterization of SiC Amorphous Thin Films,* International Journal of Thermophysics **33**, 1000 (2012).

[45] A. K. Roy, B. L. Farmer, V. Varshney, S. Sihn, J. Lee, and S. Ganguli, *Importance of Interfaces in Governing Thermal Transport in Composite Materials: Modeling and Experimental Perspectives,* ACS Applied Materials & Interfaces **4**, 545 (2012).

[46] M. Panzer, G. Zhang, D. Mann, X. Hu, E. Pop, H. Dai, and K. Goodson, *Thermal properties of metal-coated vertically aligned single-wall nanotube arrays,* Journal of Heat Transfer **130**, 052401 (2008).

[47] K. H. Baloch, N. Voskanian, and J. Cumings, *Controlling the thermal contact resistance of a carbon nanotube heat spreader,* Applied Physics Letters **97**, 063105 (2010).

[48] B. A. Cola, J. Xu, and T. S. Fisher, *Contact mechanics and thermal conductance of carbon nanotube array interfaces,* International Journal of Heat and Mass Transfer **52**, 3490 (2009).

[49] T. L. Bergman, F. P. Incropera, and A. S. Lavine, *Fundamentals of Heat and Mass Transfer* (John Wiley & Sons, 2011).

[50] S. Kiwan, *Thermal analysis of natural convection porous fins,* Transport in Porous Media **67**, 17 (2006).

[51] D. A. Nield, A. Bejan, and . Nield-Bejan, *Convection in porous media*, Vol. 3 (Springer, 2006).

[52] Y. Tian and C.-Y. Zhao, *Natural convection investigations in porous phase change materials,* Nanoscience and Nanotechnology Letters **3**, 769 (2011).

[53] F. Santagata, C. Farriciello, G. Fiorentino, H. Van Zeijl, C. Silvestri, G. Zhang, and P. Sarro, *Fully back-end TSV process by Cu electro-less plating for 3D smart sensor systems,* Journal of Micromechanics and Microengineering **23** (2013), 10.1088/0960-1317/23/5/055014.

[54] S. Cho, V. Sundaram, R. R. Tummala, and Y. K. Joshi, *Impact of copper through-package vias on thermal performance of glass interposers,* IEEE Transactions on Components, Packaging and Manufacturing Technology **5**, 1075 (2015).

[55] *Boschman Technologies - Film-Assisted Molding,* .

[56] *APC - Advanced Packaging Center,* .

[57] R. Poelma, H. Van Zeijl, and G. Zhang, *Through polymer via (tpv) and method to manufacture such a via,* (2017), uS Patent 9,576,882.

5

SELF-DIRECTED FOLDING TECHNIQUE

5.1. INTRODUCTION

CNT microstructures consisting of VA-CNTs have high surface area to volume ratio. For applications like chemical and optical sensing, heat spreader and passive components, VA-CNT structures can be unpractical. An attractive alternative could be provided by high density horizontally aligned CNT (HA-CNT) sheets. This planar arrangement shows higher robustness than the VA counterpart, enabling the introduction of CNTs in standard microfabrication processes. To obtain HA-CNTs two approaches are available: in-situ synthesis of horizontally aligned CNTs [1–3] or permutation from VA-CNT to HA-CNT induced by external stimulations. The first approach is severely limited in its applicability by the exclusive use of a quartz or sapphire substrate to promote the unidirectional growth and a CVD growth temperature of 900°C, or by using challenging catalyst deposition techniques resulting in poor CNT coverage. Therefore, to integrate massive quantity of HA-CNTs into MEMS/NEMS devices, the self-assembly and the horizontal redirection of VA-CNTs by external stimulation is the most suitable solution. The permutation can be mechanically induced (rolling or domino pushing effect) [4, 5], liquid induced by immersion or evaporation [6–9], or layer-by-layer assembly given by a combination of manual handling and bonding through liquid densification [10]. In order to retain the initial CNTs alignment and to obtain an effective transformation into horizontal CNTs all the mentioned techniques require optimization of the external forces applied and a deep understanding of the working principle. Figure 5.1 gives a comprehensive overview of the above-mentioned techniques implemented by

various research groups and indicates the main challenges to be faced. Most of them require custom made systems[4, 5, 9], while other involve heavy manual handling [8, 10]. In this chapter, we explore how to control the generation of HA-CNT sheets by liquid assisted flattening process by using two different barrier layers, Al_2O_3 and ZrN.

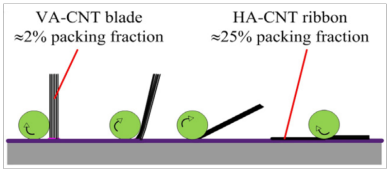
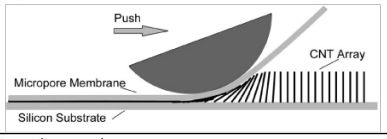
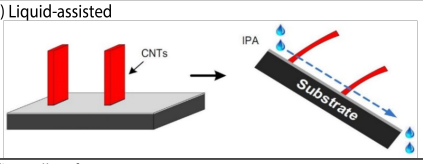
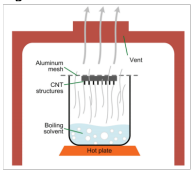
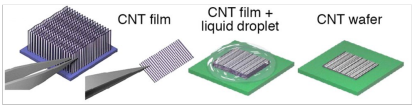
Flattening technique	Challenges	Ref
(a) Mechanical Rolling 	• Minimizing defects and contamination induced by the rolling process in CNTs; • Adhesion between CNTs and the roller; • Good control of the initial width of the array and the force applied to the roller;	[4]
(b) Domino pushing 	• To achieve thin layer and uniform thickness; • Contamination induced by the rolling process and micropore membrane usage.;	[5]
(c) Liquid-assisted 	• Control of the catalyst shape and microstructure aspect ratio; • Tilting angle; • Limited control on the orientation;	[8]
(d) Capillary forming 	• Precise control over the condensation and evaporation of the liquid; • Control of the catalyst shape and microstructure aspect ratio; • Limited control on the orientation;	[9]
(e) Layer-by-layer 	• Manually intensive procedure; • Position and orientation of the film; • Wrinkles induced on the CNT film during the manipulation;	[10]

Figure 5.1: Overview of the different type of flattening techniques that make usage of external stimuli. The figures were reproduced with the permission from (a) [4], (b) [5] (c) [8] (d) [9] (e) [10].

5.2. SELF-DIRECTED FOLDING TECHNIQUE

Among the techniques to obtain HA-CNT sheets indicated, we selected a liquid-assisted flattening approach because it is easy to implement and is suitable for wafer-scale processing. It consists of inducing the VA-CNT densification and the horizontal alignment through the immersion in an alcohol solution and the withdrawal of the sample, by cap-

illary adhesion, as reported for the first time by Hayamizu et al. [6]. Our process starts with the CVD growth of dense arrays of VA-CNTs on a silicon substrate provided with a barrier and catalyst layer. This layer stack consisting of 10 nm/1.8 nm of Al_2O_3/Fe or 10 nm/0.8 nm of ZrN/Fe, is lithographically patterned to define a rectangular feature. To achieve the desired HACNT sheets, the wafer is perpendicularly immersed in an isopropyl alcohol (IPA) solution and then dried while kept at a tilting angle of 45° (Figure 5.2). The dipping angle, the time range and the tilting angle during the drying process, need to be carefully determined.

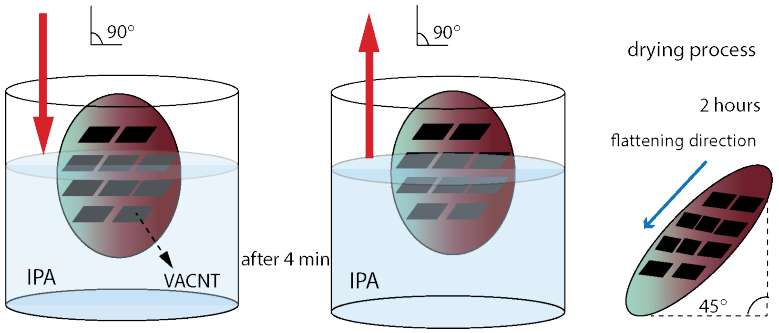


Figure 5.2: Schematic illustration of the flattening process procedure. The wafer is first dipped perpendicularly in the IPA solution. The wafer is left inside for 4 minute and then removed gently, while keeping always the same position. Then the wafer is dried under a fume mood for 2 hours with a tilting angle of 45°.

It is well known that a self-assembly of CNTs can be induced by capillary action of liquids including water, acetone, IPA and methanol [11, 12]. During the liquid evaporation from the CNT forest, capillary forces arise inducing a reassembly of the nanoarchitecture through strong VdW interactions. The key element to induce the CNT assembly is the liquid evaporation from the array, as demonstrated in [12]. The horizontal folding of the VA-CNT array originates from the studies carried on the capillary-driven assembly of CNT forests, with the additional aim to obtain uniform densification instead of nested patterns (see Appendix (A)). Moreover, the densification effects on VA-CNT micropins have been observed and reported in Chapter (4) (Section 4.5.2). IPA is used as liquid to induce the self-assembly because it can easily evaporate at room temperature and has good wettability to both the CNTs and the employed substrate (ZrN and Al_2O_3), thus producing effective attractive forces while in contact with both.

Figure 5.3 reports the time laps permutation from rectangular patterned VA-CNT arrays to HA-CNT blocks and a schematic illustration of the evolution. The VA-CNT in the IPA solution retains their initial shape and orientation during the immersion period as well as during the sample withdrawal. After few seconds the VA-CNT sponta-

neously shrinks and starts to fold along the horizontal direction (Figure 5.3 (b)). The result is a self-directed dense HA-CNT block strongly bound to the substrate. The permutation originates during the liquid evaporation phase. As observed from the frames reported, the permutation time varies from VA-CNTs to VA-CNTs. The dynamic of the self-directed folding of HA-CNT has been studied in detail by [7, 13] and is here briefly reported. After removing the sample from the solution, a thin layer of IPA infiltrates the VA-CNT nanofoam and wets the substrates forming a meniscus around the microstructure sidewall. During this phase the VA-CNTs experiences shrinkage towards the structure barycenter due to the internal capillary forces and the strong VdW interactions. The resulting structure is smaller and unbalanced, due to the densification (reduction of the CNT interspacing) and tends to fold into a certain direction (**densification phase**). Consequently, the meniscus becomes higher on the side facing the tilt direction and destabilizes the entire structure (**tilting phase**) that starts to buckle. An IPA layer is now trapped between the CNT sidewall and the substrate, which produces attractive forces, thus pushing the CNT array downward onto the substrate (**buckling phase**).

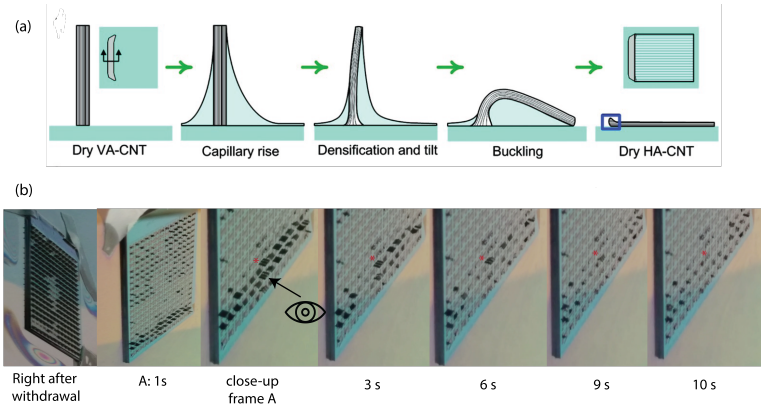


Figure 5.3: (a) Illustration of the various phases experienced by the VA-CNT array. Figure adapted with the permission from [7]. (b) Time laps of the permutation from VA-CNTs to HA-CNTs of various arrays. The first frame shows that most of the VA-CNT arrays on the withdrawn wafer retain their orientation. The eye marker is used to drive your attention toward the pointed microsctructure and its permutation over time.

Figure 5.4 (a) illustrates the rectangular microstructure of VA-CNTs, described in width (W) and thickness (T), while the final array description includes the height (H). The resulting HA-CNT substantially retains both the width (w) and the height (h) after the permutation, while the thickness, t, is the parameter that reflects the enhanced packing density. For example, in a VA-CNT microstructure with W=50µm, T=10µm and H=300µm, the densification ratio, defined as the ratio between the initial and the final thickness ($D_r = T/t$) is approximately 20. The permutation from VA-CNT to HA-CNT not

only changes the initial orientation of the array but even causes a morphological variation of the CNT nanofoam, by increasing the packing density (~ 1540 tubes μm^{-2} for the mentioned example). As observed in Figure 5.4 (d), the as-grown CNT array consists of wavy interlaced multiwalled carbon nanotubes (MWCNTs), oriented perpendicular to the substrate, entangled by VdW interactions. The resulting HA-CNT morphology consists of compacted CNTs in which the initial alignment is retained (see Figure 5.4 (e)).

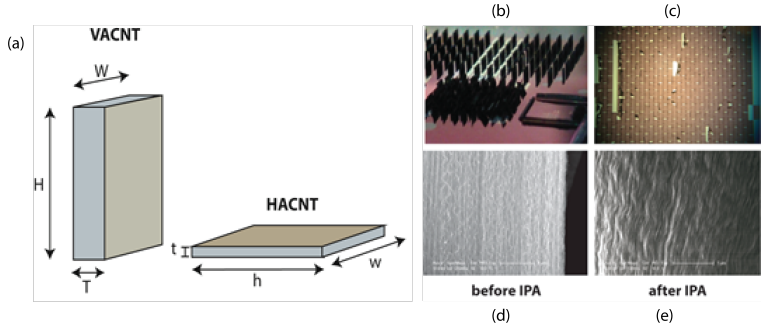


Figure 5.4: (a) Schematic representation reporting the geometrical characteristic of a VA-CNT and a HA-CNT. (b) SEM picture of a VA-CNT arrays and (c) the resulting HA-CNT sheets. Both the width and the height, $W \approx w$ and $H \approx h$ are retained. The thickness t is ~20 times smaller than the T. (d-e) SEM close-up on the nanofoam morphology prior and after the self-directed folding.

5.2.1. SELF-DIRECTED FOLDING DYNAMIC

The observation of the self-directed folding dynamic shows that various parameters play a role during the different process phases. The final result is the sum of all these intrinsic parameters. Therefore, to gain control on the outcome these parameters need to be analysed and the process engineered accordingly. In particular, it is necessary:

- to investigate the best catalyst island sizes for the optimization of the densification phase;
- to be able to predict the bending direction of the VA-CNT during the folding phase. For this, it is important to control the meniscus height formed along the structure. Consequently, the aspect ratio of the VA-CNT and substrate response to the wetting liquid, are major variables to control for both the tilting and buckling phase.

In the following sections the three phases of the flattening method and the related key parameters to be optimized are discussed in detail.

5.2.2. DENSIFICATION PHASE

When the sample is removed from the liquid solution, the densification phase starts. During this phase, a meniscus forms over the outer surface of the structure as well as among neighboring nanotubes within the array. Therefore, internal and external capillary forces act simultaneously on the VA-CNT provoking the structure shrinkage. The internal capillary forces developed within the VA-CNT microstructure can be tuned by varying the wetting liquid used, the catalyst island shape, and the CNT morphology (i.e. tube diameter, distance among adjacent tube). The external capillary forces mainly dependent from the surface tension of the liquid used and the catalyst island size. Both internal and external capillary forces have parameters in common: catalyst island size and liquid surface tension, γ. The catalyst patterned area, expressed in terms of W and T (see Figure 5.4), can be easily changed by simply varying the lithographically defined pattern. The minimum feature width is 2-3µm. This limit is dictated by the exposure resolution of the mask alignment system used (EVG 420 Aligner). A catalyst island with $W > T$ implies larger contact area between the liquid and the overall VA-CNT surface, which introduces larger external surface tension on the W side. Therefore, the resulting VA-CNT is more prone to flatten perpendicular to the W side than to the T side. When $W \approx T$ (similar dimensions), the surface tensions on both sides are competitive, and there is no preference on the flattening orientation of the VA-CNT.

The internal aggregation of the CNTs within the microstructure is well described by the fiber aggregation model reported by Py et al. [14] and applied to the vertically aligned CNT [15, 16]. Briefly, adjacent CNTs withdrawn from a liquid stick together for a certain length, called critical sticking length L_{stick}, in order to balance the competition between the capillary and elastic energy (Figure 5.5 (a)). L_{stick} represents the distance between the substrate and the initial contact point of two fibers during the elasto-capillary densification, and is expressed by [14, 15]:

$$L_{stick} = C_1 \sqrt{s \sqrt{\frac{E_{cnt} \pi b^3}{4\gamma}}} \tag{5.1}$$

where the numerical constant C1 depends on the wetting condition, s is the nanotube spacing, b is the nanotube radius, E_{CNT} is the Young's modulus of the individual nanotube, γ is the liquid surface tension. For a cluster of CNTs, the multi-fiber sticking distance, $L_{N_{stick}}$ in expressed as:

$$L_{Nstick} = C_2 L_{stick} \sqrt{\beta} N^{3/8} \tag{5.2}$$

where C_2 is a numerical constant depending on the sub-cluster arrangement and wetting condition, β is a pre-factor that depends on CNT arrangements, and N is the number of CNTs within the cluster (Figure 5.5 (b)). It has been experimentally observed that to obtain a dense cylinder, without internal voids, the CNT bundle has to be higher than $L_{N_{stick}}$ [14]. The equations indicate that the internal aggregation of CNTs depends on the as-grown packing density (through s, R and N) and the height of the array. The bundle densification rises internal shear stress in the microstructure due to both the CNT entanglement and the tube-tube attraction exerted by the van der Waals forces, thus inducing the structure deflection toward a certain direction.

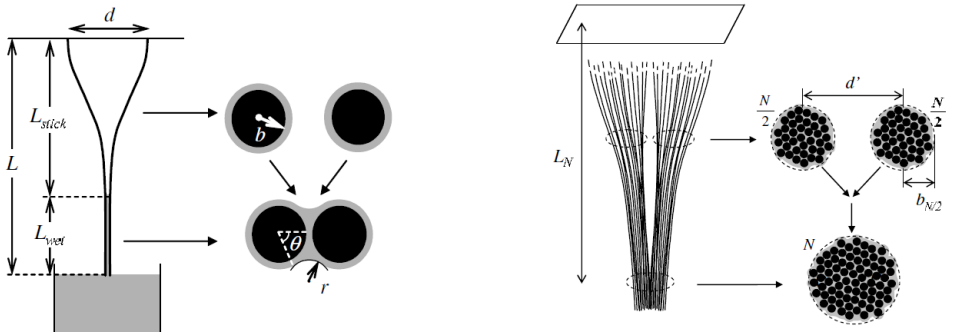


Figure 5.5: (a) Sketch illustrating two fibers sticking after withdrawn from a solution. (b) Aggregation of N fibers resulting from the self-similar clumping of two bundles of size $N/2$. This image was extracted from [14].

5.2.3. TILTING PHASE

After the CNT densification, the elastic microstructure is tilted towards the desired direction due to internal shear stresses developed during the capillary forming. The instability induced by capillary forces is observed even in elastic structures with small sizes or low elastic modulus [17]. In this phase we consider the entire VA-CNT microstructure and not the single nanotubes inside the array. The VA-CNT microstructures have the tendency to minimize the energy, which implies to minimize the interfacial energies between solid-liquid (VA-CNTs-IPA), solid-air (VA-CNTs-air), liquid-air (IPA-air), named γ_{sl}, γ_{sv}, γ_{lv}, respectively[18]. The capillary force, F_c, depends on the three interfacial energies as well as the system geometry. A pressure discontinuity is generated at the interface of the components, highlighted by a meniscus formation around the VA-CNT perimeter. Figure 5.6 illustrates the meniscus formed at the interface between a perfectly perpendicular VA-CNT structure and a capillary induced bended one. For the

perpendicular array the meniscus height is equal on both sides, while for the inclined array the meniscus facing the tilted side is higher than the opposite one [7].

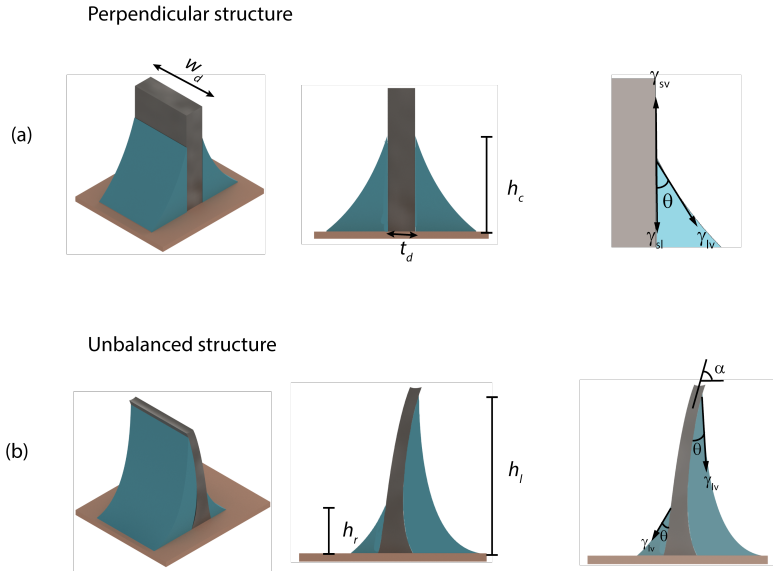


Figure 5.6: Meniscus height rise at the sidewall of the microstructure. (a) symmetric force applied to the structure when it is perfectly perpendicular to the substrate. (b) unbalanced structure has asymmetric menisci at its sidewalls.

The meniscus shape of an elastic wall depends on the balance between the Laplace (first term Equation (5.3)) and hydrostatic pressures (second term Equation (5.3))[19]:

$$\frac{\gamma_{lv}}{R} = \rho g h_c \tag{5.3}$$

where R, g, ρ, and h_c are the meniscus surface curvature, the gravitational acceleration, the density of the liquid and the capillary rise, respectively. The sidewall shape of microstructure facing the liquid highly influences the surface curvature. Under the assumption of perfectly wetting conditions, only the γ_{lv} has to be considered. For a perfect straight perpendicular wall (Fig 5.5 (a)), Neukirch et al. [19] found that the capillary rise is equal to:

$$h_c^2 = 2L_c^2(1-\cos\theta) \tag{5.4}$$

where $L_c = \sqrt{\gamma_{lv}/\rho g}$ is the capillary length, θ is the contact angle CNT-liquid interface. Tawfick et al. [7] found a solution of the equation for both sides on a tilted sidewall (Figure 5.6 (b)):

$$h_r^2 = 2L_c^2(1-\sin(\theta+\alpha-\frac{\pi}{2})) \tag{5.5}$$

$$h_l^2 = 2L_c^2(1-\sin(\theta-\alpha+\frac{\pi}{2})) \tag{5.6}$$

where α is the angle between the VA-CNT structure and the substrate. The reported equations are important to understand the parameters that influence the capillary rise and consequently, the magnitude of the capillary force applied on the microstructure that causes the buckling of the VA-CNT and drives the transformation in HA-CNT sheet. Therefore, the liquid and materials have to be selected based on their surface tensions.

5.2.4. BUCKLING PHASE

When the liquid evaporates off the surface and the structure reaches the proper bending, the buckling phase starts. As shown in Figure 5.6, after a sufficient tilting the elastic microstructure is not able to counteract the interfacial attraction induced by the surface tension of the liquid trapped among the sidewall and the substrate. The flattening of the VA-CNT on the substrate occurs abruptly, as observed by the time lapse (Figure 5.3). Since the pressure inside the liquid is lower than the external pressure, the microstructure experiences a force, F_c, acting at its perimeter that pushes the VA-CNT down to the substrate ($F_c = 2\gamma_{lv} w \cos(\theta)$ for a vertical beam of width w).

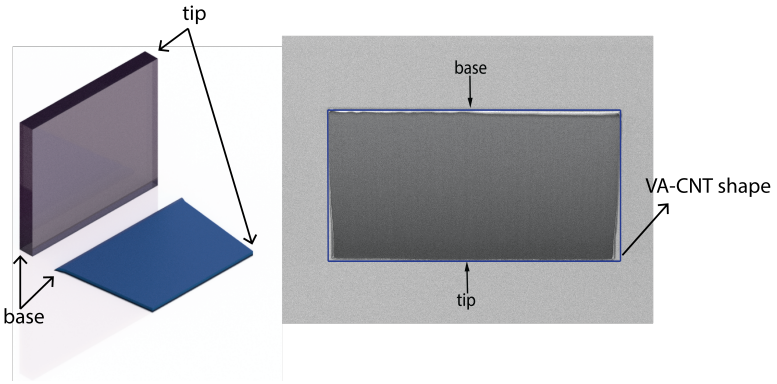


Figure 5.7: SEM image showing the microstructure tapering after the flattening process. The blue line highlight the initial shape of the VA-CNT array.

The VA-CNT buckling occurs when the F_c experienced by the system is larger than Euler's critical load, F_{el} [19]:

$$F_{el} = \frac{\pi}{2}^2 \frac{EI}{L_d^2} \tag{5.7}$$

where E, I and L_d in our case are the Young's modulus of the densified array, the second moment of area of the wall section, and height of the densified microstructure, respec-

tively. F_{el} decreases whit the wall height L_d. The minimum height L_{bk}, called capillary buckling length, above which the VA-CNT can buckle, is obtained by equating F_{el} with F_c [19]:

$$L_{bk} = \frac{\pi}{2}\sqrt{\frac{EI}{2\gamma_{lv}w}} \tag{5.8}$$

where $I = wt^3/12$ for a rectangular wall where w and t are the width and the thickness of the densified VA-CNT. $L_{bk} \propto t^{3/2}$ and it is independent from w. As soon as the wall buckles, the capillary force is amplified. Moreover, when the liquid evaporates the meniscus recedes, thus flattening the microstructure and creating an HA-CNT sheet. The HA-CNT results on a tapered patch anchored to the substrate by van der Waals forces (Figure 5.7). The microstructure tapering is a consequence of the densification dynamic of the array.The vertical array geometrical factors to be engineered for the buckling phase are the width due to $F_c \propto w$, the height due to $F_{el} \propto 1/L_d^2$ and the thickness due to $L_{bk} \propto t^{3/2}$.

In conclusion, to achieve an HA-CNT sheet at the end of the liquid flattening process, it is firstly required a proper initial bending of the VA-CNT. The bending can be achieved by inducing an asymmetric force from the meniscus, thus playing with VA-CNT aspect ratio and feature shape, combined with the internal stress developed by capillary forces in the microstructure. Secondly, the microstructure must be tall enough to fold and collapse on the substrate, thus avoiding the free-standing tilting after the liquid evaporation.

5.3. FLATTENING PROCESS ENGINEERING

High-aspect ratio vertically aligned CNTs are successfully grown on Al_2O_3, and ZrN, using Fe catalyst, at a temperature of 650°C [20–22]. In the next sections, we report for the first time the application and the engineering of the flattening process on VA-CNT grown on Fe/ZrN and as comparison, the same procedure is applied on VA-CNT on Fe/Al_2O_3. The main advantage in growing CNTs directly on top of an electrical conductive layer as ZrN is to reduce the contact resistance between the CNTs and the substrate. In particular, the HA-CNT sheets on both Al_2O_3 and ZrN substrates are compared in terms of thickness and CNT packing density.

5.3.1. CATALYST ISLAND OPTIMIZATION

The solvents such as acetone, IPA and methanolare used for the flattening process due to the good wettability shown with the CNTs as well as the substrate, the fast evaporation

rate at room temperature and the effective drying. The remaining parameters to be engineered to achieve well flattened sheets are related to the VA-CNTs. As explained before, the catalytic island size could be directly varied during the micro-fabrication process, by changing the lithographic process, with the only limiting factor the process resolution itself. Similarly, since the VA-CNT height can be controlled by varying the CNT growth time (60-80 µm min^{-1}), the aspect ratio of the array, defined as the ratio between the array height and width (AR= H/W), can be precisely tuned. Tests have therefore been performed to find the best W/T ratio of the catalyst island, which combined with a certain fixed H, creates an unbalanced VA-CNT structure after the densification phase. The obtained microstructure can be effectively self-oriented during the IPA evaporation phase, creating an HA-CNT firmly tethered to the substrate. However, these parameters are all intrinsically related and complex to control simultaneously. As example, to achieve a proper buckling the array height H has to be greater than the capillary buckling length L_b, which is related to the array thickness t after the densification. The latter is a result of the array densification, that in order to be as effective as possible, needs to have a $W > T$ (see Section 5.2.2), thus changes Young's modulus E and consequently F_{el}. To overcome this parameter concatenation, we started from the analysis carried out by Li et. al.[8]. They affirm that to have a good control over the flattening process the W/T of the catalyst island should be > 3. Starting from this suggestion, we engineer the permutation from VA-CNT to HA-CNT by varying the W and the T over a wide range, while keeping H fixed. Specifically, the following ranges are used:

$$\begin{bmatrix} 10\,\mu m & <W< & 1cm \\ 3\,\mu m & <T< & 40\,\mu m \end{bmatrix}$$

H fixed to ~ 100 µm or ~ 400 µm

A qualitative characterization of the obtained features on both barrier layers is carried out by collecting SEM images before and after the self-directed folding. To sort out the collected data and to choose the most promising aspect ratios, an analysis criterion was defined: *the VA-CNT has to be perpendicular to the substrate, while the resulting HA-CNT almost retain the initial W and L.*

During the carried experiments, it has been observed that as soon as the VA-CNTs show a preferential orientation right after their synthesis, the HA-CNT sheets achieved are independent from the liquid assisted flattening technique. Therefore, it is necessary to have perpendicular VA-CNTs to have a good control of the final sheet. The carried qualitative analysis focuses on the perpendicular VA-CNT microstructures and not the pre-tilted ones. The results of the performed qualitative analysis are reported in Fig-

ure 5.8 for CNTs grown on Fe/ Al_2O_3 at a fixed H of 100µm and 400µm, Figure 5.8 (a) and (b) respectively, while for the CNTs on Fe/ZrN in Figure 5.9 (a) and (b) for H=100µm and 400µm, respectively.

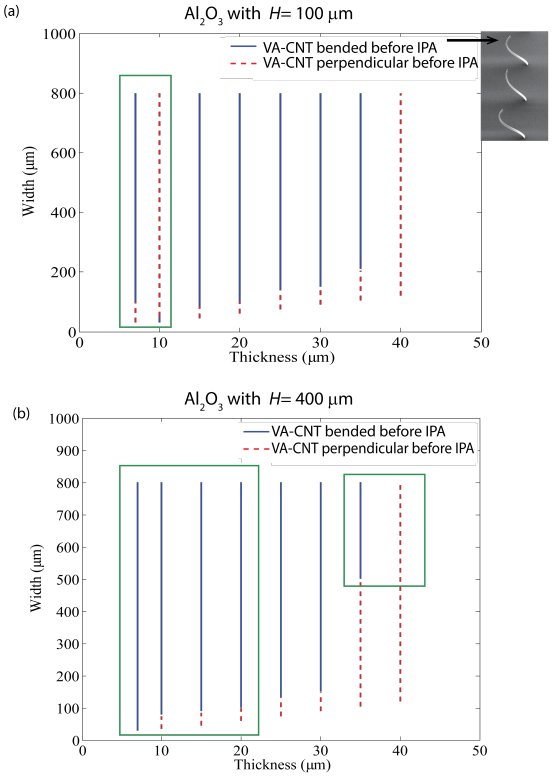


Figure 5.8: Qualitative graph to evaluate the aspect ratio of various VA-CNT microstructures on Al_2O_3 under two different heights. (a) $H \sim 100\mu m$ and (b) $H \sim 400\mu m$. The VA-CNT microstructures perpendicular to the substrate before IPA are highlighted by dashed red line, while the bended ones in solid blue line. After performing the flattening, the combinations that give well flattened HA-CNT sheets are grouped in the green rectangles. The inset show a bended VA-CNT before IPA.

The results obtained from the CNT on **Fe/Al_2O_3** are summarized below.

- For $H = 100\mu m$ to obtain a well-flattened HA-CNT sheet the W and the T can be selected as follows: $3\mu m \leq T \leq 10\mu m$ and $W \geq 50\mu m$ (Figure 5.8 (a)). These ranges are quite narrow. In fact, H is not enough to unbalance the structure unless the T reaches its lowest range value, while the W has to be long enough to increase the external surface tension applied from the liquid on the structure.
- For $H = 400\mu m$ the flattening process is hard to control due to the prominent AR of the structure. As illustrated in Figure 5.8 (b), most of the VA-CNTs show a

preferential orientation and when flattened the achieved HA-CNT reshapes in an unexpected way. These phenomena are discussed later in Section 5.3.3.

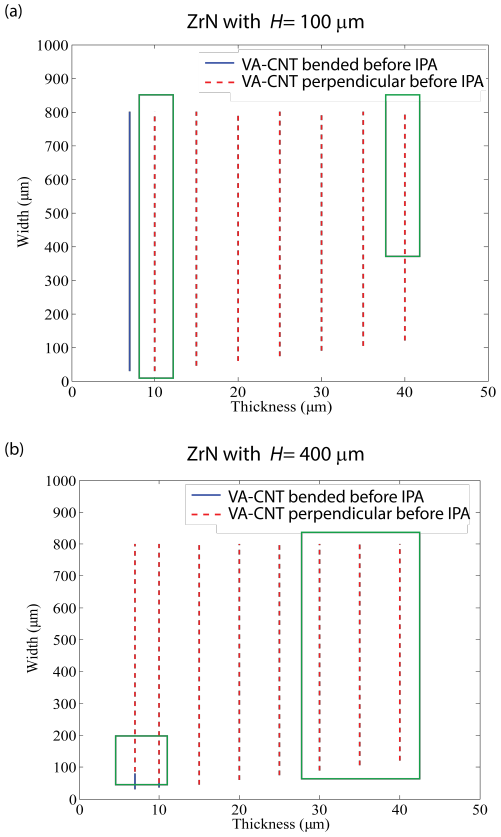


Figure 5.9: Qualitative graph to evaluate the aspect ratio of various VA-CNT microstructures on ZrN under two different heights. (a) $H \sim 100\mu m$ and (b) $H \sim 400\mu m$. The VA-CNT microstructures perpendicular to the substrate before IPA are highlighted by dashed red line, while the bended ones in solid blue line. After performing the flattening, the combinations that give well flattened HA-CNT sheets are grouped in the green rectangles.

The examination of the folded HA-CNTs obtained from CNTs grown on **Fe/ZrN** are summarized below.

- For $H = 100\mu m$ all the catalyst patterns realized result in perfectly aligned VA-CNTs after the growth process. However, after the IPA immersion only the arrays with $T \leq 10\mu m$ and $W/T \geq \mathbf{5}$ or $T = 40\mu m$ and $W/T > \mathbf{8}$ result well flattened and suitable to become HA-CNT sheets. (Figure 5.9 (a)).

- For $H = 400\,\mu m$ the flattening process shows a better control in comparison to the CNT grown on Al_2O_3, despite the prominent AR of the microstructure. Figure 5.9 (b) shows that $T \geq 30\,\mu m$ and $W/T > \mathbf{3}$ or $T \leq 10\,\mu m$ and $W/T \geq 5$ provide the best HA-CNT sheets.

In conclusion, from CNTs grown on Fe/ZrN we can achieve HA-CNTs for a broader folding regime in comparison to the ones on Fe/Al_2O_3. Based on the reported analysis, we can choose the catalyst island dimensions to be in the folding regime for both support catalyst layers. VA-CNTs with a fixed $T = 10\,\mu m$ and a W spanning from 50 to $800\,\mu m$ and H around $100\,\mu m$ or $400\,\mu m$, are considered the most promising for integration at wafer-scale (see Chapter (6)) due to the good control during the flattening process, the flexibility in width range and the high packing density (Figure 5.10). At the lowest investigated H both layers give the same result, while for the maximum investigated H the CNTs grown on ZrN show higher control in orientation for a wider range of catalyst island size.

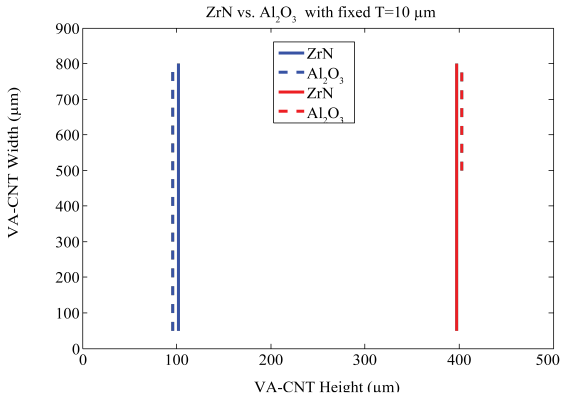


Figure 5.10: Validity range (considering a fixed $T = 10\,\mu m$) to achieve HA-CNT sheets on both barrier layers respecting the criteria above-mentioned. The CNT grown on Fe/ZrN show broader range in comparison to the Fe/Al_2O_3 ones.

5.3.2. HA-CNT THICKNESS

Once achieved the HA-CNT sheets, it is important to measure the thickness variation in both the longitudinal (x) and the transverse (y) direction (see inset Figure 5.11) using a surface profilometer. The reported measurements refer to HA-CNT sheets obtained from VA-CNT arrays of $T = 10\,\mu m$, $W = 50\,\mu m$ and $H = 300\,\mu m$. The resulting HA-CNTs sheet shows difference in thickness uniformity most likely due to the barrier layers. The thickness component along the x-direction, t_x, ranges from 108 nm to 718 nm for the

HA-CNT on ZrN from the base to the tip (Figure 5.11 (a)), while for the Al_2O_3 a good thickness uniformity is obtained on the central area of the sheet of ~370 nm (Figure 5.11 (b)). Two clear peaks corresponding to the VA-CNT base and tip appears on all the profiles. This is a consequence of the buckling phase. When comparing the thickness along

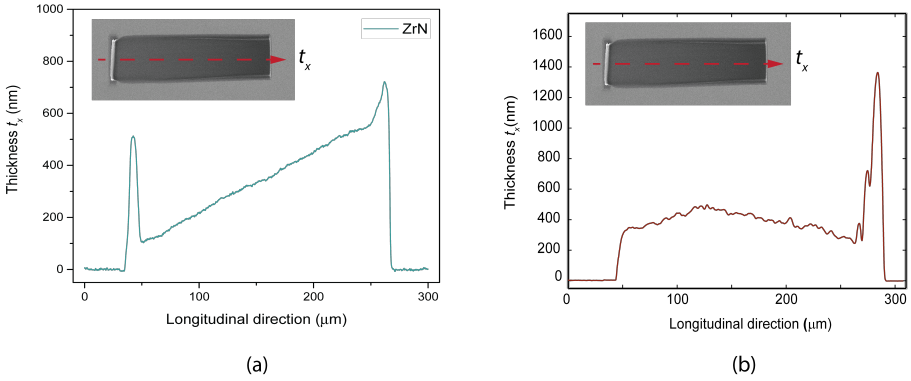


Figure 5.11: Thickness of a HA-CNT sheets on ZrN (a) and Al_2O_3 (b) with initial thickness of $T = 10\mu m$ and width $W = 50\mu m$ after the immersion in IPA. Inset: SEM image shows the direction of the x direction. The two spikes are caused by the folded sheets edges.

the y-direction, t_y, we see that both sample are more uniform (Figure 5.12). The measured thickness variation is visible even under SEM inspection (Figure 5.13).

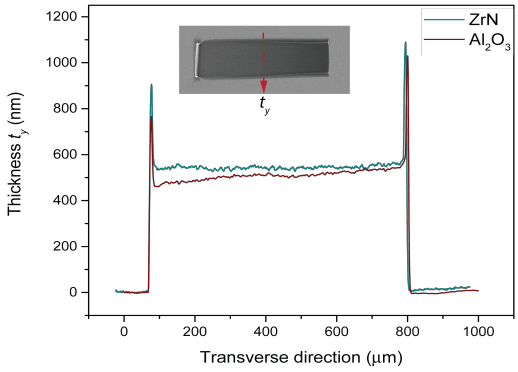


Figure 5.12: Thickness along y-direction of the HA-CNT sheets on Al_2O_3 (red line) and ZrN (blue line). The two spikes are caused by the sheets edges.

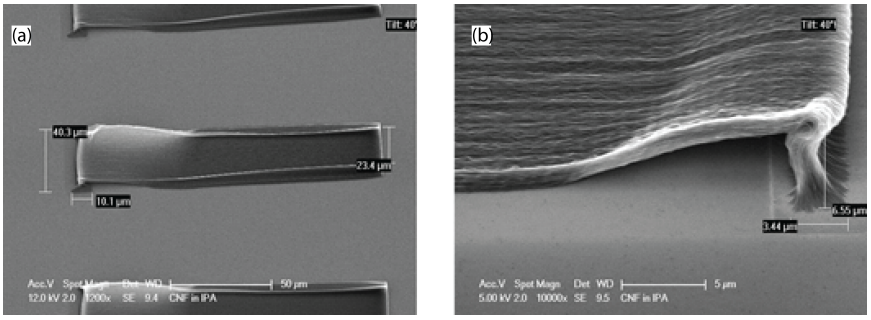


Figure 5.13: SEM image showing the thickness variation of buckled HA-CNT sheets and the folding at the edges.

When HA-CNT sheets have to be used in electrical applications, it is fundamental to choose the parameter combinations that provide the most uniform thickness, to achieve reproducible and predictable electrical performance.

5

5.3.3. PECULIAR EFFECTS

During the investigation of the best procedure to achieve a reproducible flattening process, some peculiar effects have been found (see SEM images in Figure 5.14). These peculiar responses are observed in samples achieved on both barrier layers. In particular, they mostly appear when a VA-CNT structure has to interact with neighboring ones, and/or their aspect ratio is not included in the optimized range. For these arrangements the sample withdrawn and the tilting angle during the drying process are the process steps with the highest influence. A higher incidence rate of these peculiar arrangements has been observed in HA-CNT sheets on Al_2O_3, supposedly for some difference at the barrier-IPA interface.

Figure 5.14 (a-b) displays the so-called “open loop effect” for individual or multiple VA-CNT structures. It occurs in individual structure probably when the VA-CNTs are so high that the IPA evaporates faster than the flattening time frame. In interacting structures the “open loop effect” is observed when the wafer is dried in ambient temperature at 0°tilting angle. The obtained pinning it is most likely caused by a dewetting of the liquid on the substrate[23]. Figure 5.14 (c-d) shows an unsuccessful attempt to achieve a large area HA-CNT film obtained by overlapping several structure.

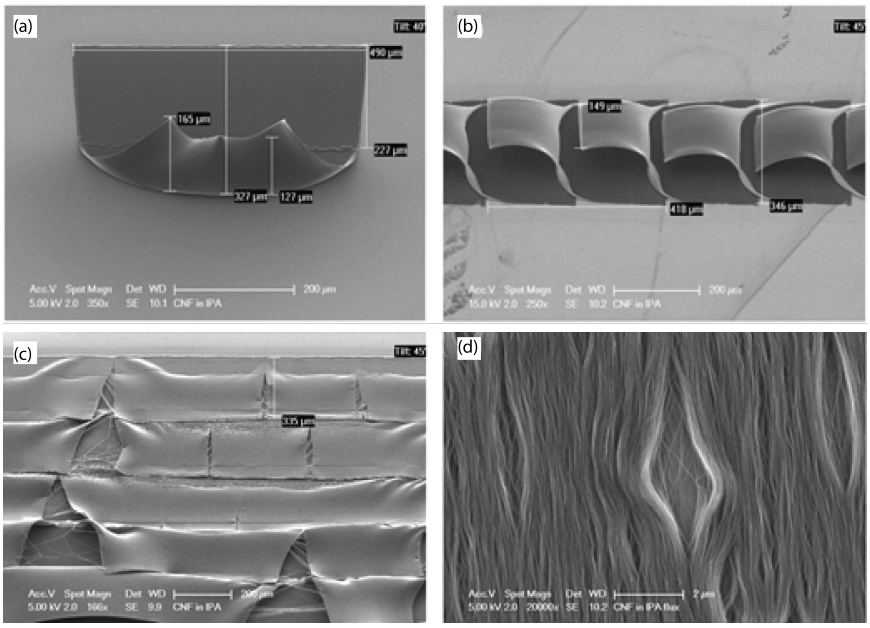


Figure 5.14: SEM images of unsuccessfully attempts to achieve well flattened HA-CNT sheets. "Open loop effect" of (a) individual and (b) interacting structures. (c-d) Frayed HA-CNT films after the IPA evaporation.

5.3.4. Al_2O_3 AND ZrN HA-CNT SHEETS

We have observed how a HA-CNT sheet strongly depends on the initial VA-CNT shape as well as withdrawn and drying conditions. However, two other aspects may contribute to the success of the flattening process: any difference among the grown CNTs (i.e packing density, crystallinity) and the barrier layer wettability. In this section, we briefly discussed these two aspects and their possible influence on the achieved HA-CNT sheets.

In Chapter (2), we correlated the two barrier layers and the catalytic particle density with the obtained CNT packing densities. Here we report the packing density variation before and after the flattening process of both the Al_2O_3 and ZrN CNTs (in Table 5.1). The substantial increase in packing density due to the densification is still far from the ideal one. The ideal packing density of a CNT forest with diameter tubes of 8 nm is ~ 1.67 $\times$ 10^4 tubes μm^{-2}, considering a tube spacing of 0.34 nm, which is the value of the interlayer spacing of the bulk graphite crystal. This implies that despite the densification induced, the spacing among CNTs it is still consistent. Moreover, as observed in the previous section within the HA-CNT sheet the density is not uniform. This is caused by both the nonuniformities already present on the VA-CNTs and from the relation between aspect ratio and liquid evaporation rate. In particular, a VA-CNT array can present denser

regions that densify first and acts as starting point of the whole array densification process, as observed also by others [17]. From the collected information, it seems that as-grown denser CNTs have a higher densification ratio after the IPA immersion. The CNT packing density is one of the parameter that influences the mechanical behaviour of the microstructure and reflects in the effective Young's modulus E. In particular, it has been reported that the E increases while the CNT density increases [16, 24].

Table 5.1: Material and geometric properties carbon nanotube and a-SiC coating.

	Al_2O_3-CNTs dry	Al_2O_3-CNTs wet	ZrN-CNTs dry	ZrN-CNTs wet
CNTs density (tubes μm^{-2})	112	$2.1 \cdot 10^3$	68	$1.3 \cdot 10^3$

The other parameter that influences the E is the number of defects in the nanotubes. In fact, vacancy defects in an individual CNT provoke a significant reduction of the E up to 13%, when the nanotube contains 2% of broken C-C bond [25]. To investigate the effects of flattening on CNTs quality, the Raman spectra of CNT samples achieved on both ZrN and Al_2O_3 were collected prior and after the flattening process. After the flattening process both Raman spectra shown an increase in D-band peak, which is disorder induced. The I_D/I_G ratio increases from 0.6 to 0.9 for the ZrN VA- and HA-CNTs, respectively; and from 0.9 to 1.1 for Al_2O_3 VA- and HA-CNTs, respectively.

The sessile drop test results, reported in Chapter (2), on both bare barrier layers and as-grown CNT forests, shows no substantial variation in terms of surface energy between Al_2O_3 and ZrN and the two CNT forests. Moreover, the IPA shows high wettability for all the investigated samples, making the determination of the contact angle inaccurate. Therefore, the hypothesis regarding the difference in barrier layer and CNT forest wettability can't be proven.

5.4. CONCLUSION

In conclusion, engineering of liquid assisted flattening process of two sample sets comprising VA-CNTs grown on Al_2O_3 and ZrN have been reported. In particular, through an extensive qualitative analysis on the VA-CNT aspect ratio in order to achieve well flattened HA-CNT sheets were investigated for both barrier layers. HA-CNT sheets on ZrN shown a higher flexibility in terms of catalyst island size in comparison to the ones on Al_2O_3. The resulting building blocks made of HA-CNTs were characterized in thickness, packing density and quality. The differences observed among the two samples (HA-

CNT obtained from Al_2O_3 and ZrN) might likely be attributed to the barrier layer and their packing density. As future work, we suggest to further optimize the catalyst island shape to achieve better thickness uniformity in longitudinal direction.

REFERENCES

[1] H. Guerin, D. Tsamados, H. Le Poche, J. Dijon, and A. M. Ionescu, *In-situ grown horizontal carbon nanotube membrane,* Microelectronic Engineering **97**, 166 (2012).

[2] L. Ding, D. Yuan, and J. Liu, *Growth of High-Density Parallel Arrays of Long Single-Walled Carbon Nanotubes on Quartz Substrates,* Journal of the American Chemical Society **130**, 5428 (2008).

[3] J. Lu, J. Miao, T. Xu, B. Yan, T. Yu, and Z. Shen, *Growth of horizontally aligned dense carbon nanotubes from trench sidewalls,* Nanotechnology **22**, 265614 (2011).

[4] S. Tawfick, K. O'Brien, and a. J. Hart, *Flexible high-conductivity carbon-nanotube interconnects made by rolling and printing,* Small **5**, 2467 (2009).

[5] D. Wang, P. Song, C. Liu, W. Wu, and S. Fan, *Highly oriented carbon nanotube papers made of aligned carbon nanotubes,* Nanotechnology **19**, 075609 (2008).

[6] Y. Hayamizu, T. Yamada, K. Mizuno, R. C. Davis, D. N. Futaba, M. Yumura, and K. Hata, *Integrated three-dimensional microelectromechanical devices from processable carbon nanotube wafers.* Nature nanotechnology **3**, 289 (2008).

[7] S. Tawfick, M. De Volder, and A. J. Hart, *Structurally Programmed Capillary Folding of Carbon Nanotube Assemblies,* Langmuir **27**, 6389 (2011).

[8] H. Li, W. Liu, A. M. Cassell, F. Kreupl, and K. Banerjee, *Low-Resistivity Long-Length Horizontal Carbon Nanotube Bundles for Interconnect Applications—Part II: Characterization,* IEEE Transactions on Electron Devices **60**, 2870 (2013).

[9] M. De Volder, S. H. Tawfick, S. J. Park, D. Copic, Z. Zhao, W. Lu, and A. J. Hart, *Diverse 3D Microarchitectures Made by Capillary Forming of Carbon Nanotubes,* Advanced Materials **22**, 4384 (2010).

[10] T. Yamada, N. Makiomoto, A. Sekiguchi, Y. Yamamoto, K. Kobashi, Y. Hayamizu, Y. Yomogida, H. Tanaka, H. Shima, H. Akinaga, D. N. Futaba, and K. Hata, *Hierarchical three-dimensional layer-by-layer assembly of carbon nanotube wafers for integrated nanoelectronic devices,* Nano Letters **12**, 4540 (2012).

[11] H. Liu, S. Li, J. Zhai, H. Li, Q. Zheng, L. Jiang, and D. Zhu, *Self-Assembly of Large-Scale Micropatterns on Aligned Carbon Nanotube Films,* Angewandte Chemie International Edition **43**, 1146 (2004).

[12] N. Chakrapani, B. Wei, A. Carrillo, P. M. Ajayan, and R. S. Kane, *Capillarity-driven assembly of two-dimensional cellular carbon nanotube foams.* Proceedings of the National Academy of Sciences of the United States of America **101**, 4009 (2004).

[13] Z. Xiao, Y. Chai, Y. Li, M. Sun, and P. C. H. Chan, *Integration of horizontal carbon nanotube devices on silicon substrate using liquid evaporation,* in *2010 Proceedings 60th Electronic Components and Technology Conference (ECTC)* (IEEE, 2010) pp. 943–947.

[14] C. Py, R. Bastien, J. Bico, B. Roman, and a. Boudaoud, *3D aggregation of wet fibers,* Europhysics Letters (EPL) **77**, 44005 (2007).

[15] Z. Liu, L. Ci, S. Kar, P. M. Ajayan, and J. Q. Lu, *Fabrication and electrical characterization of densified carbon nanotube micropillars for IC interconnection,* IEEE Transactions on Nanotechnology **8**, 196 (2009).

[16] M. De Volder, S. J. Park, S. H. Tawfick, D. O. Vidaud, and A. J. Hart, *Fabrication and electrical integration of robust carbon nanotube micropillars by self-directed elastocapillary densification,* Journal of Micromechanics and Microengineering **21**, 12 pp. (2010), arXiv:1009.1592 .

[17] J.-L. Liu and X.-Q. Feng, *On elastocapillarity: A review,* Acta Mechanica Sinica **28**, 928 (2012).

[18] D. Chandra and S. Yang, *Capillary-Force-Induced Clustering of Micropillar Arrays: Is It Caused by Isolated Capillary Bridges or by the Lateral Capillary Meniscus Interaction Force?* Langmuir **25**, 10430 (2009).

[19] S. Neukirch, B. Roman, B. de Gaudemaris, and J. Bico, *Piercing a liquid surface with an elastic rod: Buckling under capillary forces,* Journal of the Mechanics and Physics of Solids **55**, 1212 (2007).

[20] S. Vollebregt, S. Banerjee, F. D. Tichelaar, and R. Ishihara, *The growth of carbon nanotubes on electrically conductive ZrN support layers for through-silicon vias,* Microelectronic Engineering **156**, 126 (2016).

[21] S. Vollebregt and R. Ishihara, *Carbon Nanotubes as Vertical Interconnects for 3D Integrated Circuits,* in *Carbon Nanotubes for Interconnects* (Springer International Publishing, 2016) pp. 195–213.

[22] C. Silvestri, B. Morana, G. Fiorentino, S. Vollebregt, G. Pandraud, F. Santagata, G. Q. Zhang, and P. M. Sarro, *CNT bundles growth on microhotplates for direct measurement of their thermal properties,* in *2014 IEEE 27th International Conference on Micro Electro Mechanical Systems (MEMS)* (IEEE, 2014) pp. 48–51.

[23] Hyunhyub Ko, , Sergiy Peleshanko, and V. V. Tsukruk*, *Combing and Bending of Carbon Nanotube Arrays with Confined Microfluidic Flow on Patterned Surfaces,* (2004), 10.1021/JP031229E.

[24] Y. Gao, T. Kodama, Y. Won, S. Dogbe, L. Pan, and K. E. Goodson, *Impact of nanotube density and alignment on the elastic modulus near the top and base surfaces of aligned multi-walled carbon nanotube films,* Carbon **50**, 3789 (2012).

[25] R. Raffie, Roham; Pourazizi, *Evaluating the Influence of Defects on the Young's Modulus of Carbon Nanotubes Using Stochastic Modeling,* Materials Research **14**, 758 (2014).

6

INTEGRATION AND CHARACTERIZATION OF HA-CNT SHEETS

This chapter is based on:

1. **Cinzia Silvestri**, Federico Marciano, Bruno Morana, Violeta Podranovic, Sten Vollebregt, Kouchi Zhang, Pasqualina M Sarro. "Horizontally aligned carbon nanotube scaffolds for freestanding structures with enhanced conductivity". *In 30th IEEE International Conference on Micro Electro Mechanical Systems (MEMS 2017)*, Las Vegas, USA, pp. 266-269, 2017.
2. **Cinzia Silvestri**, Michele Riccio, René H. Poelma, Andrea Irace, Guo Qi Zhang, Pasqualina M. Sarro. "Enhanced Thermal Transport in Horizontally Aligned Carbon Nanotube sheets by Conformal Coatings".To be submitted to *Nanoscale*, 2017.

6.1. INTRODUCTION

Our approach to go from nano- to macroscale using HA-CNT sheets are appealing for applications such as chemical and optical sensing, heat spreading and local routing, for which the vertical orientation of CNTs might result unpractical. This planar arrangement shows higher robustness than the VA counterpart, thus increasing the possibility to introduce CNTs in standard microfabrication processes. For this purpose, two challenges are solved in this chapter.

Firstly, we need to integrate large area HA-CNT sheets at wafer-scale on pre-processed wafers. Therefore, a wafer-scale process is developed to integrate the optimized HA-CNT sheets, obtained on both Al_2O_3 and ZrN barrier layers (Chapter (5)). The developed approach allows to realize a variety of MEMS structures, ranging from large area membranes to suspended interconnects. However, the integration of the CNTs grown on electrical conductive ZrN has been proved to be challenging. Consequently, a section is dedicated to Fe/ZrN CNT synthesis on Pt, TiN, SiO_2 and SiN_x.

Secondly, we want to enhance and tune the material properties at macroscale, while improving the manufacturability. As demonstrated on the VA-CNT micropins (Chapter (4)), by infiltrating nanoscale conformal coatings on CNT nanofoams is possible to improve their thermal performance and mechanical behavior [1, 2]. This procedure is a valuable alternative to effectively enhance the material properties of nanofoam like materials. In this chapter, we present a method to exploit the morphology of the HA-CNT array as scaffold for creating reinforced heterostructures with tailored material properties, like electrical and thermal conductivity. The obtained HA-CNT sheets are subjected to nanometer scale conformal coatings of Al_2O_3 or a non-stoichiometric a-SiC, following the same procedure as Chapter (4). By characterizing the HA-CNTs prior and after the coating infiltration, an impressive enhancement in electrical and thermal conductivity is measured, an indication of the potential of CNT-based scaffolds as scalable and functional building blocks for suspended interconnects, heat spreaders and novel chemical and optical sensors. Figure 6.1 schematically summarizes the process steps to achieve the final sample to characterize.

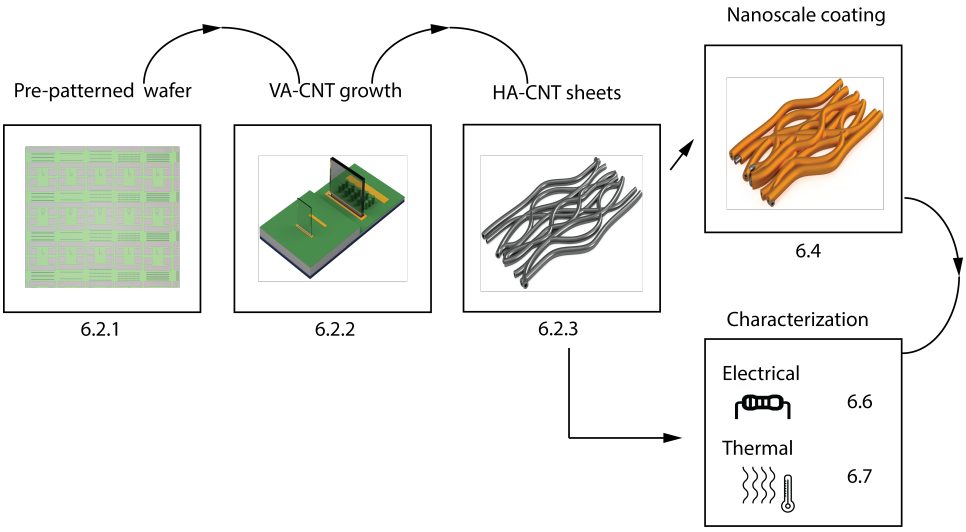


Figure 6.1: The concept map shows the topics elaborated throughout the chapter. The number underneath the block indicates the section (or subsection) where that module is specified.

6.2. FABRICATION PROCESS

6.2.1. PHASE 1: PRE-PATTERNED WAFER

The integration process of the HA-CNT sheets has been developed through several iterations and was inspired by the work published by Y.Hayamizu et al.[3]. In his work Hayamizu reported for the first time the integration of HA-CNT sheets on Si, by using a mixture of liquid-assisted flattening technique and electron-beam (EB) lithography. We chose to take it a step further, by synthesizing the CNTs as last step on pre-patterned Si wafers to keep the cleanroom compatibility, avoiding not scalable techniques like EB lithography. A schematic drawing of the main fabrication process steps for the two most interesting structures, suspended interconnects and membranes, are depicted in Figure 6.2. The integration of a HA-CNT sheet on a membrane is quite relevant for heat confinement in thermal measurement. In fact, as observed in Chapter (3), the low thermal conductivity of the SiN_x membrane allows to localize the heat and force the thermal dissipation through the VA-CNTs. Therefore, because the effective thermal conductivity of the HA-CNT sheets is not known a priori, we applied the same heat confinement architecture to direct the heat through the nanotube length.

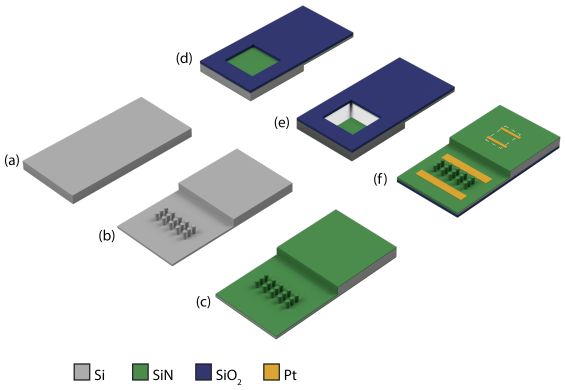


Figure 6.2: Main steps for the definition of the membranes and suspended interconnects. (a) On a single-side polished wafer the pillar structures for the suspended interconnects are defined through a photolithographic step. (b) DRIE is used to etched down those structures up to 7 mm deep into the Si substrate. (c) 400 nm of LPCVD SiN_x is deposited on the patterned wafer. (d) On the wafer backside a hard mask made of 6 mm of PECVD SiO_2 is deposited and then patterned by photolithography to define the membrane opening. The 400 nm of nitride on the window opening was then removed by RIE. (e) DRIE process is performed on th ewafer backside to etch through the wafer (ca 500µm) and to land on the nitride layer on the front side. Now the membranes are released. (f) A bi-layer of Ta/Pt metal stripes are evaporated and patterned by lift-off technique. The dotted white line highlights the area corresponding to the suspended nitride membrane.

The process starts from a single-side polished Si wafer of 500µm thick (Figure 6.2 (a)). In order to create the Si pillar structures of the suspend interconnects, the bottom half of the wafer is thinned down by DRIE. The pillars can vary in shape, spacing and number, depending on the lithographic step. Their height is limited to 7µm to reduce the high topography that can negatively affect the photoresist film coverage SiN_x (b)). Right after, a 400 nm thick LPCVD SiN_x layer is deposited to provide electrical isolation to the Si pillars as well as to create the future suspended membrane (Figure 6.2 (c)). Meanwhile, on the bottom side of the wafer a layer of 6µm thick PECVD SiO_2 is deposited, patterned and etched by RIE to define the membranes ((Figure 6.2 (d-e)). Subsequently, a 1µm Al layer is sputtered at 25°C on the wafer front side to protect the SiN_x layer and prevent damages during the membrane release done by DRIE of the Si substrate. After landing on the nitride layer, the membranes are completely released by removing the Al mask in PES [1]. The two basic structures for the membrane and suspended interconnects are now defined. Next step is to define the electrical contacts. The metal chosen is Pt due to its highly linear TCR even at high temperatures. However, it represents a possible source of contamination for the cleanroom environment, therefore is deposited as one of the last fabrication steps. Two valuable alternatives in

[1] It is a Al etchant containing: a mixtures of 1-5% HNO_3 (Al oxidation), 65-75% H_3PO_4 (to dissolve the Al_2O_3), 5-10% CH_3COOH (for wetting and buffering), and H_2O dilution to define the etch rate at given temperature [4].

terms of TCR linearity range and cleanroom compatibility are molybdenum (Mo) and titanium nitride (TiN) [5, 6]. Sputtered Mo would allow the membrane release to be done after the metal deposition and so avoiding the long evaporation process required for Pt. However, Mo is prone to oxidize and it is easily etched in solutions containing HNO_3 even in low percentage. TiN would give the same advantages as Mo but attention has to be given to the stress and composition of the layer as high-stress TiN has an almost constant TCR, while low-stress TiN has a nonlinear TCR [6]. After the membranes release, a bi-layer of 20/160 nm of Ta/Pt is evaporated and patterned by lift-off process, using NMP at 80°C. It is necessary to avoid the usage of the ultrasonic bath not to damage the membranes (Figure 6.2 (f)). A prolonged vacuum thermal annealing step at 1000 °C is then performed on the wafers to stabilize the electrode resistivity. The wafer is now ready for the second phase: the CNT synthesis. A detailed flowchart is reported in Appendix (C). Figure 6.3 reports the optical images of the fabricated pre-patterned wafer.

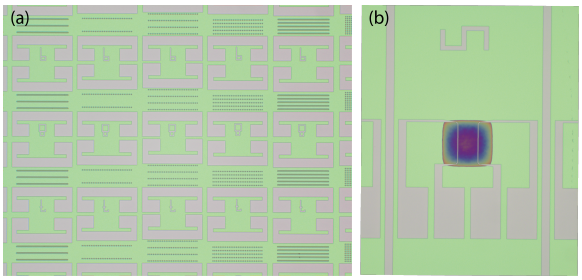


Figure 6.3: Optical images of the structure created on the pre-patterned Si wafer. (a) Suspended interconnects with different pillar shape and density. (b) SiN_x membrane for thermal characterization.

6.2.2. PHASE 2: CNT SYNTHESIS

The second phase of the process consists in growing the VA-CNTs on the lithographically defined patterns. In particular, Fe catalyst islands of 10µm in thickness (T) and width (W) ranging from 30µm to 800µm are patterned on top of the Pt electrodes (Figure 6.4 (a)).

To grow CNT of predefined shapes on Al_2O_3 or ZrN, different lithographic steps must be performed depending on the barrier layer selected. Briefly, for the CNTs synthetized on the layer stack Al_2O_3/Fe made by 30/1.2 nm, the Fe is patterned by lift-off to define the rectangular catalyst islands. For the CNTs grown on 30/0.8 nm of ZrN/Fe, the wafer is coated with positive photoresist and then patterned to define a mask for the wet etching. The wafer is immersed in 10% HNO_3 solution at 50°C for the Fe etching, and then in 0.5% HF at ambient temperature to remove the ZrN. A rinsing and drying of the wafer is

performed after each etching step. The process ended with the photoresist removal in NMP at room temperature. The wafer with the defined catalyst islands (Figure 6.4 (a)) is then loaded in the CVD reactor at 650°C and a deposition process is run for a time interval depending on the targeted CNT height (Figure 6.4 (b)). The distance between the electrodes is varied depending on the CNT height to investigate.

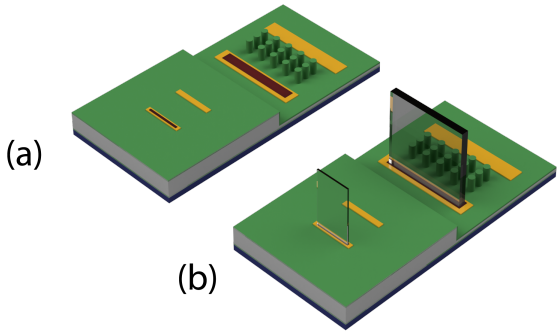


Figure 6.4: VA-CNT synthesis. (a) After sputtering the barrier layer, Al_2O_3 or ZrN, the Fe catalyst nanoparticles are evaporated and patterned according to the desired feature size. (b) The wafer is then placed in the CVD reactor for the CNT synthesis. The growth time depends on the targeted CNT height.

6.2.3. PHASE 3: SPATIALLY PROGRAMMABLE FOLDING

The third phase consists in inducing the permutation from VA-CNTs to HA-CNT sheets by applying the liquid-assisted flattening process reported in Chapter (5). The sample is perpendicularly immersed and withdrawn from the IPA and then dried in ambient air while kept at a tilting angle of 45°. After removing the sample from the solution, a thin layer of IPA infiltrates the VA-CNT nanofoam and wets the substrates, inducing the permutation into HA-CNTs. An example of the achieved membrane and suspended interconnect based on HA-CNT sheets on a pre-processed wafer are shown in Figure 6.5. In Figure 6.6 the large versatility of the building blocks based on HA-CNTs is highlighted. The reported successful attempts in integrating HA-CNT sheets and the performed coating procedure, regards only the CNT synthetized on Al_2O_3 barrier layer. Therefore, if not specifically mentioned, from now on we always refer to CNT synthetized on Al_2O_3. In Section 6.3, a detailed investigation of the possible cause of failure in growing the CNT on pre-processed wafer with ZrN as barrier layer is reported.

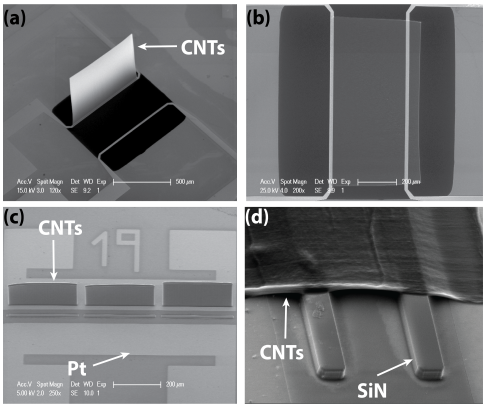


Figure 6.5: SEM images of the achieved membrane (a-b) and suspended interconnects (c-d). (a) VA-CNTs grown on suspended Platinum (Pt) contacts before the flattening procedure.(b) After the IPA treatment a large area CNT membrane is obtained. (c) VA-CNTs grown on Pt to connect the contacts pads. (d) Suspended interconnects after the flattening method.

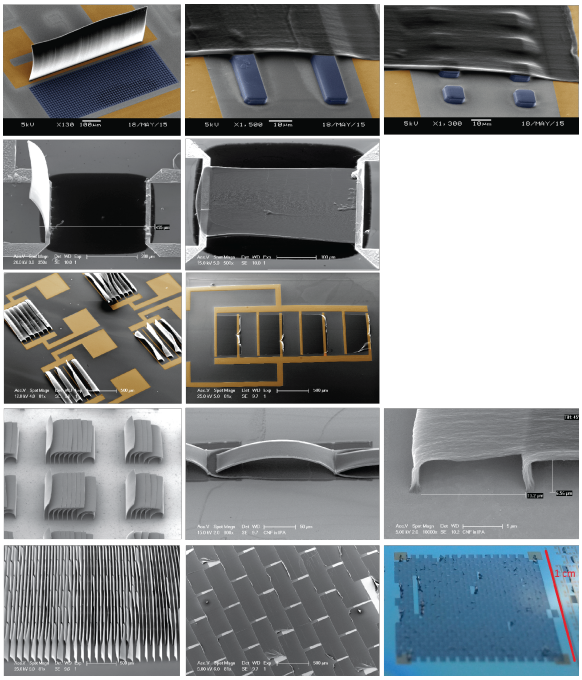


Figure 6.6: Building blocks based on HA-CNT sheets. (a) Multiple suspended interconnections made of HA-CNTs. (b) Large area CNT membranes suitable for CNT-based sensors and heat spreaders. (c) Sensitive layer made of HA-CNTs above interdigitated electrodes. (d) CNT "waves" that can be used for CNT-based micro-channels and self sealing. (e) Large area CNT films made of alternating HA-CNT sheets (1×1 cm).

6.3. INTEGRATION BOTTLENECKS FOR ZRN BARRIER LAYER

After removing the ZrN samples from the CVD reactor we were expecting to find high aspect ratio VA-CNT grown on top of the pre-defined locations. On the contrary, we observed that:

1. Almost no VA-CNT growth occurred on top of the layer stack made of Pt/ZrN;
2. Uneven growth or sparse nanotube growth on the SIN_x layer, depending on catalyst island size;
3. Non-uniform growth rate along the wafer;

Having a perfect synergy between the countless combination of parameters like catalyst nanoparticles, effective interaction barrier-catalytic layer, carbon feedstock, etc. can make the CNT synthesis process not easy to tune. While CNT growth from catalyst nanoparticles evaporated on Al_2O_3 layer has been widely reported [7–9],there are no other reports on CNTs grown on ZrN layer except by our research group [10–12]. In this work three crucial steps have been found to be critical during the fabrication process: the ZrN layer patterning, the CNT growth on metal substrates and the CVD reactor condition.

To understand and solve the failure mechanism related to the fabrication process, three sets of experiments are carried out. On a Si wafer, 400 nm of thermal SiO_2 (*sample set 1*) or LPCVD SiN_x (*sample set 2*) are deposited (Figure 6.7 (a)). Four square patches of 5×5 mm are defined on their surface: a square patch of sputtered Ti/TiN (10/50 nm at 350°C), another of evaporated Ta/Pt (20/160 nm) and the remaining two patches are made of SiO_2 or SiN_x depending on the sample set. On each set a 30 nm of ZrN and 0.8 nm of Fe are deposited. Through photolithographic patterning, five subsample sets are created (Figure 6.7 (b)): **(A)** Fe patterned with the same dimensions of the square patches; **(B)** Fe patterned creating small catalyst islands; **(C)** non-patterned ZrN in combination with **(A)** and **(B)**; **(D)** patterned ZrN in combination with **(A)** and **(B)**. The last subsample (E) is made of non-patterned Fe and ZrN to obtain CNT forest on TiN, Pt, SiO_2 and SiN_x. The samples are then loaded in the CVD reactor for the VA-CNTs growth. In order to achieve high-aspect ratio CNTs and to avoid possible loading effects occurring in patterned samples, the optimum settings suggested in [11, 12] were used.

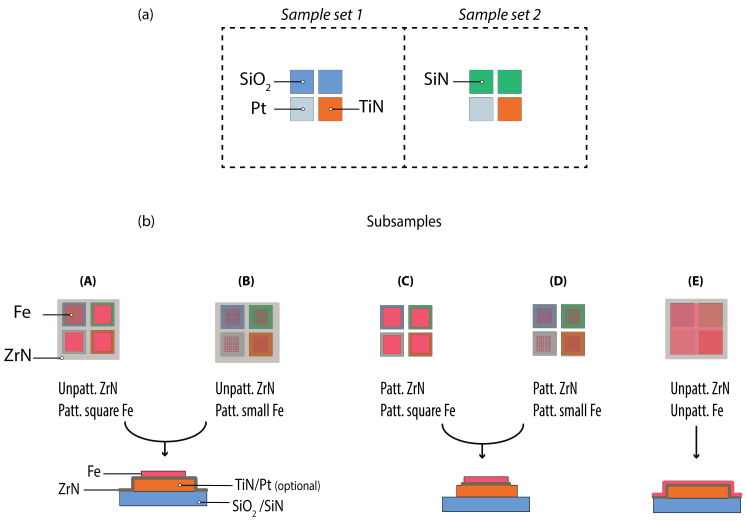


Figure 6.7: (a) Illustration of the sample sets. (b) subsamples, including their cross-sections.

The achieved samples are then analysed by SEM and optical inspection. The collected results are summarized in Figure 6.8 and Figure 6.9 for the *sample set 1* and *sample set 2*, respectively. Following, we discuss in detail the experiments related to samples with the ZrN barrier layer, but the same design of experiment was performed on samples with the Al_2O_3 barrier layer. The latter tests reveal a successful VA-CNT growth on Al_2O_3 independently from the substrate material.

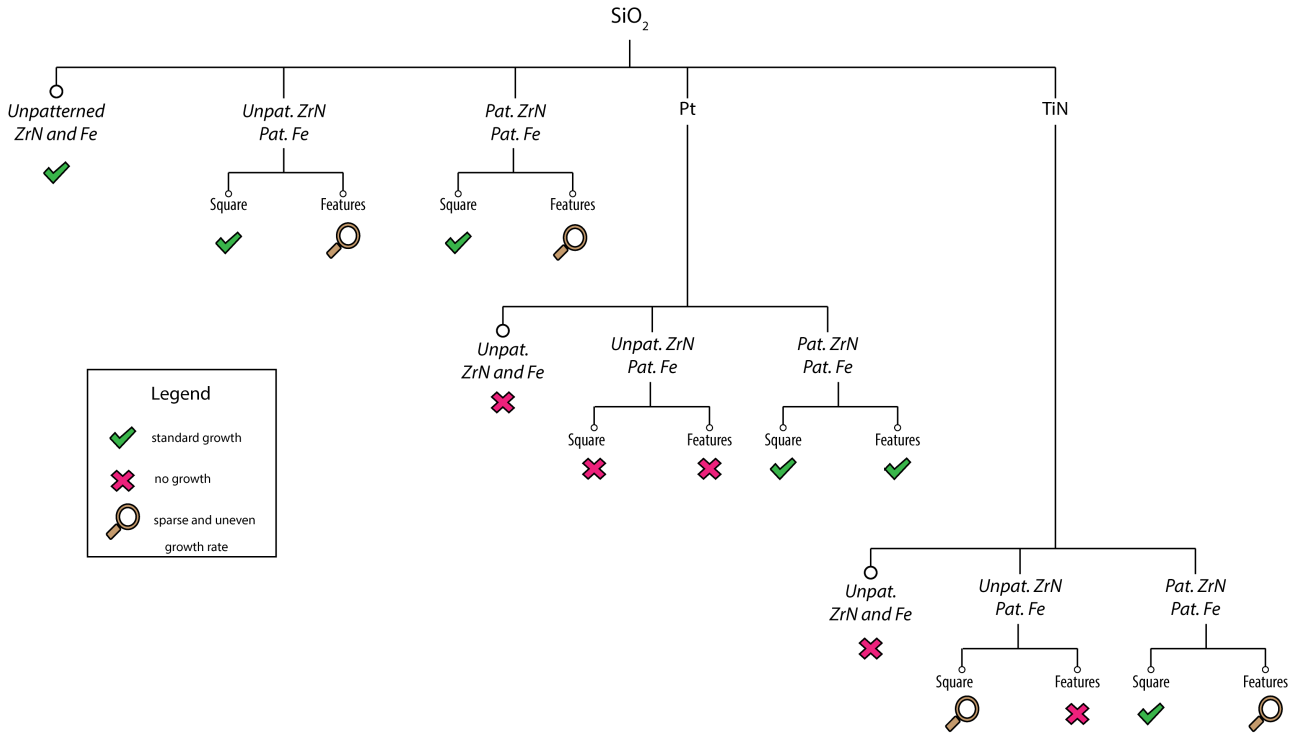


Figure 6.8: Schematic overview of the data collected by SEM and optical microscope after the CVD growth of CNTs of the sample sets based on SiO_2 substrate.

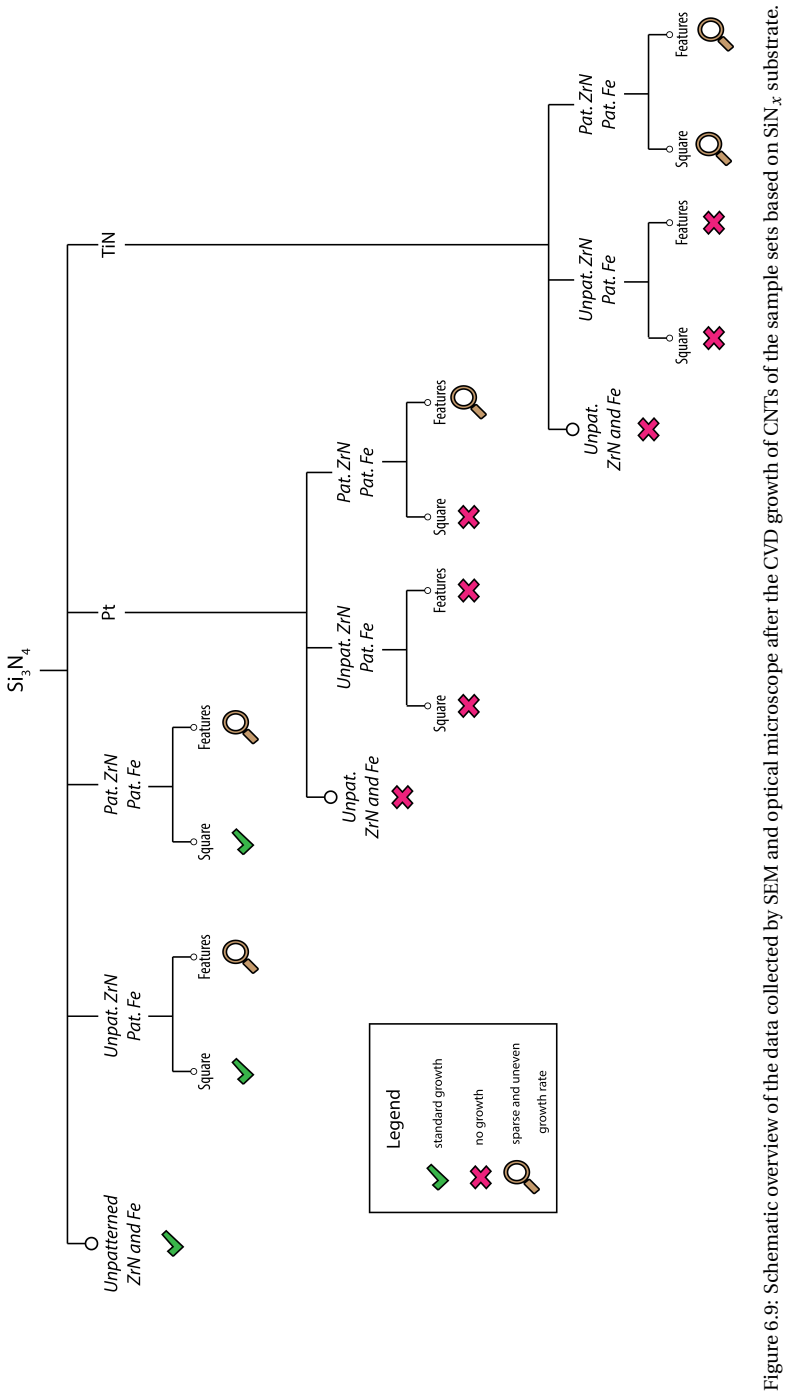


Figure 6.9: Schematic overview of the data collected by SEM and optical microscope after the CVD growth of CNTs of the sample sets based on SiN_x substrate.

From the carried experiments is possible to draw the following conclusions:

1. CNTs forests, resulting from unpatterned ZrN and Fe, grow only on the nonconductive substrates (SiO_2 and SiN_x). The CNT growth process largely depends on the surface energy interactions between catalyst and barrier layer. However, in our case, even the substrate underneath has a certain influence on the whole synthesis process.

2. When considering feature sizes smaller than 500µm the CNTs growth on ZrN results more challenging. Independently on the underlayer, the geometry of the catalyst pattern and the proximity with other catalyst islands play a significant role. The relationship between the growth of a CNT array and its feature size as well as the close presence of neighbouring arrays has been systematically studied by Bronikowski [13]. Under identical CVD growth conditions, he concluded that larger and densely packed features promote a higher-yield of the grown CNT arrays, while the smaller and not densely packed features showed to fail in the array growth obtaining only sparse nanotubes. As demonstrated by Banerjee10 this is valid even on the CNT grown on ZrN barrier layer, and here confirmed by the difficulty in growing VA-CNTs with smaller features in comparison to the square patches.

3. On conductive substrates, there is a higher chance to achieve VA-CNTs by patterning the ZrN layer. However, the wet etchant used for the ZrN layer, 0.5% HF at ambient temperature, is quite aggressive (etching rate estimated around 1.2 nm sec^{-1}). A larger undercut of the masking layer is observed in the smaller structures (two-side undercut of 2.5 mm), while in the square patches a two-side undercut of 1µm is measured. This can cause the complete removal of ZrN layer under the photoresist masking layer when the features are smaller than 500µm, like the ones used in the fabrication process explained in the Section 6.2.2. To mitigate this issue, the ZrN layer thickness has been increased from 10 to 30 nm. Although the most suitable solution was to use dry etching, in our process flow it cannot be applied due to the membrane presence and equipment contamination issues.

4. Independently on the structure size, patterning the Fe and leaving the ZrN unpatterned on metal layers, leads mostly to uneven or no aligned growth. The interaction between the layer of the stack is not clearly understood and a failure component due to the CVD reactor condition and/or the catalyst evaporation cannot be excluded. The CNT synthesis on ZrN showed to work only in a limited catalytic layer thickness range (from 0.5 to 0.8 nm), thus turning the entire CVD process

highly sensitive to the evaporation step. Studies found in literature focused on the CNT synthesis on metal layers such as copper (Cu) [14], stainless steel and palladium wire [15] and Inconel [16]. However, all of them prevent the diffusion of the catalyst Fe by passivating the metal surface with an extra layer of SiO_2 or Al_2O_3. Even if the growth process on ZrN still need to be optimized and completely understood, it has the potential to provide an inherently better than the currently employed solution to reduce the CNT-metal substrate contact resistance.

The observed instability of the growth process is not only related to the catalytic and the barrier layers, but also to the CVD reactor which is affected by both spatially and time-varying gradients [17]. In fact, the carried experiments showed a strong dependence of the VA-CNT growth success rate from the reactor temperature, the sample position within the chuck and the reactor memory effect. Therefore, before the CNT synthesis on ZrN the following precautions are taken: firstly, the reactor chamber is cleaned using an oxygen plasma recipe. Secondly, a long dummy run is performed to pre-heat the reactor. Thirdly, the samples are loaded in the centre of the chuck where the temperature is higher and more uniform.

6.4. COATING PROCEDURE

HA-CNTs sheets are a promising way to integrate massive quantity of CNTs at wafer-scale. Their interwoven morphology provide a unique opportunity for creating reinforced heterostructures with tailored material properties. As mentioned in Chapter (1), CNTs have been used in composite mostly as a secondary material to improve thermal, mechanical and electrical performace [18–22]. However, a new trend is to employ CNT as primary material, to be used as scaffold for a novel class of hybrid composite [23–25]. This will open to a novel class of composite materials with tailored thermal, electrical and mechanical properties.

We applied the same thin layers and consequently, same coating procedures used in Chapter (4) for the VA-CNTs. The HA-CNT sheets are thus subjected to a nanometer scale ceramic coatings of Al_2O_3 or non-stoichiometric a-SiC. The obtained heterogeneous composites based on CNT scaffolds are named Al_2O_3/HA-CNTs and a-SiC/HA-CNTs depending on the coating used (Figure 6.10).

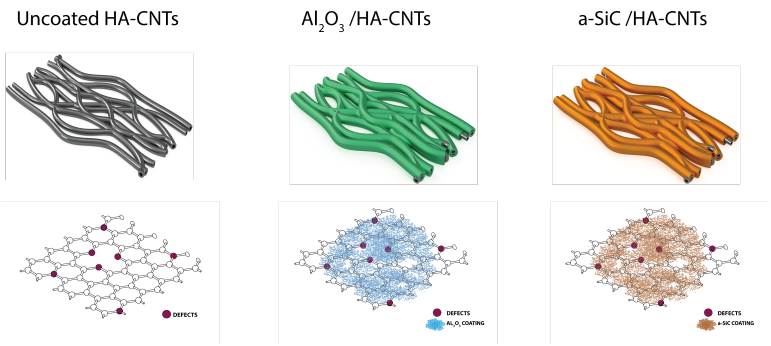


Figure 6.10: Schematic illustration of the uncoated and coated HA-CNT sheets. The coating nucleation starts from the interaction between localized CNT surface defect sites (purple dots) or at the CNT-CNT junctions and the precursor gases. These experiments are carried on HA-CNT originated from the combination of Fe/Al_2O_3 as catalyst and barrier layer.

6.5. MORPHOLOGICAL CHARACTERIZATION

The morphology, the packing density and the quality of CNTs are monitored after performing the crucial fabrication steps: VA-CNT growth, permutation in HA-CNTs and after the coating infiltrations. These data are collected by acquiring CNT Raman spectra with 514 nm laser wavelength, and by SEM inspection. More details on the morphological characterization techniques applied to nanotubes are given in Chapter (2).
Figure 6.11 shows the morphological variation starting from the as-grown VA-CNT nanofoam, to the HA-CNT sheets, ending with the coated HA-CNTs. The adopted deposition techniques allow nanoscale accuracy of the deposited layers thickness. The coating thickness obtained around the nanotube surface, 14.4 ± 1 nm for the a-SiC and 12.5 ± 1 nm for the Al_2O_3, agrees with the one measured on a bare Si wafer by ellipsometry.

As determined by SEM inspection, the regular foam-like VA-CNTs are packed with an estimated density of 112 tubes μm^{-2}. After the flattening procedure, the resulting HA-CNT morphology consists of compacted CNTs (~2120 tubes μm^{-2}) in which the initial alignment is retained.

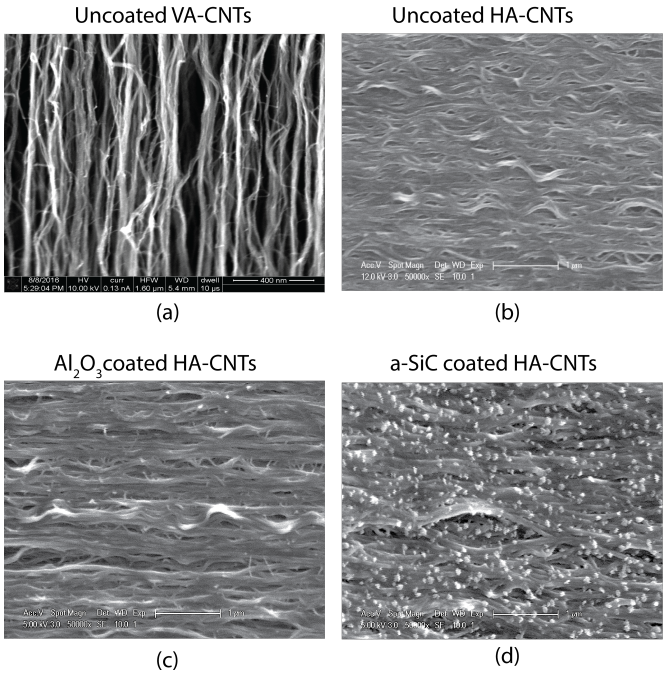


Figure 6.11: SEM close ups of the CNT morphology: (a) as-grown VA-CNT, (b) densified HA-CNT sheet, (c) Al_2O_3 hybrid sheet, (d) a-SiC hybrid sheet. The nanotube average diameter varies from 15 nm when uncoated to 39-44 nm when coated.

Raman spectroscopy, performed at different stages of the process, shows the structural evolution from the as-grown vertically aligned CNTs to the hybrid composite creation (Figure 6.12). The intensity ratio between the D-band (~1345 cm^{-1}) and the G-bands (~1586 cm^{-1}), I_D/I_G, indicates the quality variations. Specifically, the I_D/I_G ratios are 0.67, 0.92, 1, and 0.97 for the VA-CNT, the HA-CNT, the Al_2O_3/HA-CNT and the a-SiC/HA-CNT, respectively. The initial high defectivity of the HA-CNT sheet is beneficial for the coating. In fact, the surface defects provide bonding sites for the coating nucleation. Therefore, no functionalization treatments are required on the CNT scaffold prior to the coating procedures. The intensity of the G-band peak is weakened in both the Al_2O_3/HA-CNT and the a-SiC/HA-CNT sheets due to the coating thickness, which is in agreement with other researche [26].

As previously reported [27], VA-CNTs and consequently, HA-CNTs show crystallinity and alignment variations over the length due to the growing process (Section 2.3.4). As for the uncoated HA-CNTs, the I_D/I_G ratios versus the position along the HA-CNT length (tip, centre and bottom) of the coated ones have been analysed. The achieved results did not show any significant variation of the I_D/I_G ratios with the position.

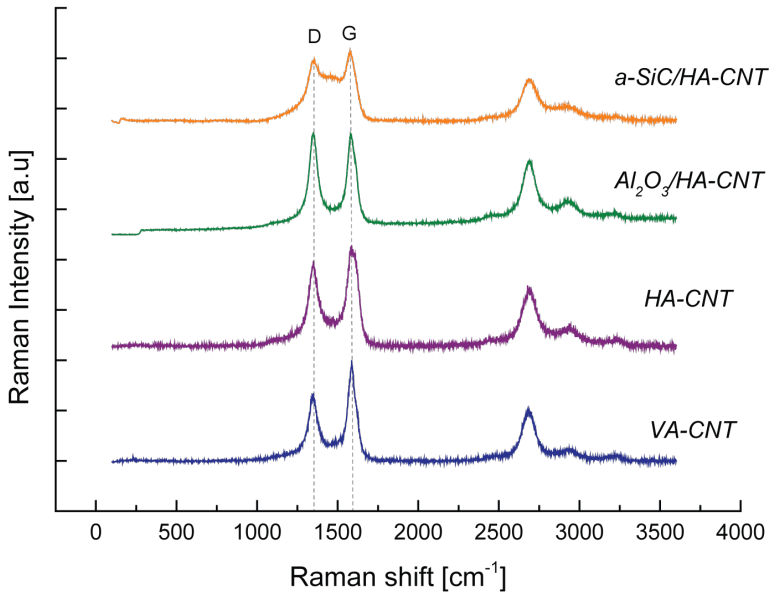


Figure 6.12: Raman spectra collected during the different stages of the fabrication process. The flattening process slightly affects the as-grown CNT quality and a clearly hybrid composite is formed after the a-SiC coating.

6.6. ELECTRICAL CHARACTERIZATION OF HA-CNT SHEETS

In microelectronic applications pure metals are heavily used due to their low electrical resistivity. However, the operating temperature is often higher than room temperature. In this scenario pure metals with their positive TCR do not represent the best solution. In fact, they do not counteract the temperature increasing and they can even become a source of extra heating due to their resistance increase and geometric constrains. Since a negative TCR is commonly observed in CNT sheets [28–30], they have emerged as valuable alternative to metals. The ideal case is represented by a resistor with zero or rather small TCR.

In the following sections the electrical performance of various structures based on HA-CNT sheets are discussed. First, the HA-CNT sheets originated by the two barrier layers under investigation, Al_2O_3 and ZrN, are measured. As the integration of CNT grown on ZrN support layer (see Section 6.3) proved to be rather cumbersome, only a few suspended interconnects samples on Pt electrodes are successfully realized. They are used only for a partial comparison with the ones based on Al_2O_3 in terms of contact and intrinsic resistance of the HA-CNT sheets in Section 6.6.1 and Section 6.6.2. Then, in Section 6.6.3 the electrical anisotropy of HA-CNT sheets is investigated by using

large squared assemblies of HA-CNT sheets (1×1 cm), named films. Recently, electrical [31],thermal [32],and mechanical [33] anisotropies of HA-CNT are attracting attention. Due to the macroscopic dimension of the obtained HA-CNT films, the material properties can be investigated with conventional methods rather than peculiar method as often used to characterize nanomaterials. In the final Section 6.6.4 the effects of the coatings on the electrical performance of HA-CNT sheets are observed by comparing the sample resistance values prior and after the procedure. In particular, we propose for the first time the thin coating as strategy to enhance the electrical conductivity of HA-CNT sheets.
The mentioned electrical characterizations are performed in two-point configuration by providing a low input current to avoid the sample self-heating. The current-voltage (I-V) measurements of the obtained structures are performed on a Cascade probe station and an Agilent 4156C Semiconductor Parameter Analyzer in DC mode.

Prior to start analysing the obtained results, we would like to briefly introduce the nomenclature used and the electrical transport phenomena involved in HA-CNT sheets. Since the HA-CNT sheets are three-dimensional (see Figure 6.13), the effective electrical conductivity (as well as the thermacl conductivity) has components in three directions: *x*; *y*; *z*. The nanotubes length is along the *x-axis* and the sheet cross section lies on the *y-z plane*.



Figure 6.13: Three-dimensional sketch representing a HA-CNT sheet. The *x-axis* lies along the axial tube direction, *y-axis* along the radial direction of the tube and *z-axis* along the sheet thickness.

The electrical conduction on the *x-axis*, specifically the one along an individual MWCNT, depends on the diameter and length of the tube as well as the defect density [34]. Along the *y-axis* and the *z-axis*, numerous overlapping among parallel CNTs are created during the liquid-assisted flattening technique. The densification process has shortened the spacing among adjacent tubes down to the van der Walls contact distance, and consequently increasing the contact area of the CNT both in-plane and

along the thickness. The resulting morphology expands the carrier transport across the in-plane direction. However, because the CNT-CNT junctions act as electrical boundaries, the preferential direction of the electrical transport will be along the tube length (*x-axis*) rather than the *y*- or *z*- directions. The CNT-CNT resistance heavily depend on the overlapping area and on the intertube spacing [35]. The junction resistance is lower when the CNT are in direct contact, while it strongly increases when the carrier transport is through tunnelling among separated tubes [36–38]. Therefore, most likely the electrons prefer to percolate across the interwoven nanotube sheet instead of tunnelling. Moreover, the electron transport through tunnelling requires high thermal energy, thus increasing the electron tunnelling probability at higher temperatures [37].

6.6.1. RESISTANCE MEASUREMENT OF UNCOATED HA-CNTS

As observed by the Raman spectroscopy (Figure 2.3.4), the CNT grown on ZrN exhibit higher degree of crystallinity and lower defect density in comparison to the Al_2O_3. Therefore, to understand if the crystallinity difference is reflected on the electrical performance, a comparison in carried out between HA-CNTs derived from CNTs grown on the two barrier layers. Moreover, the ZrN layer has a lower resistivity than the Al_2O_3 layer, therefore a lower contact resistance is expected. The resistance measurements are carried out on suspended interconnects structures, different in lengths (400 µm, 250 µm and 100 µm), obtained on Al_2O_3 and ZrN barrier layers (Figure 6.14 (a)).

The total electrical resistance, R_M, can be expressed as the sum of the HA-CNT sheet intrinsic resistance, R_{HA-CNT}, and the contact resistances (HA-CNT-metal), R_{c1} and R_{c2}:

$$R_M = R_{c1} + R_{c2} + R_{HA-CNT} \tag{6.1}$$

where R_{c1} is the contact resistance between the HA-CNT root and the electrode, R_{c2} is the one related to the contact between the HA-CNT sheet tip and the electrode (see Figure 6.14 inset). By measuring the R_M as function of the different HA-CNT sheet lengths, the sum $R_{c1} + R_{c2}$ is inferred from the least square fitting at zero length, $l = 0$, in the R_M - length plot (Figure 6.14 (b)). The method adopted to characterize the contact resistance and the HA-CNT sheet intrinsic resistance is known as transfer length method (TLM) [39]. It should be noticed that R_{c2} depends on the initial height of the synthetized VA-CNT array. Considering a fixed electrode distance, a higher VA-CNT array originates a longer HA-CNT, thus increasing the overlap area between the HA-CNT sheet tip and the bridged electrode. Therefore, while the R_{c1} is constant with respect to the length, the R_{c2} depends on the sheet length. All the measured sample sets had the same overlap

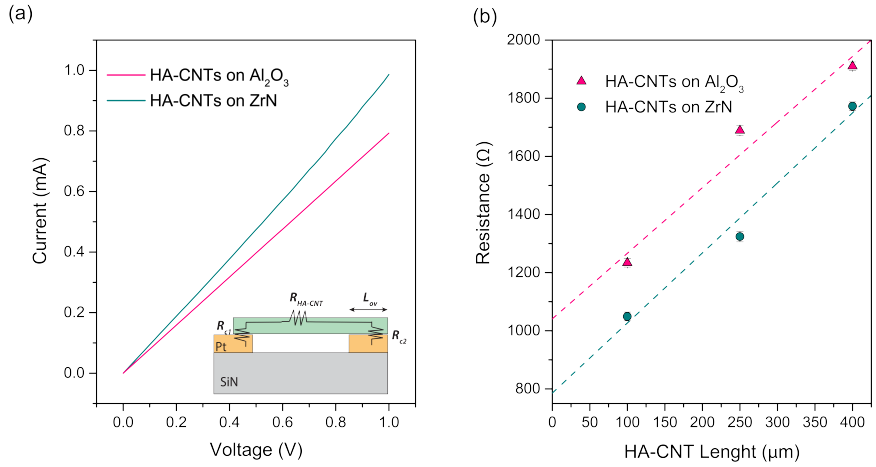


Figure 6.14: (a) I-V characteristic for different HA-CNT sheets synthesized on Al_2O_3 or ZrN barrier layer. The inset shows a sketch with the contact resistance contributes R_{c1} and R_{c2} and the sheet resistance R_{HA-CNT}. The R_{c2} strongly depends on the overlap length L_{ov}. (b) Resistance vs. HA-CNT sheet lenght (l). In particular, l ranges from 400μm down to 100μm. The transfer length method was used to estimate the resistance components. The dashed lines represent the linear fitting of the data. For l=0μm the sum $R_{c1} + R_{c2}$ is found for both barrier layers.

length, L_{ov}, in order to highlight only the length dependency of the R_{HA-CNT}. Table 6.2 displays the obtained resistances. The recorded difference between the HA-CNT sheets on Al_2O_3 and on ZrN is due to R_{c1}+R_{c2}. Therefore, even if the HA-CNTs grown on ZrN have higher quality this can't be precisely determined by our measurement method.

Table 6.1: Parameters obtained from the linear fitting of Figure 6.14 (b). r_{HA-CNT} is the resistance per unit length ($\Omega\ \mu m^{-1}$).

Barrier layer	$R_{c1} + R_{c2}$ Ω	r_{HA-CNT} $\Omega\mu m^{-1}$
Al_2O_3	1041 ± 116	2.25 ±0.4
ZrN	786 ± 83	2.4 ±0.29

As future step, it might be interesting to investigate the R_{c2} dependency on the overlap length (L_{ov}). Ghatge et al. have predicted a decrease in contact resistance by increasing the graphene-metal overlap [40]. Moreover, since every employed method to extrapolate the contact resistance over the total one has its own approximations, it is recommended to use multiple measurement structures (such as contact chains, Kelvin method, four-point method) in future experiments [39].

6.6.2. CONTACT RESISTANCE HA-CNT/HA-CNTS

The pre-patterned wafer contains a structure we named "domino", that can be used to characterize the contact resistance among overlapping HA-CNTs sheets, named R_{HH}. The investigated structure can be constituted by 1, 3, 6, 9 and 13. The domino arrangement aims at proving the possibility to overcome the limitation of the HA-CNT length, due to the growth saturation during the CNT synthesis, by sequentially aligning sheets. Every sheet overlaps the subsequent one for a certain length called $L_{CNT-CNT}$. This length depends on the height uniformity of the synthesised VA-CNT arrays. In the image shown in Figure 6.15 (a) the length of each HA-CNT sheets varies between 495-510µm. The total length of a stripe depends on the number of sheets involved in the domino structure. As observed by performing electrical measurements, the resistance increases linearly by increasing the number of sheets involved in the domino structure (Figure 6.15 (b)).

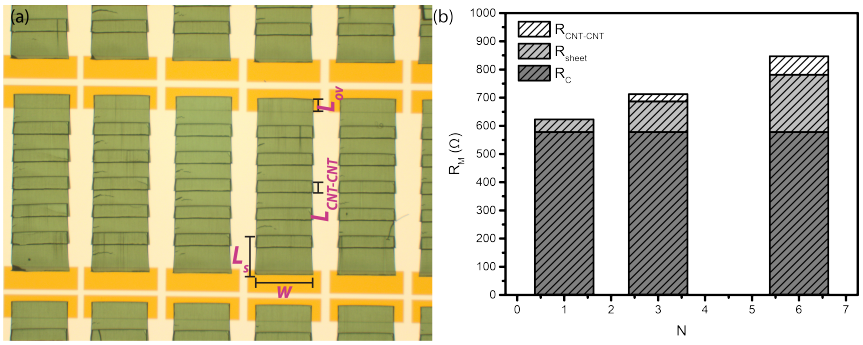


Figure 6.15: (a) Domino structure composed by sequentially flattened HA-CNT sheets obtained on Al_2O_3 barrier layer. The overlap length between adjacent sheets is called $L_{CNT-CNT}$. In the picture the $L_{CNT-CNT}$ varies from 148µm to 155µm. The total length of the stripe depends on how many sheets are participating to the domino structure. (b) Resistance contributes of three domino structure.

The contact resistances between CNT-metal, R_{c1}+R_{c2}, and overlapped HA-CNT sheets, R_{HH}, are determined by TLM method. The sum R_{c1}+R_{c2} corresponds to the resistance value achieved at l = 0, here defined R_C. By assuming an average sheet length, L_s, of 502.5µm and an average $L_{CNT-CNT}$=151.5µm, the measured domino resistance can be described as follow:

$$R_M = R_C + R_s + R_{H-H} \tag{6.2}$$

$$R_M = R_C + r_s(N \cdot L_s - (N-1) \cdot L_{CNT-CNT}) + (N-1) \cdot L_{CNT-CNT} \cdot r_{HH} \tag{6.3}$$

where N is the number of sheets involved in the domino structure, r_s and r_{HH} are the length dependent resistances ($\Omega\ \mu m^{-1}$) of the sheet and HA-CNT/HA-CNT junction, re-

spectively. The average r_s is 0.09 Ω μm^{-1}, inferred by N=1, while the r_{HH} is 0.087Ω μm^{-1}. The stacked column chart reported in Figure 6.15 (b) highlights the resistance contributes that pertain to the total resistance of three domino structures.

Considering a copper-based interconnects, equal in dimensions to a 6 HA-CNT sheets domino structure, the resulting resistances are ~0.1 Ω [41] and ~269 Ω for the first and the latter, respectively. The carried comparison demonstrates that several improvements should be made to employ the domino structure on practical applications such as local routing. Therefore, strategies to decrease the resistance of the sheets to bring these CNT assemblies a step forward towards state of the art applications are needed.

6.6.3. ELECTRICAL ANISOTROPY

To characterize the anisotropic electrical transport on large area CNT based film, we create a 1×1 cm HA-CNT sheets (Figure 6.16 (a)). Empirically we found that is not possible to directly synthetize VA-CNT array of 1 cm in width. In fact, in such samples a detachment of the entire densified array and consequently, a curling up of the whole structure is observed after IPA immersion. The maximum array width that can be achieved to avoid the curling up effect is 800 µm. Therefore, to cover a large area, misaligned patches of HA-CNT sheets are fabricated. The resulting film and the current-voltage characteristics are shown in Figure 6.16. The possible electron pathways along the square patch and the corresponding resistances are: the parallel direction, $R_{//}$, and the perpendicular direction, $R^{\perp}$, to the HA-CNT alignment. The film anisotropy is given by the ratio $R^{\perp}$/ $R_{//}$. As observed from the I-V characteristics, the $R_{//}$ is lower than $R^{\perp}$ and the anisotropy ratio is 2.48. Since the electrical conductivity in the graphene plane of a CNT is orders of magnitude higher than that among adjacent graphene planes, the electrons are predominantly flowing through the outermost wall of a MWCNT, while the inter-shell conduction is highly discouraged [42]. This generates the observed material anisotropy. Moreover, the achieved electronic anisotropy is lower in comparison to the one measured on magnetically aligned CNTs ($R^{\perp}$/ $R_{//}$ = 6.2-8) [31] and buckypapers ($R^{\perp}$/ $R_{//}$ = 7.3) [33], demonstrating that obtained large scale HA-CNT sheets are inherently better than the CNT-based composite having different alignment techniques.

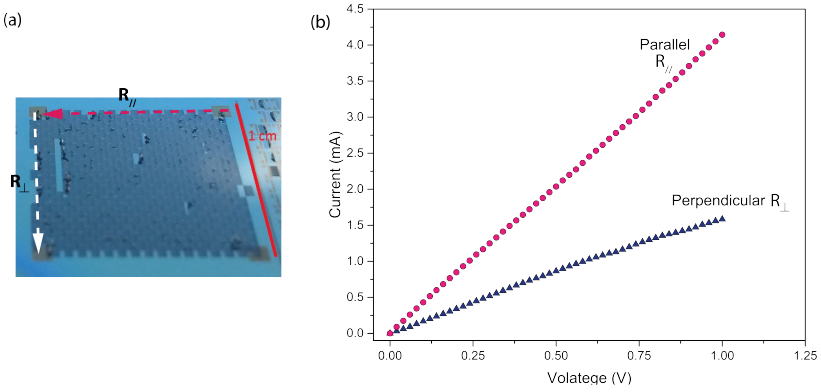


Figure 6.16: (a) Optical image of the HA-CNT film of squared area equal to 1 cm^2. The current flow perpendicular (white line) and parallel (red line) to the tube alignment direction are shown. (b) Current-voltage characteristics measured perpendicular, parallel or diagonal to the HA-CNT alignment.

The manufactured large area conductive patches can be potentially used in combination of the gas sensing capabilities of CNTs. Gas sensing application requires high surface area, good electronics properties and mechanical and environmental stability. However, the most used approach requires tedious processes to obtain random CNT networks, that due to their randomise distribution of the tubes need to be electrically characterized before their usage [43]. A step toward the commercialization of CNT-based sensor is represented by the possibility to perpendicular align CNT arrays. The well-defined orientation allows to increase the sample reproducibility as well as performing surface treatment to selectively increases the detection sensitivity and selectivity of the tubes to gases or even for protein detection [43, 44]. Other interesting applications are related to electronic skin and flexible electronic. However, it is necessary to lower the CNT growth temperature or to adopt transfer techniques on flexible substrates. Finally, the high area coverage and the low thickness of the HA-CNT films can be employed as TIM or heat spreader depending on their thermal performance.

6.6.4. ELECTRICAL CONDUCTIVITY ENHANCEMENT THROUGH COATINGS

Here the electrical conductivity improvement of HA-CNT sheets through a-SiC and Al_2O_3 infiltration is investigated. The I-V trends of the a-SiC/HA-CNTs and the Al_2O_3/HA-CNTs suspended on the membranes are reported in Figure 6.17. In this section, all the HA-CNT sheets studied originated from the permutation of VA-CNT grown on 30 nm of sputtered Al_2O_3 as barrier layer. The electrical response of the investigated samples is measured and compared to the one before the coating procedure. The measurements

are performed on HA-CNT sheets with $w = 800\,\mu m$, $t = 6\,\mu m$ and a distance between the electrodes of $400\,\mu m$ (Figure 6.17 inset).

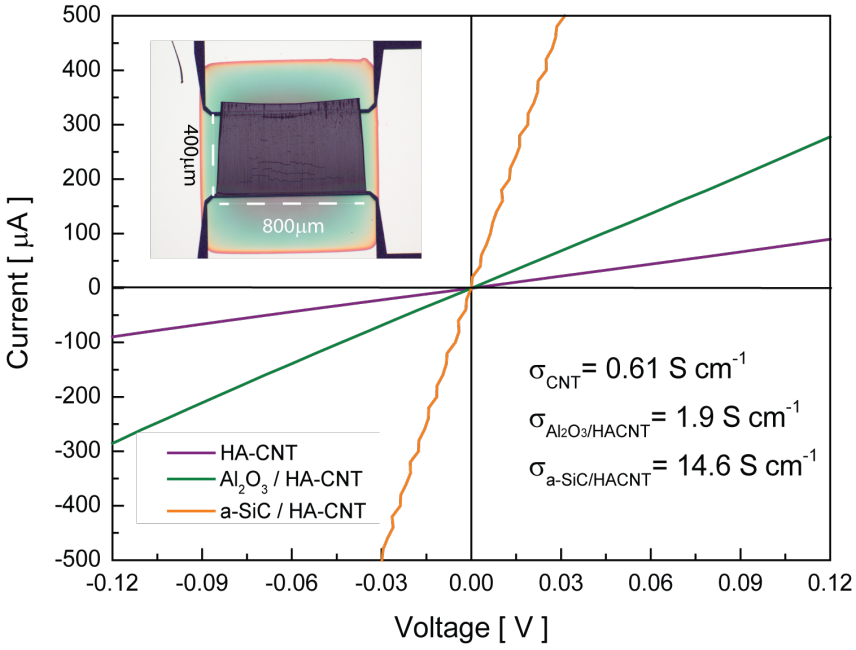


Figure 6.17: I-V curve before and after the coating procedure of the HA-CNT sheets (inset). The contact resistance was subtracted from the measurements. The HA-CNT conductivity increases of ~209% by coating the sheets with Al_2O_3 and of ~2276% by adding a-SiC thin layer.

The pristine HA-CNT sheets exhibit a conductivity of 0.61 S·cm-1, while a substantial increase is recorded for the hybrid ones: 1.9 and 14.6 $S{\cdot}cm^{-1}$ for Al_2O_3/HA-CNTs and a-SiC/HA-CNTs, respectively. The impressive enhancement in electrical conductivity corresponds to 209% for Al_2O_3/HA-CNTs and 2276% for the a-SiC/HA-CNTs. To the best of our knowledge nobody has ever reported such as enhancement on coated CNTs arrays. The drastic increase of the sheet conduction can be attributed to at least one of the following aspects: the infiltrated material (interface resistance and porosity variation, nanotube doping), CNT annealing.

The electrical conductivity enhancement might be symptomatic of the support of the infiltrated thin layers to overcome high resistivity sites within the scaffold, such as CNT-CNT junctions, separated CNTs at tunnelling distance in both *x-y plane* and *y-z plane* and defects along the nanotube. The coating increases the CNT diameter. Consequently, it facilitates the creation of new interfaces among adjacent tubes that were not in contact before or at tunnelling distance. In all cases the arisen interface resis-

tance CNT/coating is more favourable than the initial situation (tunnelling or even no conduction). The magnitude of the interface resistance in general, and CNT/coating in particular, depends on the energy-band diagram for the CNT-material interface. Since it has been demonstrated that the by increasing the inter-tube contact area or decreasing the inter-tube space the resistance interface decreases [45], we can expect a reduction of the contact interface due to increased surface area through the coatings.

Moreover, the coating infiltration within the CNT scaffold implies a further porosity reduction, and depending on the material and deposition conditions, a CNT doping effect. Various studies carried on the effect of porosity variation on fiber [45], 3D CNT network [46], buckypaper [47], have shown resistivity decrease due to porosity reduction. Therefore, this is probably one of the causes of the resistivity reduction in both Al_2O_3 and a-SiC coated HA-CNT samples. However, the electrical conductivity enhancement of the a-SiC/HA-CNT sheet is so consistently higher than the Al_2O_3/HA-CNT one that suggested the existence of additional factors such as doping effect.

It has been reported that by substituting a carbon atom in the nanotube lattice with an element of different valence electrons the number of available states in the CNT increases [48]. The type of state (electron-donor or electron-acceptor) depends on the bonding of the dopant element and the lattice. The most common dopants are nitrogen (N) or boron (Br), which are next to carbon in the periodic table of elements. Considering the gas precursors involved in the coating procedure, we focused our attention on two possible doping elements: N as carrier gas in the ALD process; dichlorosilane (SiH_2Cl_2) as precursor in the a-SiC deposition by LPCVD. The incorporation of N, that has an extra electron in comparison to C (electron donor), in MWCNT it has been extensively studied (N-doped CNTs) [49]. The *in situ* doping insertion of N occurs during the CNT synthesis, an example in the CVD reactor by tuning the synthesis recipe at elevated temperature (825°C) [50]. N-doped CNTs can be even obtained by post-treatment. However, high temperatures are required (800-1200 °C) [51]. Therefore, to the best of our knowledge we can exclude N incorporation in CNTs during the Al_2O_3 deposition due to the low process temperature (350°C). The inclusion of Si into CNTs and the tailoring of the electrical and thermal properties has been reported by others [52–57]. As the N, Si introduce donor-like states above the pristine CNT Fermi level, thus further decreasing the already small CNT band gap and increasing its electrical conductivity. The *in situ* incorporation of Si in CNT lattice is performed using an aerosol-based CVD system with a solution decomposed at 760 °C [54, 56]. The temperature required for the heteroatom insertion is the same as the one adopted during the LPCVD process. During the LPCVD process 65 sccm of SiH_2Cl_2, used as Si source, over 35 sccm of acetylene (C_2H_2), used

as carbon source, in 5% H_2 (carrier gas) reacted with the CNT surface at elevated temperature (760 °C) and at low pressure (1 mbar). The inserted Si atom is expected to be highly reactive, serving as binding centre to other atoms or molecules [57]. Therefore, most likely the substantial enhancement of the a-SiC/HA-CNT is due to the influence of Si on the CNT structure. Further investigation needs to be done to better understand the doping mechanisms.

The CNT transport properties are strongly dependent on the crystalline structure and defect density, a possible cause of the resistance reduction of the coated sheets is the CNT purification due to heat treatment. Many researchers have reported a defect-reduction and structural enhancement of MWCNT by performing an annealing [58–60]. However, the mentioned thermal treatments are performed at temperature ranges from 1500 °C to 2000 °C or even higher. Consequently, we can exclude that both coating processes can cause a crystallinity improvement or purification of CNTs. This is confirmed by the unaltered I_D/I_G ratio between the uncoated and annealed sample.
In conclusion, the total contact resistance reduction of the Al_2O_3/HA-CNT is most likely due to coating related effects, while for the a-SiC/HA-CNT might be a combination of coating and doping.

6.7. ELECTRO-THERMAL CHARACTERIZATION

In the following sections the thermal performance of pristine HA-CNTs, Al_2O_3/HA-CNTs and a-SiC/HA-CNTs are discussed. Prior to evaluate the effective thermal conductivity of the above-mentioned sample, the used measurement method, which consists on the direct joule heating of the sample, requires three steps. First, the TCR of the various samples must be quantified. After performing the calibration, a temperature rise was induced within the sample by providing high input currents and thus self-heating the sample itself. This second step was performed in both air and vacuum and the achieved results were analysed under the assumption of one dimensional heat transport. As final step, high resolution IR maps were collected while powering the samples and preliminary data on the sheets average k_{eff}.

6.7.1. THERMAL COEFFICIENT OF RESISTANCE (TCR)

In Chapter (3) the procedure to determine the TCR of the Pt spiral was introduced. The TCR gives a straightforward link between resistance and temperature of the material under investigation. In this section the TCR obtained from HA-CNT sheets, subjected to different treatments, is discussed: as grown, thermal annealed and coated HA-CNTs.
Firstly, the current range at which no detectable Joule heating effects on the resistance

is determined (for I_0 = ± 50 μA constant resistance, R=R_0). Then, the sample is heated up through an external temperature controlled chuck, and R_0 is collected at each temperature step, from 298 K to 473 K (Figure 6.18 (a)). The temperature dependence of the R_0 of HA-CNT sheets is highlighted.

The resistance of both the pristine HA-CNT sheet and the Al_2O_3/HA-CNTs decreases while the temperature increases, implying a negative TCR. In particular, the resistance at 473 K is reduced by 76% and 68% for the uncoated and Al_2O_3/HA-CNTs, respectively. The TCR was calculated as follow:

$$TCR = \frac{1}{R_0}\frac{dR(T)}{dT} \tag{6.4}$$

R_0 being the average resistance at T_0=298 K. TCR ranges from 8034 ppm K^{-1} to 1970 ppm K^{-1} and from 5403 ppm K^{-1} to 2156 ppm K^{-1} for the pristine and the Al_2O_3/HA-CNT sheets, respectively (Figure 6.18 (b)). The obtained negative values suggest a semiconductor behaviour of the two samples. It is worth noting that even at high temperature, the Al_2O_3 hybrid composite has a lower resistance than the pristine sheet. The negative temperature dependence originates mainly from the amount of conduction channels within the MWCNT that in parallel are contributing to the heat transport. In fact, with increasing the temperature the number of conduction channels increases. Consequently, more electrons participate to the heat transfer, lowering the resistance enough to counteract the increase in the electron–phonon scattering rate [61–63].

In contrast, the total resistance of a-SiC/HA-CNTs sheets increases with the temperature, indicating a positive TCR. The obtained a-SiC composite sheet shows a resistance variation of 17% over the entire investigated temperature range. Further analysis reveals TCR values ranging from 1188 ppm K^{-1} to 861 ppm K^{-1} for the a-SiC. It emerges a metallic like response. We can exclude a resistivity variation of the electrodes. In fact, an annealing of the pre-processed wafers have been performed prior the CNT synthesis. We can exclude even a richer concentration of metallic nanotubes in that sheet after performing Raman inspection. Therefore, the causes of the drastic change of the sheet thermal behaviour might likely be related to the CNT doping though Si atom insertion, as explained in Section 6.6.4.

As observed in other CNT composites [64–66], the temperature dependence of TCR, reported in Figure 6.18 (b), is the outcome of three phenomena that the electrons experience while moving through the CNT network: thermal assisted tunnelling transport at the tubes-tubes junctions and thermal expansion of the HA-CNT sheet.

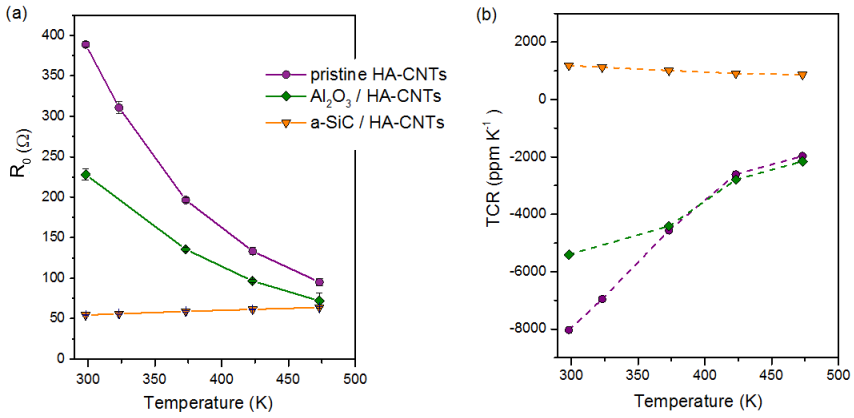


Figure 6.18: Thermoresistive characteristics of the HA-CNT sheets subjected to different treatments: (a) R_0 versus temperature; (b) Temperature dependence of TCR.

Further investigations are required to understand the interplay between the metallic and semiconducting TCR behaviours of the heterogeneous composites. However, the ability to tune the material thermoresistive response and the conductivity, plus the lightweight and the integration in polymer composite, make the HA-CNT sheets attractive candidate resistor in wearable electronic device and heating and temperature sensor system. In particular, we envision the possibility to achieve a hybrid resistor with constant resistance over temperature (stable TCR=0) by stacking and tuning two HA-CNT sheets with the different TCR.

6.7.2. REMOTE JOULE HEATING ON HA-CNTS

Above $I > I_0$ the resistance of a HA-CNT sheet varies due to Joule heating (Figure 6.19) in both air and vacuum. In fact, a detectable sample self-heating occurred after 0.5 mA for all the investigated samples. As anticipated by the TCR, the trends of the pristine HA-CNTs and the Al_2O_3/HA-CNTs show a semiconductor-like behaviour (their resistance decreases with temperature increase), while the a-SiC/HA-CNTs trend indicates a metallic-like behaviour (its resistance increases with temperature increase).

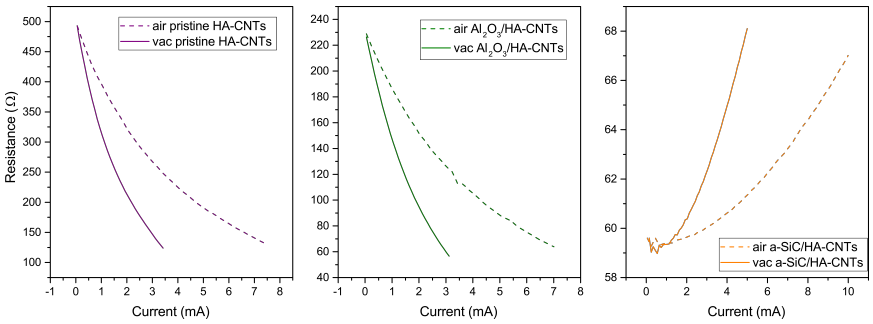


Figure 6.19: Resistance-current plots for (a) pristine HA-CNTs, (b) Al_2O_3/HA-CNTs and (c) a-SiC/HA-CNTs.

A qualitative estimation of the k_{eff} of a HA-CNT sheet can be obtained by using the one-dimensional heat transfer equation along a cutline of the high-resolution IR maps, collected at the lowest possible current (Figure 6.20). Assuming no heat losses due radiation and convection, the heat conduction equation can be written as [67]:

$$-k_{eff}\frac{dT(x)}{dx} = \frac{I^2R}{A_c} \tag{6.5}$$

where A_c is the surface normal to the heat flow direction, $I^2R = P_{air}$ is the heat transferred through the HA-CNT sheet. The thermal maps well describe the heat distribution throughout the HA-CNT sheets. The Al_2O_3/HA-CNTs and the pristine HA-CNTs are progressively heated from the cold side (corresponding to T_b) to the hot side (corresponding to T_{tip}). However, the surface temperature distribution on the Al_2O_3 results more uniform than the pristine one. The a-SiC/HA-CNTs get just slightly heated up as observed by the electro-thermal characterization. The highest temperature difference alongside the diagonal of the a-SiC coated sheet is 7 K for an input current of 7 mA (Figure 6.20) (c)). The average effective thermal conductivity of each sample is achieved based on the Equation (6.5) and the data are reported in Table 6.2 .

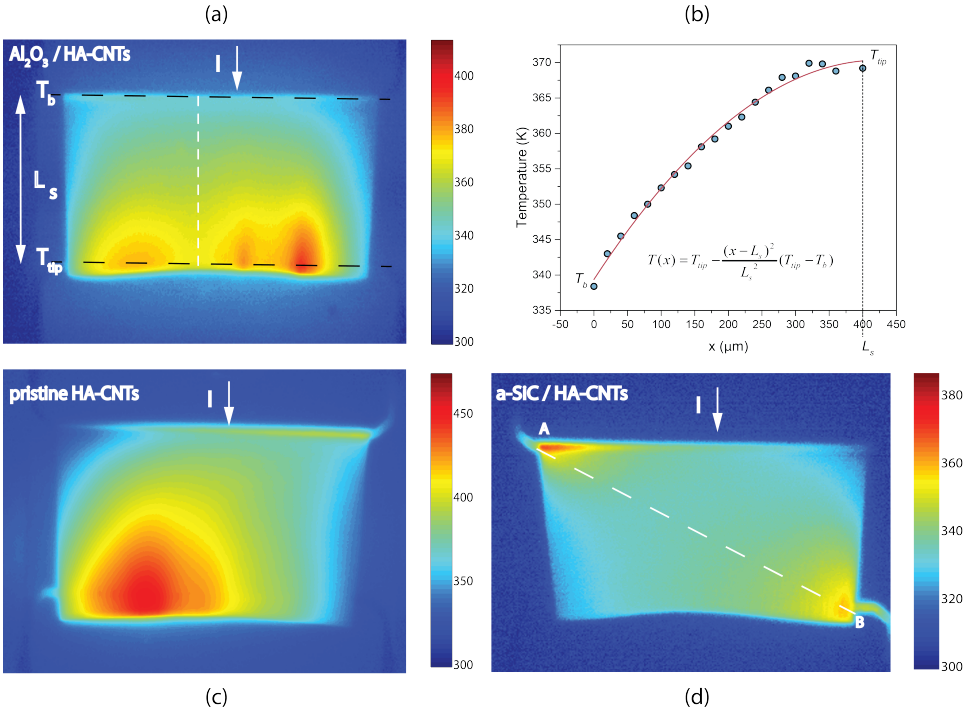


Figure 6.20: IR maps of (a) Al_2O_3/HA-CNTs (c) pristine HA-CNTs and (d) a-SiC/HA-CNTs collected by proving an input current equal to 7 mA. (b) report the temperature profile along the dashed white cutline of the Al_2O_3/HA-CNTs. While the diagonal dashed lines in (d) represent the maximum temperature difference achieved on a-SiC/HA-CNTs equal to 7 K.

Table 6.2: Average k_{eff} calculated by I=7mA. The apex [d] indicates the extra value extracted from the diagonal line of the a-SiC/HA-CNTs (dashed white line in Figure 6.20 (d)).

Pristine HA-CNTs	Al_2O_3/HA-CNTs	a-SiC/HA-CNTs
9.4 (W m^{-1} K^{-1})	9.6 (W m^{-1} K^{-1})	260 (W m^{-1} K^{-1}) [d]84 (W m^{-1} K^{-1})

The reported k_{eff} values have to be considered as a qualitative estimation. An more accurate model, which include conductive and radiative heat dissipation, and better contact between the HA-CNT sheets and the electrode is therefore required. As demonstrated in Chapter (3), neglecting the convective and radiative contributes could result in a significant modelling error. Therefore, the reported findings have to be considered as preliminary and a starting point for further studies.

6.8. CONCLUSION

We have presented electrical and thermal conductivities from heterogeneous materials based on HA-CNTs. Promising results have been obtained from HA-CNTs after performing coatings of Al_2O_3 and a-SiC. In particular, an unprecedented electrical conductivity enhancement of 209% for Al_2O_3/HA-CNTs and 2276% for the a-SiC/HA-CNTs has been achieved. From the thermal point of view, the Al_2O_3 coating increases the temperature distribution uniformity, while the a-SiC coating allows to achieve the thermal conductivity up 260 W m^{-1} K^{-1}. Moreover, it has been observed that the by coating HA-CNTs with a-SiC is possible to tune the TCR from positive to negative.Further investigation need to be carried to understand the phenomenon behind this behaviour change as well as the TCR temperature dependence caused by the material thermal expansion.

REFERENCES

[1] R. H. Poelma, B. Morana, S. Vollebregt, E. Schlangen, H. W. van Zeijl, X. Fan, and G. Q. Zhang, *Tailoring the Mechanical Properties of High-Aspect-Ratio Carbon Nanotube Arrays using Amorphous Silicon Carbide Coatings,* Advanced Functional Materials **24**, 5737 (2014).

[2] R. H. Poelma, X. Fan, Z. Y. Hu, G. Van Tendeloo, H. W. Van Zeijl, and G. Q. Zhang, *Effects of Nanostructure and Coating on the Mechanics of Carbon Nanotube Arrays,* Advanced Functional Materials **26**, 1233 (2016).

[3] Y. Hayamizu, T. Yamada, K. Mizuno, R. C. Davis, D. N. Futaba, M. Yumura, and K. Hata, *Integrated three-dimensional microelectromechanical devices from processable carbon nanotube wafers.* Nature nanotechnology **3**, 289 (2008).

[4] MicroChemicals, *Aluminum etching,* (2013).

[5] L. Mele, F. Santagata, E. Iervolino, M. Mihailovic, T. Rossi, a. T. Tran, H. Schellevis, J. F. Creemer, and P. M. Sarro, *A molybdenum MEMS microhotplate for high-temperature operation,* Sensors and Actuators, A: Physical **188**, 173 (2012).

[6] J. Creemer, D. Briand, H. Zandbergen, W. van der Vlist, C. de Boer, N. de Rooij, and P. Sarro, *Microhotplates with TiN heaters,* Sensors and Actuators A: Physical **148**, 416 (2008).

[7] M. Kumar and Y. Ando, *Chemical Vapor Deposition of Carbon Nanotubes: A Review on Growth Mechanism and Mass Production,* Journal of Nanoscience and Nanotechnology **10**, 3739 (2010).

[8] A. Magrez, J. W. Seo, R. Smajda, M. Mionić, and L. Forró, *Catalytic CVD Synthesis of Carbon Nanotubes: Towards High Yield and Low Temperature Growth,* Materials **3**, 4871 (2010).

[9] A.-C. Dupuis, *The catalyst in the CCVD of carbon nanotubes—a review,* Progress in Materials Science **50**, 929 (2005).

[10] S. Vollebregt, S. Banerjee, F. D. Tichelaar, and R. Ishihara, *The growth of carbon nanotubes on*

electrically conductive ZrN support layers for through-silicon vias, Microelectronic Engineering **156**, 126 (2016).

[11] S. Vollebregt, *Carbon Nanotubes as Vertical Interconnects in 3D Integrated Circuits*, Ph.D. thesis, Delft University of Technology (2014).

[12] S. Banerjee, *Super-growth of CNTs based on ZrN for TSV application*, Ph.D. thesis, Delft University of Technology (2014).

[13] M. J. Bronikowski, *CVD growth of carbon nanotube bundle arrays,* Carbon **44**, 2822 (2006).

[14] H. Sugime, S. Esconjauregui, L. D'Arsié, J. Yang, A. W. Robertson, R. A. Oliver, S. Bhardwaj, C. Cepek, and J. Robertson, *Low-Temperature Growth of Carbon Nanotube Forests Consisting of Tubes with Narrow Inner Spacing Using Co/Al/Mo Catalyst on Conductive Supports,* ACS Applied Materials & Interfaces **7**, 16819 (2015).

[15] M. Delmas, M. Pinault, S. Patel, D. Porterat, C. Reynaud, and M. Mayne-L'Hermite, *Growth of long and aligned multi-walled carbon nanotubes on carbon and metal substrates,* Nanotechnology **23**, 105604 (2012).

[16] L. Gao, A. Peng, Z. Y. Wang, H. Zhang, Z. Shi, Z. Gu, G. Cao, and B. Ding, *Growth of aligned carbon nanotube arrays on metallic substrate and its application to supercapacitors,* (2008).

[17] G. Li, S. Chakrabarti, M. Schulz, and V. Shanov, *The effect of substrate positions in chemical vapor deposition reactor on the growth of carbon nanotube arrays,* (2010).

[18] B. Arash, Q. Wang, and Varadan, *Mechanical properties of carbon nanotube/polymer composites,* Scientific Reports **4**, 6479 (2014).

[19] K. Song, Y. Zhang, J. Meng, E. Green, N. Tajaddod, H. Li, and M. Minus, *Structural Polymer-Based Carbon Nanotube Composite Fibers: Understanding the Processing–Structure–Performance Relationship,* Materials **6**, 2543 (2013).

[20] A. M. Marconnet, N. Yamamoto, M. a. Panzer, B. L. Wardle, and K. E. Goodson, *Thermal conduction in aligned carbon nanotube-polymer nanocomposites with high packing density.* ACS nano **5**, 4818 (2011).

[21] Y. Wang, Z. Xu, L. Chen, Y. Jiao, and X. Wu, *Multi-scale hybrid composites-based carbon nanotubes,* Polymer Composites **32**, 159 (2011).

[22] W.-Y. Ko, Y.-F. Chen, K.-M. Lu, K.-J. Lin, and Y., *Porous honeycomb structures formed from interconnected MnO2 sheets on CNT-coated substrates for flexible all-solid-state supercapacitors,* Scientific Reports **6**, 18887 (2016).

[23] X. Tian, M. E. Itkis, and R. C. Haddon, *Application of hybrid fillers for improving the through-plane heat transport in graphite nanoplatelet-based thermal interface layers,* Scientific reports **5**, 13108 (2015).

[24] S. Faraji, K. Stano, C. Rost, J.-P. Maria, Y. Zhu, and P. D. Bradford, *Structural annealing of carbon coated aligned multi-walled carbon nanotube sheets,* Carbon **79**, 113 (2014).

[25] Z. Zhou, X. Wang, S. Faraji, P. D. Bradford, Q. Li, and Y. Zhu, *Mechanical and electrical prop-*

erties of aligned carbon nanotube/carbon matrix composites, Carbon **75**, 307 (2014).

[26] K. Fu, O. Yildiz, H. Bhanushali, Y. Wang, K. Stano, L. Xue, X. Zhang, and P. D. Bradford, *Aligned Carbon Nanotube-Silicon Sheets: A Novel Nano-architecture for Flexible Lithium Ion Battery Electrodes,* Advanced Materials **25**, 5109 (2013).

[27] S. Vollebregt, P. Padmanabhan, C. Silvestri, and P. M. Sarro, *Crystallinity variations over the length of vertically aligned carbon nanotubes grown by chemical vapour deposition,* in *41st Micro and Nano Engineering conference* (2015).

[28] D. Jung, D. Kim, K. H. Lee, L. J. Overzet, and G. S. Lee, *Transparent film heaters using multi-walled carbon nanotube sheets,* Sensors and Actuators A: Physical **199**, 176 (2013).

[29] N. J. Blasdel, E. K. Wujcik, J. E. Carletta, K.-S. Lee, and C. N. Monty, *Fabric Nanocomposite Resistance Temperature Detector,* IEEE Sensors Journal **15**, 300 (2015).

[30] C. Fung, V. Wong, R. Chan, and W. Li, *Dielectrophoretic Batch Fabrication of Bundled Carbon Nanotube Thermal Sensors,* IEEE Transactions On Nanotechnology **3**, 395 (2004).

[31] J. E. Fischer, W. Zhou, J. Vavro, M. C. Llaguno, C. Guthy, R. Haggenmueller, M. J. Casavant, D. E. Walters, and R. E. Smalley, *Magnetically aligned single wall carbon nanotube films: Preferred orientation and anisotropic transport properties,* Journal of Applied Physics **93**, 2157 (2003).

[32] L. Qiu, X. Wang, G. Su, D. Tang, X. Zheng, J. Zhu, Z. Wang, P. M. Norris, P. D. Bradford, and Y. Zhu, *Remarkably enhanced thermal transport based on a flexible horizontally-aligned carbon nanotube array film.* Scientific reports **6**, 21014 (2016).

[33] Y. Inoue, Y. Suzuki, Y. Minami, J. Muramatsu, Y. Shimamura, K. Suzuki, A. Ghemes, M. Okada, S. Sakakibara, H. Mimura, and K. Naito, *Anisotropic carbon nanotube papers fabricated from multiwalled carbon nanotube webs,* Carbon **49**, 2437 (2011).

[34] P. R. Bandaru, *Electrical Properties and Applications of Carbon Nanotube Structures,* Journal of Nanoscience and Nanotechnology **7**, 1239 (2007).

[35] M. B. Jakubinek, M. B. Johnson, M. A. White, C. Jayasinghe, G. Li, W. Cho, M. J. Schulz, and V. Shanov, *Thermal and electrical conductivity of array-spun multi-walled carbon nanotube yarns,* Carbon **50**, 244 (2012).

[36] A. Li, A. E. Bogdanovich, and P. D. Bradford, *Aligned carbon nanotube sheet piezoresistive strain sensors,* Smart Materials and Structures **24**, 095004 (2015).

[37] J.-H. Pöhls, M. B. Johnson, M. A. White, R. Malik, B. Ruff, C. Jayasinghe, M. J. Schulz, and V. Shanov, *Physical properties of carbon nanotube sheets drawn from nanotube arrays,* Carbon **50**, 4175 (2012).

[38] M. Inaba, C.-Y. Lee, K. Suzuki, M. Shibuya, M. Myodo, Y. Hirano, W. Norimatsu, M. Kusunoki, and H. Kawarada, *Contact Conductivity of Uncapped Carbon Nanotubes Formed by Silicon Carbide Decomposition,* The Journal of Physical Chemistry C **120**, 6232 (2016).

[39] Y. Jiang, P. Wang, and L. Lin, *Characterizations of contact and sheet resistances of vertically*

aligned carbon nanotube forests with intrinsic bottom contacts, Nanotechnology **22**, 365704 (2011).

[40] M. Ghatge and M. Shrivastava, *Physical Insights on the Ambiguous Metal-Graphene Interface and Proposal for Improved Contact Resistance,* IEEE Transactions on Electron Devices **62**, 4139 (2015).

[41] B. K. Kaushik and M. K. Majumder, *Interconnects,* (Springer India, 2015) pp. 1–15.

[42] B. Bourlon, C. Miko, L. Forró, D. C. Glattli, and A. Bachtold, *Determination of the Intershell Conductance in Multiwalled Carbon Nanotubes,* Physical Review Letters **93**, 176806 (2004).

[43] C. Wei, L. Dai, A. Roy, and T. B. Tolle, *Multifunctional chemical vapor sensors of aligned carbon nanotube and polymer composites,* Journal of the American Chemical Society **128**, 1412 (2006).

[44] H. Chen, J. Huang, D. W. H. Fam, and A. I. Y. Tok, *Horizontally aligned carbon nanotube based biosensors for protein detection,* Bioengineering **3**, 23 (2016).

[45] M. Miao, *Electrical conductivity of pure carbon nanotube yarns,* Carbon **49**, 3755 (2011).

[46] W. Zhao, Y. Li, S. Wu, D. Wang, X. Zhao, F. Xu, M. Zou, H. Zhang, X. He, and A. Cao, *Highly Stable Carbon Nanotube/Polyaniline Porous Network for Multifunctional Applications,* ACS Applied Materials & Interfaces , acsami.6b11984 (2016).

[47] L. Liu, Q. Yang, and J. Shen, *Correlation between Porosity and Electrical-Mechanical Properties of Carbon Nanotube Buckypaper with Various Porosities,* Journal of Nanomaterials **2015**, 1 (2015).

[48] L. Duclaux, *Review of the doping of carbon nanotubes (multiwalled and single-walled),* Carbon **40**, 1751 (2002).

[49] P. Ayala, R. Arenal, M. Rümmeli, A. Rubio, and T. Pichler, *The doping of carbon nanotubes with nitrogen and their potential applications,* Carbon **48**, 575 (2010).

[50] R. M. Silva, M. C. Ferro, J. R. Araujo, C. A. Achete, G. Clavel, R. F. Silva, and N. Pinna, *Nucleation, Growth Mechanism, and Controlled Coating of ZnO ALD onto Vertically Aligned N-Doped CNTs,* Langmuir **32**, 7038 (2016).

[51] Q. Wei, X. Tong, G. Zhang, J. Qiao, Q. Gong, and S. Sun, *Nitrogen-Doped Carbon Nanotube and Graphene Materials for Oxygen Reduction Reactions,* Catalysts **5**, 1574 (2015).

[52] R. Bian, J. Zhao, and H. Fu, *Silicon–doping in carbon nanotubes: formation energies, electronic structures, and chemical reactivity,* Journal of Molecular Modeling **19**, 1667 (2013).

[53] P. Gowrisankar and K. Udhayakumar, *Electronic properties of boron and silicon doped (10, 0) zigzag single-walled carbon nanotube upon gas molecular adsorption: a dft comparative study,* Journal of Nanomaterials **2013**, 149 (2013).

[54] J. Campos-Delgado, I. O. Maciel, D. A. Cullen, D. J. Smith, A. Jorio, M. A. Pimenta, H. Terrones, and M. Terrones, *Chemical Vapor Deposition Synthesis of N-, P-, and Si-Doped Single-Walled Carbon Nanotubes,* ACS Nano **4**, 1696 (2010).

[55] H. Jiang, D. Zhang, and R. Wang, *Silicon-doped carbon nanotubes: a potential resource for the detection of chlorophenols/chlorophenoxy radicals,* Nanotechnology **20**, 145501 (2009).

[56] A. A. Koós, R. J. Nicholls, F. Dillon, K. Kertész, L. P. Biró, A. Crossley, and N. Grobert, *Tailoring gas sensing properties of multi-walled carbon nanotubes by in situ modification with Si, P, and N,* Carbon **50**, 2816 (2012).

[57] R. J. Baierle, S. B. Fagan, R. Mota, A. J. R. da Silva, and A. Fazzio, *Electronic and structural properties of silicon-doped carbon nanotubes,* Physical Review B **64**, 085413 (2001).

[58] K. Behler, S. Osswald, H. Ye, S. Dimovski, and Y. Gogotsi, *Effect of Thermal Treatment on the Structure of Multi-walled Carbon Nanotubes,* Journal of Nanoparticle Research **8**, 615 (2006).

[59] J. Zhao, Y. Zhang, Y. Su, X. Huang, L. Wei, E. S.-W. Kong, and Y. Zhang, *Structural improvement of CVD multi-walled carbon nanotubes by a rapid annealing process,* Diamond and Related Materials **25**, 24 (2012).

[60] R. Jin, Z. X. Zhou, D. Mandrus, I. N. Ivanov, G. Eres, J. Y. Howe, a. a. Puretzky, and D. B. Geohegan, *The effect of annealing on the electrical and thermal transport properties of macroscopic bundles of long multi-wall carbon nanotubes,* Physica B: Condensed Matter **388**, 326 (2007).

[61] A. Naeemi and J. D. Meindl, *Physical Modeling of Temperature Coefficient of Resistance for Single- and Multi-Wall Carbon Nanotube Interconnects,* IEEE Electron Device Letters **28**, 135 (2007).

[62] H. Li, W.-Y. Yin, K. Banerjee, and J.-F. Mao, *Circuit Modeling and Performance Analysis of Multi-Walled Carbon Nanotube Interconnects,* IEEE Transactions on Electron Devices **55**, 1328 (2008).

[63] R. Lu, J. J. Shi, F. J. Baca, and J. Z. Wu, *High performance multiwall carbon nanotube bolometers,* Journal of Applied Physics **108**, 084305 (2010).

[64] S. Gong, Z. Zhu, and Z. Li, *Electron tunnelling and hopping effects on the temperature coefficient of resistance of carbon nanotube/polymer nanocomposites,* Physical Chemistry Chemical Physics **19**, 5113 (2017).

[65] S.-E. Lee, K.-S. Moon, and Y. Sohn, *Temperature dependence of contact resistance at metal/mwnt interface,* Applied Physics Letters **109**, 021605 (2016).

[66] G. E. Fernandes, J. H. Kim, A. K. Sood, and J. Xu, *Giant temperature coefficient of resistance in carbon nanotube/phase-change polymer nanocomposites,* Advanced Functional Materials **23**, 4678 (2013).

[67] C.-T. Hsieh, C.-E. Lee, Y.-F. Chen, J.-K. Chang, and H.-s. Teng, *Thermal conductivity from hierarchical heat sinks using carbon nanotubes and graphene nanosheets,* Nanoscale **7**, 18663 (2015).

7

CONCLUSIONS AND RECOMMENDATIONS

7.1. FROM SPACELAND TO FLATLAND

Thermal material properties play a fundamental role in the thermal management of microelectronic systems. This thesis aims at investigating the possibility to adopt CNT-based materials as on-chip thermal management solutions. A novel MEMS *in-situ* characterization platform was developed with controllable hotspot and integrated temperature sensor to measure the heat transfer performance of CNT array microstructures. The CNT microstructures were studied in two different geometrical configurations, vertical and horizontal (Spaceland and Flatland), with differents coatings, and in different physical domains, thermal and electrical. The nanoporous morphology of CNT arrays offers the unique opportunity to tailor their properties and functionality through nanoscale coatings. To perform the above-mentioned investigations, we allocate many efforts in developing fabrication processes, for both CNT microstructures, compatible with MEMS integration.

7.1.1. VERTICALLY ALIGNED CNTS - SPACELAND

The porous nature of carbon nanotube (CNT) arrays results in a very high surface area to volume ratio, which makes the material attractive for surface driven heat transfer mechanisms. In this thesis we report experimental investigations of the thermal performance of high-aspect ratio CNT nanofoam, directly grown on top of a suspended MEMS microhotplate with integrated temperature sensor and power controller. The non-destructive

in-situ characterization method, that combines electrical characterization and high-resolution thermographic analysis, can be used for any hierarchical structured porous materials. The employed experimental procedure allowed us to perform the investigations over a broad range of temperatures (294.15-575 K). We report for the first time the temperature dependence of the heat transfer coefficient in free air of CNT nanofoam.

The VA-CNT foam-like morphology allows the infiltration of conformal coatings within the array, achieving a CNT based composite with enhanced thermal performances and increased mechanical stability. The formation of a coated CNT network using a few nanometers of amorphous silicon carbide contributes to substantially increase in effective thermal conductivity (up to 181%). The high-aspect ratio coated VA-CNT micropin were successfully encapsulated by wafer-level film assisted molding procedure. This open to the opportunity to use coated VA-CNTs as through package thermal and electrical vias. The infiltration of specific coatings in the foam-like morphology will be required also for applying VA-CNT arrays in special thermal devices: thermoacoustic transducers, thermochromic displays and heat dissipation coatings and nanotexturing for solar devices.In addition, the results obtained are significant for theoretical modelling.

The main limitation to the *in-situ* heterogeneous integration of lithographically defined VA-CNT micropins with MEMS and ICs for hot spots cooling is represented by the relatively high growth temperature and the thermal contact resistance between the substrate and the CNTs.

7.1.2. HORIZONTALLY ALIGNED CNTS - FLATLAND

HA-CNT sheets are appealing for applications such as chemical and optical sensing, heat spreading and local routing, for which the vertical orientation of CNTs might result unpractical. Therefore, it is necessary to move from Spaceland to Flatland. The planar arrangement, achieved by permutation from VA-CNT to HA-CNT, was studied to overcome some of the challenges encountered in TIM based on VA-CNTs and CNT-polymer composites, such as mechanical stability or predictable thermal paths. The effects of the self-directed folding technique used are on the higher mechanical stability of HA-CNT sheet, achieved by flattening the array, and on the increased interaction among well oriented and closely packed tubes, due to densification.

The folding technique used is optimized for CNTs synthetized on both insulating (Al_2O_3) and electrical conductive (ZrN) barrier layers. Multiple suspended interconnections, large-area membranes, sensitive layers and micro-channels, all based on HA-CNT sheets were integrated at wafer scale.

As demonstrated on the VA-CNT micropins (Chapter (4)), by infiltrating nanoscale conformal coatings on CNT nanofoams is possible to improve their thermal performance and mechanical behavior. Therefore, also HA-CNT sheets have been used as scaffold to create novel materials with tailored thermal and electrical behaviour. By characterizing the HA-CNTs prior and after the silicon carbide coating infiltration, an impressive enhancement in electrical and thermal conductivity is measured (the thermal conductivity increases from 9.4 $W\,m^{-1}\,K^{-1}$ to 260 $W\,m^{-1}\,K^{-1}$ by coating with 15 nm of amorphous silicon carbide). The implementation of HA-CNT sheet is not only limited to thermal management but has potential for chemical and optical sensing and actuators.

7.2. SUGGESTIONS AND FUTURE WORKS

The results achieved in this thesis provided insights about the thermal behaviour of the VA-CNT micropins as well as thermal and electrical behaviour of HA-CNTs. Moreover, the potential of use CNTs as material for thermal management solutions was demonstrated. While the performance enhancement through nanocoatings and the non-destructive *in-situ* thermal characterization method represents the breakthroughs of this research, more it will be required to use CNT-based materials for thermal management of microelecronic systems:

- It is compulsory to lower the CNT growth temperature to reach the CMOS compatibility. However, the lower the growth temperature, the higher the amount of CNT defects. This might lower the CNT thermal conductivity. Therefore, both aspects needs to be taken into account when tuning the CVD growth of nanotubes.

- Growth on Al_2O_3 and ZrN barrier layers result in high-aspect ratio CNTs. However, the ZrN growth requires synergy between the catalyst nanoparticles, barrier-catalytic layer, carbon feedstock, CVD reactor growth conditions (temperature and flow rate) and catalyst island dimensions. This makes their effective growth quite challenging. Tests to improve the recipe stability are therefore necessary, in order to exploit the advantage to grow CNTs directly on an electrically conductive layer.

- Wafer-level encapsulation of a-SiC coated VA-CNT micropin have shown the possibility to create through mold structures that can be used as through package thermal and electrical vias. It is strongly recommended to improve the infiltration depth of ALD deposited materials.

- Although many electro-thermal investigations have been carried out throughout

this thesis, there are still topics that deserve attention. A detailed transient thermal analysis on the VA-CNTs can determine the transient thermal response of the heated element by analysing the specific heat, c_p, as function of porosity and temperature.

- A detailed theoretical model which takes into account the foam-like morphology and its variation due to coatings is required to study the convective heat transfer in VA-CNTs. For this reason, nitrogen absorption-desorption measurements need to be carried out to accurately determine the surface area involved in convective heat transfer.

- The HA-CNTs have still many aspects to be optimized and many applications to be developed. As reported in Chapter (6), by tuning the coating layer it is possible to alter the material behaviour and consequently the temperature coefficient of resistance (TCR). To achieve interconnects not subjected to self-heating could be interesting to combine two sheets one semiconductor and the other one metallic, by performing two different coatings, in order to achieve a bilayer with a total TCR equal or around zero.

- The thermal management is not the only potential field in which both VA- and HA- CNT can be applied. In our research group, many applications related to VA-CNT have been successfully realized: electrodes for micro-electrode arrays (MEA), 3D interconnects, supercapacitors and structural materials with tuned properties. It might be interesting to investigate VA-CNT as sensing layer of a gas sensor due to its high surface area. Moreover, investigating on ferromagnetic coating of VA-CNTs can be interesting for creating programmable routing interconnects using a localized magnetic field.

A

APPENDIX A

A.1. SUPPORTING INFORMATION CHAPTER 2

A.1.1. WATER DROPLETS ON CNTS

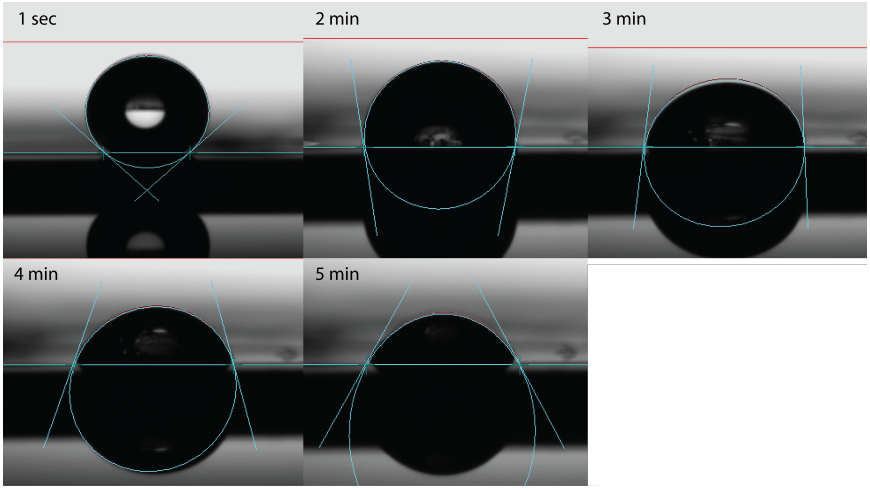


Figure A.1: Time lapse of a water droplet on CNT forest grown on Al_2O_3 barrier layer. The water droplet is not stable and it starts seeping into the CNT forest voids after few minutes.

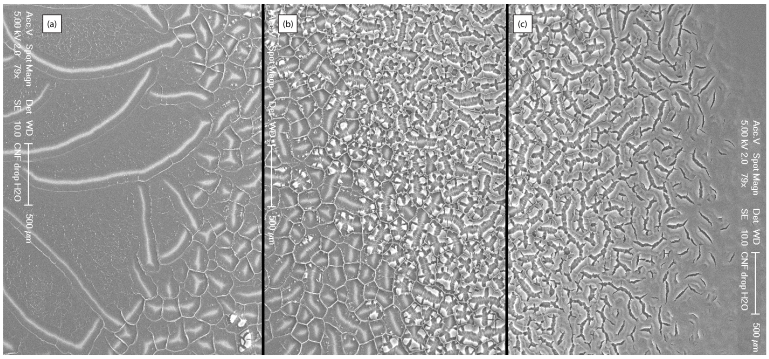


Figure A.2: Impact of a DI water droplet on the CNT forest. The progressive water evaporation it is visible on the forest morphology. In particular, (a) corresponds to the droplet centre, (b) and (c) correspond to circumferences with increasing distance to the centre.

A.1.2. AFM APPLIED ON HA-CNT SHEETS

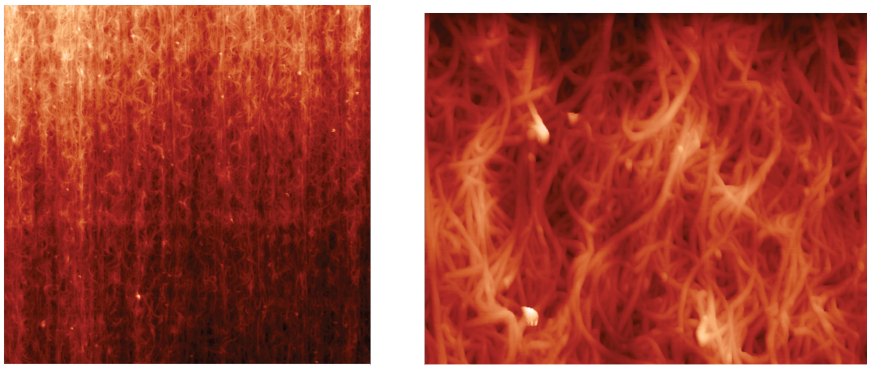


Figure A.3: The morphology HA-CNT sheets as well as their thickness can be determined by AFM. (a) AFM map of an area of $10\,\mu m^2$ and (b) close-up of an area of $2\,\mu m$ by $1.4\,\mu m$

B

APPENDIX B

B.1. FLOWCHART OF VA-CNTS ON MICROHOTPLATE

B.1.1. MHP FABRICATION

Main steps for the fabrication of a microhotplate. Starting material: Single side polished wafer of 500µm

- Si substrate with full wafer alignment markers
- Full cleaning line
- Deposition of 200 nm low-stress SiN_x (recipe 4INCHST)
- Thickness inspection
- Lithography: Negative resist (CO-Nlof-3µm); use mask DS1834-Pt, BOX 414; Manual X-link bake (115°C for 90 sec); Use development program: Dev –X-link bake
- Inspection linewidth and overlay: no Pt for at least 5 mm from the edge after lift-off
- DUV bake (program: lift-off)
- Tepla flash program 6. Remark: Tepla should be at room temperature before starting.
- Evaporation of 20 nm Ta and 160 nm Pt, T<85°C
- Lift-off (SAL lab): NMP 70°C

- Wafer cleaning
- Deposition of 200 nm low-stress SiN_x (recipe LSSINNEW)
- Thickness inspection
- Annealing 1000°C
- Manual lithography backside: HDMS; 1.4µm SPR3017 positive photo-resist; Softbake; use mask DS 1834-KOH, BOX 414; Post exposure bake; development in MF322
- Inspection linewidth and overlay
- Dry etching of LPCVD nitride to open the windows (program StdSiN)
- Inspection
- O_2 cleaning
- Cleaning procedure
- Manual lithography frontside: HDMS; 1.4µm SPR3017 positive photo-resist; Softbake; use mask DS 1834–CB, BOX 414; Post exposure bake; development in MF322
- Inspection linewidth and overlay
- Dry etching of LPCVD nitride to open the contact pads (in Alcatel to land on Pt)
- O_2 cleaning
- Cleaning procedure
- KOH for membrane release KOH 33% at 85°C; Temp oil = 100°C, t= 6hr 30min.

B.1.2. CNT SYNTHESIS

Main steps required to grow CNTs

- Al_2O_3 spattering 30 nm. Use recipe Al2O3-30nm-100°C after performing a target cleaning
- Manual lithography frontside: HDMS; 1.4µm with AZ Nlof 2070 negative photoresist; Softbake; use mask DS 1834-CNT-V2, BOX 432; Post exposure bake; development in MF322

- Inspection linewidth and overlay
- Catalyst evaporation 1.2 nm Fe, recipe 11
- Lift-off (SAL lab): NMP 80°C
- Wafer cleaning
- Inspection
- CNT growth 650 °C tune time depending on the targeted height

C

APPENDIX C

C.1. FLOWCHART OF HA-CNTS ON PRE-PATTERNED WAFERS

C.1.1. WAFER PATTENING

Main steps for the fabrication of the pre-patterned wafer Starting material: Double side polished wafer of 400 µm

- Si substrate with full wafer alignment markers
- Full cleaning line
- Lithography: Resist (CO-3012-3.1 µm); use mask KOH-3N , BOX 464; development DP2
- Inspection linewidth and overlay
- DRIE etching of pillars
- O_2 cleaning
- Full cleaning line
- TEOS deposition 500 nm
- Thickness inspection
- Deposition of 400 nm low-stress SiN_x (recipe 4INCHST)
- Thickness inspection

- Backside deposition of 6µm PECVD oxide
- Cleaning procedure
- pure Al sputtering 1µm (recipe Al-p-1000nm-25)
- Lithography backside: Negative resist (CO-Nlof-3.1µm); use mask KOH-3N , BOX 464; Manual X-link bake(115°C for 90 sec); Use development program: Dev –X-link bake
- Inspection linewidth and overlay
- Backside etching for windows opening (PECVD oxide+SIN+TEOS) recipe STDOXID; recipe STDSIN;
- O_2 cleaning
- Cleaning line for metals
- DRIE etching for membrane release (Use sequence NEP-throughwafer-xxx)
- O_2 extensive cleaning
- Cleaning line for metals
- Al removal in PES
- TEOS removal in BHF
- Manual lithography frontside: HDMS; 1.4µm with AZ Nlof 2070 negative photo-resist; Softbake; use mask DS 1978-Pt, BOX 464; Post exposure bake; development in MF322
- Evaporation of 20 nm Ta and 160 nm Pt, T < 85°C
- Lift-off (SAL lab): NMP 70°C
- Wafer cleaning

C.1.2. VA-CNT SYNTHESIS

Main steps required to grow CNTs. Here we report the procedure for the Al_2O_3 as barrier layer

- Al_2O_3 or ZrN spattering 30 nm. Use recipe Al2O3-30nm-100°C or ZrN-30nm-350°C after performing a target cleaning

- Manual lithography frontside: HDMS; 1.4µm with AZ Nlof 2070 negative photoresist; Softbake; use mask DS 1978-CNT, BOX 464; Post exposure bake; development in MF322
- Inspection linewidth and overlay
- Catalyst evaporation 1.2 nm Fe, recipe 11
- Lift-off (SAL lab): NMP 80°C
- Wafer cleaning
- Inspection
- CNT growth 650 °C tune time depending on the targeted height

After the VA-CNT synthesis the liquid assisted flattening process is applied as explained in details in Chapter (5).

NOMENCLATURE

A_{array}	Cross sectional area of a CNT array
A_c	Cross sectional area of the micropin
A_{CNT}	Average cross sectional area of a single nanotube
A_s	Micropin surface area
$A_{s_{TOT}}$	Device surface area
b	Nanotube radius
D	Micropin diameter
d_{CNT}	Average nanotube diameter
D_r	Densification ratio
E	Effective Young's modulus of the VA-CNT array
E_{CNT}	Young's modulus of the individual nanotube
F_c	Capillary force
F_{el}	Euler's critical load
g	Gravitational acceleration
k	Thermal conductivity of other materials involved
k_{CNT}	Thermal conductivity of an individual MWCNT in VA-CNT
k_{eff}	Effective thermal conductivity
H	Height of VA-CNT array
H_c	Equivalent natural convective heat transfer coefficient
h_c	Capillary rise
H_{rad}	Radiative heat transfer coefficient
H_{TOT}	Total heat transfer coefficient
J	Current density provided to the MHP
L	Micropin lenght
L_{bk}	Capillary buckling length
L_c	Corrected micropin length
$L_{CNT-CNT}$	Overlap length between adjacent HA-CNT sheets
L_d	Height of the densified microstructure
$L_{N_{stick}}$	Multi-fiber sticking distance

L_{ov}	Overlap length between HA-CNT sheet and electrode
L_s	Average HA-CNT sheet length
L_{stick}	Critical sticking length
N	Number of HA-CNT sheets involved
N_{CNT}	Number of CNTs per unit area
P	Micropin perimeter
P_{air}	Power dissipated in air
P_{cond}	Power dissipated through conduction
P_{conv}	Power dissipated through convection
P_{rad}	Power dissipated through radiation
P_{vac}	Power dissipated in vacuum
Q_{MHP}	MHP heat transfer rate
Q_{pin}	Single micropin heat transfer rate
$Q_{Tot_{device}}$	MHP + micropin configuration heat transfer rate
Q_{Tpin}	Multipin heat transfer rate
r	Length dependent resistance
R	Meniscus surface curvature
R_c	Contact resistance
R_{HA-CNT}	HA-CNT resistance
R_{HH}	Contact resistance among overlapping HA-CNTs sheets
s	Nanotube spacing
T	Thickness of VA-CNT array
t	Densified thickness of HA-CNT array
T_{avg}	Average temperature measured from the MHP
T_b	Micropin base temperature
T_{max}	Maximum temperature
T_o	Reference temperature
T_s	Temperature along the micropin
T_{tip}	Micropin tip temperature
T_∞	Ambient temperature
W	Width of VA-CNT array
w	Densified width of HA-CNT array

Greek letters:

α	Thermal coefficient of resistance
ϵ	Material emissivity

γ	liquid surface tension
ρ	Porosity
ρ	Density of the liquid
ρ_o	Resistivity at reference temperature
σ	Stefan-Boltzmann constant (5.67×10^{-8} W m^{-2} K^{-4})
σ_e	Linearized electrical conductivity of the Pt spiral

Subscripts

$6m$	Multipin configuration
Al_2O_3	CNT arrays (VA- or HA-CNTs)subjected to alumina coating
$a-SiC$	CNT arrays (VA- or HA-CNTs) subjected to amorphous silicon carbide coating

SUMMARY

The performances of microelectronic and optoelectronic devices are often severely limited by high temperatures and insufficient heat management. Therefore, when considering device fabrication and packaging, it is important to select materials based on their thermal performance. The increasing demand for more integrated functionality and miniaturization of microelectronic systems is pushing the limits of traditional cooling and packaging approaches. In fact, thermal management may well be the major bottleneck of the next electronics revolution. Efficient thermal management solutions are required at chip level as well as at system level. For example, heat dissipation is fundamental in microprocessor and integrated circuits (ICs) as in current mobile electronic or in server farms. Moreover, self-heating in applications like high power light-emitting diodes and solar cells affects their long-term stability. Therefore, novel cooling solutions are being developed based on nanotechnologies and functional nanomaterials. In particular, nanomaterials are mainly used as localized on-chip cooling solutions. They span from harvesting thermal energy, by using piezoelectric nanowires and super-lattice thin films, to heat spreading through graphene layers or nanocrystalline diamond, towards carbon nanotubes (CNTs) as thermal interface material (TIM) and heat sinks.

In this respect, CNT-based macroscopic composite materials appear to be a promising candidate for achieving effective local heat dissipation. In fact, CNTs are one of the few nanoscale materials that can be grown from a bottom-up template, which is lithographically defined and patterned using a CMOS compatible process. This makes the material extremely suitable for large-scale integration with microelectronics, replacing the need for heterogeneous integration and assembly of bulky macro-cooling solutions. It is well known that carbon allotropes and their derivatives possess superior thermal properties. This thesis aims at investigating the possibility to adopt CNT-based materials as building blocks for on-chip cooling solutions. CNTs can grow fast (growth rate of around 20 $\mu m\ min^{-1}$) and can span size scales ranging from nanometers to centimeters. Our effort were allocated to the design, fabrication, characterization and enhancement of both high-aspect-ratio vertically-aligned CNTs (VA-CNTs) as well as nanometer functional thin films based on horizontally aligned CNTs (HA-CNTs). Individual carbon nanotube has shown superior thermal, mechanical, electrical and optical properties.

Unfortunately, these excellent properties are difficult to be preserved in macroscopic applications. Therefore, for analysing and predicting microelectronic system performance, it is imperative that the CNT material properties are characterized and optimized. To characterize the thermal performance of several VA-CNT configurations a novel measurement approach was developed combining MEMS microhotplates (MHPs) with high-resolution thermographic analysis. We quantify the equivalent natural convective heat transfer coefficient between solid–air interface (H_c), the radiative heat transfer coefficient (H_{rad}) and the CNT nanofoam effective thermal conductivity (k_{eff}) over a wide temperature range. In particular, at the VA-CNT nanofoam demonstrated a gradually increase of the effective thermal conductivity with temperature from: 1.04 W m^{-1} K^{-1} at 369 K to 2.24 W m^{-1} K^{-1} at 510 K. To achieve HA-CNTs, a self-directed folding technique is optimized for CNTs synthetized on both insulating (alluminum oxide (Al_2O_3)) and electrical conductive (zirconium nitride (ZrN)) barrier layers. The achieved HA-CNT sheets were integrated at wafer scale, and thermally and electrically characterized. They show high robustness thus increasing the possibility to introduce CNTs in standard microfabrication processes. For both VA- and HA-CNTs, we present a method to take advantage of their foam-like morphology by using them as scaffolds for creating reinforced heterostructures with tailored material properties. In particular, we achieved up to 181% of thermal conductive transport enhancement in VA-CNTs conformally coated with a nanometer layer of amorphous silicon carbide (a-SiC). In HA-CNTs, an impressive enhancement in electrical conductivity is measured, approximately 209% for the Al_2O_3 coated HA-CNTs and 2276% for the a-SiC ones. From the thermal point of view, the Al_2O_3 coating increases the temperature distribution uniformity of the HA-CNT sheet, while after coating the sheets whit a-SiC, the thermal conductivity increases from 9.4 W m^{-1} K^{-1} to 260 W m^{-1} K^{-1}. The observed thermal transport capability of CNT nanofoam provides crucial insights for their application as localized and customized on-chip cooling solutions for consumer electronics. In addition, the results obtained are significant for theoretical modelling, as well as for several devices: thermoacoustic transducers, thermochromic displays, chemical and optical sensors, and nanotexturing for solar devices.

SAMENVATTING

De prestaties van micro-elektronische en opto-elektronische apparaten worden vaak sterk beperkt door hoge temperaturen en onvoldoende warmte-management. Bij de fabricage en encapsulatie van deze apparaten, is het daarom belangrijk materialen te selecteren op basis van hun thermische prestatie. De toenemende vraag naar meer geïntegreerde functionaliteit en miniaturisatie van micro-elektronische systemen verschuift de grenzen van traditionele koeling en verpakkings-benaderingen. In feite, kan thermisch management wellicht het belangrijkste knelpunt zijn van de volgende elektronische revolutie. Efficiënte thermische-management oplossingen zijn zo- wel op chip-niveau als op systeemniveau vereist. Warmte-disspatie is bijvoorbeeld fundamenteel in microprocessors en geïntegreerde schakelingen (IC's) zoals in de huidige mobiele elektronica of in servergroepen. Bovendien, beïnvloedt zelf-verwarming de lange-termijn stabiliteit van applicaties zoals hoog vermogen lichtgevende diodes en zonnecellen. Daarom worden nieuwe koeloplossingen ontwikkeld op basis van nanotechnologieën en functionele nanomaterialen. In het bijzonder worden nanomaterialen voornamelijk gebruikt als gelokaliseerde on-chip koeloplossingen. Deze oplossingen lopen uiteen van het verzamelen van thermische energie, door gebruik te maken van piëzo-elektrische nanodraden en 'super-lattice' dunne-films, via warmte verspreiden via grafeen-lagen of nano-kristallijne diamanten, tot aan koolstof nanobuizen (CNT's) als thermisch koppel-materiaal (TIM) en koelblokken.

In dit verband lijken CNT-gebaseerde macroscopische composietmaterialen een veelbelovende kandidaat te zijn voor het bereiken van effectief lokale warmteafvoer. In feite zijn CNT's een van de weinige nanoschaalmaterialen die kunnen worden gekweekt uit een bottom-up kunnen worden gegroeid, die lithografisch gedefinieerd en gepatroneerd zijn met behulp van een CMOS-compatibel proces. Dit maakt het materiaal uitermate geschikt voor grootschalige integratie met micro-elektronica, waardoor de behoefte aan heterogene integratie en montage van omvangrijke macro-koeloplossingen wordt vervangen. Het is algemeen bekend dat koolstof-allotropen en hun afgeleiden superieure thermische eigenschappen bezitten. Dit proefschrift heeft tot doel de mogelijkheid te onderzoeken om CNT-gebaseerde materialen te gebruiken als bouwstenen voor on-chip koeloplossingen. CNT's kunnen snel groeien (groeitempo van ongeveer

20 µm min^{-1}) en kunnen in grootte variëren van nanometer tot centimeter. Onze inspanningen werden toegewezen aan het ontwerp, fabricage, karakterisering en de verbetering van zowel de hoge aspect-ratio driedimensionale (3D) microarchitecturen gemaakt van verticaal uitgelijnde CNT's (VA-CNT's), als de nanometer-functionele dunne films op basis van horizontaal uitgelijnde CNT's (HA-CNT's) voor elektronische en thermische toepassingen op grote oppervlaktes.

Een individuele koolstof nanobuis heeft superieure thermische, mechanische, elektrische en optische eigenschappen laten zien. Helaas zijn deze uitstekende eigenschappen moeilijk te behouden in macroscopische toepassingen. Daarom is het van essentieel belang dat de CNT-materiaaleigenschap- pen worden gekarakteriseerd en geoptimaliseerd, zodat micro-elektronische systeemprestaties geanalyseerd en voorspeld kunnen worden. Om de thermische prestaties van verschillende VA-CNT configuraties te karakteriseren, werd een nieuwe meetmethode ontwikkeld die MEMS microhotplates (MHP's) combineerde met thermografische analyse met hoge resolutie. Wij kwantificeren de equivalente natuurlijke convectieve warmteoverdrachtscoëfficiënt tussen de solide-lucht overgang (H_c), de radiatieve warmteoverdrachtscoëfficiënt (H_{rad}) en effectieve thermische geleidbaarheid (k_{eff}) van de CNT nanofoam over een breed temperatuurbereik. In het bijzonder vertoonde zich bij de VA-CNT nanofoam een geleidelijke toename van de effectieve thermische geleidbaarheid door temperatuur van: 1.04 W m^{-1} K^{-1} bij 369 K tot 2.24 W m^{-1} K^{-1} bij 510 K. Om HA-CNT's te verwezenlijken is een zelfgerichte vouwtechniek geoptimaliseerd voor CNT's die op zowel isolerend (aluminiumoxide (Al_2O_3)) als op elektrisch geleidende (zirkoniumnitride (ZrN)) barrièrelagen zijn gesynthetiseerd. De verkregen HA-CNT vellen werden geïntegreerd op wafelschaal, en thermisch en elektrisch gekarakteriseerd. Ze tonen een hoge robuustheid, waardoor de mogelijkheid om CNT's in standaard microfabricatie processen te introduceren wordt verhoogd.

Voor zowel VA- als HA-CNT's presenteren wij een methode om gebruik te maken van hun schuimachtige morfologie door ze te gebruiken als steigers voor het creëren van versterkte heterostructuren met aangepaste materiaal eigenschappen. In het bijzonder hebben we tot 181% verbetering van de thermische geleidend warmtetransport in VA-CNT's behaald die gecoat zijn met een nanometer-laag van amorf siliciumcarbide (a-SiC). Bij HA-CNT's wordt een indrukwekkende verbetering in elektrische geleidbaarheid gemeten, ongeveer 209% voor de Al_2O_3-gecoate HA-CNT's en 2276% voor de a-SiC HA-CNT's. Vanuit het thermische oogpunt vergroot de Al_2O_3-coating de uniformiteit van de temperatuurverdeling van het HA-CNT-vel, terwijl na het coaten met a-SiC de warmtegeleidingsvermogen stijgt van 9.4W m^{-1} K^{-1} tot 260 W m^{-1} K^{-1}.

De waargenomen thermische transportmogelijkheid van CNT nanofoam biedt cruciale inzichten voor hun toepassing als gelokaliseerde en aangepaste on-chip koeloplossingen voor consumentenelektronica. Bovendien zijn de verkregen resultaten belangrijk voor theoretische modellering, evenals voor meerdere apparaten: thermo-akoestische transducers, thermochrome displays, chemische en optische sensoren en nano-texturing voor zonne-apparatuur.

List of Publications

Journal Papers

1. **Cinzia Silvestri**, Michele Riccio, René H. Poelma, Bruno Morana, Sten Vollebregt, Fabio Santagata, Andrea Irace, Kouchi Zhang, Pasqualina M. Sarro. "Thermal characterization of carbon nanotube foam using MEMS microhotplates and thermographic analysis".*Nanoscale*, Volume 8, pp. 8266-8275, 2016.

2. **Cinzia Silvestri**, Michele Riccio, René H. Poelma, Aleksandar Jovic, Bruno Morana, Sten Vollebregt, Andrea Irace, Guo Qi Zhang, Pasqualina M. Sarro. "Enhancing Thermal Transport Efficiency in High Aspect Ratio Carbon Nanotube Arrays by Conformal Coatings". Submitted to *Nanoscale*, 2017.

3. **Cinzia Silvestri**, Michele Riccio, René H. Poelma, Andrea Irace, Guo Qi Zhang, Pasqualina M. Sarro. "Enhanced Thermal Transport in Horizontally Aligned Carbon Nanotube sheets by Conformal Coatings".To be submitted to *Na-noscale*, 2017.

4. Nikolas Gaio, **Cinzia Silvestri**, Berend van Meer, Sten Vollebregt, Christine L. Mummery, Ronald Dekker."Fabrication and characterization of an Upside-down Carbon Nanotube (CNT) Microelectrode array (MEA)". *IEEE Sensors Journal*, Volume 16, Issue 24, pp. 8685-8691, 2016.

5. Fabio Santagata, Catello Farriciello, Giuseppe Fiorentino, Henk W. van Zeijl, **Cinzia Silvestri**, Kouchi Zhang, Pasqualina M. Sarro. "Fully back-end TSV process by Cu electro-less plating for 3D smart sensor systems", *Journal of Micromechanics and Microengineering*, Volume 23, pp. 55014, 2013.

CONFERENCE PAPERS AND PRESENTATIONS

1. **Cinzia Silvestri**, Federico Marciano, Bruno Morana, Violeta Podranovic, Sten Vollebregt, Kouchi Zhang, Pasqualina M. Sarro. "Horizontally aligned carbon nanotube scaffolds for freestanding structures with enhanced conductivity". *In 30th IEEE International Conference on Micro Electro Mechanical Systems (MEMS 2017) (MEMS 2017)*, Las Vegas, USA, pp. 266-269, 2017.

2. **Cinzia Silvestri**, Paolo Piacciafoco, Bruno Morana, Fabio Santagata, Kouchi Zhang, Pasqualina M. Sarro. "Electro-thermal simulation and characterization of vertically aligned CNTs directly grown on a suspended microhoplate for thermal management applications". *In IEEE Sensors Conference*, Valencia, Spain, pp. 827-830, 2014.

3. **Cinzia Silvestri**, Bruno Morana, Giuseppe Fiorentino, Sten Vollebregt, Gregory Pandraud, Fabio Santagata, Kouchi Zhang, P.M. Sarro. "CNT bundles growth on microhotplates for direct measurement of their thermal properties". *In 27th IEEE International Conference on Micro Electro Mechanical Systems (MEMS 2014)*, San Francisco, USA, pp. 48-51, 2014.

4. **Cinzia Silvestri**, Kouchi Zhang, Pasqualina M. Sarro. *ICT.Open*, Amersfoort, The Netherlands, 22-23 March, 2016.

5. **Cinzia Silvestri**, Fabio Santagata, Kouchi Zhang, Pasqualina M. Sarro. *NanoCity 2015*, Amsterdam, The Netherlands, 21 June, 2016.

6. **Cinzia Silvestri**, Fabio Santagata, Kouchi Zhang, Pasqualina M. Sarro. *NanoCity 2015*, Amersfoort, The Netherlands, 5-6 October, 2015.

7. **Cinzia Silvestri**, Kouchi Zhang, Pasqualina M. Sarro. *MicroNano Conference 2015*, Amsterdam, The Netherlands, 12-13 December, 2015.

8. **Cinzia Silvestri**, Fabio Santagata, Kouchi Zhang, Pasqualina M. Sarro. *NanoCity 2014*, Utrecht, The Netherlands, 27-28 October, 2014.

9. Bruno Morana, **Cinzia Silvestri**, Fredrick J. Creemer, Pasqualina M. Sarro. "All-SiC surface micromachined nanoreactor for in-situ transmission electron microscopy". *In 29th IEEE International Conference on Micro Electro Mechanical Systems (MEMS 2016)*, Shanghai, China, pp. 753-756, 2016.

10. William Quiros Solano, Nikolas Gaio, **Cinzia Silvestri**, Gregory Pandraud, Pasqualina M. Sarro. "PEDOT:PDMS: a conductive and flexible polymer for sensor integration

in Organ-on-Chip platforms". *In Procedia Engineering: Proceedings of the 30th anniversary Eurosensors Conference*, Budapest, Hungary, pp. 1184-1187, 2016.

11. Nikolas Gaio, Berend van Meer, **Cinzia Silvestri**, Saeed Khoshfetrat Pakazad, Sten Vollebregt, Christine L. Mummery, Ronald Dekker."Upside-down Carbon Nanotube (CNT) Micro-electrode Array (MEA)". *In IEEE Sensors Conference*, Busan, South Korea, Volume 16, Issue 24, pp. 1-4, 2015.

12. Fabio Santagata, Giovanni Almanno, Sten Vollebregt, **Cinzia Silvestri**, Kouchi Zhang, Pasqualina M. Sarro."Carbon Nanotube based heat-sink for solid state lighting". *In 8th IEEE Int. Conf. Nano/Micro Engineered and Molecular Systems (NEMS)*, Suzhou, China, 2013.

13. Sten Vollebregt, Preethi Padmanabhan, **Cinzia Silvestri**, Pasqualina M. Sarro. "Crystallinity variations over the length of vertically aligned carbon nanotubes grown by chemical vapour deposition". *In 41st Micro and Nano Engineering conference*, The Hague, The Netherlands, 2015.

PROPOSAL CONTRIBUTIONS

- Design, fabrication and testing of an user-friendly interface for organ on chips". Project Leader: Cinzia Silvestri. STW take-off phase 1.
- "Towards realistic barriers: Bringing microfabrication and Organ-on-Chips technology together to model cellular barriers." NanoInside Pilot Project Proposal. Funded by NanoNextNL.
- "BIOND: A universal Organ on chip platform". Project Leader: Ronald Dekker. NanoNextNL Valorisation Programme.

HONORS AND AWARDS RELATED TO THIS THESIS

- **Oral presentation**
  IEEE International Conference on Micro Electro Mechanical Systems 2017 (MEMS 2017), Las Vegas, USA, 26-30 January.

- **Best Paper Award - Track 1**
  IEEE Sensor Conference 2014, Valencia, Spain

- **Oral presentation**
  IEEE International Conference on Micro Electro Mechanical Systems 2014 (MEMS 2014), San Francisco, USA, 22-26 January.